DISS. ETH NO. 23533

HUBBARD MODELS ON GENERAL LATTICES: A DYNAMICAL CLUSTER APPROXIMATION APPROACH

A thesis submitted to attain the degree of

DOCTOR OF SCIENCES of ETH ZURICH

(Dr. sc. ETH Zurich)

presented by

JAKUB IMRIŠKA

Mgr., Comenius University in Bratislava

born on 23.08.1986

citizen of
Slovak Republic

accepted on the recommendation of

Prof. Dr. Matthias Troyer, examiner
Prof. Dr. Emanuel Gull, co-examiner

2016

Jakub Imriška
Hubbard models on general lattices:
A dynamical cluster approximation approach
Diss. ETH No. 23533

Digital Object Identifier DOI: 10.3929/ethz-a-010657714
E-mail jimriska@phys.ethz.ch

Contents

Abstract

The topic of this thesis is simulation of the Hubbard model on general lattices in strongly correlated regime. We approached the task with the dynamical cluster approximation (DCA), a cluster extension of the dynamical mean-field theory. That is a controlled approximation which approaches the exact solution asymptotically in cluster size. The cluster size determines the resolution of the piece-wise constant approximated lattice self energy in the reciprocal space. It exhibits reduced finite size effects and sign problem when compared to finite lattice simulations. We used it in a connection with the numerically exact continuous-time auxiliary field quantum Monte Carlo impurity solver.

This thesis includes three main projects in which we exploited the strengths of the DCA method. The first of them contains a quantitative comparison of the numerical results with the experimental measurements in a realization of the Hubbard model utilizing ultracold atoms in optical lattices. The system of interest was defined on a cubic lattice with enhanced hopping along a single lattice axis. An important outcome was an estimate of heating during the lattice ramp up process in the experiment. We calculated the temperature and the entropy density at the Néel transition and provided quantities currently inaccessible in the experiment.

The second project deals with stacked lattices with planes made of honeycomb or square lattices. There we searched for parameter regions suitable for adiabatic interaction driven cooling at and away from the half filling. We found the critical temperatures of the Néel transition for various anisotropy ratios and interaction strengths in both lattices. To achieve that, we measured four point correlators, and obtained the patch-wise constant approximation of the particle-hole irreducible vertex, used to obtain the corresponding susceptibility. To the best of our knowledge, this was the first DCA study with susceptibility measurement on a non-Bravais lattice.

In the third study we inspect the sign problem plagued Haldane model with the Hubbard interaction. The DCA method allows investigation with moderately sized clusters at sufficiently low temperature to effectively investigate the ground state

phase diagram. The frequency dependent treatment is beyond the simple static mean-field approximation that has been applied to the model in the past. While the mean-field methods predict a continuous transition from the non-magnetic Chern insulator to the antiferromagnetic insulator via a topologically non-trivial long-range ordered phase, a first order phase transition preempting the intermediate phase is found in our simulations. Valuable insight comes from analysis of different clusters, bringing up hints that in this model it is essential to respect the spatial symmetries at all levels of the employed approximation. Along with the need of accurate representation of the high symmetry reciprocal points of the model.

Zusammenfassung

Gegenstand dieser Arbeit ist Simulation des Hubbard-Modells auf verschiedenen generellen Gittern im stark korrelierten Regime. Diese Aufgabe haben wir mittels *dynamical cluster approximation* (DCA) gelöst. DCA ist eine Clustererweiterung der dynamischen Molekularfeldtheorie (DMFT). Die Näherung ist kontrolliert, da sich die DCA Lösung asymptotisch in der Clustergrösse der exakten Lösung nähert. Die Clustergrösse bestimmt die Auflösung der stückweise konstant approximierten Selbstenergie im reziproken Raum. Im Vegleich mit Simulationen auf endlichen Gittern weist DCA reduzierten Effekt der endlichen Gittergrösse, sowie auch des sogenannten Vorzeichenproblems auf. Wir haben die Methode in Verbindung mit dem numerisch exakten *continuous-time auxiliary field* Quantum Monte Carlo Störstellenprogramm benutzt.

Diese Dissertation beinhaltet drei Hauptprojekte, in welchen wir die Stärken von DCA zu Nutze machen. Das erste umfasst den quantitativen Vergleich der numerischen Lösung mit experimentellen Messungen in einer Realisation des Hubbard-Modells mittels ultrakalten Atomen in optischen Gittern. Das Gitter war kubisch mit vergrösserten Hüpfamplituden entlang einer der Gitterachsen. Wichtiger Ausgang dieser Studie war eine Abschätzung der Erwärmung während des Gitteraufschaltens im Experiment. Wir haben die Néel-Temperatur und die dazugehörige Entropiedichte berechnet.

Das zweite Projekt befasst sich mit gestapelten Gittern, die in der Ebene Quadrat- oder Wabengitter aufweisen. Im Rahmen dieses Projekts haben wir geeignete Parameterregionen für adiabatische interaktionsgeförderte Kühlung gesucht, bei beliebiger Füllung. Wir haben die kritische Temperatur des Néelschen Übergangs für verschiedene Anisotropiequotienten und Interaktionsgrössen in beiden Gittern bestimmt. Dafür haben wir Vierpunktkorrelationen gemessen, aus denen wir die stückweise konstante Annäherung des Teilchen-Loch-irreduziblen Vertex bekommen haben, welche zur Berechnung der antiferromagnetischen Suszeptibilität dient. Dies ist die erste uns bekannte DCA Studie mit Suszeptibilitätsmessung für ein allgemeines Gitter.

Die dritte Studie inspiziert das Modell von Haldane mit Hubbard-Interaktion, dessen Untersuchung unter dem Vorzeichenproblem leidet. Die DCA Methode ermöglicht Untersuchung mit moderat grossen Clustern bei genügend niedriger Temperatur, um effektiv das Grundzustandphasendiagram zu bestimmen. Die frequenzabhängige Behandlung ist der einfachen statischen Molekularfeldnäherung, die früher auf das Modell angewandt wurde, überlegen. Die Molekularfeldnäherung sagt die Existenz eines topologisch nichttrivialen und zudem geordneten Zustandes vorher. Nach unserer Simulation nach ist dieser Zustand nicht präsent, und anstatt eines kontinuierlichen Phasenübergangs von nichtmagnetischem Chern Isolator zu antiferromagnetischem Isolator finden wir einen Phasenübergang mit springendem Ordnungsparameter. Einen wertvollen Hinweis erhalten wir aus der Analyse der Simulation weiterer Cluster: für dieses Modell scheint es essenziell, dass die Näherung die Gittersymmetrien auf allen Ebenen respektiert. Ausserdem stellt sich heraus, dass eine akkurate Representation der hochsymmetrischen reziproken Punkte wichtig ist.

1 Model systems

1.1 Introduction

The complete understanding of the condensed matter physics seems to be within reach as the governing principles are established, unlike in the high energy physics where the goal is to unveil the foundations. Indeed, for most phenomena in condensed matter physics it is enough to take into account non-relativistic quantum mechanics with particles interacting via the Coulomb interaction. By adding a coupling to magnetic and gravitational field ([7]), and by taking into account the relativistic corrections (spin-orbit coupling, Rashba term), we cover practically all condensed matter phenomena. However, the presented simplicity is misleading and we are still far from the full understanding of condensed matter systems. Direct treatment of the equation of motion, the Schrödinger's equation,

$$i\hbar\frac{\mathrm{d}}{\mathrm{d}t}\left|\psi\right\rangle = \hat{H}\left|\psi\right\rangle \ , \qquad \text{or} \qquad i\hbar\frac{\mathrm{d}}{\mathrm{d}t}\hat{\rho} = \left[\hat{H},\hat{\rho}\right] \ , \tag{1.1}$$

is for many-body problems unrealistic due to exponentially large Hilbert space for state $|\psi\rangle$, upon which the density matrix operator $\hat{\rho} = \sum_i |\psi_i\rangle\, p_i \,\langle\psi_i|$ acts; with $\sum_i p_i = 1$, $p_i \geq 0$, $\{|\psi_i\rangle\}$ is a (many-body) basis. While problems with a large configurational space also appear in classical physics dealing with large number of degrees of freedom, there are important differences – among them most prominent is the *exponential* instead of *linear* growth of the configuration space dimension as a function of system size due to the quantum superposition principle, which allows for an entanglement of particles irrespective of distance. Indistinguishability of the particles and the corresponding fermionic or bosonic statistics[1] is other major difference. The concepts of statistical physics can be applied both in classical and quantum case, but the key task – macroscopic property prediction based on a microscopic model – requires evaluation of the summands in the partition sum of

[1] Or even more exotic anyonic or non-abelian statistics [8, 9, 10].

the microscopic model. A common origin of the difficulty in both the classical and quantum problems are non-linearities, *e.g.* the convective derivative term $(\mathbf{v} \cdot \nabla)\,\mathbf{v}$ in hydrodynamics and the interaction terms in the quantum case. Effective solution methods exist in both cases for linear problems.

These technical difficulties could be thought of as marginal, expecting only quantitative changes rather than qualitatively new phenomena, as observed in the Landau theory of Fermi liquids. However, in large ($N \to \infty$) ensembles of degrees of freedom, entirely new phenomena may arise once the adiabatic connection to the weakly-interacting phase is broken, typically via a symmetry breaking of the underlying principles [11].The effective low energy theory for these large collections may be often given in terms of emergent particles that have properties unrelated to those of the underlying constituents – for example the massless Dirac fermions [12, 13], Cooper pairs of electrons [14], or composite fermions with fractional charge [15].

It is therefore essential in condensed matter physics to proceed both analytically and synthetically. The goal of the analytic investigations is to simplify the existing complex systems of a real material while preserving its characteristic properties. Ideally, a solid understanding of the simplified model can be obtained. The findings are then to be synthesized for (at least partial) understanding of the materials. A highly intriguing example of this (on-going) process deals with a class of high-T_c superconductors from the family of "cuprates". These become increasingly important both in scientific and commercial applications. The high-T_c "cuprates" superconductors are layered compounds with CuO_2 planes. Although there is still some controversy regarding the actual mechanism responsible for the superconductivity, there is a strong indication of a completely different mechanism based on the repulsive electron-electron interactions, as opposed to the attrative phonon-mediated interation between electrons in conventional superconductors [14]. The complex structure of cuprates with a large unit cell can be reduced to an effective two-dimensional model on a decorated square lattice (Lieb lattice) of Cu^{3+} and O^{2-} ions [16], which may be further simplified by effectively integrating out the oxygens [17]. Numerical studies of the resulting single band Hubbard model [18] on a square lattice then provide approximative solution and validate the model, as the model's phase diagram qualitatively reproduces the generic high-T_c phase diagram [19, 20, 21, 22].

The vast majority of condensed matter simulations employs the Born–Oppenheimer approximation [23], treating the much heavier nuclei as classical particles. The wavefunction of electrons is then parametric dependent on the nuclei positions and the nuclei move in potential energy surface given by the electronic energies. As the next step, an effective low-energy theory for the electrons is constructed, integrating out the core electrons and the unoccupied electronic degrees of freedom high above the Fermi level. The detective-like work, as performed by Rice *et*

al. [16, 17] and others for cuprates, guided by intuition and few experimental signatures, is nowadays typically replaced by a bandstructure calculation performed with density functional theory (DFT) [24, 25]. DFT, even though it is an uncontrolled method, provides sufficiently good description for great variety of materials. Its polynomial complexity [26] enables calculations with large structural units, taking into account thousands of orbitals. Its computational inexpensiveness together with its predictive power makes the method widely used in material science.

The class of *strongly correlated materials* is not well captured by DFT. Still, DFT may guide the complexity reduction of the full system to an effective low-energy model. The effective quantum model of fermions is to be solved either approximatively or numerically, but often a combination of both approximation and numerics is chosen. In fact, there is a zoo of numerical approaches that typically include some physically motivated simplification. We may categorize the approaches with respect to their amount of control over the approximation. Uncontrolled approximation may often give us a relatively cheap solution with questionable quality, whereas controlled approaches give us unbiased results but often at a (prohibitively) high cost. For example, exact diagonalization can handle complicated models with arbitrary interactions, but just for small system with not more than 50 two-state orbitals. Perturbative approaches work well in the vicinity of the point around which the expansion is performed. A partial control of the perturbative methods is available if contributions of several orders are calculated and if the series is convergent. The diagrammatic Monte Carlo [27, 28] performs random walk over the order, the diagram topology, and the internal variables. Typically it is formulated directly in the thermodynamic limit. The method enables routinely to evaluate diagram contributions up to the sixth order with reasonable accuracy [29]. Nevertheless, the very interesting regime of Hubbard model with moderate on-site interaction U of the order of non-interacting bandwidth cannot be reliably accessed with this method. A very successful branch of methods solves finite quantum lattice systems by introducing fluctuating auxiliary fields, which serve for decomposition of the density-density interactions into non-interacting terms coupling to the auxiliary fields [30, 31]. For any fixed configuration of the fluctuating fields, the system is non-interacting and thus permits the use of the Wick's theorem [32]. Furthermore, the problem is mapped onto a classical problem in $d + 1$ dimensions. The mapping is based either on the Suzuki–Trotter discretization [33, 34] or on the (formally infinite) perturbation expansion. The auxiliary fields are sampled with Metropolis algorithm [35]. The methods in this family [36, 37, 38, 39, 40] are jointly referred to as determinantal quantum Monte Carlo (DQMC). They turn out to be extremely powerful if all configurations contribute to the partition sum with a weight of the same sign, in which case the stochastic sampling error decreases proportionally to the inverse square root of the number of independent measurements. If the "weights" are not of definite

sign, Metropolis sampling can be applied with a cheap trick of sampling according to the *magnitude* of the "weights". Unfortunately, the average of any physical observable is then obtained as the ratio of two averages: that of the product of configuration weight sign and the observable's estimator value, and that of the configuration weight sign. The latter of the two averages can be arbitrarily close to zero, rendering large uncertainties of all observables. This issue is termed as the *sign problem* [41]. The noise to signal ratio grows in general exponentially with the system size and the inverse temperature [42]. Certain classes of problems allow for a sign-problem-free simulation [43] thanks to a special problem structure enabling to prove non-negativity of the configuration weights. Recently, it was unveiled that the sign problem in DQMC has its origin in a non-trivial topological invariant of the sampled configurations [44].

For 1D systems at zero temperature, the density-matrix renormalization group (DMRG) method [45] is a highly effective numerical treatment with an excellent control of the precision and the ability to perform real time evolution [46, 47]. The motivation for its wave function Ansatz in form of the matrix product states (MPS) [48] comes from the *area law* for the entanglement entropy [49], ensuring that for sufficiently large system the ground state lies in a low entanglement entropy sector, which is efficiently represented by MPS. Even though DMRG is primary a method suitable for 1D systems, its 1D MPS Ansatz can also provide good variational ground state of 2D models [50]. The MPS Ansatz was extended to 2D [51], where its usage is much more challenging. The high (polynomial) complexity of the algorithm considerably restricts the matrix sizes for the Ansatz. Nevertheless, the method is capable to find competitive ground state candidates [52].

Dynamical mean-field theory (DMFT) was introduced via the limit of an infinite coordination number [53]. Georges and Kotliar noticed that for the Hubbard interaction, the self energy becomes purely local in such a limit [54, 55]. DMFT is a mean-field construction for fermionic quantum systems, treating all neighbors of a site as a mean field with time dependence – thus it received the adjective *dynamic*. Despite the lack of control within DMFT, it became widely used. In material studies, it is used in a combination with DFT for strongly correlated orbitals [56, 57]. Ambiguity with double counting of the exchange-correlation contributions from DFT and DMFT remains a tricky issue [58]. Extensions of DMFT to clusters [59] provide a systematic way for inclusion of larger length scales. These are identical to DMFT for single site "clusters", and approach an accurate description of the lattice problem for larger cluster size. Apart from dynamical cluster approximation (DCA) [60], presented in more detail in Chap. 2, the cellular DMFT (CDMFT) [61] is widely used. They differ in the way of mapping the lattice problem to the impurity problem – see Sec. 2.1 for more details. A computationally less expensive method related to DMFT is the density matrix embedding theory [62], which lacks the frequency dependence but still allows for computation of dynamical quantities

(on the real axis) [63].

The above paragraphs on various numerical approaches should not be regarded as an exhaustive list of available numerical methods. An extensive comparison of a multitude of numerical methods for condensed matter systems is given in [64].

Most of the theoretically studied models were inspired by existing materials. Quantitative investigation of the models by experimental measurements performed on materials would be an alternative way of "solving" the models. An attempt in this direction was made for the Hubbard model [65]. Tuning the effective model parameters in materials can be achieved in a limited range of parameters by *e.g.* application of pressure, or change of the chemical composition. For two-dimensional samples, the substrate significantly influences the properties of the investigated sample, which can be avoided by making suspended samples [66]. These aspects show that a model study by experiments on materials is possible but not at all straightforward.

A very different route to an experimental realization of condensed matter lattice models is their engineering in a totally artificial way, using neutral ultracold atoms in optical lattices; for a review articles on the topic see [67, 68, 69]. In short, the optical lattice is produced with counter-propagating laser beams creating a standing wave. The atoms experience an AC Stark shift forcing them to move to nodes or antinodes, depending on the laser detuning with respect to the atomic resonance frequency. The realization of optical lattice with several laser beams allows to create various lattice geometries: simple cubic, square, triangular, honeycomb, and Kagome lattice; for an review see [70]. The atoms are confined typically in a quadratic potential trap, although a box potential can be realized as well [71]. The hopping amplitudes given by the overlap of Wannier orbitals can be tuned too [72]. The onsite interaction strength can be tuned with an external magnetic field using the Feshbach resonance with a bound state. One possibility to create artificial gauge fields is to periodically modulate the position of the optical lattice sites [73]. The experimental observables measured in equilibrium are directly comparable with numerical data, enabling quantitative checks in both directions, from numerics to the experiment and vice versa [74, 75]. Although an experimental realization straightforwardly allows for non-equilibrium measurements, the behavior may be influenced by realization-dependent higher energy degrees of freedom, especially for fast quenches.

1.2 Non-interacting system

An essential building block in the many-body theory used for solving of the quantum problems is a Green's function of a solvable problem. The many-body machinery then employs perturbation theory around the known solution. As a solvable

problem is typically taken a non-interacting system. We consider a non-interacting time-independent Hamiltonian,

$$\hat{H}_0 = \sum_{\alpha,\gamma} \hat{c}^\dagger_\alpha \, h_{\alpha\gamma} \, \hat{c}_\gamma \,, \tag{1.2}$$

where α, γ label orthogonal single-particle basis states. Operator $\hat{c}^\dagger_\alpha$ ($\hat{c}_\alpha$) acts in the Fock space build upon the chosen single-particle basis by creation (annihilation) of a fermion in state α. We denote the single-particle basis size by n. Since h is a hermitian matrix, it can be diagonalized by a unitary U, $h = U \Xi U^+$ with real-valued $\Xi = \mathrm{diag}(\varepsilon_1, \ldots, \varepsilon_n)$, and columns of U being the (normalized) eigenvectors of h ordered accordingly to the eigenvalues ε_i. In such a (rotated) basis,

$$\hat{H}_0 \;=\; \sum_i \varepsilon_i \, \hat{d}^\dagger_i \, \hat{d}_i \,, \qquad\qquad \hat{d}^\dagger_i = \sum_\alpha U_{\alpha i} \hat{c}^\dagger_\alpha \,, \qquad \hat{d}_i = \sum_\alpha U^*_{\alpha i} \hat{c}_\alpha \,. \tag{1.3}$$

1.2.1 Green's function

We will work with the imaginary-time Matsubara Green's functions, for an overview see [76, 77], defined by[2]

$$G_{\alpha\gamma}(\tau) \;\equiv\; -\left\langle \hat{c}_\alpha(\tau) \, \hat{c}^\dagger_\gamma(0) \right\rangle \qquad \text{for } 0 < \tau < \beta \,, \tag{1.4}$$

$$G_{\alpha\gamma}(\tau - \beta) \;\equiv\; -G_{\alpha\gamma}(\tau) \qquad \text{for } 0 < \tau < \beta \,, \tag{1.5}$$

where $\hat{A}(\tau) \equiv e^{\tau \hat{H}} \, \hat{A} \, e^{-\tau \hat{H}}$ is the operator $\hat{A}$ in Heisenberg picture, $\beta = 1/T$ is the inverse temperature,[3] $\left\langle \hat{X} \right\rangle = \frac{1}{Z} \mathrm{Tr} \left\{ e^{-\beta \hat{H}} \hat{X} \right\}$ denotes the thermal average of the operator $\hat{X}$, and $Z \equiv \mathrm{Tr} \left\{ e^{-\beta \hat{H}} \right\}$ is the partition function. The chemical potential is assumed to be subtracted from $\hat{H}$. We further define the Fourier transformed ($\tau \to i\omega_m$) Matsubara Green's function,[4]

$$G_{\alpha\gamma}(\tau) \;=\; \frac{1}{\beta} \sum_{m=-\infty}^{\infty} G_{\alpha\gamma}(i\omega_m) e^{-i\omega_m \tau} \,, \tag{1.6}$$

$$G_{\alpha\gamma}(i\omega_m) \;=\; \int_0^\beta \mathrm{d}\tau e^{i\omega_m \tau} G_{\alpha\gamma}(\tau) \,, \tag{1.7}$$

[2] The definition is equivalent to the standard definition, $G_{\alpha\gamma}(\tau) := -T_\tau \left\langle \hat{c}_\alpha(\tau) \, \hat{c}^\dagger_\gamma(0) \right\rangle$ for $\tau \in (-\beta, \beta)$, where the time-ordering operator T_τ moves operators at the later times to the left from operators at the earlier times, while taking into account the fermionic statistics of the creation (annihilation) operator.

[3] We use convention with the Boltzmann constant k_B and the reduced Planck constant $\hbar$ equal to unity, *i.e.* the units of temperature, energy, and (imaginary) time coincide.

[4] In fact, $G_{\alpha\gamma}(i\omega_m) = \int_\tau^{\tau+\beta} \mathrm{d}\tau' \, e^{i\omega_m \tau'} G_{\alpha\gamma}(\tau')$ for any $\tau \in (-\beta, 0]$.

where the fermionic Matsubara frequencies ω_m are odd Fourier frequencies,[5]

$$\omega_m = \frac{\pi(2m+1)}{\beta}\,, \qquad m \in \mathbb{Z}\,. \tag{1.8}$$

The Green's function of the non-interacting $\hat{H}_0$ may be obtained in a closed form. In the diagonal representation $d_i^\dagger$ (Eq. 1.3) we find,

$$G^0_{ij}(\tau) \equiv -\left\langle \hat{d}_i(\tau)\, \hat{d}_j^\dagger(0) \right\rangle = -\delta_{ij} \frac{e^{-\tau\varepsilon_i}}{1+e^{-\beta\varepsilon_i}}\,, \qquad \text{for } 0<\tau<\beta\,. \tag{1.9}$$

Performing the Fourier transformation from τ to $i\omega_m$ we get

$$G^0_{ij}(i\omega_m) \equiv \int_0^\beta \mathrm{d}\tau\; e^{i\omega_m\tau} G^0_{ij}(\tau) = -\frac{\delta_{ij}}{\varepsilon_i - i\omega_m}\,. \tag{1.10}$$

It is now easy to get back to the original basis $c_\alpha^\dagger$,

$$G^0_{\alpha\gamma}(\tau) = -\left\langle \hat{c}_\alpha(\tau)\, \hat{c}_\gamma^\dagger(0) \right\rangle = \sum_{i,j} U_{\alpha i} G^0_{ij}(\tau) U^+_{j\gamma} = \sum_i U_{\alpha i} G^0_{ii}(\tau) U^+_{i\gamma}\,, \tag{1.11}$$

$$G^0_{\alpha\gamma}(i\omega_m) = -\int_0^\beta \mathrm{d}\tau\; e^{i\omega_m\tau} \left\langle \hat{c}_\alpha(\tau)\, \hat{c}_\gamma^\dagger(0) \right\rangle = \sum_i U_{\alpha i} G^0_{ii}(i\omega_m) U^+_{i\gamma}\,. \tag{1.12}$$

The non-interacting Matsubara representation Green's function can be then elegantly written in a matrix form[6]

$$G^0(i\omega_m) = -U \begin{pmatrix} (\varepsilon_1 - i\omega_m)^{-1} & 0 & 0 \\ 0 & \ddots & 0 \\ 0 & 0 & (\varepsilon_n - i\omega_m)^{-1} \end{pmatrix} U^+ \tag{1.13}$$

$$= (i\omega_m \mathbb{1}_n - h)^{-1}\,. \tag{1.14}$$

In the above formula, $\mathbb{1}_n$ is an $n \times n$ unit matrix.

1.2.2 Lattice model

We consider a non-interacting model on a general d-dimensional lattice with ℓ sites per unit cell.

We decompose the real space position i of a site into its unit cell Bravais vector $\mathbf{r}$ and the intracell site label $\alpha \in \{1, 2, \ldots, \ell\}$, where $\mathbf{r}$ is an integer linear

[5] The even frequency Fourier components of $G_{\alpha\gamma}(\tau)$ in range $(-\beta, \beta)$ vanish due to the property 1.5.

[6] Row index corresponds to α and column index to γ.

combination of the lattice basis vectors $\mathbf{a}_i$. We assume the model Hamiltonian to have the form,

$$\hat{H}_0 = -\sum_{\mathbf{r},\mathbf{r}',\alpha,\alpha',\sigma,\sigma'} t_{\mathbf{r}\alpha\sigma\mathbf{r}'\alpha'\sigma'} \hat{c}^\dagger_{\mathbf{r}\alpha\sigma} \hat{c}_{\mathbf{r}'\alpha'\sigma'} + \sum_{\alpha,\sigma} V_{\alpha\sigma} \sum_{\mathbf{r}} \hat{c}^\dagger_{\mathbf{r}\alpha\sigma} \hat{c}_{\mathbf{r}\alpha\sigma} \,, \tag{1.15}$$

where $\sigma \in \{\uparrow, \downarrow\}$ stands for the spin projection onto some arbitrary quantization axis. We constrain the Hamiltonian to be translationally symmetric hermitian,

$$t_{\mathbf{r}\alpha\sigma\mathbf{r}'\alpha'\sigma'} = t_{(\mathbf{r}-\mathbf{R})\alpha\sigma(\mathbf{r}'-\mathbf{R})\alpha'\sigma'} \,, \qquad t_{\mathbf{r}\alpha\sigma\mathbf{r}'\alpha'\sigma'} = \left(t_{\mathbf{r}'\alpha'\sigma'\mathbf{r}\alpha\sigma}\right)^* \,, \qquad V_{\alpha\sigma} \in \mathbb{R} \,, \tag{1.16}$$

where the site- and spin-dependent potential allows Zeeman coupling to magnetic field along the quantization axis, $V_{\alpha\sigma} \equiv V_\alpha - h_\alpha \sigma$. We restrict ourselves to the case with absent spin-flipping terms, *i.e.* with conserved total spin projection. This constrains the hopping amplitudes to be diagonal in spin indices, $t_{\mathbf{r}\alpha\sigma\mathbf{r}'\alpha'\sigma'} \equiv \delta_{\sigma\sigma'} t_{\mathbf{r}\alpha\mathbf{r}'\alpha'\sigma}$ such that the Green's function is diagonal in the spin indices, $G^0_{\sigma\sigma'} = \delta_{\sigma\sigma'} G^0_\sigma$. The local $V_{\alpha\sigma}$ term may be absorbed into the general hopping term by redefining $\tilde{t}_{\mathbf{r}\alpha\mathbf{r}'\alpha'\sigma} \equiv t_{\mathbf{r}\alpha\mathbf{r}'\alpha'\sigma} - V_{\alpha\sigma}\delta_{\mathbf{r}\mathbf{r}'}\delta_{\alpha\alpha'}$. Exploiting the translational invariance, we may simplify the notation for the hoppings

$$\tilde{t}_{\mathbf{r}\alpha\mathbf{r}'\alpha'\sigma} = \tilde{t}_{\mathbf{0}\alpha(\mathbf{r}'-\mathbf{r})\alpha'\sigma} \equiv \tilde{t}_{(\mathbf{r}'-\mathbf{r})\alpha\alpha'\sigma} \,, \tag{1.17}$$

and write the Hamiltonian in a more condensed form,

$$\hat{H}_0 = -\sum_{\mathbf{r},\boldsymbol{\Delta},\alpha,\alpha',\sigma} \tilde{t}_{\boldsymbol{\Delta}\alpha\alpha'\sigma} \hat{c}^\dagger_{\mathbf{r}\alpha\sigma} \hat{c}_{(\mathbf{r}+\boldsymbol{\Delta})\alpha'\sigma} \,. \tag{1.18}$$

We assume a finite system of L cells with the periodic boundary conditions. This enables the use of the Fourier transformation (FT), immensely simplifying the lattice problem. Without loss of generality, we choose the FT to be of the form,[7]

$$\hat{c}^\dagger_{\mathbf{r}\alpha\sigma} = \frac{1}{\sqrt{L}} \sum_{\mathbf{k}} e^{-i\mathbf{k}\cdot(\mathbf{r}+\mathbf{r}_\alpha)} \hat{c}^\dagger_{\mathbf{k}\alpha\sigma} \,, \qquad \hat{c}_{\mathbf{r}\alpha\sigma} = \frac{1}{\sqrt{L}} \sum_{\mathbf{k}} e^{i\mathbf{k}\cdot(\mathbf{r}+\mathbf{r}_\alpha)} \hat{c}_{\mathbf{k}\alpha\sigma} \,. \tag{1.19}$$

The Hamiltonian $\hat{H}_0$ in the reciprocal space representation takes the form

$$\hat{H}_0 = -\sum_{\mathbf{k},\alpha,\alpha',\sigma} \hat{c}^\dagger_{\mathbf{k}\alpha\sigma} \, \tilde{t}_{\mathbf{k}\alpha\alpha'\sigma} \, \hat{c}_{\mathbf{k}\alpha'\sigma} \,, \tag{1.20}$$

[7] The widely used alternative form of FT lacks the phase factors $e^{\pm i\mathbf{k}\cdot\mathbf{r}_\alpha}$. The change to that convention is done via a simple unitary transformation. The choice does not affect any physical outcome if the problem is solved (numerically) exactly. See motivation for this form in the context of DCA in Sec. 2.4.

where $\tilde{t}_{\mathbf{k}\alpha\alpha'\sigma}$ is the Fourier-transformed $\tilde{t}_{\mathbf{\Delta}\alpha\alpha'\sigma}$,

$$\tilde{t}_{\mathbf{k}\alpha\alpha'\sigma} \equiv t_{\mathbf{k}\alpha\alpha'\sigma} - \delta_{\alpha\alpha'} V_{\alpha\sigma} \,, \qquad t_{\mathbf{k}\alpha\alpha'\sigma} \equiv \sum_{\mathbf{\Delta}} t_{\mathbf{\Delta}\alpha\alpha'\sigma} e^{i\mathbf{k}\cdot\mathbf{\Delta}} e^{i\mathbf{k}\cdot(\mathbf{r}_{\alpha'} - \mathbf{r}_{\alpha})} \,. \tag{1.21}$$

The form of the Hamiltonian 1.20 for a given $\mathbf{k}$ and σ is equivalent to that of Eq. 1.2. Therefore, the dispersion for each $\mathbf{k}$, σ is given by the spectrum of the $\ell \times \ell$ matrix $-\tilde{T}_{\mathbf{k}\sigma}$ with matrix elements

$$\left(\tilde{T}_{\mathbf{k}\sigma}\right)_{\alpha\alpha'} = \tilde{t}_{\mathbf{k}\alpha\alpha'\sigma} \,. \tag{1.22}$$

1.2.3 Non-interacting lattice Green's functions

Using the block-diagonal form of the non-interacting lattice Hamiltonian given in Eq. 1.20 and the general Green's function result, Eq. 1.14, we immediately get

$$G_{(\mathbf{k}\alpha\sigma)(\mathbf{k}\alpha'\sigma)}(i\omega_m) = \left[\left(i\omega_m + \tilde{T}_{\mathbf{k}\sigma}\right)^{-1}\right]_{\alpha\alpha'} \,. \tag{1.23}$$

Combining this with the result of Eq. 1.10 and using the block-diagonal structure of the Hamiltonian both in $\mathbf{k}$ and σ we arrive at

$$G_{(\mathbf{k}\alpha\sigma)(\mathbf{k}'\alpha'\sigma')}(i\omega_m) = \delta_{\mathbf{k}\mathbf{k}'}\delta_{\sigma\sigma'} \left[\left(i\omega_m + \tilde{T}_{\mathbf{k}\sigma}\right)^{-1}\right]_{\alpha\alpha'} \,. \tag{1.24}$$

For a later convenience, we modify the notation and omit the labels $\mathbf{k}'$ and σ' from now on, assuming that these are equal to $\mathbf{k}$ and σ, resp. Moreover, as done in Eq. 1.14, we treat $G_{\mathbf{k}\sigma}(i\omega_m) = \left(i\omega_m + \tilde{T}_{\mathbf{k}\sigma}\right)^{-1}$ as an $\ell \times \ell$ matrix, encoding all possible (ordered) pairs of the intracell labels α and α'.

The real space Green's function is a function of the real space distance only. We obtain it by FT,

$$G_{\mathbf{r}\alpha\mathbf{r}'\alpha'\sigma}(i\omega_m) = \frac{1}{L}\sum_{\mathbf{k}} e^{i\mathbf{k}\cdot(\mathbf{r}+\mathbf{r}_{\alpha}-\mathbf{r}'-\mathbf{r}_{\alpha'})} G_{\mathbf{k}\alpha\alpha'\sigma}(i\omega_m) \,. \tag{1.25}$$

The corresponding inverse transformation is given by

$$G_{\mathbf{k}\alpha\alpha'\sigma}(i\omega_m) = \frac{1}{L}\sum_{\mathbf{r},\mathbf{r}'} e^{-i\mathbf{k}\cdot(\mathbf{r}+\mathbf{r}_{\alpha}-\mathbf{r}'-\mathbf{r}_{\alpha'})} G_{\mathbf{r}\alpha\mathbf{r}'\alpha'\sigma}(i\omega_m) \,. \tag{1.26}$$

Clearly, the same form holds for the imaginary-time representation.

1.3 Symmetries

In this section we examine the impact of symmetries on the single particle imaginary-time (*i.e.* temperature) Green's function,

$$G_{ab}(\tau,\tau') = -\left\langle \hat{c}_a(\tau)\,\hat{c}_b^\dagger(\tau')\right\rangle = -\frac{1}{Z}\,\mathrm{Tr}\left\{e^{-(\beta-\tau)\hat{H}}\;\hat{c}_a\;e^{-(\tau-\tau')\hat{H}}\;\hat{c}_b^\dagger\;e^{-\tau'\hat{H}}\right\}, \quad (1.27)$$

valid for $0 < \tau' < \tau < \beta$, where a and b label some orthonormal single particle basis. In the previous section we already encounter some symmetries of the non-interacting system. This section deals with them again in the context of a general time-independent and hermitian Hamiltonian.

The practical value of the present section is three-fold. Firstly, for a numerical treatment it is advantageous to treat real-valued observables without the unnecessary imaginary part of a complex floating point number. Secondly, a symmetrization reduces noise in a stochastic simulation. Finally, symmetry compatibility with an approximation used for solving of a particular model may be important.

1.3.1 Translational symmetry in (imaginary) time

For a time-independent Hamiltonian, the translational invariance of the causal Green's function,[8] $G_{ab}^{\mathrm{causal}}(t,t') = G_{ab}^{\mathrm{causal}}(t-t',0)$ implies translational invariance of the corresponding temperature Green's function, $G_{ab}(\tau,\tau') = G_{ab}(\tau-\tau',0)$.[9] That implies the possibility to work with single-frequency Fourier transformed Green's function, so-called Matsubara Green's function,

$$G_{ab}(i\omega_n) = \int_0^\beta \mathrm{d}\tau\; e^{i\omega_n\tau} G_{ab}(\tau)\,. \quad (1.28)$$

It significantly simplifies the usage of the Dyson equation, Fig. 1.1, relating the Green's function G with the bare Green's function G^0 and self energy Σ,

$$G_{ab}(\tau_a,\tau_b) = G^0_{ab}(\tau_a,\tau_b) + \sum_{c,d}\int \mathrm{d}\tau_c \int \mathrm{d}\tau_d\; G^0_{ac}(\tau_a,\tau_c)\,\Sigma_{cd}(\tau_c,\tau_d)\,G_{db}(\tau_d,\tau_b)\,, \quad (1.29)$$

which can be Fourier transformed to Matsubara frequencies,

$$G_{ab}(i\omega_n) = G^0_{ab}(i\omega_n) + \sum_{c,d}\; G^0_{ac}(i\omega_n)\;\Sigma_{cd}(i\omega_n)\;G_{db}(i\omega_n)\,. \quad (1.30)$$

[8] The causal Green's function is defined by $G_{ab}^{\mathrm{causal}}(t,t') = -iT_\tau\left\langle \hat{c}_a(t)\,\hat{c}_b^\dagger(t')\right\rangle$.

[9] In Eq. 1.27, which implicitly uses the time-independency of $\hat{H}$, the cyclic property of trace allows for straightforward proof of $G_{ab}(\tau,\tau') = G_{ab}(\tau-\tau',0)$.

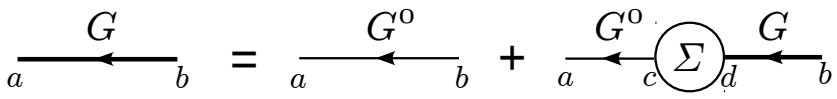

Figure 1.1: The Dyson equation displayed schematically. Depending on the representation, a, b, c, and d include the space coordinate and the imaginary time, or the space coordinate only.

1.3.2 General properties of single particle Green's functions

The Green's function in Eq. 1.27 is defined via a trace over the full many-body Hilbert space of the operator $\hat{O} \equiv e^{-(\beta-\tau)\hat{H}}\, \hat{c}_a\, e^{-\tau\hat{H}}\, \hat{c}_b^\dagger$, setting $\tau' = 0$ in conformity with previous section. We use[10]

$$\langle\Psi|\, \hat{O}\, |\Psi\rangle = \langle\Psi|\, \hat{O}^\dagger\, |\Psi\rangle^* \tag{1.32}$$

for every summand of the trace to get

$$G_{ab}(\tau) = -\frac{1}{Z}\, \mathrm{Tr}\left\{\hat{O}^\dagger\right\}^* . \tag{1.33}$$

The adjoint of $\hat{O}$ equals to

$$\hat{O}^\dagger = \hat{c}_b\, e^{-\tau\hat{H}}\, \hat{c}_a^\dagger\, e^{-(\beta-\tau)\hat{H}} , \tag{1.34}$$

where we used that $e^{\alpha\hat{H}}$ is self-adjoint (hermitian) operator for any real α, and that the operator $\hat{c}_a$ is adjoint (hermitian conjugate) of $\hat{c}_a^\dagger$. Since $\hat{O}^\dagger$ appears in Eq. 1.33 only under the trace, we are free to cyclically permute terms of $\hat{O}^\dagger$ in that expression. So we find

$$G_{ab}(\tau) = -\frac{1}{Z}\, \mathrm{Tr}\left\{e^{-(\beta-\tau)\hat{H}}\, \hat{c}_b\, e^{-\tau\hat{H}}\, \hat{c}_a^\dagger\right\}^* = G_{ba}^*(\tau) , \tag{1.35}$$

using $Z \in \mathbb{R}$.[11] For the Matsubara frequency temperature Green's function defined in Eq. 1.28 we thus find,

$$G_{ab}(i\omega_n) = G_{ba}^*(-i\omega_n) . \tag{1.36}$$

[10] The relation can be shown starting from the definition of the adjoint operator $\hat{O}^\dagger$,

$$\langle\Psi|\, \hat{O}\, |\Phi\rangle \equiv \left\langle\Psi\right|\, \hat{O}\Phi\Big\rangle = \left\langle\hat{O}^\dagger\Psi\right|\, \Phi\Big\rangle = \left\langle\Phi\right|\, \hat{O}^\dagger\Psi\Big\rangle^* = \langle\Phi|\, \hat{O}^\dagger\, |\Psi\rangle^* , \tag{1.31}$$

if we set $|\Psi\rangle = |\Phi\rangle$.

[11] $Z \in \mathbb{R}$ can be proved using Eq. 1.32 for $\hat{O} = e^{-\beta\hat{H}}$.

For the special case $a = b$, Eq. 1.35 guarantees purely real onsite Green's function,[12]

$$G_{ab}(\tau) = G^*_{ba}(\tau), \qquad \Rightarrow \qquad G_{aa}(\tau) \in \mathbb{R}\,. \tag{1.37}$$

Further, $G_{aa}(\tau) < 0$ for $0 < \tau < \beta$, which may be verified in the many-body eigenbasis $\{|\psi_n\rangle\}$ of $\hat{H}$ (Lehmann representation),

$$\begin{aligned} G_{aa}(\tau) &= -Z^{-1}\ \mathrm{Tr}\left\{e^{-(\beta-\tau)\hat{H}}\ \hat{c}_a\ e^{-\tau\hat{H}}\ \hat{c}^\dagger_a\right\} &(1.38)\\ &= -\underbrace{Z^{-1}}_{>0}\ \sum\nolimits_n \underbrace{e^{-(\beta-\tau)\varepsilon_n}}_{>0} \sum\nolimits_m \underbrace{e^{-\tau\varepsilon_m}}_{>0}\ \underbrace{|\lambda^a_{mn}|^2}_{\geq 0}, &(1.39)\end{aligned}$$

where we used decomposition $\hat{H} = \sum_n \varepsilon_n\, |\psi_n\rangle\langle\psi_n|$, $\hat{c}^\dagger_a = \sum_{m,n} \lambda^a_{mn}\, |\psi_m\rangle\langle\psi_n|$, $\hat{c}_a = \sum_{m,n} (\lambda^a_{nm})^*\, |\psi_m\rangle\langle\psi_n|$, with $\sum_{m,n} |\lambda^a_{mn}|^2 > 0$.[13]

1.3.3 Conservation of total spin projection

If the Hamiltonian does not contain any spin-flipping term, *e.g.* a spin-orbit coupling, a magnetic field which is not aligned with the quantization axis, or a (spontaneous) pairing field, then the total spin projection is a good quantum number, *i.e.* a conserved quantity, which implies that the Green's functions are diagonal in the spin projection σ, $\left\langle \hat{c}_{a\sigma}(\tau)\ \hat{c}^\dagger_{b\sigma'}(0)\right\rangle \propto \delta_{\sigma\sigma'}$.

1.3.4 Translational symmetry

The symmetry implies $\left\langle \hat{c}_{\mathbf{r}\alpha\sigma}(\tau)\ \hat{c}^\dagger_{\mathbf{r}'\alpha'\sigma'}(0)\right\rangle = \left\langle \hat{c}_{(\mathbf{r}-\mathbf{r}')\alpha\sigma}(\tau)\ \hat{c}^\dagger_{\mathbf{0}\alpha'\sigma'}(0)\right\rangle$. The important consequence is, as in the case of time-invariant Hamiltonian discussed above, that $\left\langle \hat{c}_{\mathbf{k}\alpha\sigma}(\tau)\ \hat{c}^\dagger_{\mathbf{k}'\alpha'\sigma'}(0)\right\rangle \propto \delta_{\mathbf{k}\mathbf{k}'}$.[14]

The Fourier transformed Green's function is according to Eq. 1.19 of the form,

$$G_{\mathbf{k}\alpha\alpha'} = \frac{1}{L} e^{-i\mathbf{k}\cdot(\mathbf{r}_\alpha - \mathbf{r}_{\alpha'})} \sum_{\mathbf{r},\mathbf{r}'} e^{-i\mathbf{k}\cdot(\mathbf{r}-\mathbf{r}')} G_{\mathbf{r}\alpha\mathbf{r}'\alpha'}. \tag{1.40}$$

Exploiting Eq. 1.37, 1.36 we get

$$G_{\mathbf{k}\alpha\alpha'}(\tau) = G^*_{\mathbf{k}\alpha'\alpha}(\tau)\,, \qquad G_{\mathbf{k}\alpha\alpha'}(i\omega_n) = G^*_{\mathbf{k}\alpha'\alpha}(-i\omega_n)\,. \tag{1.41}$$

[12] In complete analogy it is possible to show that the instantaneous (equal-time) density-density correlations $\langle \hat{n}_a\, \hat{n}_b\rangle$ are purely real.

[13] From anticommutation relation $\left\{\hat{c}^\dagger_a, \hat{c}_a\right\} = \hat{1}$ one may obtain constraint $\sum_m (\lambda^a_{nm} {\lambda^a_{n'm}}^* + {\lambda^a_{mn}}^* \lambda^a_{mn'}) = \delta_{nn'}$. By that $\exists m,\ n\ :\ \lambda^a_{mn} \neq 0$.

[14] In a usual setup with single site per cell, at an phase transition, the translational symmetry may be lowered. For example, at the Néel transition on a square lattice, the unit cell doubles its volume and $G(\mathbf{k}, \mathbf{k}+\mathbf{Q})$ becomes non-zero for the antiferromagnetic reciprocal vector $\mathbf{Q} = \left(\frac{\pi}{a}, \frac{\pi}{a}\right)$.

1.3.5 Real-valued Hamiltonian

If the Hamiltonian contains only real-valued terms with respect to Fock space creation and annihilation operators, built upon some orthonormal single particle basis,[15] then $e^{-\tau\hat{H}}$ is a real and symmetric matrix with respect to the Fock basis. Let us label the orthonormal single particle basis by a, b. Then operators $\hat{c}_a^\dagger$, $\hat{c}_b$ are represented by real matrices.[16] Then the imaginary-time Green's function,

$$G_{ab}(\tau) = -\left\langle \hat{c}_a(\tau)\, \hat{c}_b^\dagger(0) \right\rangle = -\frac{1}{Z}\,\mathrm{Tr}\left\{ e^{-(\beta-\tau)\hat{H}}\, \hat{c}_a\, e^{-\tau\hat{H}}\, \hat{c}_b^\dagger \right\}\ , \qquad 0 < \tau < \beta\ , \tag{1.42}$$

is necessarily *purely real*, implying $G_{ab}(i\omega_n) = G^*_{ab}(-i\omega_n)$. Another consequence is $G_{ab}(\tau) = G_{ba}(\tau)$, arising from Eq. 1.37.

If the single particle basis was a real space basis build upon $c^\dagger_{\mathbf{r}\alpha\sigma}$, then in combination with the translational symmetry we obtain

$$G_{\mathbf{k}\alpha\alpha'}(\tau) = G_{-\mathbf{k}\alpha'\alpha}(\tau) = G^*_{-\mathbf{k}\alpha\alpha'}(\tau)\,, \tag{1.43}$$

and

$$G_{\mathbf{k}\alpha\alpha'}(i\omega_n) = G^*_{-\mathbf{k}\alpha\alpha'}(-i\omega_n) = G_{-\mathbf{k}\alpha'\alpha}(i\omega_n)\,. \tag{1.44}$$

The real-valuedness of the real space Hamiltonian relates to the time-reversal symmetry, which is for a Hamiltonian conserving the total spin projection and without any spin-dependent terms[17] equivalent to the constraint on real-valuedness of $\hat{H}$ in the real space representation.

1.3.6 Particle-hole symmetry

A particle-hole symmetric Hamiltonian has an invariant form under some kind of particle-hole transformation. A particle-hole transformation replaces particles with holes, which in operators means a correspondence of a creation operator to some new annihilation operator and vice versa. A typical, physically motivated particle-hole transformation is of the form,[18]

$$\hat{h}^\dagger_{\mathbf{r}A\sigma} = \hat{c}_{\mathbf{r}A\bar{\sigma}}\ , \qquad \hat{h}^\dagger_{\mathbf{r}B\sigma} = -\hat{c}_{\mathbf{r}B\bar{\sigma}} \tag{1.47}$$

$$\Rightarrow \qquad \hat{n}'_{\mathbf{r}\alpha\sigma} = \hat{h}^\dagger_{\mathbf{r}\alpha\sigma}\hat{h}_{\mathbf{r}\alpha\sigma} = \hat{c}_{\mathbf{r}\alpha\bar{\sigma}}\hat{c}^\dagger_{\mathbf{r}\alpha\bar{\sigma}} = 1 - \hat{n}_{\mathbf{r}\alpha\bar{\sigma}}\ . \tag{1.48}$$

[15] The Hamiltonian 1.15 is real-valued with respect to the real space basis iff $t_{\mathbf{r}\alpha\sigma\mathbf{r}'\alpha'\sigma'} \in \mathbb{R}$, and $V_{\alpha\sigma} \in \mathbb{R}$.

[16] With elements from $\{0, \pm 1\}$.

[17] For Hamiltonian 1.15 it would mean $t_{\mathbf{r}\alpha\sigma\mathbf{r}'\alpha'\sigma'} = \delta_{\sigma\sigma'} t_{\mathbf{r}\alpha\mathbf{r}'\alpha'}$.

[18] The interchange of the spin σ to $\bar{\sigma}$ reflects that a destruction of an $\uparrow$ electron creates a hole with spin $\downarrow$, as the hole carries opposite spin, since

$$\hat{S}^z_i = \frac{1}{2}\left(\hat{n}_{i\uparrow} - \hat{n}_{i\downarrow}\right) = -\frac{1}{2}\left(\hat{n}'_{i\uparrow} - \hat{n}'_{i\downarrow}\right)\ . \tag{1.45}$$

As an example we take a 2-sublattice real bipartite Hamiltonian with sublattices A, B,[19]

$$\begin{aligned}\hat{H} &= -\sum_{\mathbf{r},\boldsymbol{\Delta},\sigma} t_{\boldsymbol{\Delta}} \left(\hat{c}^\dagger_{\mathbf{r}+\boldsymbol{\Delta}B\sigma}\hat{c}_{\mathbf{r}A\sigma} + \hat{c}^\dagger_{\mathbf{r}A\sigma}\hat{c}_{\mathbf{r}+\boldsymbol{\Delta}B\sigma}\right) + \sum_{\alpha,\sigma}(V_{\alpha\sigma}-\mu)\sum_{\mathbf{r}}\hat{n}_{\mathbf{r}\alpha\sigma} \\ &\quad + U\sum_{\mathbf{r},\alpha}\hat{n}_{\mathbf{r}\alpha\uparrow}\hat{n}_{\mathbf{r}\alpha\downarrow} - \frac{U}{2}\sum_{\mathbf{r},\alpha,\sigma}\hat{n}_{\mathbf{r}\alpha\sigma}\,, \end{aligned} \tag{1.49}$$

which after the transformation retains the same form,

$$\begin{aligned}\hat{H} &= -\sum_{\mathbf{r},\boldsymbol{\Delta},\sigma} t_{\boldsymbol{\Delta}} \left(\hat{h}^\dagger_{\mathbf{r}+\boldsymbol{\Delta}B\sigma}\hat{h}_{\mathbf{r}A\sigma} + \hat{h}^\dagger_{\mathbf{r}A\sigma}\hat{h}_{\mathbf{r}+\boldsymbol{\Delta}B\sigma}\right) - \sum_{\alpha,\sigma}(V_{\alpha\bar{\sigma}}-\mu)\sum_{\mathbf{r}}\hat{n}'_{\mathbf{r}\alpha\sigma} \\ &\quad + U\sum_{\mathbf{r},\alpha}\hat{n}'_{\mathbf{r}\alpha\uparrow}\hat{n}'_{\mathbf{r}\alpha\downarrow} - \frac{U}{2}\sum_{\mathbf{r},\alpha,\sigma}\hat{n}'_{\mathbf{r}\alpha\sigma} + \underbrace{L\sum_{\alpha,\sigma}(V_{\alpha\sigma}-\mu) + 2UL}_{\text{irrelevant constant}}\,, \end{aligned} \tag{1.50}$$

with L being the number of unit cells. Now we are able to read out that the Hamiltonian is particle-hole symmetric for $V_{\alpha\sigma} - \mu = -(V_{\alpha\bar{\sigma}} - \mu)$.

We use the fact that a particle-hole symmetric Hamiltonian possesses the same form written in particle operators ($\hat{c}$, $\hat{c}^\dagger$) and in the hole operators ($\hat{h}$, $\hat{h}^\dagger$). Thus we may write

$$\begin{aligned} G_{\sigma ij}(\tau) &= -\frac{1}{Z}\,\mathrm{Tr}\left\{e^{-(\beta-\tau)\hat{H}}\,\hat{h}_{i\sigma}\,e^{-\tau\hat{H}}\,\hat{h}^\dagger_{j\sigma}\right\} \\ &= -\frac{1}{Z}\,\mathrm{Tr}\left\{e^{-\tau\hat{H}}\,\hat{h}^\dagger_{j\sigma}\,e^{-(\beta-\tau)\hat{H}}\,\hat{h}_{i\sigma}\right\} \\ &= -\frac{s_i s_j}{Z}\,\mathrm{Tr}\left\{e^{-\tau\hat{H}}\,\hat{c}_{j\bar{\sigma}}\,e^{-(\beta-\tau)\hat{H}}\,\hat{c}^\dagger_{i\bar{\sigma}}\right\} = s_i s_j G_{\bar{\sigma}ji}(\beta-\tau)\,, \end{aligned} \tag{1.51}$$

where s_i is a sublattice factor equal to 1 (-1) for i being a site in the sublattice A (B), in accordance with Eq. 1.47. A direct consequence for $i = j$ is that the filling per site is equal to one, $\sum_\sigma n_{i\sigma} = 1$. Another consequence for the paramagnetic case, $G_\sigma = G_{\bar{\sigma}}$, is mirror symmetry in τ around $\beta/2$ for the local Green's function, $G_{ii}(\tau) = G_{ii}(\beta - \tau)$

However, in order to exploit a model system we may define the particle-hole transformation differently – with same spin,

$$\hat{h}^\dagger_{\mathbf{r}A\sigma} = \hat{c}_{\mathbf{r}A\sigma}\,, \qquad \hat{h}^\dagger_{\mathbf{r}B\sigma} = -\hat{c}_{\mathbf{r}B\sigma}\,. \tag{1.46}$$

[19] To make connection with previously introduced notation, it is a special case with $l = 2$, $t_{\boldsymbol{\Delta}AA} = 0 = t_{\boldsymbol{\Delta}BB}$ and $t_{\boldsymbol{\Delta}AB}, U \in \mathbb{R}$. The lattice is bipartite, as there are no hoppings between sites of the same sublattice. However, purely imaginary hoppings on the same sublattice would not destroy the particle-hole symmetry.

A simple calculation reveals that the Green's function in Matsubara frequency representation equals to

$$G_{\sigma ij}(i\omega_n) = \int_0^\beta \mathrm{d}\tau\, e^{i\omega_n\tau} G_{\sigma ij}(\tau) = s_i s_j \int_0^\beta \mathrm{d}\tau\, e^{i\omega_n\tau} G_{\bar{\sigma} ji}(\beta-\tau) \quad (1.52)$$

$$= s_i s_j \underbrace{\int_0^\beta \mathrm{d}\tau' \underbrace{e^{i\omega_n(\beta-\tau')}}_{-e^{-i\omega_n\tau'}} G_{\bar{\sigma} ji}(\tau')}_{-G^*_{\bar{\sigma} ji}(i\omega_n)}, \quad (1.53)$$

which for $i = j$ and paramagnetic case results in the consequence that $G_{\sigma jj}(i\omega_n)$ is purely imaginary. Eq. 1.53 implies

$$G_{\sigma\alpha\gamma}(\mathbf{k},\tau) = s_\alpha s_\gamma G_{\bar{\sigma}\gamma\alpha}(-\mathbf{k},\beta-\tau), \quad (1.54)$$

$$G_{\sigma\alpha\gamma}(\mathbf{k},i\omega_n) = -s_\alpha s_\gamma G_{\bar{\sigma}\gamma\alpha}(-\mathbf{k},-i\omega_n). \quad (1.55)$$

If we assume in addition that the real space Hamiltonian is purely real, the Green's function in real space imaginary-time representation is purely real. That implies for the reciprocal representation the following,

$$G_{\sigma\alpha\gamma}(\mathbf{k},\tau) = s_\alpha s_\gamma G^*_{\bar{\sigma}\gamma\alpha}(\mathbf{k},\beta-\tau), \quad (1.56)$$

$$G_{\sigma\alpha\gamma}(\mathbf{k},i\omega_n) = -s_\alpha s_\gamma G^*_{\bar{\sigma}\gamma\alpha}(\mathbf{k},i\omega_n). \quad (1.57)$$

Another use of the particle-hole symmetry is away from half filling, for obtaining the properties at chemical potential $-\mu$ (filling $2-n$) based on measurements at chemical potential μ (filling n).

1.3.7 Inversion symmetry

Note that a general lattice with multi-site unit cells does in general not exhibit inversion symmetry. Next subsection on point group symmetries covers the inversion symmetry in the case of Bravais lattices with single site per unit cell and the case of inversion symmetry for general lattices when the inversion preserves the sublattice index.

Here we examine in more detail the case of lattice with two sites per unit cell, which is important for many applications, as it is a natural choice of unit cell for description of classical antiferromagnetic state. We assume the inversion operation to have the form

$$I:\ (\mathbf{r},\alpha) \mapsto (-\mathbf{r},\bar{\alpha}), \qquad \bar{\alpha} = \begin{cases} A & \text{for} \quad \alpha = B, \\ B & \text{for} \quad \alpha = A. \end{cases} \quad (1.58)$$

That changes the orientation of all relative real space vectors to its opposite,

$$I : \mathbf{r} + \mathbf{r}_\alpha - \mathbf{r}' - \mathbf{r}_{\alpha'} \mapsto -\left(\mathbf{r} + \mathbf{r}_\alpha - \mathbf{r}' - \mathbf{r}_{\alpha'}\right) . \tag{1.59}$$

For the Green's function of a model symmetric with respect to I that implies

$$G_{\alpha\beta}(\mathbf{r}) = G_{\bar{\alpha}\bar{\beta}}(-\mathbf{r}) , \qquad \text{and} \qquad G_{\alpha\beta}(\mathbf{k}) = G_{\bar{\alpha}\bar{\beta}}(-\mathbf{k}) . \tag{1.60}$$

So far we did not specify the effect of the inversion on the spin. Physical spin, as a pseudovector, does not change under space inversion. However, we may examine the combined symmetry of space inversion and spin flip, which appears in the context of Néel phase. Assuming symmetry of the Hamiltonian under the transformation $(\mathbf{r}, \alpha, \sigma) \mapsto (-\mathbf{r}, \bar{\alpha}, \bar{\sigma})$,[20] which is compatible with classical antiferromagnetic order, and real-valuedness of the real space Hamiltonian we get

$$G_{\sigma AA}(\mathbf{k}, i\omega_n) = G_{\bar{\sigma}BB}(\mathbf{k}, i\omega_n) , \tag{1.61}$$

$$G_{\sigma AB}(\mathbf{k}, i\omega_n) = G_{\bar{\sigma}AB}(\mathbf{k}, i\omega_n) , \qquad G_{\sigma BA}(\mathbf{k}, i\omega_n) = G_{\bar{\sigma}BA}(\mathbf{k}, i\omega_n) . \tag{1.62}$$

In combination with the particle-hole symmetry under transformation of the form given in Eq. 1.47,[21] one obtains Green's function with this structure,[22]

$$G_\sigma(\mathbf{k}, i\omega_n) = \begin{pmatrix} a & b \\ b^* & -a^* \end{pmatrix} , \qquad G_{\bar{\sigma}}(\mathbf{k}, i\omega_n) = \begin{pmatrix} -a^* & b \\ b^* & a \end{pmatrix} , \tag{1.63}$$

$$G_{\sigma\alpha\beta}(-\mathbf{k}, i\omega_n) = G_{\sigma\beta\alpha}(\mathbf{k}, i\omega_n) . \tag{1.64}$$

In the paramagnetic phase, as $G_\sigma = G_{\bar{\sigma}}$, a becomes purely imaginary.

For a special, so-called "time-reversal symmetric" $\mathbf{k}$-point such that $2\mathbf{k}$ is a reciprocal lattice vector $\mathbf{b}$ (*e.g.* $-\mathbf{k}$ and $\mathbf{k}$ are the same quasimomenta),[23] we get $b = b_0 e^{-i\mathbf{b}\cdot(\mathbf{r}_A - \mathbf{r}_B)/2}$ with real b_0. The Dyson equation delivers the same form for the self energy.

1.3.8 Point group symmetries

Let us assume a point group G, elements of which leave the real space Hamiltonian invariant. Further, we assume that the symmetry operations $g \in G$ act trivially on the intracell index α. In that case,

$$G_{\alpha\beta}(\mathbf{r} - \mathbf{r}') = G_{\alpha\beta}(g(\mathbf{r} + \mathbf{r}_\alpha - \mathbf{r}' - \mathbf{r}_\beta) - \mathbf{r}_\alpha + \mathbf{r}_\beta) , \tag{1.65}$$

[20] It requires $V_{A\sigma} = V_{B\bar{\sigma}}$, $t_{\mathbf{k}AA} = t_{-\mathbf{k}BB}$, and $t_{\mathbf{k}AB} = t_{-\mathbf{k}BA}$.

[21] Additionally requiring $t_{\mathbf{k}AA} = -t_{-\mathbf{k}AA}$ (enabling purely imaginary hoppings between sites on same sublattice)) and $V_{A\sigma} = -V_{A\bar{\sigma}}$.

[22] The row corresponds to the site index α and column to the site index β.

[23] The "time-reversal symmetric" $\mathbf{k}$-points are located at the surface of the Brillouin zone. Additionally, the $\Gamma = \mathbf{0}$ is a "time-reversal symmetric" point.

where $g(\mathbf{r})$ denotes the transformation of a vector $\mathbf{r}$ by the action of the operation g. With the definition of the Fourier transformation given in Eq. 1.40 we get for the Green's function in reciprocal space

$$\begin{aligned} G_{\alpha\beta}(\mathbf{k}) &= \sum_{\mathbf{r}} e^{-i\mathbf{k}\cdot(\mathbf{r}+\mathbf{r}_\alpha-\mathbf{r}_\beta)}\, G_{\alpha\beta}(\mathbf{r}) && (1.66)\\ &= \sum_{\mathbf{r}} e^{-ig(\mathbf{k})\cdot g(\mathbf{r}+\mathbf{r}_\alpha-\mathbf{r}_\beta)}\, G_{\alpha\beta}(g(\mathbf{r}+\mathbf{r}_\alpha-\mathbf{r}'-\mathbf{r}_\beta)-\mathbf{r}_\alpha+\mathbf{r}_\beta) && (1.67)\\ &= \sum_{\tilde{\mathbf{r}}} e^{-ig(\mathbf{k})\cdot(\tilde{\mathbf{r}}+\mathbf{r}_\alpha-\mathbf{r}_\beta)}\, G_{\alpha\beta}(\tilde{\mathbf{r}}) = G_{\alpha\beta}(g(\mathbf{k}))\,, && (1.68) \end{aligned}$$

where we used invariance of the scalar product under the action of g. Notice that this convenient result would not hold in this simple form for the conventional choice of the FT (1.19) omitting the phase factors $e^{-i\mathbf{k}\cdot(\mathbf{r}_\alpha-\mathbf{r}_\beta)}$.

2 Dynamical cluster approximation

The dynamical cluster approximation (DCA) is a quantum cluster theory mapping a lattice problem selfconsistently onto an impurity [60, 78, 79, 59]. As such, it may be viewed as a cluster extension of the dynamical mean-field theory (DMFT) [55]. It preserves translational invariance, unlike the cluster extension of DMFT known as cellular DMFT (CDMFT) [80, 61].

In DMFT, the self energy of the lattice is approximated by a dynamical but completely local function. The motivation for that is given in models with predominantly local interaction as the self energy is in such models fairly localized when compared to the Green's function. That can be verified using diagrammatic expansion, but it is visible also in the high-frequency behavior, see Eq. A.43 for the case of the Hubbard interaction. Therefore, the self energy is relatively flat in the reciprocal space. The lattice self energy is in the DMFT approximated by the self energy of the impurity, onto which is mapped the original lattice model,

$$\Sigma^{\mathrm{lat}}(\mathbf{k}, i\omega_n) \approx \Sigma^{\mathrm{imp}}(i\omega_n)\,. \tag{2.1}$$

The DMFT mapping of the lattice problem onto the impurity is a requirement that the impurity Green's function equals to the local lattice Green's function,

$$G^{\mathrm{imp}}(i\omega_n) = \frac{1}{\Omega_{\mathrm{BZ}}} \int_{\mathrm{BZ}} \mathrm{d}\mathbf{k}\, G^{\mathrm{lat}}(\mathbf{k}, i\omega_n)\,, \tag{2.2}$$

where BZ stands for the Brillouin zone and Ω_{BZ} denotes its volume. The DMFT is exact in these limits:[1]

- ▷ vanishing interaction, because self energy vanishes in that case,
- ▷ infinite interaction, as the model is local in that limit,
- ▷ infinite coordinate number, as the spatial fluctuations are negligible in that case.

[1] The first two limits are in case of particle-hole symmetric models at half filling correctly captured also by the second order weak coupling perturbation.

DCA maps the original lattice problem onto impurities consisting of more sites called cluster. This enables capturing non-local correlations on the simulated cluster impurity. DCA approximates the self energy with dynamical function, which is patch-wise constant in the reciprocal space,

$$\Sigma^{\mathrm{lat}}(\mathbf{K}+\tilde{\mathbf{k}}, i\omega_n) \approx \Sigma^{\mathrm{imp}}(\mathbf{K}, i\omega_n)\,, \tag{2.3}$$

where $\mathbf{K}$ denotes a cluster reciprocal point and $\tilde{\mathbf{k}}$ is a reciprocal vector within the DCA patch – precise definitions of a cluster and DCA patch corresponding to the cluster are provided in the Sec. 2.2. With larger cluster the DCA self energy gains finer resolution in the reciprocal space. The mapping of DCA is analogous to that of DMFT, Eq. 2.2, when written in the cluster reciprocal representation,

$$\forall \mathbf{K}:\ G^{\mathrm{imp}}(\mathbf{K}, i\omega_n) = \frac{L}{\Omega_{\mathrm{BZ}}} \int_{\text{DCA patch}} \mathrm{d}\tilde{\mathbf{k}}\, G^{\mathrm{lat}}(\mathbf{K}+\tilde{\mathbf{k}}, i\omega_n)\,, \tag{2.4}$$

where L denotes the number of unit cells in the cluster. The DCA approximation Eq. 2.3 and the DCA mapping Eq. 2.4 ensure conservation of the cluster (grained) quasi-momenta $\mathbf{K}$. DCA can be derived using the locator approach, tiling the lattice to isolated clusters and performing expansion in the intercluster hopping while neglecting the intercluster self energy. Alternatively, it can be obtained in a diagrammatic approach based on the quasi-momentum conservation at the resolution of the cluster, *i.e.* at the grained $\mathbf{K}$ level, neglecting the finer quasi-momenta $\tilde{\mathbf{k}}$. Both approaches are worked out in [59].

Similarly to DMFT, the DCA solution is obtained iteratively, as there is no known way to solve the Eqs. 2.3, 2.4 directly. The iterative solution uses a DCA selfconsistency loop consisting of the following steps:

1. Start with a guess of $G^{0,\mathrm{imp}}$, which is to be used as an input in an impurity solver computing G^{imp}.[2]

2. The (impurity) self energy is obtained via the Dyson equation,

$$\Sigma(\mathbf{K}, i\omega_n) = G^{0,\mathrm{imp}}(\mathbf{K}, i\omega_n)^{-1} - G^{\mathrm{imp}}(\mathbf{K}, i\omega_n)^{-1}\,. \tag{2.5}$$

3. The patch averaged lattice Green's function is computed,

$$\bar{G}^{\mathrm{lat}}(\mathbf{K}, i\omega_n) = \frac{L}{\Omega_{\mathrm{BZ}}} \int_{\text{DCA patch}} \mathrm{d}\tilde{\mathbf{k}}\, \left[G^{0}(\mathbf{K}+\tilde{\mathbf{k}}, i\omega_n)^{-1} - \Sigma(\mathbf{K}, i\omega_n)\right]^{-1}\,. \tag{2.6}$$

[2] A good initial guess of $G^{0,\mathrm{imp}}$ is the DCA-patch averaged $G^{0,\mathrm{lat}}$ (see Subsec. A.4.4) or a $G^{0,\mathrm{imp}}$ of a converged simulation at similar physical parameters.

4. A new guess for the bare impurity Green's function to be used in step 1 is obtained, again via the Dyson equation,

$$G^{0,\mathrm{imp}}(\mathbf{K}, i\omega_n) = \left[\bar{G}^{\mathrm{lat}}(\mathbf{K}, i\omega_n)^{-1} + \Sigma(\mathbf{K}, i\omega_n)\right]^{-1} , \tag{2.7}$$

   where we used the mapping Eq. 2.4.

The selfconsistency loop is schematically depicted in Fig. 2.1. Maximum difference of $G^{\mathrm{imp}}(\mathbf{K}, i\omega_n)$ in subsequent iterations can be used as a convergence criterion.

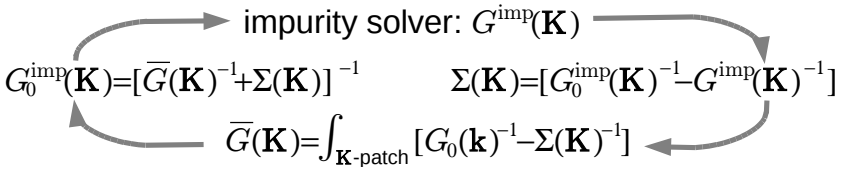

Figure 2.1: The DCA approximation Eq. 2.3 and the DCA mapping Eq. 2.4 are solved iteratively, performing the selfconsistency loop.

We mentioned that the DCA lattice self energy is in the reciprocal space approximated by a patch-wise constant function, where the resolution is given by the number of patches L in the Brillouin zone, *i.e.* by the cluster size. There were attempts to apply some smoothing of the lattice self energy. However, it turned out that smoothing may in general lead to a causality breaking [81]. A DCA extension with self energy treated on the same level as the Green's function was developed by *P. Staar et al.* [82]. Their DCA$^+$ uses interpolated self energy and instead of the approximation 2.3 he imposes condition that the patch averaged lattice self energy needs to be equal to the impurity self energy. Although causality violation was not rigorously excluded for DCA$^+$, for the examined model problems it was not observed [21].

Any reasonable cluster theory should recover the exact solution in the limit of infinite cluster size, $L \to \infty$. In DCA, the patches shrink with growing cluster and they become point-like for $L \to \infty$, *i.e.* the patch-averaging becomes trivial and so does the selfconsistency loop. The difference between the self energy Σ^{DCA} obtained in a DCA simulation with respect to the true lattice self energy Σ is asymptotically given by ([59]),

$$\Sigma = \Sigma^{\mathrm{DCA}} + O\left(L^{-2/d}\right) , \tag{2.8}$$

see example in Fig. 2.7, 2.8.

2.1 Comparison of DCA to competing methods

Although DCA is a cluster extension of DMFT, its features and especially the solution techniques are closely related to simulations of quantum models on finite lattices with periodical boundary conditions. The finite lattice simulations lack the selfconsistency loop, so they can be viewed as a single iteration of the DCA selfconsistency loop with $G^{0,\mathrm{imp}} = G^{0,\mathrm{lat}}$ and without any patch averaging. The number of iterations to find a converged DCA solution is typically of the order of 10. The need to perform several iterations is an extra complexity with respect to the finite lattice simulations. On the other hand, DCA has the approximation on the level of the self energy, which is an irreducible quantity showing stronger localization in the real space for models with local interaction. In a high-temperature phase, DCA data allows reliable extrapolations to the thermodynamic limit using moderately sized clusters. Possibility to obtain reliable data for extrapolations with smaller clusters is of great importance, especially for problems with severe sign problem [42, 41], as that increases noise to signal ratio exponentially with βL. The sign problem itself is reduced in DCA with respect to the finite lattice simulation on the same cluster [79].

Both solution by DCA and the finite lattice simulation with periodical boundary conditions converge to the thermodynamic limit as $L^{-2/d}$ in the single particle Green's function [83]. Ref. [83] shows also an example, in which the finite lattice simulation Green's function and DCA Green's function converge with larger cluster to the thermodynamic limit from opposite directions, enabling bounding of the results. From a point of view of the requirements on the impurity solver of the quantum problem, DCA needs an impurity solver working with the effective action, *e.g.* Hirsch–Fye solver [37, 79] or the numerically exact continuous time auxiliary field (CT-AUX) [39] (see review [84]), or a Hamiltonian based QMC with need of additional (discretized) bath to mimic the impurity action given by $G^{0,\mathrm{imp}}$ [85]. Finite lattice simulations may employ QMC approach working both with an effective action or with Hamiltonian formulation [36, 40] (without any extra sites). Note that the scaling of CT-AUX is $(\beta U N)^3$, whereas the Hamiltonian based approaches scale like $\beta U N^3$.

DCA, unlike the finite lattice simulations, enables symmetry breaking as a consequence of its mean-field character on distance scales beyond the cluster size. That simplifies measurements in an ordered phase. Clearly, the data close to the phase transition needs then to be interpreted with care. Susceptibility measurement is in the DCA much more involved than in the finite lattice simulations as it involves solving of the Bethe–Salpeter equation and requires thus measurement of four-point correlators with at least two frequencies. Further details on the susceptibility measurement are in Subsecs. 3.4.6 and 4.4.1.

The competing quantum cluster theory of DCA is the CDMFT. In CDMFT, one treats the intercluster hoppings differently from the intracluster hoppings – the impurity is a cluster with open boundary conditions, which couples to the bath via the surface sites. In DCA, all hoppings are treated in the same way – the impurity has periodical boundary conditions and the coupling to the bath also respects the translational symmetry. As a consequence, the DCA impurity couples to the mean field with every site, whereas in CDMFT only the boundary sites couple to the bath states. That results in a slower convergence of Σ^{CDMFT} to the true lattice self energy ([59]),

$$\Sigma = \Sigma^{\mathrm{CDMFT}} + O\left(L^{-1/d}\right) , \tag{2.9}$$

compare with 2.8. The translational invariance is in DCA respected on all levels. This alone might be necessary for simulations of specific models [86]. Moreover, it may influence the efficiency of measurements in the impurity solver as the number of observables in a DCA simulation is proportional to L rather than to L^2 in the case of CDMFT; discussed in Sec. B.2. The advantage of CDMFT lies in fast convergence of local observables measured in the impurity center when the examined state has exponentially falling correlations [59], *i.e.* when it is far from a phase transition.

2.2 DCA cluster

A real space lattice $\mathscr{A}$ in d dimensions is defined by d independent basis vectors $\mathbf{a}_i$, $i \in \{1, \ldots, d\}$. A lattice point $\mathbf{r} \in \mathscr{A}$ is an integer linear combination of the basis vectors $\mathbf{a}_i$. A reciprocal lattice $\mathscr{B}$ exists to each real space lattice $\mathscr{A}$. Its basis vectors are denoted by $\mathbf{b}_i$, and they are defined by $\mathbf{a}_i \cdot \mathbf{b}_j = 2\pi\delta_{ij}$. The lattice points $\mathbf{r}$ refer in the context of Subsec. 1.2.2 to the cell vectors, and not necessarily to the individual sites.[3]

A cluster is for us a primitive cell of a superlattice $\tilde{\mathscr{A}}$ defined by basis vectors $\tilde{\mathbf{a}}_i$. These must be integer linear combinations of the lattice basis vectors,

$$\tilde{\mathbf{a}}_i = \sum_j n_{ij}\mathbf{a}_j , \qquad n_{ij} \in \mathbb{Z} . \tag{2.10}$$

The basis vectors $\tilde{\mathbf{a}}_i$ of the superlattice we refer to as the cluster basis vectors. The requirement on being a primitive cell of a (super)lattice ensures that the cluster can perfectly (without any empty spaces or overlaps) tile the d-dimensional space,

[3] In case of models defined on Bravais lattices there is a single site per unit cell and therefore we may identify the cell vector $\mathbf{r}$ with the real space position of a site, but for a general (non-Bravais) lattice this is not possible.

which is a legitimate constraint for any cluster method with periodical boundary conditions. All choices of a primitive cell for a given superlattice $\tilde{\mathscr{A}}$ produce equivalent results provided the model on the cluster has periodical boundary conditions.[4] In particular, any choice of a primitive cell of the given superlattice is equivalent to the parallelotope[5] defined by the cluster basis vectors, see illustration in Fig. 2.2.

Various sets of cluster basis vectors may form the same superlattice. For example, the superlattice build upon $\tilde{\mathbf{a}}_1$ and $\tilde{\mathbf{a}}_2$ is the same as the superlattice with basis vectors $\tilde{\mathbf{a}}_1$, $\tilde{\mathbf{a}}_2 - \tilde{\mathbf{a}}_1$. Studies [87, 88] provide the form of n_{ij} which guarantees unique description of the superlattice, which can be utilized *e.g.* for a systematic generation of all different superlattices.

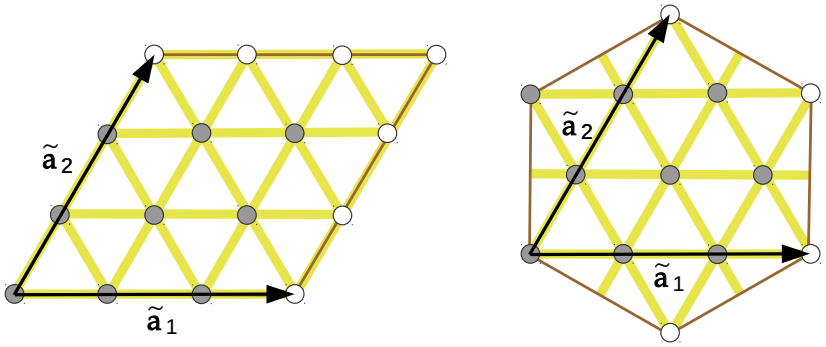

Figure 2.2: Here we show two differently shaped primitive cells corresponding to the same superlattice defined by the basis vectors $\tilde{\mathbf{a}}_i$. On the left we display the primitive cell in a form of a parallelogram, whereas on the right we show a symmetric choice of the primitive cell. The underlying lattice is a triangular lattice with sites shown as circles. Each white circle corresponds via periodical boundary conditions to one of the gray sites on the boundary of the cluster.

The oriented volume of a cluster is given by the determinant of the matrix n_{ij}. Its absolute value, *i.e.* the number of cells contained, is denoted by L. The L cells of the original real space lattice $\mathscr{A}$ that belong to the cluster constitute its real space representation $\mathbf{r}_i$, $i \in \{1, \ldots, L\}$. While for a diagonal n_{ij} it is trivial to obtain the set $\{\mathbf{r}_i\} \equiv \mathscr{C}$ of cluster real space vectors, it can be always be generated by this procedure:

1. Start with $\mathscr{C} = \{\mathbf{0}\}$.

[4] The DCA cluster has periodical boundary conditions.

[5] A parallelotope is the generalization of the parallelogram in $d = 2$ and the parallelepiped in $d = 3$ to any d.

2. Loop over $r = 1, \ldots, d$:

   (a) Find the lowest non-zero integer k such that there exists $\mathbf{r} \in \mathscr{C}$ for which $k\mathbf{a}_r - \mathbf{r}$ is a vector of the superlattice $\tilde{\mathbf{A}}$, *i.e.* for which $\frac{1}{2\pi}(k\mathbf{a}_r - \mathbf{r}) \cdot \tilde{\mathbf{b}}_j$ is an integer for all $j = 1, \ldots, d$.[6]

   (b) Set $\mathscr{C}' = \{\mathbf{r} + q\mathbf{a}_r : \mathbf{r} \in \mathscr{C}, q = 0, 1, \ldots, k-1\}$.

   (c) Replace $\mathscr{C}$ by $\mathscr{C}'$.

3. $\mathscr{C}$ contains L real space vectors $\mathbf{r}_i$, which can be used as real space representation of the cluster.

We denote the reciprocal lattice with respect to the superlattice $\tilde{\mathscr{A}}$ by $\tilde{\mathscr{B}}$. Its basis vectors are $\tilde{\mathbf{b}}_i$ such that $\tilde{\mathbf{a}}_i \cdot \tilde{\mathbf{b}}_j = 2\pi\delta_{ij}$, see example in Fig. 2.3. The reciprocal representation of the cluster consists of L reciprocal vectors $\mathbf{K}_i$ of the lattice $\tilde{\mathscr{B}}$, which belong to some primitive cell of $\mathscr{B}$. The problem of finding some valid reciprocal representation of the cluster is analogous to the problem of finding its real space representation discussed above.

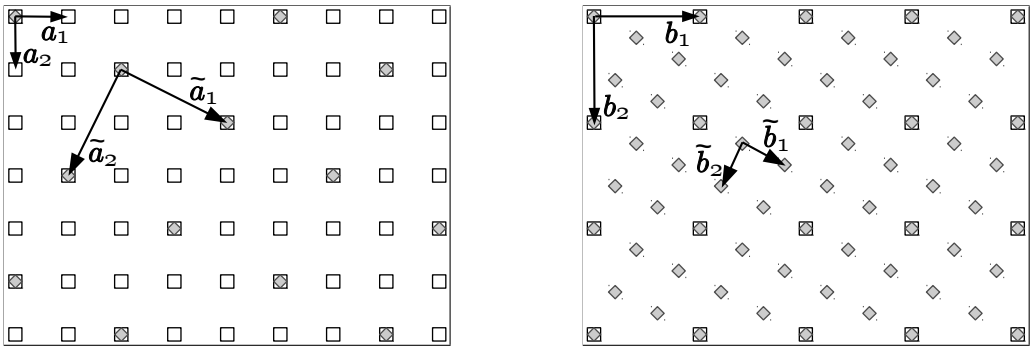

Figure 2.3: On the left is the real space lattice $\mathscr{A}$ consisting of the white squares, and the superlattice $\tilde{\mathscr{A}}$ consisting of the gray tilted squares. On the right is the reciprocal lattice $\mathscr{B}$ (white squares) and the reciprocal superlattice $\tilde{\mathscr{B}}$ (gray tilted squares).

Non-zero off-diagonal elements in n_{ij} complicate the usage of fast FT (FFT) for the change from the real space to the reciprocal representation and *vice versa*. The gain arising from allowing of general n_{ij} is in larger number of available clusters with given L which would otherwise not be accessible. This is especially important

[6] This condition can be easily done in integer arithmetic, as $\tilde{\mathbf{b}}_j = \sum_{l=1}^{d} \tilde{b}_{jl}\mathbf{b}_l$, with $\tilde{b}_{jl} = (n^{-1})_{lj}$, *i.e.* all $\tilde{b}_{jl}$ are integer multiples of $\frac{1}{L}$.

if there are physical considerations due to which the clusters need to respect some symmetries or if there are some constraints on the cluster due to the model, as those often greatly reduce the number of cluster candidates with reasonably bounded L. For clusters on the simple cubic lattice several useful criteria can be found in [89]; for the clusters on the square lattice see [90]. These rely heavily on counts of full shells of neighbors of an arbitrary cluster site, which is a heuristic criterion for models lacking longer-ranged hoppings or interactions.

As argued above, permitting clusters with general n_{ij} is a valuable benefit. The FFT in space is crucial for efficient implementation of some measurements, *e.g.* for the susceptibility measurement described in Subsec. 3.4.6. In order to perform the FFT, which we accomplished with the library FFTW [91], suitable permutation of the cluster sites $\mathbf{r}_i$ and cluster reciprocal points $\mathbf{K}_j$ is to be found.[7] The goal of the permutations is to get the table of integers,[8]

$$F_{ij} = \left(\frac{L}{2\pi} \mathbf{r}_i \cdot \mathbf{K}_j \right) \bmod L \,, \tag{2.11}$$

to match the table of integers F'_{ij} for some diagonal $d' \times d'$ matrix n'_{ij},

$$F'_{ij} = \left(\sum_{a=1}^{d'} x_a(i)\, k_a(j) \frac{L}{n'_{aa}} \right) \bmod L \,, \tag{2.12}$$

where the positions and momenta are ordered in a standard form, an example for $d' = 3$ follows,

$$i = x_1(i) + x_2(i)\, n'_{11} + x_3(i)\, n'_{11}\, n'_{22} \,, \tag{2.13}$$

$$j = k_1(j) + k_2(j)\, n'_{11} + k_3(j)\, n'_{11}\, n'_{22} \,. \tag{2.14}$$

Such choice of order of cluster real space and reciprocal points enables straightforward use of the FFTW library.[9] The lowest non-zero entry m in the table F_{ij} equals to the greatest common divisor of $\left\{ \frac{L}{n'_{11}}, \ldots, \frac{L}{n'_{d'd'}} \right\}$.[10] Since reordering of $\mathbf{r}_i$ is a permutation of the rows of the table F_{ij}, and any swap of the rows cannot change the content of any column, the content of the columns of the table F_{ij} is an invariant.[11] Same applies for the exchange of columns. These invariants enable quick check if the row and column permutation of F_{ij} may result in F'_{ij} and it reduces the complexity of the reordering.

[7] The permutation may not be unique. An example showing non-uniqueness exists already for $d = 1$, $L = 3$, where simultaneous swap of $x_2 = a$ with $x_3 = 2a$ and $k_2 = \frac{2\pi}{3a}$ with $k_3 = \frac{4\pi}{3a}$ leaves the FT of the same form.

[8] The modulo operation mod is meant in mathematical convention, *e.g.* $-1 \mod 7 = 6$.

[9] Clearly it must hold $L = \Pi_{i=1}^{d'} n'_{ii}$, $n'_{ii} \in \mathbb{Z}$, $n'_{ii} \geq 1$, $1 \leq d' \leq d$.

[10] The largest entry of n' can be chosen to be $\frac{L}{m}$, which then completely determines n' when $d = 2$.

[11] The order of the columns may be changed by swap of two $\mathbf{K}$ vectors.

2.3 DCA patch

The DCA patch is a primitive cell of $\tilde{\mathscr{B}}$. Thus it perfectly tiles the reciprocal space. Its volume is L-times smaller than the volume Ω_{BZ} of the Brillouin zone of the original lattice $\mathscr{A}$.[12] The shape of a DCA patch is ambiguous.[13] However, as the DCA patch enters the DCA approximation in Eq. 2.4, its choice may influence the quality of the approximation. The averaging (mean-field) effects are caused by the dispersion over the DCA patch. Since typically the dispersion is isotropic, a natural patch choice is a patch minimizing the largest distance k_{max} of any of its points from its center. This property has the primitive cell according to the Wigner–Seitz construction. In addition, it inherits the symmetry of the superlattice $\tilde{\mathscr{A}}$.[14] In case of anisotropic dispersion, the same consideration leads to the patch minimizing the largest distance from its center, but with a distance function taking into account the anisotropy, $\|\mathbf{k}\|^2 = \sum_{i=x,y,z} t_i^2 k_i^2$. For the construction of the Wigner–Seitz primitive cell in 3D we used QHULL [92].

The integration over a patch is performed as a sum of (analytically carried out) integrals of quadratic interpolants over small simplices. These are obtained first by splitting the DCA patch to large simplices with a single corner in the patch center and d corners at the patch boundary. In the second step we discretize each of the large simplices to a large number of small simplices.[15]

2.4 Dynamical cluster approximation for non-Bravais lattices

The DCA in its original setting was formulated for models defined on a Bravais lattice, *i.e.* with single site per unit cell. The DCA solution was assumed to obey the translational symmetry of the lattice. For the description of a spontaneous or artificial symmetry breaking, an extension of the DCA was established. For

[12] The Brillouin zone of a lattice $\mathscr{A}$ is the Wigner–Seitz choice of the primitive cell of the reciprocal lattice $\mathscr{B}$.

[13] A simple choice is the primitive cell of $\tilde{\mathscr{B}}$ in shape of a parallelotope centered at $\mathbf{0}$ with basis vectors equal to the basis vectors of $\tilde{\mathscr{B}}$.

[14] The Wigner–Seitz construction has to be done in the reciprocal space using the Cartesian coordinates, as opposed to the reduced coordinates which are given with respect to the reciprocal lattice basis vectors $\mathbf{b}$.

[15] In 3D, we cut each large simplex (= tetrahedron) to cubes, tetrahedra, and cubes without a single tetrahedron. Integration over the composite shapes takes into account all possible tilings onto tetrahedra – *e.g.* we symmetrize over all 16 possible tilings of a cube to 6 tetrahedra with equal volume.

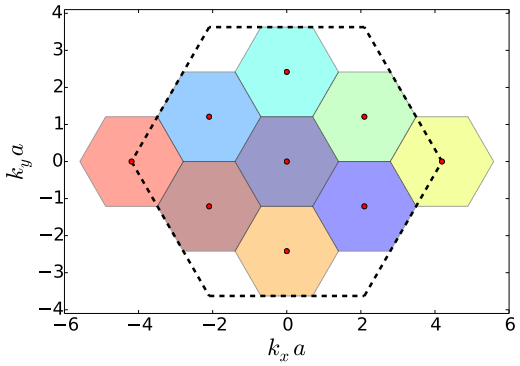

Figure 2.4: Reciprocal space picture of the cluster shown in Fig. 2.2 (either of those two variants). The dashed line hexagon is the Brillouin zone boundary of the lattice $\mathscr{A}$. Small red circles show the set of L reciprocal $\mathbf{K}$ points of the cluster. The small hexagons are DCA patches shifted to have centers at the cluster reciprocal $\mathbf{K}$ points, visualizing the areas of patch averaging in Eq. 2.4. The DCA patch is the Brillouin zone of the superlattice $\tilde{\mathscr{A}}$. The real space nearest neighbor site distance is denoted by a.

example, in order to account for the translational symmetry breaking at the AF reciprocal vector $\mathbf{Q}$, the Eqs. 2.4, 2.6 remain in the same form, but all involved objects become 2×2 matrices of the form [59],

$$\tilde{G}_\sigma(\mathbf{k}, \tau) = -\left\langle \tilde{\Psi}_{\mathbf{k}\sigma}(\tau)\tilde{\Psi}^\dagger_{\mathbf{k}\sigma} \right\rangle , \tag{2.15}$$

with spinor

$$\tilde{\Psi}^\dagger_{\mathbf{k}\sigma} = \left(c^\dagger_{\mathbf{k}\sigma},\, c^\dagger_{\mathbf{k}+\mathbf{Q}\sigma} \right) , \qquad \tilde{\Psi}_{\mathbf{k}\sigma} = \left(\tilde{\Psi}^\dagger_{\mathbf{k}\sigma} \right)^\dagger , \tag{2.16}$$

and the $\mathbf{k}$ vectors are restricted to the magnetic Brillouin zone, which has half the volume of the original Brillouin zone.

The above physical situation can be equally well described with the formalism using multisite cells introduced in Subsec. 1.2.3. Following this we divide the lattice into two sublattices, A and B, by which we enlarge the unit cells to contain one A and one B site. Similarly as in the approach using spinors $\tilde{\Psi}_{\mathbf{k}\sigma}$, we restrict ourselves to the magnetic Brillouin zone. We also use the Green's function in matrix form,

$$G_\sigma(\mathbf{k}, \tau) = -\left\langle \Psi_{\mathbf{k}\sigma}(\tau)\Psi^\dagger_{\mathbf{k}\sigma} \right\rangle , \tag{2.17}$$

just with differently defined spinor,

$$\Psi^\dagger_{\mathbf{k}\sigma} = \left(c^\dagger_{\mathbf{k}A\sigma},\, c^\dagger_{\mathbf{k}B\sigma} \right) , \qquad \Psi_{\mathbf{k}\sigma} = \left(\Psi^\dagger_{\mathbf{k}\sigma} \right)^\dagger . \tag{2.18}$$

Due to the form of FT 1.19 with the (non-standard) phase factors $e^{\pm i\mathbf{k}\cdot\mathbf{r}_\alpha}$, the transformation from $\Psi_{\mathbf{k}\sigma}$ to $\tilde{\Psi}_{\mathbf{k}\sigma}$ is given by a $\mathbf{k}$-independent unitary transformation $U_{\mathbf{k}}$,

$$\tilde{\Psi}^\dagger_{\mathbf{k}\sigma} = \Psi^\dagger_{\mathbf{k}\sigma} U_{\mathbf{k}}\,, \qquad \tilde{G}_\sigma(\mathbf{k}) = U^+_{\mathbf{k}} G_\sigma(\mathbf{k}) U_{\mathbf{k}}\,, \qquad U_{\mathbf{k}} = \frac{1}{\sqrt{2}}\begin{pmatrix} 1 & 1 \\ 1 & -1 \end{pmatrix}. \tag{2.19}$$

The $\mathbf{k}$-independence of $U_{\mathbf{k}}$ enables to perform basis change by $U_{\mathbf{k}}$ in the Eqs. 2.4 and 2.3 to change $\tilde{G}$, $\tilde{\Sigma}$ to G, Σ in both equations while keeping their form *intact*.[16] For a general $\mathbf{k}$-dependent unitary transformation between $\tilde{\Psi}^\dagger_{\mathbf{k}\sigma}$ and $\Psi^\dagger_{\mathbf{k}\sigma}$, additional $\tilde{\mathbf{k}}$-dependent factors would arise in the transformed Eq. 2.4, as that sums Green's functions at different $\mathbf{k}$ vectors (within a patch).

Clearly, we could have defined the FT 1.19 without the intracell phase factors $e^{\pm i\mathbf{k}\cdot\mathbf{r}_\alpha}$, with creation operators $\hat{c}'^\dagger_{\mathbf{k}\alpha\sigma}$. Further we could have defined the spinor $\Psi'^\dagger_{\mathbf{k}\sigma} = \left(\hat{c}'^\dagger_{\mathbf{k}A\sigma}, \hat{c}'^\dagger_{\mathbf{k}B\sigma}\right)$ and still keep the form of the approximation, Eqs. 2.4, 2.3, unchanged. Since the transformation between $\tilde{\Psi}$ and Ψ' is $\mathbf{k}$-dependent,[17] we would have defined a *different* approximation.[18] Within this section we refer to that approximation as DCA_0.[19]

That said, we define the DCA for any non-Bravais lattice[20] to be given by Eqs. 2.4 and 2.3 meant for Green's function of form given in Eq. 2.17, with FT prescribed by Eq. 1.19.

If we are to compare the above defined DCA for non-Bravais lattices with the other candidate, DCA_0, the only difference is in the FT. Apart from the important equivalence of the DCA for non-Bravais lattice with the DCA for broken translational symmetry, valid for a Bravais lattice with arbitrarily enlarged unit cell, the form of FT 1.19 reduces the averaging effect in Eq. 2.6 by reduction of variation of $t_{\mathbf{k}\alpha\alpha'}$ within a DCA patch (for $\alpha \neq \alpha'$), as illustrated on the example of tight-binding model on the honeycomb lattice in Fig. 2.5. That is connected with the fact that the off-diagonal elements ($\alpha \neq \alpha'$) of the Green's functions and self

[16] For this it is sufficient if $U_{\mathbf{k}}$ may be written as a product of a $\mathbf{k}$-dependent scalar and a $\mathbf{k}$-independent $\ell \times \ell$ matrix. By that it is clear, that for $\ell = 1$ the presence or absence of the intracell phase factors in FT does not play any role for DCA.

[17] The transformation from $\tilde{\Psi}^\dagger$ to $\Psi'^\dagger$, $\tilde{\Psi}^\dagger_{\mathbf{k}\sigma} = \Psi'^\dagger_{\mathbf{k}\sigma} U'_{\mathbf{k}}$, is given by the unitary transformation $U'_{\mathbf{k}} = \frac{1}{\sqrt{2}}\begin{pmatrix} e^{i\mathbf{k}\cdot\mathbf{r}_A} & 0 \\ 0 & e^{i\mathbf{k}\cdot\mathbf{r}_B} \end{pmatrix}\begin{pmatrix} 1 & 1 \\ 1 & -1 \end{pmatrix} = \frac{1}{\sqrt{2}}\begin{pmatrix} e^{i\mathbf{k}\cdot\mathbf{r}_A} & e^{i\mathbf{k}\cdot\mathbf{r}_A} \\ e^{i\mathbf{k}\cdot\mathbf{r}_B} & -e^{i\mathbf{k}\cdot\mathbf{r}_B} \end{pmatrix}$.

[18] In an exact treatment, any ($\mathbf{k}$-dependent) unitary transformation is just a change of the basis, and therefore cannot have any impact on the physical observables. However, the quality of an approximative method may be basis dependent, as the approximation may be better suited to some particular basis choice.

[19] This DCA version was used in [93].

[20] These might not only be a Bravais lattice with enlarged unit cell, but also a general lattice which does not permit description as a lattice with single site per unit cell.

energy obtain a phase factor when translated by a reciprocal lattice vector $\mathbf{b} \in \mathscr{B}$, $G(\mathbf{k}+\mathbf{b}) = U_{\mathbf{b}}^{+} G(\mathbf{k}) U_{\mathbf{b}}$ with diagonal unitary matrix $(U_{\mathbf{b}})_{\alpha\alpha'} = \delta_{\alpha\alpha'} e^{i\mathbf{b}\cdot\mathbf{r}_\alpha}$, see in Fig. 2.9.[21] The selfconsistency condition of DCA_0 is equivalent to that of the CDMFT [61] in the limiting case of a cluster consisting of a single (enlarged) cell. Finally, we already worked out in Subsec. 1.3.8 the impact of the form of FT 1.19 on the Green's function with respect to point group symmetries. These are not masked by any additional phase factors since the FT does not introduce any bias by the choice of the unit cell and reflects the original point group symmetry of the real space problem.

For a non-Bravais lattice, the form of FT given in Eq. 1.19 was used in previous study [86] on the Hubbard model on the honeycomb lattice.

As an example system we show the self energy of the Hubbard model on the honeycomb lattice in Figs. 2.7, 2.8, and 2.9. The self energy is in these plots interpolated after the convergence of the DCA selfconsistency loop. The asymptotic behavior of the self energy is examined in Figs. 2.7, 2.8.

2.5 Bipartite cluster for a Bravais lattice

For a study of a model defined on a Bravais lattice with anticipated antiferromagnetic (AF) ordering, the cluster has to be bipartite, *i.e.* it must contain the AF reciprocal vector $\mathbf{Q} = \frac{1}{2}\sum_{i=1}^{d} \mathbf{b}_i$ in its reciprocal representation. Otherwise, artificial frustration is introduced by the cluster geometry, see Fig. 2.6. The cluster is

[21] This makes it desirable to work with a fixed set of $\mathbf{K}$ vectors. In Subsec. 4.4.1 we encounter a phase factor accounting for the need to shift a $\mathbf{K}$ vector by a reciprocal lattice vector $\mathbf{b} \in \mathscr{B}$. Since the only place where the choice of the basis matters is the patch averaging step 2.6, one could use the default FT convention omitting the phase factors and switch to the convention with those only for the averaging step.

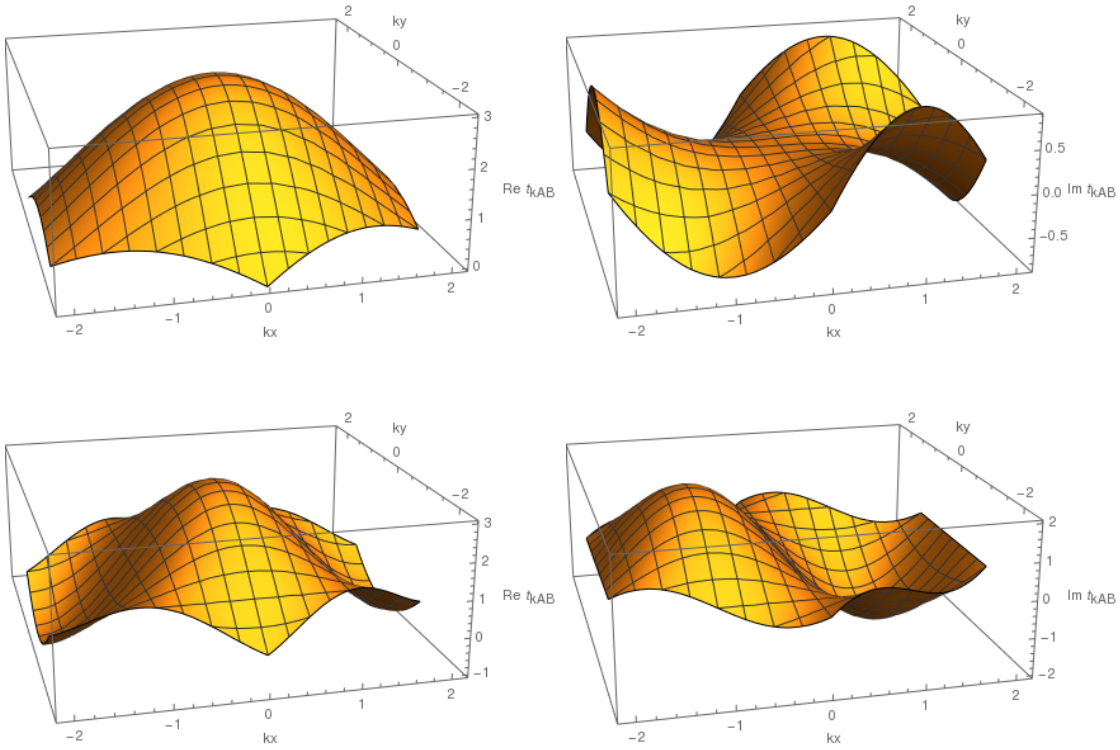

Figure 2.5: We display the hopping amplitude $t_{\mathbf{k}AB}$ for the tight-binding model on the honeycomb lattice with hopping $t = 1$. The top row displays the real (left) and imaginary (right) part of $t_{\mathbf{k}AB}$ assuming the FT of form 1.19. The bottom row shows the real (left) and imaginary (right) part of $t_{\mathbf{k}AB}$ assuming the FT omitting the intracell phase factors $e^{\pm i\mathbf{k}\cdot\mathbf{r}_\alpha}$ present in 1.19.

bipartite if and only if[22]

$$\forall i = 1, \ldots, d : \left(\sum_{j=1}^{d} n_{ij} \right) \bmod 2 = 0 \,. \tag{2.23}$$

[22]The proof is straightforward. The basis vectors of the reciprocal superlattice $\tilde{\mathscr{B}}$ are

$$\mathbf{d}_i = \sum_{j=1}^{d} \left(n^{-1}\right)_{ji} \mathbf{b}_j \,, \qquad i = 1, \ldots, d \,. \tag{2.20}$$

The cluster is bipartite if there exist integers a_i such that $\sum_{i=1}^{d} a_i \mathbf{d}_1 = \mathbf{Q} = \frac{1}{2} \sum_{i=1}^{d} \mathbf{b}_i$, which is equivalent to the set of equations,

$$\forall j = 1, \ldots, d : \frac{1}{2} = \sum_{i=1}^{d} \left(n^{-1}\right)_{ji} a_i \,. \tag{2.21}$$

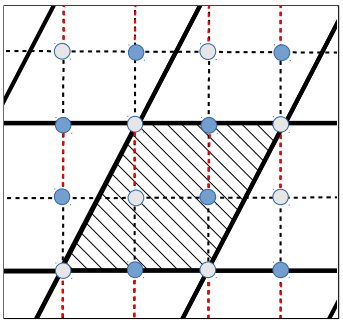

Figure 2.6: The hatched region is an example of a non-bipartite cluster. The bipartition of the square lattice and the cluster tiling are *incommensurate*, which causes frustration on the periodical boundaries of the cluster. The red dashed lines visualize frustrated bonds.

As described in Sec. 2.4, we could simulate the translational symmetry breaking using formalism of $\tilde{G}$ based on spinors $\tilde{\Psi}$. Further, we proved that equivalently we may use the formalism with doubled cells with G based on Ψ. Here we find the requirements on the enlarged unit cell and the cluster. We assume a 2 or 3-dimensional Bravais lattice, and as the enlarged unit cell we take two neighboring sites. Let us denote the basis vectors of the Bravais lattice as $\mathbf{a}'_1$, $\mathbf{a}'_2$ (, $\mathbf{a}'_3$). The AF reciprocal vector $\mathbf{Q}$ fulfills $e^{i\mathbf{Q}\cdot\mathbf{a}'_i} = -1$ for all basis vectors $\mathbf{a}'_i$.

In the description with two sites per unit cell we denote the two sublattices by A and B. Further, we fix the position of site A (B) within a cell to be $\mathbf{0}$ ($\mathbf{a}'_1$). Some care needs to be taken for an appropriate choice of the lattice vectors $\mathbf{a}_i$ corresponding to this enlarged unit cell – in order to be compliant with the anticipated AF order these need to be chosen such that $e^{i\mathbf{Q}\cdot\mathbf{a}_i} = 1$. A particular example is $\mathbf{a}_1 = 2\mathbf{a}'_1$, $\mathbf{a}_2 = \mathbf{a}'_2 \pm \mathbf{a}'_1$ (, $\mathbf{a}_3 = \mathbf{a}'_3 \pm \mathbf{a}'_1$).[23] Any cluster with doubled unit cells satisfying the condition $e^{i\mathbf{Q}\cdot\mathbf{a}_i}$ is then automatically bipartite, *i.e.* in the single site per cell description it contains the reciprocal $\mathbf{Q}$ in its cluster reciprocal space.

The criterion 2.23 is obvious from the solution of the above equation set,

$$\frac{1}{2}\sum_{j=1}^{d} n_{ij} = a_i \,. \tag{2.22}$$

[23]Be aware that choice $\mathbf{a}_1 = 2\mathbf{a}'_1$, $\mathbf{a}_2 = \mathbf{a}'_2$ would not be a good choice for description of the AF phase with translational invariance assumed for the enlarged unit cell. For a 2D problem, a symmetric choice for the basis vectors is $\mathbf{a}_1 = \mathbf{a}'_1 + \mathbf{a}'_2$, $\mathbf{a}_2 = \mathbf{a}'_1 - \mathbf{a}'_2$. In 3D one may use $\mathbf{a}_1 = \mathbf{a}'_2 + \mathbf{a}'_3$, $\mathbf{a}_2 = \mathbf{a}'_1 + \mathbf{a}'_3$, and $\mathbf{a}_3 = \mathbf{a}'_1 + \mathbf{a}'_2$.

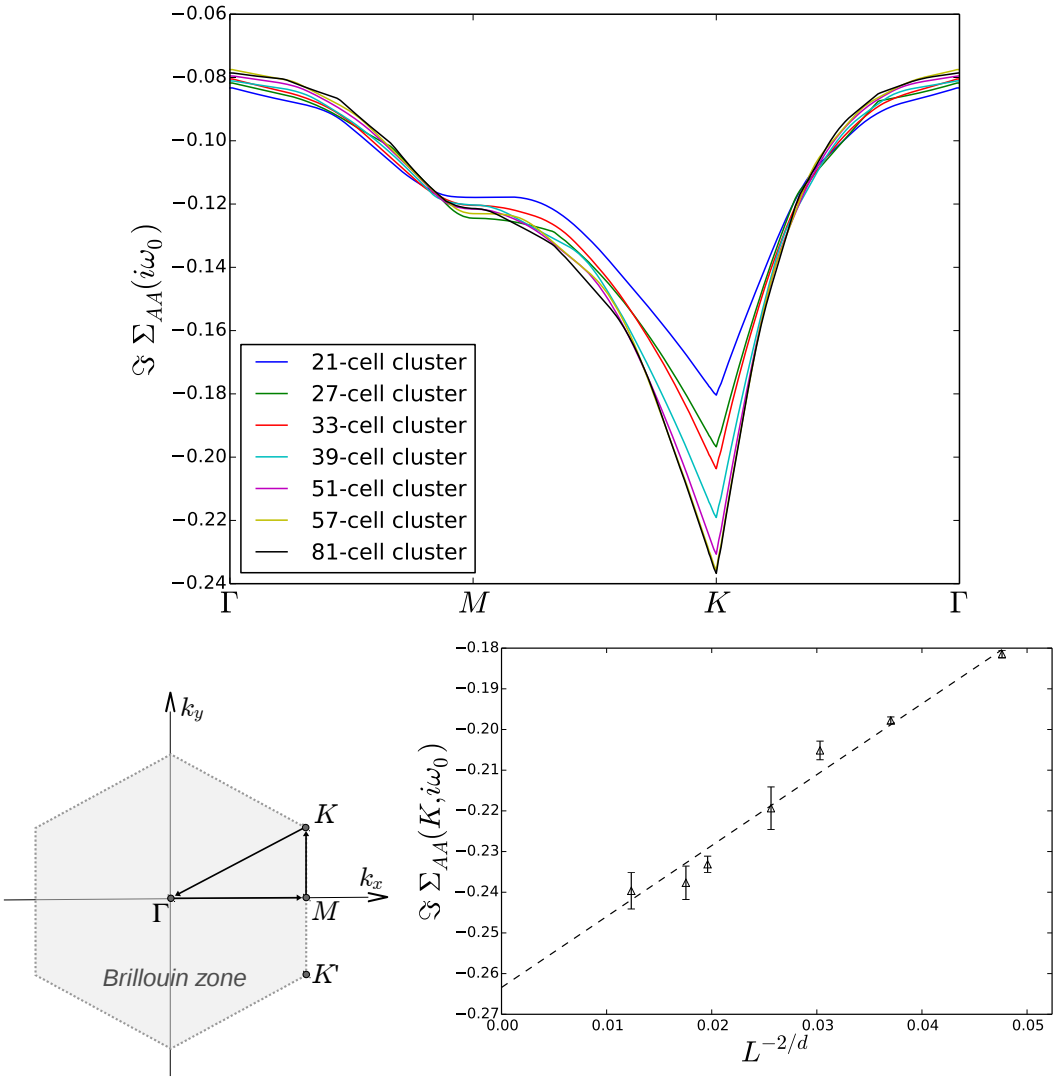

Figure 2.7: The top figure shows the imaginary part of the self energy element AA at Matsubara frequency $i\omega_0 = \pi T$ along the high-symmetry path $\Gamma - M - K - \Gamma$ of the Brillouin zone of the honeycomb lattice ($d = 2$), displayed in bottom left figure. The investigated model was the Hubbard model on the honeycomb lattice with $U = 4t$ and $\beta t = 10$ with enforced spin symmetrization, at half filling. For the top figure we used natural neighbor interpolation of the DCA impurity data known at the reciprocal superlattice $\mathscr{B}'$. The interpolation was applied only in the postprocessing. Notice the fact that the natural neighbor interpolation never overshoots. The bottom right plot shows the convergence of the imaginary part of $\Sigma_{AA}(K, i\omega_n)$ with the cluster size L. All clusters used to obtain data for these plots contain the K and K' points in their cluster reciprocal space and none of them contains the M point. The 33-cell and the 51-cell clusters break the 3-fold rotational symmetry, therefore we symmetrized the interpolated data.

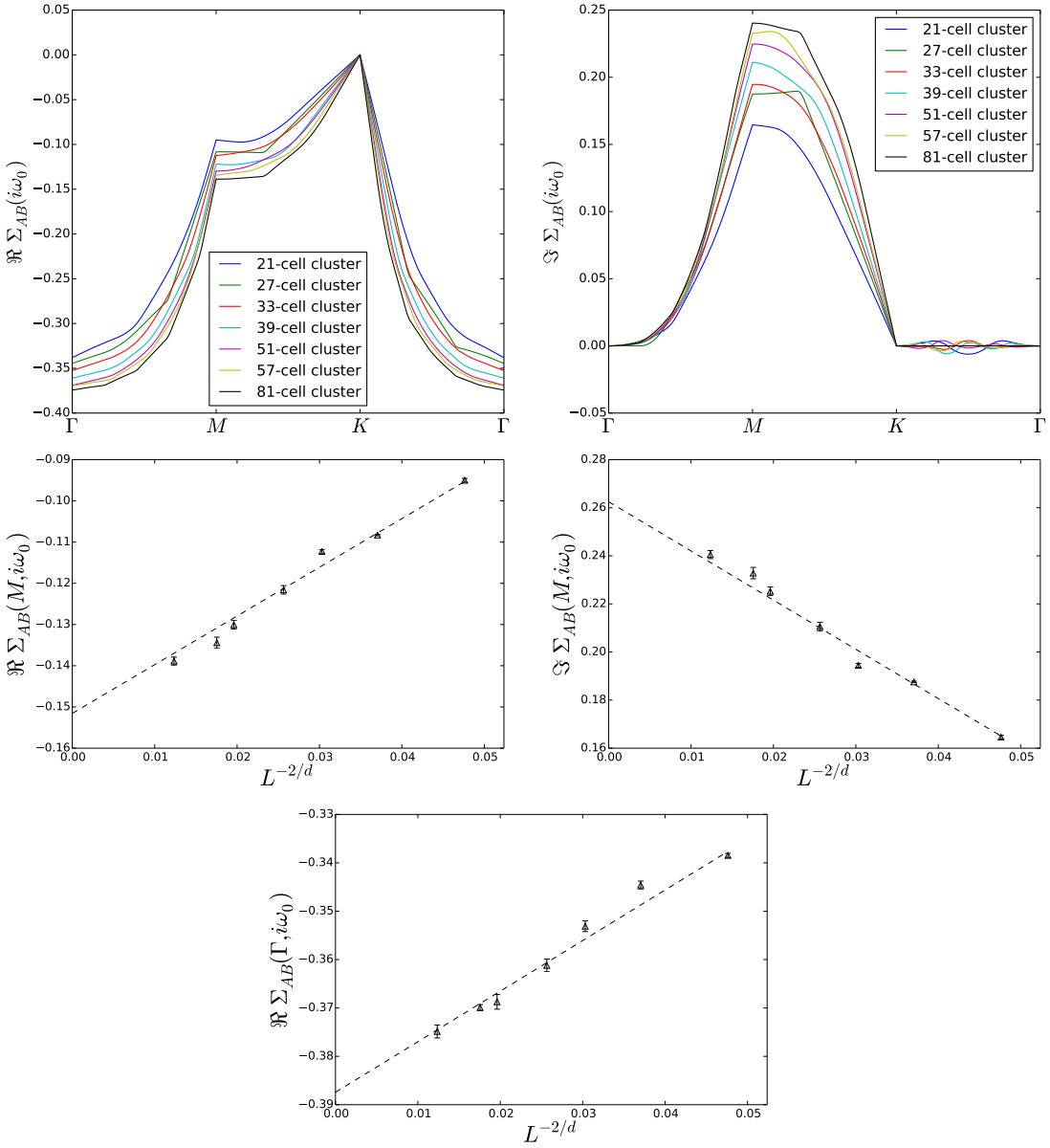

Figure 2.8: In the top row there are analogous plots as in Fig. 2.7(top), but for different components of the 2×2 self energy matrix. The other plots shows convergence at the high symmetry points Γ and M. Since none of the clusters directly contained the M point in its reciprocal representation, the natural neighbor interpolation was applied to obtain data for the convergence plots at M point (center row). According to discussion in Subsec. 1.3.7, the real and imaginary part of Σ_{AB} at the "time-reversal symmetric" points (Γ, M) are dependent. That constrains $\Im\Sigma_{AB}(\Gamma) = 0$. $G_{AB}(K) = 0 = \Sigma_{AB}(K)$ due to the 3-fold rotational symmetry, as K rotated by 120° equals to K translated by a reciprocal lattice vector, giving rise to constraint $G_{AB}(K) = G_{AB}(K)\, e^{2\pi i/\sqrt{3}}$.

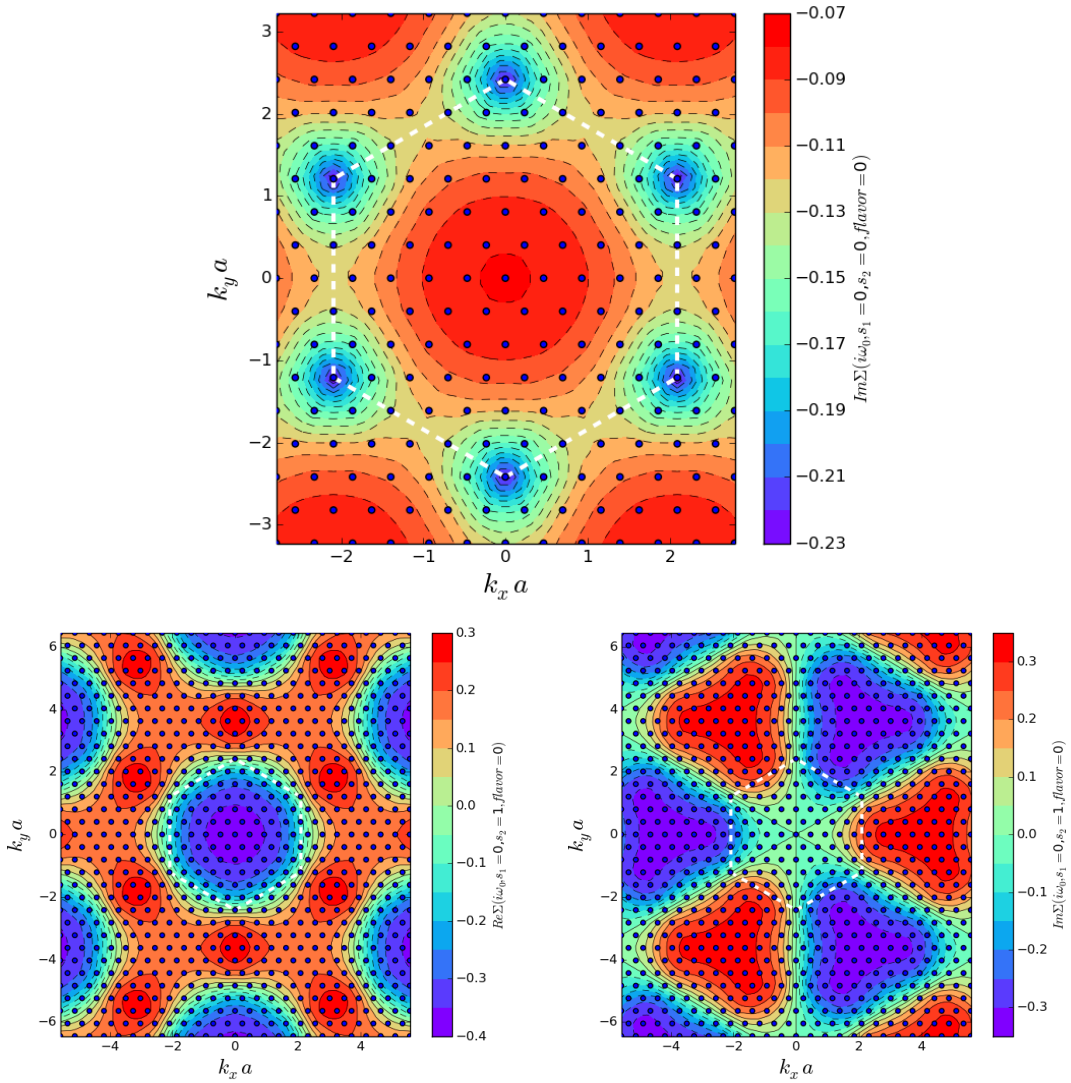

Figure 2.9: Plot of independent components of the self energy at Matsubara frequency $i\omega_0 = \pi T$ obtained on a 81-cell cluster. The investigated model was the Hubbard model on the honeycomb lattice with $U = 4t$ and $\beta t = 10$ with enforced spin symmetrization, at half filling. According to Subsec. 1.3.7, only the imaginary part of the AA component of Σ (top figure) along with real (bottom left) and imaginary (bottom right) part of Σ_{AB} are independent. The small blue circles are the points of the reciprocal superlattice $\mathscr{B}'$, at which the impurity self energy was computed. Natural neighbor interpolation was used to produce the plots. The Brillouin zone boundary is displayed as white dashed hexagon. Σ_{AB} is translationally symmetric with respect to shift by a reciprocal lattice vector $\mathbf{b} \in \mathscr{B}$ with additional phase factor, $\Sigma_{AB}(\mathbf{k}+\mathbf{b}) = \Sigma_{AB}(\mathbf{k})\, e^{i\mathbf{b}\cdot(\mathbf{r}_B - \mathbf{r}_A)}$, due to the form of FT 1.19.

3 Anisotropic Hubbard model on a cubic lattice

We study the anisotropic 3D Hubbard model with increased nearest-neighbor tunneling amplitudes along one direction using the DCA and local density approximation (LDA), and compare the results to a quantum simulation experiment of ultracold fermions in an optical lattice. Our results agree with the experimental observations and show that the lowest achieved experimental temperature is below the strong tunneling amplitude. The study provides estimate of heating in the process of lattice loading. We characterize the system by examining the spin correlations beyond neighboring sites and determine the distribution of density, entropy and spin correlation in the trapped system. We furthermore investigate the dependence of the critical entropy at the Néel transition on anisotropy and show that anisotropy is not favorable for long-range magnetic order in terms of its critical entropy.

This chapter is based on [1, 5] done in a collaboration with experimental physicists working with ultracold atoms in optical lattice. Lei Wang performed the LDA supplied with the equation of states (EOS) obtained with DCA using the CT-AUX impurity solver. Mauro Iazzi contributed with finite lattice QMC data obtained with LCT-INT [40], which was not presented in the published version, but served for consistency check. Emanuel Gull provided the CT-AUX implementation, which was further developed by the author of the thesis. The EOS extrapolations and the DCA simulations were also performed by the author of the thesis. The experimental data was obtained by Daniel Greif, Thomas Uehlinger, Gregor Jotzu, Gregor and Leticia Tarruell in the group of Prof. Tilman Esslinger.

3.1 Introduction

The controlled setting of ultracold fermions in optical lattices offers the possibility to directly realize the Hubbard model [69, 94] in an experiment and has allowed for studying the metal to Mott-insulator crossover [95, 96]. At half-filling, mag-

netic correlations are expected to arise at lower temperatures, as a consequence of super-exchange, and ultimately create a *Néel phase* characterized by long-range antiferromagnetic order. While this has so far not been accessed experimentally, short-range quantum magnetism has been observed in a recent experiment [97]. In particular, anti-ferromagnetic spin correlations on neighboring sites were measured using an anisotropic simple cubic lattice configuration, in which the tunneling along one direction was enhanced. In contrast to previous measurements, where a perturbative high-temperature expansion was sufficient to describe the system [75, 98, 99], understanding this new quantum simulation experiment requires a more sophisticated theoretical approach. Open questions included the influence of the anisotropy on the temperature of the system and the entropy distribution in the trap.

Although the thermodynamics, spin correlations and Néel transition temperature for the isotropic 3D Hubbard model have been calculated with different numerical methods [100, 101, 102, 103, 104], the anisotropic Hubbard model was only studied in the Heisenberg limit [105], where the Néel temperature was found to drop continuously to zero as the interchain coupling decreases. However, the experiment [97] is carried out at weak to intermediate interaction strength, where charge fluctuations cannot be ignored. In this study we investigate the dependence of Néel temperature on anisotropy and the behavior of the strength, range and orientation of spin correlations in the experimentally relevant parameter regimes.

3.2 Model

The Hamiltonian of the anisotropic Hubbard model on a cubic lattice is given by

$$\begin{aligned}\hat{H} &= -t\sum_{\mathbf{r},\sigma}\left(\hat{c}^{\dagger}_{\mathbf{r}+\mathbf{e}_x\sigma}\hat{c}_{\mathbf{r}\sigma}+h.c.\right)\\ &\quad -t'\sum_{\mathbf{r},\sigma}\left(\hat{c}^{\dagger}_{\mathbf{r}+\mathbf{e}_y\sigma}\hat{c}_{\mathbf{r}\sigma}+\hat{c}^{\dagger}_{\mathbf{r}+\mathbf{e}_z\sigma}\hat{c}_{\mathbf{r}\sigma}+h.c.\right)\\ &\quad +U\sum_{\mathbf{r}}\hat{n}_{\mathbf{r}\uparrow}\hat{n}_{\mathbf{r}\downarrow}-\mu\sum_{\mathbf{r},\sigma}\hat{n}_{\mathbf{r}\sigma},\end{aligned} \tag{3.1}$$

where $\hat{c}^{\dagger}_{\mathbf{r}\sigma}$ ($\hat{c}_{\mathbf{r}\sigma}$) creates (annihilates) a fermion at lattice site $\mathbf{r}$ with spin $\sigma\in\{\uparrow,\downarrow\}$; $\hat{n}_{\mathbf{r}\sigma}\equiv\hat{c}^{\dagger}_{\mathbf{r}\sigma}\hat{c}_{\mathbf{r}\sigma}$ denotes the occupation number operator; $\mathbf{e}_i$ denotes the unit vector (setting the lattice spacing to 1) along the direction $i\in\{x,y,z\}$. The system has the tunneling amplitude t along the x-axis and t' in the directions y, z as shown in Fig. 3.1. The repulsive on-site interaction energy is denoted by $U>0$ and the chemical potential by μ. The ratio t/t' will be referred to as the anisotropy of the system. We consider $t/t'\geq 1$, covering the range from an isotropic 3D system to

weakly coupled 1D chains. The half filling ($n = 1$) corresponds to $\mu = U/2$, which is the particle-hole symmetric point, see Subsec. 1.3.6.

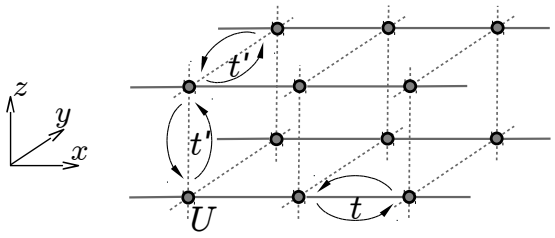

Figure 3.1: Sketch of the investigated anisotropic Hubbard model defined on a cubic lattice. For $t' \ll t$ it may be viewed as set of weakly coupled 1D chains.

3.3 Numerical simulation

The study focuses on two different parameter ranges:

- ▷ For the direct comparison with the experiment we provide numerical data at an experimentally accessible temperature. Since a fully *ab initio* simulation of 10^5 fermionic particles in the optical lattice is beyond the capabilities of current numerical simulations, a simplification was needed to fulfill the task. We utilize DCA providing the EOS extrapolated to the thermodynamic limit. To take into account the trapping potential in the experiment, we use LDA, which has been proven to be accurate in the temperature region relevant for comparison with the experiment [106, 107, 108].

- ▷ For the Néel temperature estimates at half filling we perform simulations at lower temperature than those accessible by the experiment.In order to find the entropy at the Néel transition, the EOS at half filling had to be obtained as well.

We study the physical properties of Eq. 3.1 with DCA, using the numerically exact continuous time auxiliary field quantum Monte Carlo impurity solver [39, 109]. All simulations were carried out within the paramagnetic (PM) phase, therefore we could use the standard DCA version for Bravais lattices [59], *i.e.* with single site per unit cell ($\ell = 1$).

3.4 Observables

3.4.1 Measurement of equation of states

We have calculated the thermodynamic properties including energy (e) and density (n) per site at a given chemical potential μ and the inverse temperature $\beta = 1/T$ (setting $k_B = 1$).

Calculation of the entropy

The entropy per site $s(\beta)$ is obtained by numerical integration

$$s(\beta) \;=\; s(\beta_0) + f(\beta)\beta - f(\beta_0)\beta_0 - \int_{\beta_0}^{\beta} f(\beta')\,\mathrm{d}\beta', \tag{3.2}$$

at fixed μ, with $f(\beta) = e(\beta) - \mu n(\beta)$.[1] The integration was carried out with quadratic interpolants on an irregular mesh on the inverse temperature axis. The value of $s(\beta_0)$ at a sufficiently small $\beta_0 \sim \frac{1}{50t}$ was obtained using the high temperature series expansion (HTSE)

$$s(\beta_0) = \ln 4 - \frac{\beta_0^2}{2}\left[\frac{U^2}{16} + \frac{(\mu - U/2)^2}{2} + t^2 + 2t'^2\right] + \frac{\beta_0^3}{8} U \left(\mu - \frac{U}{2}\right)^2 + \mathcal{O}(\beta_0^4)\,, \tag{3.5}$$

see details in Sec. D.2. The error of $s(\beta)$ is given by the error propagation of the uncertainty of the integrand $f(\beta)$. The error of e and n comes from the extrapolation to the thermodynamic limit discussed in Subsec. 3.4.2, for which n and e have to be measured on a set of differently sized clusters. In parameter regions with very low filling we obtained the EOS employing the Hartree approximation.[2] As the model possesses the particle-hole symmetry, the EOS for $n > 1$ can be readily determined from the data for $2 - n < 1$.

[1] In our system there is no work present, as the site potentials and the Zeeman term are absent. Thus we may utilize the thermodynamic relation,

$$T\mathrm{d}s = \mathrm{d}e - \mu \mathrm{d}n = \mathrm{d}(e - \mu n) + n\mathrm{d}\mu\,, \tag{3.3}$$

which we write in a form suitable for simulation with fixed chemical potential. For fixed μ we find

$$s(T) - s(T_0) = \int_{T_0}^{T} \frac{\mathrm{d}\tilde{f}(T')}{T'} = \int_{T_0}^{T} \frac{\tilde{f}'(T')\,\mathrm{d}T'}{T'} = \frac{\tilde{f}(T)}{T} - \frac{\tilde{f}(T_0)}{T_0} - \int_{T}^{T_0} \frac{\tilde{f}(T')\,\mathrm{d}T'}{T'^2}\,, \tag{3.4}$$

where $\tilde{f}(T) = e(T) - \mu n(T)$. Eq. 3.2 is obtained by substitution $\beta' = 1/T'$.

[2] In the Hartree approximation, the self energy is approximated by $\Sigma^{\mathrm{Hartree}}_{\mathbf{k}\alpha\alpha'\sigma}(i\omega_n) = U n_{\alpha\bar{\sigma}}\delta_{\alpha\alpha'}$, where the density $n_{\alpha\sigma}$ has to fulfill the selfconsistency condition, $n_{\alpha\sigma} = -\frac{1}{\Omega_{\mathrm{BZ}}}\int_{\mathrm{BZ}} \mathrm{d}\mathbf{k}\, G_{\mathbf{k}\alpha\alpha\sigma}(\tau = \beta^-)$, and $G_{\mathbf{k}\sigma}(\tau = \beta^-)$ is the FT of $G_{\mathbf{k}\sigma}(i\omega_n) = \left[G^0_{\mathbf{k}\sigma}(i\omega_n)^{-1} - \Sigma^{\mathrm{Hartree}}_{\mathbf{k}\sigma}(i\omega_n)\right]^{-1}$. The solution is found iteratively. At fixed $n_{\alpha\sigma}$, the self energy can be treated as a potential-like term and

Measurement of the density

The density n can be for a given cluster obtained easily, since it coincides with the directly measurable impurity density, as

$$n = -\sum_{\sigma} G^{\mathrm{lat}}_{\mathbf{r}\mathbf{r}\sigma}(\tau = \beta^-) = \frac{1}{\Omega_{\mathrm{BZ}}} \sum_{\sigma} \int_{\mathrm{BZ}} \mathrm{d}\mathbf{k}\, G^{\mathrm{lat}}_{\mathbf{k}\sigma}(\tau = \beta^-) = \frac{1}{L} \sum_{\mathbf{K},\sigma} G^{\mathrm{imp}}_{\mathbf{K}\sigma}(\tau = \beta^-)\,, \tag{3.6}$$

where the last equation holds for a converged DCA solution according to Eq. 2.4.[3]

Energy estimation

For the evaluation of the energy per site $e = \frac{1}{L}\left\langle \hat{H} + \mu\hat{N} \right\rangle$ we split the Hamiltonian $\hat{H}$ in Eq. 3.1 into the interacting part $\hat{H}_U = U \sum_{\mathbf{r}} \hat{n}_{\mathbf{r}\uparrow}\hat{n}_{\mathbf{r}\downarrow}$ and the rest, $\hat{H}_0$. $\hat{N} = \sum_{\mathbf{r},\sigma} \hat{n}_{\mathbf{r}\sigma}$ is the total particle number operator. We separately evaluate the interaction energy $e_{\mathrm{int}} = \frac{1}{L}\left\langle \hat{H}_U \right\rangle$ and the "kinetic" energy $e_{\mathrm{kin}} = \frac{1}{L}\left\langle \hat{H}_0 + \mu\hat{N} \right\rangle$ separately.

The interaction energy e_{int} possesses for the studied Hubbard model a simple form, $\frac{1}{L}\left\langle \hat{H}_U \right\rangle = \frac{U}{L} \sum_{\mathbf{r}} \langle \hat{n}_{\mathbf{r}\uparrow}\hat{n}_{\mathbf{r}\downarrow} \rangle$. The equal-time density-density correlation was measured on the impurity, which is *not* a DCA consistent treatment. A DCA compatible measurement would be conducted similarly as the susceptibility measurement described in Subsec. 3.4.6, with the additional need of summation over $i\nu_m$ and $\mathbf{q}$, as $\hat{n}_{\mathbf{r}\uparrow}\hat{n}_{\mathbf{r}\downarrow}$ is an instantaneous and real space localized rather then static and reciprocal space localized quantity. That would be a very expensive measurement. Since the double occupation does not diverge and is expected to be free of any discontinuities,[4] the approximation of its lattice value by the double occupation on the impurity is plausible. Within the CT-AUX impurity solver, the double occupation measurement on the impurity is conducted with use of the Wick's theorem, as presented in Eq. 3.15.

---

thus it can be absorbed into the non-interacting Hamiltonian. Therefore, the density can be obtained directly via the Fermi–Dirac distribution, $n_{\mathbf{k}\sigma} = \left[1 + e^{\beta(\varepsilon_{\mathbf{k}} - \mu)}\right]^{-1}$. Note that for the Hubbard model the Hartree and Hartree–Fock approximation coincide, as the Fock exchange potential vanishes due to missing direct interaction between particles of same spin. The Hartree approximation can be thought of as a skeletal first order perturbation theory, *i.e.* with Σ_σ considered to be a functional of G_σ.

[3] This relation does not hold exactly once we perform interpolation of the converged patch-wise constant self energy in order to obtain a continuous approximation of the lattice self energy. In the present study we exclusively used the approximation of the lattice self energy by the converged patch-wise constant DCA self energy.

[4] Those could occur at a first order phase transition.

The kinetic energy $e_{\text{kin}} = \frac{1}{L}\left\langle \hat{H}_0 + \mu\hat{N} \right\rangle$ can be evaluated in a DCA compatible way. To make the kinetic energy result applicable for general lattices, we stick to the formalism with multisite cells, as introduced in Subsec. 1.2.2. We write the amplitudes of $\hat{H}_0 + \mu\hat{N}$ in a matrix form,

$$\hat{H}_0 + \mu\hat{N} = \sum_{\mathbf{r},\mathbf{\Delta},\alpha,\alpha',\sigma} h_{\mathbf{\Delta}\alpha\alpha'} \hat{c}^\dagger_{\mathbf{r}\alpha\sigma} \hat{c}_{\mathbf{r}+\mathbf{\Delta}\alpha'\sigma} \,. \tag{3.7}$$

The kinetic energy of the lattice may thus be obtained as

$$\begin{aligned} e_{\text{kin}} &= \frac{1}{L\ell} \sum_{\mathbf{r},\mathbf{\Delta},\alpha,\alpha',\sigma} h_{\mathbf{\Delta}\alpha\alpha'} \underbrace{\left\langle \hat{c}^\dagger_{\mathbf{r}\alpha\sigma} \hat{c}_{\mathbf{r}+\mathbf{\Delta}\alpha'\sigma} \right\rangle}_{-G^{\text{lat}}_{\mathbf{\Delta}\alpha'\alpha\sigma}(\tau=\beta^-)=\delta_{\mathbf{\Delta}\mathbf{0}}\delta_{\alpha\alpha'}+G^{\text{lat}}_{\mathbf{\Delta}\alpha'\alpha\sigma}(\tau=0^+)} && (3.8) \\ &= \frac{2}{\ell}\sum_{\alpha} h_{\mathbf{0}\alpha\alpha} + \frac{1}{\ell} \sum_{\mathbf{\Delta},\alpha,\alpha',\sigma} h_{\mathbf{\Delta}\alpha\alpha'} G^{\text{lat}}_{\mathbf{\Delta}\alpha'\alpha\sigma}(\tau = 0^+) && (3.9) \\ &= \frac{2}{\ell} \operatorname*{Tr}_{\alpha} \{h_{\mathbf{0}}\} + \frac{1}{\Omega_{\text{BZ}}\ell} \sum_{\sigma} \int_{\text{BZ}} \mathrm{d}\mathbf{k} \operatorname*{Tr}_{\alpha} \left\{ h_{\mathbf{k}} G^{\text{lat}}_{\mathbf{k}\sigma}(\tau = 0^+) \right\} \,, && (3.10) \end{aligned}$$

where $L \to \infty$ denotes the number of lattice cells, which are labeled by $\mathbf{r}$ and $\mathbf{r}+\mathbf{\Delta}$. The lattice Green's function is obtained via the Dyson equation using the DCA approximation of the self energy by the self energy Σ of the impurity according to Eq. 2.3,

$$\begin{aligned} G^{\text{lat}}_{\sigma}(\mathbf{k}, i\omega_n) &= \left\{ \left[G^{0,\text{lat}}_{\sigma}(\mathbf{k}, i\omega_n) \right]^{-1} - \Sigma_{\sigma}\left[\mathbf{K}(\mathbf{k}), i\omega_n\right] \right\}^{-1} && (3.11) \\ &= \left\{ i\omega_n \mathbb{1}_{\ell} - h_{\mathbf{k}} - \Sigma^{\text{cluster}}_{\sigma}\left[\mathbf{K}(\mathbf{k}), i\omega_n\right] \right\}^{-1} \,, && (3.12) \end{aligned}$$

where $\mathbf{K}(\mathbf{k})$ is function returning the grained $\mathbf{K}$ in the centre of the DCA patch containing $\mathbf{k}$. That enables to write the formula 3.10 with patch averaging as

$$e_{\text{kin}} = \frac{2}{\ell} \operatorname*{Tr}_{\alpha} \{h_{\mathbf{0}}\} + \frac{1}{\beta\Omega_{\text{BZ}}\ell} \sum_{\sigma,n,\mathbf{K}} \operatorname*{Tr}_{\alpha} \int_{\text{patch}} \mathrm{d}\tilde{\mathbf{k}}\, h_{\mathbf{K}+\tilde{\mathbf{k}}} \left[i\omega_n \mathbb{1}_{\ell} - h_{\mathbf{K}+\tilde{\mathbf{k}}} - \Sigma_{\sigma}(\mathbf{K}, i\omega_n) \right]^{-1} \,. \tag{3.13}$$

The infinite sum over Matsubara frequencies n arising from the FT of $G^{\text{lat}}_{\sigma}(\tau = 0^+)$ cannot be handled exactly. We handled the high frequency contribution perturbatively, see details in Sec. A.1.

We used the Jackknife analysis for the error estimates of e from subsequent iterations of a DCA simulation, assuming the results from subsequent iterations being independent.[5]

[5] This assumption breaks down in the vicinity of phase transitions, where the convergence of iterative solution of the selfconsistency condition slows down and binning analysis is required on the level of iterations for correct error estimates. In such a case, the autocorrelation time may reach 10 or more iterations.

3.4.2 Extrapolation to the thermodynamic limit

The DCA results were extrapolated in cluster size according to $L^{-2/d}$, compare with Eq. 2.8, to obtain results in the thermodynamic limit [102, 110].[6] L denotes the number of sites of the clusters and $d = 3$ is the physical dimension of the lattice. Since the temperature range scanned in order to obtain the EOS was relatively high compared to the critical temperature $T_{\text{Néel}}$, this procedure supplies reliable results without necessity to employ very large clusters.

The clusters were chosen elongated in the strong tunneling direction with aspect ratio roughly proportional to the anisotropy.[7] The motivation for this is, similar to one of the arguments for the choice of the form of FT 1.19, a reduction of the variation of the bare lattice Green's function within a patch. With the exception of the smallest clusters in the anisotropic case, which were 1-dimensional chains of even length, the clusters were chosen to be bipartite to avoid artificial frustration. For the isotropic case, we used a set of bipartite clusters of 36, 56, 64 and 74 sites, with small imperfection [89]. The example extrapolations are in Fig. 3.2 on the left. Notice that for the anisotropic case the number of clusters with given proportions and of suitable size ($L \lessapprox 80$) is much more limited than the amount of clusters available for the isotropic case. In order to keep the calculations affordable we have therefore used extrapolation taking only two clusters to obtain all the anisotropic EOS. The extrapolation was done using weights proportional to the σ^{-2}, as equally weighted variant cannot provide an error estimate for only two fitted values. Using only two clusters is justified here, as the purpose of this particular task is the comparison with the experiment, which has relative errors typically at the 10% level. We have nevertheless performed checks of the extrapolations at the lowest temperature of interest (showing most pronounced finite size effects) for a few selected chemical potentials in order to clarify that the extrapolations work sufficiently well, see Fig. 3.2 on the right.

3.4.3 Measurement of the spin-spin correlations

In addition to the thermodynamic properties, we calculate the equal-time spin correlation function

$$C(\mathbf{\Delta}) \;=\; -\frac{2}{L}\sum_{\mathbf{r}} \left\langle \hat{S}^z_{\mathbf{r}} \hat{S}^z_{\mathbf{r}+\mathbf{\Delta}} \right\rangle , \tag{3.14}$$

[6] The extrapolation is reliable for clusters larger than the correlation length.

[7] A more elaborate approach using scaling of the cluster size proportional to the correlation length in the respective direction was proposed for finite lattice QMC in [111].

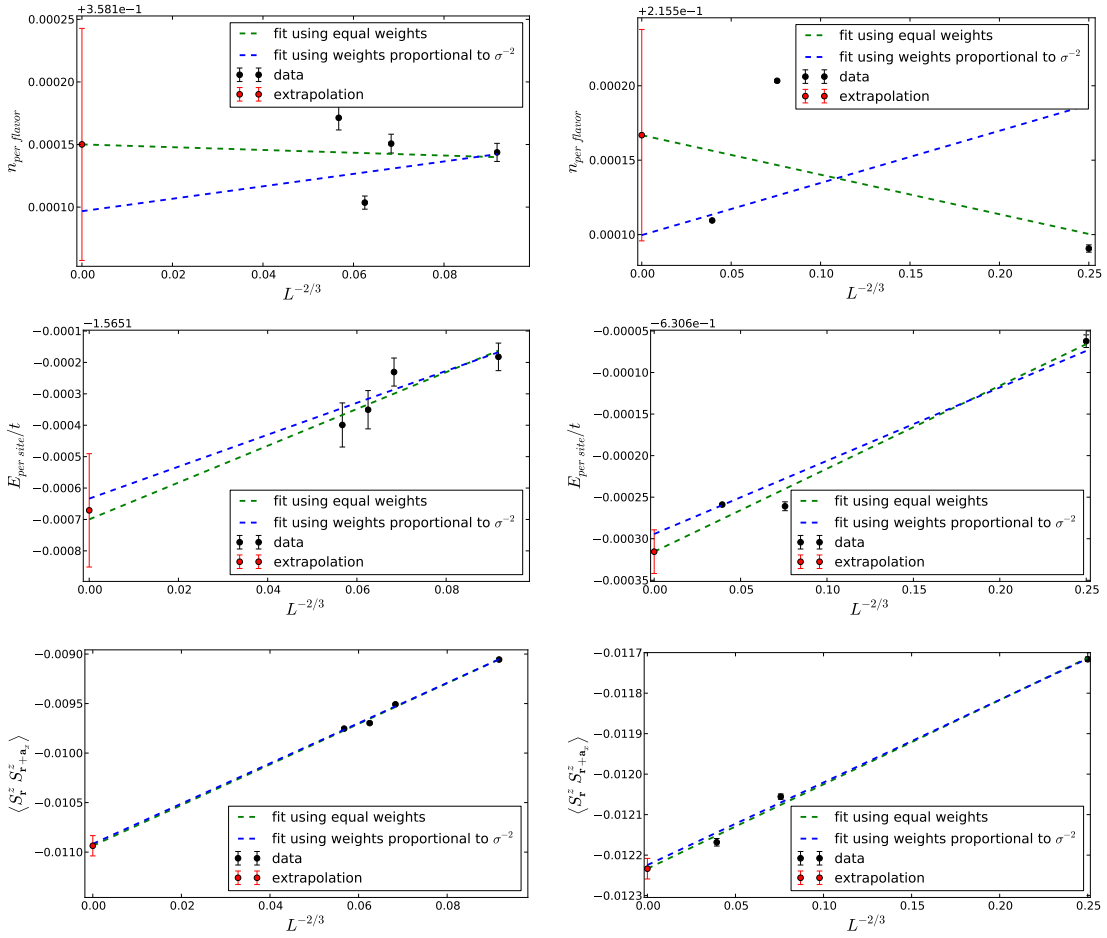

Figure 3.2: Extrapolation of the density per site and flavor ($n_{\text{per flavor}} = n/2$), energy per site ($E_{\text{per site}} = e$), and spin correlation per site $\left\langle \hat{S}^z_{\mathbf{r}} \hat{S}^z_{\mathbf{r}+\mathbf{a}_x} \right\rangle$ for a homogeneous system. The left plots show the data for the isotropic (e.g. $t/t' = 1$) system at $\mu = -0.53125t$, $U = 1.4375t$ and $\beta t = 1.8$, using clusters of 36, 56, 64 and 74 sites. The right plots correspond to an anisotropic system at $t/t' = 7.36$, $\mu = -1.28125t$, $U = 1.4375t$ and $\beta t = 1.8$, using clusters of 8, 48, and 128 sites. The extrapolation was done both using weights proportional to σ^{-2} (suitable if the dominant source of errors comes from measurement on a single cluster) and equal weights (appropriate if the systematic error of different clusters is much larger than the statistical error for a single cluster); the error of the extrapolated value is estimated conservatively as the union of both error estimates.

where $\hat{S}^z_{\mathbf{r}} = \frac{1}{2}(\hat{n}_{\mathbf{r}\uparrow} - \hat{n}_{\mathbf{r}\downarrow})$, $\boldsymbol{\Delta}$ is a non-zero lattice vector, and L is the number of sites. Similarly as the double occupation $\langle \hat{n}_{i\uparrow}\hat{n}_{i\downarrow}\rangle$, see Subsec. 3.4.1, we measure $C(\boldsymbol{\Delta})$ directly on the impurity. Although we present the form of the measurement for the case of a Bravais lattice with single site per cell (suitable for the studied model), all estimators use the site basis and therefore may be straightforwardly applied to a general lattice. The Wick's theorem is used for the actual measurement within the CT-AUX impurity solver, where the interactions are decoupled by the (fluctuating) field of auxiliary spins,

$$\langle \hat{n}_{i\sigma}\hat{n}_{j\sigma'}\rangle = \left\langle \hat{c}^\dagger_{i\sigma}\hat{c}_{i\sigma}\hat{c}^\dagger_{j\sigma'}\hat{c}_{j\sigma'}\right\rangle = \langle g_{ii\sigma}g_{jj\sigma'} + \delta_{\sigma\sigma'}g_{ij\sigma}(\delta_{ij} - g_{ji\sigma})\rangle \ , \tag{3.15}$$

with $g_{ij\sigma}$ denoting the two-point estimator for $-G_{ji\sigma}(\tau = \beta^-) = \left\langle \hat{c}^\dagger_{i\sigma}\hat{c}_{j\sigma}\right\rangle$, further discussed in Subsec. B.2.1.

Since the studied model is SU(2) symmetric, the quantity $C(\boldsymbol{\Delta})$ can be obtained as

$$C(\boldsymbol{\Delta}) = -\frac{2}{3L}\sum_{\mathbf{r}} \left\langle \hat{\mathbf{S}}_{\mathbf{r}} \cdot \hat{\mathbf{S}}_{\mathbf{r}+\boldsymbol{\Delta}}\right\rangle \tag{3.16}$$

$$= -\frac{2}{3L}\sum_{\mathbf{r}} \left\langle \hat{S}^z_{\mathbf{r}}\hat{S}^z_{\mathbf{r}+\boldsymbol{\Delta}} + \frac{1}{2}\left(\hat{S}^+_{\mathbf{r}}\hat{S}^-_{\mathbf{r}+\boldsymbol{\Delta}} + \hat{S}^-_{\mathbf{r}}\hat{S}^+_{\mathbf{r}+\boldsymbol{\Delta}}\right)\right\rangle \tag{3.17}$$

$$= -\frac{1}{6L}\sum_{\mathbf{r}} \left[\sum_{\sigma,\sigma'}(2\delta_{\sigma\sigma'} - 1)\,\langle \hat{n}_{\mathbf{r}\sigma}\hat{n}_{\mathbf{r}+\boldsymbol{\Delta}\sigma'}\rangle + 2\sum_{\sigma}\left\langle \hat{c}^\dagger_{\mathbf{r}\sigma}\hat{c}_{\mathbf{r}\bar{\sigma}}\hat{c}^\dagger_{\mathbf{r}+\boldsymbol{\Delta}\bar{\sigma}}\hat{c}_{\mathbf{r}+\boldsymbol{\Delta}\sigma}\right\rangle\right] , \tag{3.18}$$

with $\hat{\mathbf{S}}_{\mathbf{r}} = \left(\hat{S}^x_{\mathbf{r}}, \hat{S}^y_{\mathbf{r}}, \hat{S}^z_{\mathbf{r}}\right)$. The advantage of measurement $\frac{1}{3}\left\langle \hat{\mathbf{S}}_{\mathbf{r}} \cdot \hat{\mathbf{S}}_{\mathbf{r}+\boldsymbol{\Delta}}\right\rangle$ over $2\left\langle \hat{S}^z_{\mathbf{r}}\hat{S}^z_{\mathbf{r}+\boldsymbol{\Delta}}\right\rangle$ is in a reduction of the measurement errors [112] with minimal computational overhead. In the CT-AUX solver, the machinery of Wick's theorem yields simple estimator,

$$\left\langle \hat{c}^\dagger_{\mathbf{r}\sigma}\hat{c}_{\mathbf{r}\bar{\sigma}}\hat{c}^\dagger_{\mathbf{r}+\boldsymbol{\Delta}\bar{\sigma}}\hat{c}_{\mathbf{r}+\boldsymbol{\Delta}\sigma}\right\rangle = \left\langle g_{\mathbf{r}(\mathbf{r}+\boldsymbol{\Delta})\sigma}(\delta_{\boldsymbol{\Delta}\mathbf{0}} - g_{(\mathbf{r}+\boldsymbol{\Delta})\mathbf{r}\bar{\sigma}})\right\rangle \ . \tag{3.19}$$

By insertion of the above equation and the Eq. 3.15 into the Eq. 3.18 we find

$$C(\boldsymbol{\Delta}) = -\frac{1}{6L}\sum_{\mathbf{r}} \Bigg\langle \left(g_{\mathbf{rr}\uparrow} - g_{\mathbf{rr}\downarrow}\right)\left(g_{(\mathbf{r}+\boldsymbol{\Delta})(\mathbf{r}+\boldsymbol{\Delta})\uparrow} - g_{(\mathbf{r}+\boldsymbol{\Delta})(\mathbf{r}+\boldsymbol{\Delta})\downarrow}\right) - \sum_{\sigma} g_{\mathbf{r}(\mathbf{r}+\boldsymbol{\Delta})\sigma}\left(g_{(\mathbf{r}+\boldsymbol{\Delta})\mathbf{r}\sigma} + 2g_{(\mathbf{r}+\boldsymbol{\Delta})\mathbf{r}\bar{\sigma}}\right)\Bigg\rangle , \tag{3.20}$$

where we assumed $\boldsymbol{\Delta} \neq \mathbf{0}$.

In the isotropic limit ($t = t'$) we should find $C(\mathbf{e}_x) = C(\mathbf{e}_y) = C(\mathbf{e}_z)$ within the normal phase. This symmetry may be artificially broken by the cluster choice.[8] With the methodology of *Betts et al.* [89, 90], who obtained data for a large number of various clusters and tried to *a posteriori* select those which perform well in the extrapolation, we analyzed a set of clusters at $\beta t = 1.8$, $t = t'$, $\mu = U/2$, and $U = 1.4375t$. Especially, we examined a special class of clusters possessing the three-fold rotational axis $\mathbf{e}_x + \mathbf{e}_y + \mathbf{e}_z$ and a small imperfection according to [89]. Those naturally deliver $C(\mathbf{e}_x) = C(\mathbf{e}_y) = C(\mathbf{e}_z)$. However, even among this special set of clusters there are many outriders in the extrapolation, see Fig. 3.3. It has to be noted, that the problem with outriders weakens away from half filling. The data for the paper utilized (bipartite) clusters with small imperfection [89] and the spin-spin correlation for nearest neighbors was obtained by symmetrization over $\boldsymbol{\Delta} = \mathbf{e}_x, \mathbf{e}_y, \mathbf{e}_z$.

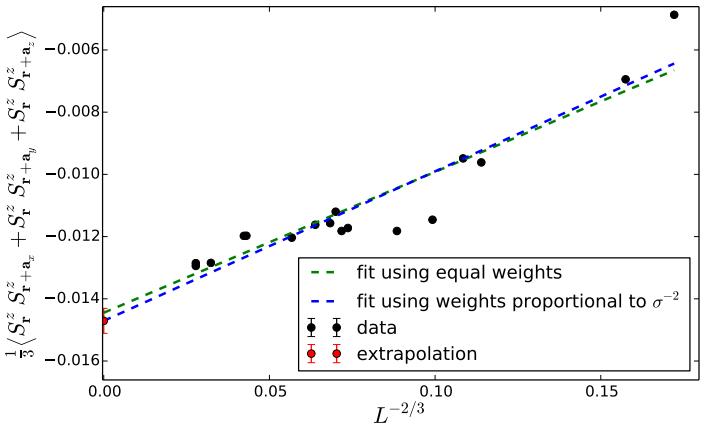

Figure 3.3: The spin-spin correlation C for nearest neighbors sites of the Hubbard model on the isotropic cubic lattice simulated at $\beta t = 1.8$, $t = t'$, $\mu = U/2$, and $U = 1.4375t$. All clusters were three-fold rotationally symmetric around $\mathbf{e}_x + \mathbf{e}_y + \mathbf{e}_z$.

3.4.4 Static antiferromagnetic susceptibility

The static antiferromagnetic (=staggered) spin susceptibility defined as an intensive quantity reads

$$\chi_{\mathrm{AF}} = \left.\frac{\partial m(h, T, \ldots)}{\partial h}\right|_{h=0}, \tag{3.21}$$

[8] Also the patch choice is important. For the patch chosen according to Sec. 2.3, *i.e.* with patch being the BZ of the superlattice $\tilde{\mathscr{A}}$, we choose the maximally symmetric patch.

where h is the strength of the staggered magnetic field with corresponding bilinear term in the Hamiltonian,

$$- h \sum_{\mathbf{r},\sigma} e^{i\mathbf{Q}\cdot\mathbf{r}} \, \sigma \, \hat{n}_{\mathbf{r}\sigma} \,, \qquad\qquad \sigma = \pm 1 \,, \tag{3.22}$$

$\mathbf{Q} \cdot \mathbf{a}_i = \pi$ is the antiferromagnetic reciprocal vector, and m is the thermal average of the magnetization operator $\hat{m}$, which is the corresponding order parameter operator to the above field, *i.e.*

$$\hat{m} = \frac{1}{N} \sum_{\mathbf{r},\sigma} e^{i\mathbf{Q}\cdot\mathbf{r}} \, \sigma \, \hat{n}_{\mathbf{r}\sigma} \,. \tag{3.23}$$

This allows us to write the Hamiltonian with coupling to the field in the form

$$\hat{H} = \hat{H}_{h=0} - hN\hat{m} \,. \tag{3.24}$$

The susceptibility might be expressed as,

$$\chi_{\mathrm{AF}} = \frac{\partial}{\partial h} \left(\frac{1}{Z} \operatorname{Tr} \left\{ \hat{m} e^{-\beta \hat{H}} \right\} \right) = N \int_0^\beta \mathrm{d}\tau \, \langle \hat{m}(\tau) \hat{m} \rangle - N\beta \, \langle \hat{m} \rangle^2 \,. \tag{3.25}$$

In the following we assume that the simulation is performed in a paramagnetic state, *i.e.* $\langle \hat{m} \rangle = 0$, which simplifies χ_{AF} to

$$\chi_{\mathrm{AF}} = N \int_0^\beta \mathrm{d}\tau \, \langle \hat{m}(\tau) \hat{m} \rangle \,. \tag{3.26}$$

Although we used $\hat{m}$ of the form suitable for a Bravais lattices, the above expression relies only on the form of the coupling in the Hamiltonian 3.24 and $\langle \hat{m} \rangle = 0$, thus it is applicable for a general lattice with appropriately defined $\hat{m}$.

3.4.5 Measurement of the static antiferromagnetic susceptibility of the impurity

This measurement does not account for the implicit dependence of the hybridization function on the staggered field, therefore it is *biased* in a DCA simulation with selfconsistent condition. In particular, it does *not* show any divergence at a continuous phase transition.[9] Despite that, it is useful for testing and for providing reasonable frequency cut-off estimate for the DCA compliant susceptibility measurement described in the following subsection 3.4.6.

[9] This measurement would be unbiased within a finite lattice QMC.

According to Eq. 3.26 and 3.23, the static AF susceptibility is for a bipartite cluster formulated with single site per cell given by,

$$\chi_{\mathrm{AF}} = \frac{1}{N} \sum_{\mathbf{r},\mathbf{r}',\sigma,\sigma'} \sigma\sigma' e^{i\mathbf{Q}\cdot(\mathbf{r}'+\mathbf{r})} \int_0^\beta \mathrm{d}\tau \, e^{i\nu_m \tau} \, \langle \hat{n}_{\mathbf{r}\sigma}(\tau) \, \hat{n}_{\mathbf{r}'\sigma'}(0) \rangle \ . \tag{3.27}$$

In the CT-AUX [39] or CT-INT [113, 114] solver, the four-point correlator may be evaluated using the Wick's theorem, since the impurity is solved as a decoupled system with fluctuating auxiliary spins or interaction vertices,

$$\begin{aligned} \langle \hat{n}_{\mathbf{r}\sigma}(\tau) \hat{n}_{\mathbf{r}'\sigma'} \rangle &= \left\langle \hat{c}^\dagger_{\mathbf{r}\sigma}(\tau) \hat{c}_{\mathbf{r}\sigma}(\tau) \hat{c}^\dagger_{\mathbf{r}'\sigma'} \hat{c}_{\mathbf{r}'\sigma'} \right\rangle & (3.28) \\ &= \langle n_{\mathbf{r}\sigma}(\tau) n_{\mathbf{r}'\sigma'} - \delta_{\sigma\sigma'} G_\sigma(\mathbf{r}\tau, \mathbf{r}'0) G_\sigma(\mathbf{r}'0, \mathbf{r}\tau) \rangle \ . & (3.29) \end{aligned}$$

It is convenient to measure χ_{AF} of the impurity in the real space and imaginary-time representation, sampling over imaginary-time difference τ.[10] The final formula for the AF static susceptibility estimator of the impurity reads[11]

$$\chi_{\mathrm{AF}} = N \int_0^\beta \mathrm{d}\tau \ \langle m(\tau) m \rangle - \frac{1}{N} \sum_{\mathbf{r},\mathbf{r}',\sigma} e^{i\mathbf{Q}\cdot(\mathbf{r}+\mathbf{r}')} \int_0^\beta \mathrm{d}\tau \, G_\sigma(\mathbf{r}\tau, \mathbf{r}'0) G_\sigma(\mathbf{r}'0, \mathbf{r}\tau) \, . \tag{3.32}$$

3.4.6 DCA static AF susceptibility

In this subsection we describe a DCA compliant measurement of the static AF susceptibility, following the review *Maier et al.* [59].[12] We use the terms *cluster*

[10] The term of χ_{AF} corresponding to the first term in Eq. 3.29,

$$N \int_0^\beta \mathrm{d}\tau \, \langle m(\tau) m \rangle = \frac{N}{\beta} \int_0^\beta \mathrm{d}\tau \int_0^\beta \mathrm{d}\tau' \, \langle m(\tau) m(\tau') \rangle = N\beta \, \langle \bar{m}^2 \rangle \ , \tag{3.30}$$

may be obtained from the two-point correlation estimators, as $\bar{m} = \frac{2}{N\beta} \sum_{\mathbf{r},\sigma,n\geq 0} \sigma e^{i\mathbf{Q}\cdot\mathbf{r}} \Re G_\sigma(\mathbf{r}, \mathbf{r}, i\omega_n)$. In contrast is the second term in Eq. 3.29 which cannot be evaluation solely from the single frequency estimator $G_\sigma(\mathbf{r}, \mathbf{r}', i\omega_n)$. The reason for this is that for an accumulation of $\langle G_\sigma(\mathbf{r}_1\tau_1, \mathbf{r}_2\tau_2) \, G_\sigma(\mathbf{r}_3\tau_3, \mathbf{r}_4\tau_4) \rangle$ it is possible to use the translational symmetry in imaginary time only once, $\langle G_\sigma(\mathbf{r}_1(\alpha+\tau_1), \mathbf{r}_2(\alpha+\tau_2)) \, G_\sigma(\mathbf{r}_3(\alpha+\tau_3), \mathbf{r}_4(\alpha+\tau_4)) \rangle$.

[11] In a complete analogy it is possible to derive the compressibility estimator valid in a finite lattice QMC,

$$\kappa = N \left(\int_0^\beta \mathrm{d}\tau \ \langle n(\tau) n \rangle - \beta \langle n \rangle^2 \right) - \frac{1}{N} \sum_{\mathbf{r},\mathbf{r}',\sigma} \int_0^\beta \mathrm{d}\tau \, G_\sigma(\mathbf{r}\tau, \mathbf{r}'0) G_\sigma(\mathbf{r}'0, \mathbf{r}\tau) \, . \tag{3.31}$$

[12] Notice that some prefactors differ in this thesis by β or L with respect to Ref. [59], as there the unnumbered definition of $\chi_{\sigma\sigma'}(q, k, k')$ is dimensionally inconsistent with $\bar{\chi}^0_{\sigma\sigma'}(q, K, K')$, Eq. 127, which we tried to fix.

and *impurity* interchangeably, as we aim to comply to [59] and both to the rest of the thesis.

We checked the consistency of this susceptibility measurement in absence of symmetry breaking field with the susceptibility obtained with small non-zero staggered field $h \to 0$ coupling to the staggered magnetization operator $\hat{m}$ as in the Eq. 3.24.

DCA approximation on two-particle quantities, measurement

As shown in Subsec. 3.4.4, the static AF susceptibility of a paramagnet (PM) may be measured as

$$\chi_{\mathrm{AF}} = \frac{N}{\beta} \int_0^\beta \mathrm{d}\tau \int_0^\beta \mathrm{d}\tau' \, \langle T_\tau \, \hat{m}(\tau) \, \hat{m}(\tau') \rangle \, . \tag{3.33}$$

A direct measurement of the above quantity on the impurity would provide us with the impurity susceptibility (see previous subsection), which is not our goal. In order to obtain a DCA consistent lattice susceptibility, we need to impose additional assumption on some two-particle quantity. Analogously to the DCA approximation on the self energy, we impose the approximation on an irreducible quantity [78],[13] in particular on the particle-hole irreducible vertex function Γ,[14]

$$\Gamma^{\mathrm{lat}}_{(\mathbf{k}n\sigma)(\mathbf{k}'n'\sigma')}(\mathbf{Q}, i\nu_m) \approx \Gamma^{\mathrm{imp}}_{(\mathbf{K}n\sigma)(\mathbf{K}'n'\sigma')}(\mathbf{Q}, i\nu_m) \, . \tag{3.34}$$

To make use of the approximation, we employ the Bethe–Salpeter equation,

$$\chi_{kk'}(\mathbf{Q}, i\nu_m) = \chi^0_{kk'}(\mathbf{Q}, i\nu_m) + \chi^0_{kk''}(\mathbf{Q}, i\nu_m)\Gamma_{k''k'''}(\mathbf{Q}, i\nu_m)\chi_{k'''k'}(\mathbf{Q}, i\nu_m), \tag{3.35}$$

where we use the Einstein's summation convention and multiindices $k \equiv (\mathbf{k}n\sigma)$. The so-called non-interacting susceptibility $\chi^0_{(\mathbf{k}n\sigma)(\mathbf{k}'n'\sigma')}(\mathbf{Q}, 0)$ is a (longitudinally) particle-hole reducible bubble diagram defined by

$$\chi^0_{(\mathbf{k}n\sigma)(\mathbf{k}'n'\sigma')}(\mathbf{Q}, 0) = -\delta_{\sigma\sigma'}\delta_{nn'}\delta_{\mathbf{k}\mathbf{k}'}\beta G_\sigma(\mathbf{k}, i\omega_n)G_{\sigma'}(\mathbf{k}' + \mathbf{Q}, i\omega_{n'}) \, . \tag{3.36}$$

The two-particle Green's function $\chi_{(\mathbf{k}n\sigma)(\mathbf{k}'n'\sigma')}(\mathbf{Q}, i\nu_m)$ is defined as follows,

$$\begin{aligned} &\chi_{(\mathbf{k}n\sigma)(\mathbf{k}'n'\sigma')}(\mathbf{Q}, i\nu_m = 0) = \\ &\quad \frac{1}{\beta} \int_0^\beta \int_0^\beta \int_0^\beta \int_0^\beta \mathrm{d}\tau_1 \, \mathrm{d}\tau_2 \, \mathrm{d}\tau_3 \, \mathrm{d}\tau_4 \, e^{-i(\omega_n\tau_1 - \omega_n\tau_2 + \omega_{n'}\tau_3 - \omega_{n'}\tau_4)} \times \\ &\quad \left\langle T_\tau c^\dagger_{\mathbf{k}+\mathbf{Q}\sigma}(\tau_1) c_{\mathbf{k}\sigma}(\tau_2) c^\dagger_{\mathbf{k}'\sigma'}(\tau_3) c_{\mathbf{k}'+\mathbf{Q}\sigma'}(\tau_4) \right\rangle \, . \end{aligned} \tag{3.37}$$

[13] For models with local (or strongly screened) interaction, the irreducible quantities have suppressed $\mathbf{k}$-dependence when compared with their reducible counterparts. Recall the bare interaction vertex is $\mathbf{k}$-independent for the Hubbard model.

[14] In the nomenclature of [115], Γ is the vertex irreducible in the longitudinal particle-hole channel, *i.e.* diagrams contributing to it cannot be separated by a vertical cut of one particle-like and one hole-like fermionic line.

We first use the Bethe–Salpeter equation in the context of the impurity. There we can directly measure both the two-particle Green's function χ_c and the Green's function needed for the evaluation of the non-interacting susceptibility χ_c^0, where the index c stands for *cluster*. These two quantities allow to extract Γ^{imp} via Eq. 3.35,

$$\Gamma^{\text{imp}}(\mathbf{Q},0) = \chi_c^0(\mathbf{Q},0)^{-1} - \chi_c(\mathbf{Q},0)^{-1}\,. \tag{3.38}$$

We continue by taking the Bethe–Salpeter eq. 3.35 in the context of the lattice. Utilizing the patch-wise constant approximation of the vertex Γ^{lat} (Eq. 3.34), we perform patch-averaging of the Eq. 3.35,[15]

$$\bar{\chi}_{KK'}(\mathbf{Q},i\nu_m) = \bar{\chi}^0_{KK'}(\mathbf{Q},i\nu_m) + \bar{\chi}^0_{KK''}(\mathbf{Q},i\nu_m)\bar{\Gamma}_{K''K'''}(\mathbf{Q},i\nu_m)\bar{\chi}_{K'''K'}(\mathbf{Q},i\nu_m)\,, \tag{3.39}$$

where the top bar indicates the patch-averaged quantities,[16]

$$\bar{f}(\mathbf{K},\mathbf{K}',\ldots) = \frac{1}{\Omega_{\text{patch}}}\int_{\text{patch}} \mathrm{d}\tilde{\mathbf{k}} \int_{\text{patch}} \mathrm{d}\tilde{\mathbf{k}}'\, f(\mathbf{K}+\tilde{\mathbf{k}},\mathbf{K}'+\tilde{\mathbf{k}}',\ldots)\,. \tag{3.40}$$

$\bar{\chi}^0$ can be evaluated using the DCA approximated lattice Green's functions. Eq. 3.39 then delivers the $\bar{\chi}$ on the lattice,

$$\bar{\chi}(\mathbf{Q},0) = \left[\bar{\chi}^0(\mathbf{Q},0)^{-1} - \Gamma^{\text{lat}}(\mathbf{Q},0)\right]^{-1}\,. \tag{3.41}$$

By inserting the approximation 3.34 and then Eq. 3.38 into the above equation we find

$$\bar{\chi}(\mathbf{Q},i\nu_m) = \left[\chi_c(\mathbf{Q},i\nu_m)^{-1} - \chi_c^0(\mathbf{Q},i\nu_m)^{-1} + \bar{\chi}^0(\mathbf{Q},i\nu_m)^{-1}\right]^{-1}\,, \tag{3.42}$$

where all of the quantities are matrices with multiindices $(\mathbf{K}n\sigma)$. The (coarse-grained) two-particle lattice Green's function can be used for the actual evaluation of the lattice susceptibility. Specifically, Eq. 3.33 might be rewritten using Fourier transformation[17] into the form

$$\chi_{\text{AF}} = \frac{1}{\Omega_{\text{BZ}}\beta^2}\sum_{\sigma,\sigma',n,n'}\sigma\sigma'\int_{\text{BZ}}\mathrm{d}\mathbf{k}\int_{\text{BZ}}\mathrm{d}\mathbf{k}'\,\chi_{(\mathbf{k}n\sigma)(\mathbf{k}'n'\sigma')}(\mathbf{Q},i\nu_m=0)\,, \tag{3.43}$$

$$= \frac{1}{N\beta^2}\sum_{\sigma,\sigma',n,n',\mathbf{K},\mathbf{K}'}\sigma\sigma'\bar{\chi}_{(\mathbf{K}n\sigma)(\mathbf{K}'n'\sigma')}(\mathbf{Q},i\nu_m=0)\,. \tag{3.44}$$

[15] Comment on the dimensionality: for a $\mathbf{k}$-independent vertex we would obtain $\bar{\Gamma}_{KK'} \approx \Omega_{\text{patch}}\Gamma_{KK'}$.

[16] The prefactor $\Omega^{-1}_{\text{patch}}$ in the averaging formula is consistent with the convention set by Eq. 3.37, according to which the elements of χ have dimension of β^3, and bare $\bar{\Gamma}^0_{\uparrow\downarrow}$ equals to $-\frac{U}{L\beta^2}$, fixed by the absence of prefactors in Eq. 3.39. Notice that prefactor $\Omega^{-2}_{\text{patch}}$ would be in Eq. 3.40 consistent with $\bar{\Gamma}^0_{\uparrow\downarrow} \propto L^0$. The natural unit choice from the diagrammatic expansion, $\bar{\Gamma}^0_{\uparrow\downarrow} = -\frac{U}{L^2\beta}$, would in Eq. 3.40 require a prefactor Ω^0_{patch}.

[17] By insertion of $\int_0^\beta \mathrm{d}\tilde{\tau}\,\delta(\tau-\tilde{\tau}) = \frac{1}{\beta}\int_0^\beta \mathrm{d}\tilde{\tau}\,e^{\pm i\omega_n(\tau-\tilde{\tau})}$.

Estimators for the DCA susceptibility

For the actual implementation of the four-point measurement in Eq. 3.37 within a CT-AUX impurity solver [39] we define an auxiliary 2-quasimomenta and 2-frequencies Green's function,

$$\tilde{g}_\sigma(\mathbf{k},\mathbf{k}',i\omega_n,i\omega_{n'}) \equiv \frac{1}{\beta L}\int_0^\beta\int_0^\beta \mathrm{d}\tau\,\mathrm{d}\tau'\, e^{i\omega_n\tau}e^{-i\omega_{n'}\tau'}\sum_{\mathbf{r},\mathbf{r}'} e^{-i\mathbf{k}\cdot\mathbf{r}}e^{i\mathbf{k}'\cdot\mathbf{r}'}\tilde{g}_\sigma(\mathbf{r}\tau,\mathbf{r}'\tau')\,, \tag{3.45}$$

with

$$\tilde{g}_\sigma(\mathbf{r}\tau,\mathbf{r}'\tau') = g^0_\sigma(\mathbf{r},\mathbf{r}',\tau-\tau') - \sum_{p,q} g^0_\sigma(\mathbf{r},\mathbf{r}_p,\tau-\tau_p)M_{pq\sigma}g^0_\sigma(\mathbf{r}_q,\mathbf{r}',\tau_q-\tau')\,, \tag{3.46}$$

according to [39]; compare with single-frequency Green's function discussed in Sec. B.2. Then we may write

$$\tilde{g}_\sigma(\mathbf{k},\mathbf{k}',i\omega_n,i\omega_{n'}) = \delta_{\mathbf{k}\mathbf{k}'}\delta_{nn'}g^0_\sigma(\mathbf{k},i\omega_n) - \frac{1}{\beta L}g^0_\sigma(\mathbf{k},i\omega_n)M_{\mathbf{k}n\mathbf{k}'n'\sigma}g^0_\sigma(\mathbf{k}',i\omega_{n'})\,, \tag{3.47}$$

with

$$M_{\mathbf{k}n\mathbf{k}'n'\sigma} = \sum_{p,q} e^{i\omega_n\tau_p}e^{-i\mathbf{k}\cdot\mathbf{r}_p}e^{-i\omega_{n'}\tau_q}e^{i\mathbf{k}'\cdot\mathbf{r}_q}M_{pq\sigma}\,, \tag{3.48}$$

which can be obtained in $\mathcal{O}\left(N_s^2 + N_s L N_\omega \ln(N_\omega) + L^2 N_\omega^2 \ln(N_\omega + L)\right)$ operations, with the frequency cut-off N_ω,[18] if using two subsequent fast FT (FFT) in space and a non-equidistant FFT from imaginary time to Matsubara frequencies (*e.g.* by the NFFT library [116]), similarly as it is described for the single-particle Green's function measurement in Sec. B.2.2. Empirically we found that the N_ω has to be kept proportional to βU in order to make the extrapolation in frequency reliable,[19] and since the CT-AUX expansion order N_s is proportional to $N\beta U$, the complexity of obtaining $M_{\mathbf{k}n\mathbf{k}'n'\sigma}$ can be given by $N_s^2 \ln N_s$, which is slower only by the logarithmic factor than obtaining $M_{\mathbf{k}n\sigma}$ for the single-particle measurements; see Subsec. B.2.3. The memory requirements, however, scale like N_s^2, which poses real limitation.

Using the Wick's theorem for the decoupled problem (with auxiliary spins or within the weak coupling expansion) we get

$$\begin{aligned}
&\chi_{(\mathbf{k}n\sigma)(\mathbf{k}'n'\sigma')}(\mathbf{Q},0) = \\
&\quad = \beta\Big\langle \tilde{g}_\sigma(\mathbf{k},\mathbf{k}+\mathbf{Q},i\omega_n,i\omega_n)\tilde{g}_{\sigma'}(\mathbf{k}'+\mathbf{Q},\mathbf{k}',i\omega_{n'},i\omega_{n'}) \\
&\qquad - \delta_{\sigma\sigma'}\tilde{g}_\sigma(\mathbf{k},\mathbf{k}',i\omega_n,i\omega_{n'})\tilde{g}_\sigma(\mathbf{k}'+\mathbf{Q},\mathbf{k}+\mathbf{Q},i\omega_{n'},i\omega_n)\Big\rangle\,.
\end{aligned} \tag{3.49}$$

[18] With the frequency cut-off N_ω we mean limitation on the Matsubara frequencies $i\omega_n$ and $i\omega_{n'}$ by $n, n' \in \{-N_\omega, -N_\omega+1, \ldots, N_\omega-1\}$.

[19] The frequency cut-off for the 4-point measurements was in practice chosen an order smaller than the frequency cut-off for the single-particle measurements.

The assumed PM symmetry implies

$$\chi_{(\mathbf{k}n\sigma)(\mathbf{k}'n'\sigma')}(\mathbf{Q},0) = \chi_{(\mathbf{k}n\bar{\sigma})(\mathbf{k}'n'\bar{\sigma'})}(\mathbf{Q},0)\,, \tag{3.50}$$

which enables separation of the magnetic and the charge channel via a unitary transformation in the spin index σ, using $U = \frac{1}{\sqrt{2}}\begin{pmatrix} 1 & 1 \\ 1 & -1 \end{pmatrix}$. In order to obtain χ_{AF} it is thus sufficient to deal with the magnetic channel only and accumulate $\chi_{c,m} = \chi_{c,\uparrow\uparrow} - \chi_{c,\uparrow\downarrow}$. Then,

$$\chi_{\mathrm{AF}} = \frac{2}{N\beta^2} \sum_{\mathbf{K},\mathbf{K}',n,n'} \bar{\chi}^0_{\uparrow\uparrow} \left(\mathbb{1} - \Gamma_m \bar{\chi}^0_{\uparrow\uparrow}\right)^{-1}\,, \tag{3.51}$$

with

$$\Gamma_m(\mathbf{Q},0) = \chi^0_{c,\uparrow\uparrow}(\mathbf{Q},0)^{-1} - \chi_{c,m}(\mathbf{Q},0)^{-1}\,. \tag{3.52}$$

We list further properties of χ which may be used to reduce the number of observables in a simulation or for implementation checks,

$$\chi_{(\mathbf{k}n\sigma)(\mathbf{k}'n'\sigma')}(\mathbf{Q},0) = \chi^*_{(-\mathbf{k}-(n+1)\sigma)(-\mathbf{k}'-(n'+1)\sigma')}(\mathbf{Q},0)\,, \tag{3.53}$$

$$\chi_{(\mathbf{k}n\sigma)(\mathbf{k}'n'\sigma')}(\mathbf{Q},0) = \chi_{(\mathbf{k}'+\mathbf{Q}n'\sigma')(\mathbf{k}+\mathbf{Q}n\sigma)}(\mathbf{Q},0)\,, \tag{3.54}$$

$$\chi_{(\mathbf{k}n\sigma)(\mathbf{k}+\mathbf{q}n\sigma)}(\mathbf{Q},0) = 0\,, \tag{3.55}$$

where the first property goes back to the FT of $M_{pq\sigma}$ (Eq. 3.48), of which we assume to be purely real.[20]

Estimate of the critical point

Search for a divergence of the susceptibility is best performed by looking at the largest eigenvalue of the Owen–Scalapino "pairing-matrix" $\Gamma\bar{\chi}^0$ crossing the value 1,[21] as the Eq. 3.42 can be written in form

$$\bar{\chi}(\mathbf{Q},0) = \bar{\chi}^0(\mathbf{Q},0)\left(\mathbb{1} - \Gamma(\mathbf{Q},0)\bar{\chi}^0(\mathbf{Q},0)\right)^{-1}\,. \tag{3.57}$$

Naturally, one has to introduce a cut-off on the frequencies in $\Gamma\bar{\chi}^0$ in order to perform the task numerically. The cut-off was chosen symmetric in $i\omega_n$ with typically

[20] In CT-AUX it is given if $\exp(\pm\gamma)$ (Sec. B.1) and $G_{ij\sigma}(\tau)$ (Subsec. 1.3.5) are purely real.

[21] Equivalently one may use $\bar{\chi}(\mathbf{Q},0) = \left(\mathbb{1} - \bar{\chi}^0(\mathbf{Q},0)\Gamma(\mathbf{Q},0)\right)^{-1}\bar{\chi}^0(\mathbf{Q},0)$, or a symmetric version

$$\bar{\chi}(\mathbf{Q},0) = \left(\bar{\chi}^0(\mathbf{Q},0)\right)^{1/2}\left(\mathbb{1} - \left(\bar{\chi}^0(\mathbf{Q},0)\right)^{1/2}\Gamma(\mathbf{Q},0)\left(\bar{\chi}^0(\mathbf{Q},0)\right)^{1/2}\right)^{-1}\left(\bar{\chi}^0(\mathbf{Q},0)\right)^{1/2}\,, \tag{3.56}$$

which may, however, cause problems because of the branch cut of the square-root in presence of purely real negative values; for particle-hole symmetric models the components of the diagonal $\bar{\chi}^0$ are purely real and positive.

12 to 24 positive frequencies. The leading eigenvalue was in each iteration extrapolated in the cut-off N_ω using a quadratic fit in N_ω^{-1} and the extrapolation was averaged over several iterations. The cut-off dependence was negligible for majority of the examined cases, with most pronounced effect in the most anisotropic case with $t/t' = 8.0$, see example extrapolations in Fig. 3.4.

For smaller clusters, for which the binning analysis of every component of $\chi_{c,m}(\mathbf{Q}, 0)$ was feasible, we performed a bias analysis for the matrix eigenvalues, following the subsection 3.4.6 of [29]. There, the author examines the leading eigenvalues as a function of number m of consecutive bins averaged before the actual eigenvalue call. In our case was the dependence of the leading eigenvalue on m^{-1} approximately linear and negligible in runs of typical duration.

The eigenvector corresponding to the eigenvalue of $\Gamma\bar{\chi}^0$ crossing unity has in all examined cases dominantly the s-wave character and is even in frequency.

For $(U/t, t/t') = (4, 8),\ (8, 2)$, spurious eigenvalues larger than unity appeared. These did not cross the unity upon cooling, but appeared via infinity. Their eigenvectors are both even and odd in frequency, and with weight concentrated at few lowest frequencies, unlike the eigenvector corresponding to the eigenvalue crossing unity. The first spurious eigenvalue appearing upon cooling corresponded in all examined cases a charge-like odd-frequency eigenvector. The followers show alternation in frequency parity and growing extent in frequency. We checked that the high-temperature (disordered) phase is stable with respect to static fields with the space symmetry of the eigenvectors corresponding to the spurious eigenvalues. The dependence of the spurious eigenvalues on the frequency cut-off is weak. Some of the spurious eigenvalues persist even with extreme truncation $N_\omega = 1$.

For the Hubbard model on the square lattice at half filling with $U = 6.0t$ we found spurious eigenvalues in the charge channel appearing around $\beta t \gtrapprox 0.875$. That corresponds according to Ref. [117] to the crossover, when the temperature becomes roughly equal to the charge gap. Upon further cooling the system starts to appear gapped in the charge channel, so ideally we would expect the charge channel eigenvalues of $\Gamma\bar{\chi}^0$ to approach $-\infty$. That does not work well, probably because Γ is computed as a difference of two inverse quantities, χ_c^{-1} and $(\chi_c^0)^{-1}$ (Eq. 3.38).

The $T_{\text{Néel}}$ was obtained by extrapolation in cluster size using the critical exponent ν, as suggested in [101],[22] based on the assumption that the transition at a given cluster happens when the ratio of correlation length and the linear size of the cluster reaches an unknown but cluster-size independent constant; see Fig. 3.5.

[22]For $t = t'$ our model is part of the universality class of the 3D $S = 1/2$ Heisenberg model and for $t \neq t'$ it belongs to the classical 3D Heisenberg universality class, both of which have a critical exponent of $\nu \approx 0.71$ [118].

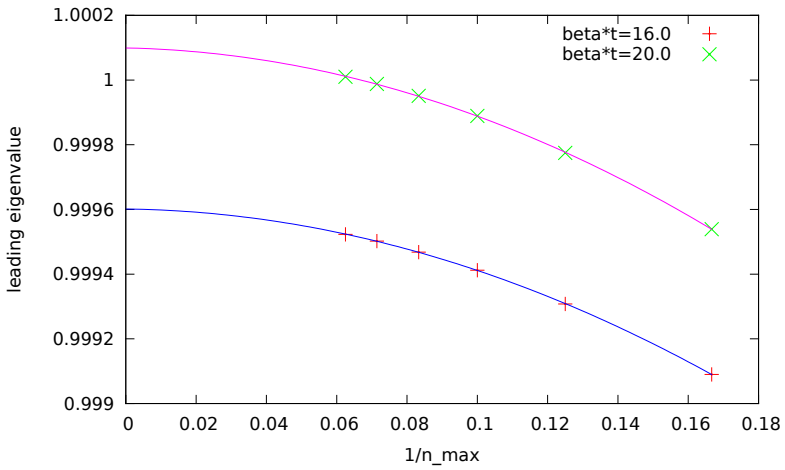

Figure 3.4: Extrapolation of the leading eigenvalue in the cut-off frequency $n_{\max}$ (in the present text referred to as N_ω) with quadratic fits in $n_{\max}^{-1}$. Obtained on a 24-site cluster for $U = 4.0t$, $t/t' = 8.0$, $\mu = U/2$.

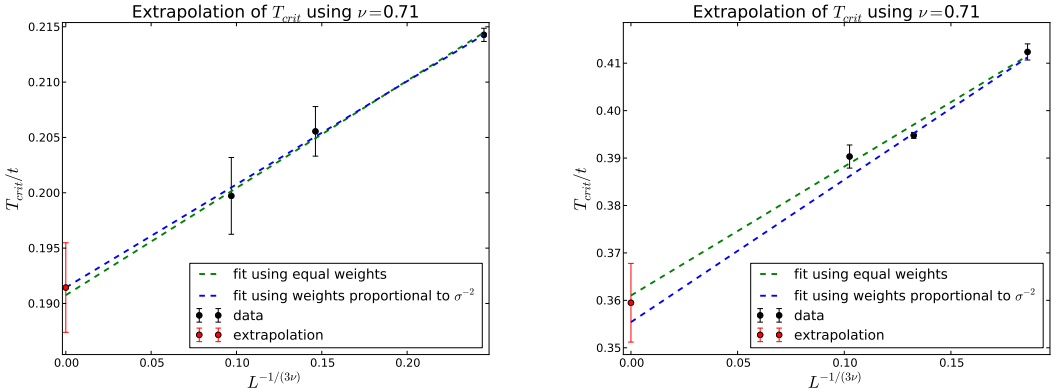

Figure 3.5: Extrapolation of the $T_{\text{Néel}}$ in the cluster size for $U = 4.0t$, $t/t' = 2.0$ (above) and for $U = 8.0t$, $t/t' = 1.0$; both at half filling.

For an *a posteriori* check of the quality of the approximation 3.34 we visualize the vertex Γ in Figs. 3.6, 3.7 for an example problem of the Hubbard model on the isotropic cubic lattice close to the Néel transition. The two-particle Green's function was measured for 64 positive and 64 negative Matsubara frequencies, *i.e.* $N_\omega = 64$. The structure of Γ in the Matsubara frequencies shown in the top row of Fig. 3.7 is qualitatively the same as it was found with DMFT in [115].[23] The

[23] The structure of the vertex function in the frequency space motivated Nan Lin in [119] to use different frequency cut-off for the diagonal and the off-diagonal entries.

impurity susceptibility measured according to Eq. 3.32 was $1.135(9)\,t^{-1}$. The DCA susceptibility obtained via Eq. 3.44 with cut-off $N_\omega = 64$ was $11.4538\,t^{-1}$ and the largest eigenvalue of $\Gamma_m \bar{\chi}^0_{\uparrow\uparrow}$ was 0.9494 (extrapolation in N_ω). The investigated system was thus close to the Néel phase transition.

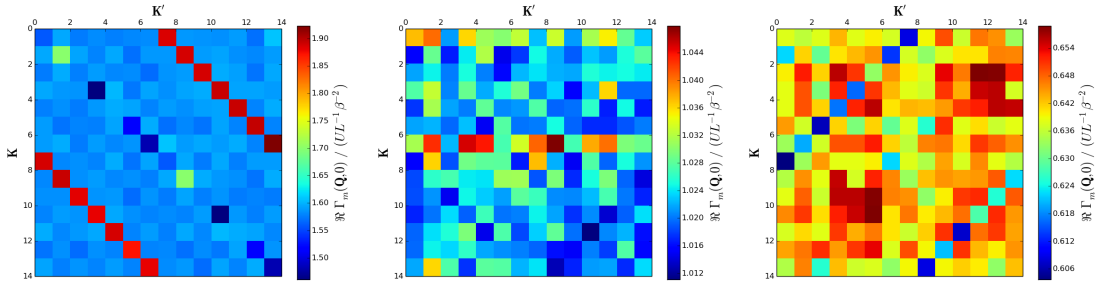

Figure 3.6: In these three color plots we display the magnetic channel of the impurity irreducible particle-hole vertex function $\Gamma_m^{\mathrm{imp}}(\mathbf{Q}, i\nu = 0)$ for $n = 18$ and $n = 18$, 0, -19 in the left, center, and right plot, respectively. The $\mathbf{K}$-dependence is most pronounced for $n = n'$, where there is enhancement for $\mathbf{K}' = \mathbf{K} + \mathbf{Q}$ and small suppression at $\mathbf{K} = \mathbf{K}'$. The center plot is highly uniform, displaying merely noise at the level of 2% and almost unrenormalized strength. The right plot for $i\omega_n = -i\omega_{n'}$ reveals little structure in the rather homogeneously suppressed bare interaction. The investigated system is the same as in Fig. 3.7.

3.5 Results

3.5.1 Spin-spin correlations

Fig. 3.8 left shows $C(\mathbf{e}_x)$ for various fillings and temperatures at fixed $t/t' = 7.36$ and $U = 1.4375t$, which are the parameters used in the experiment [97] realizing the studied model. Antiferromagnetic correlations between nearest neighbors (n.n.) correspond to positive values of $C(\mathbf{e}_x)$. The signal is greatly enhanced for $T \lessapprox t$ and close to half-filling. At fixed temperature and interaction strength, the n.n. spin correlation along the longitudinal direction $C(\mathbf{e}_x)$ is enhanced with anisotropy t/t', while the correlation along the transverse direction $C(\mathbf{e}_y)$ is suppressed, see Fig. 3.8 right. T/t' is higher in the anisotropic case and thus the development of spin correlations in the transverse direction y is suppressed. At the same time $C(\mathbf{e}_x)$ is enhanced because singlet formation is facilitated by the effective lowering of dimensionality [120]. This in turn is caused by the difference in the relevant

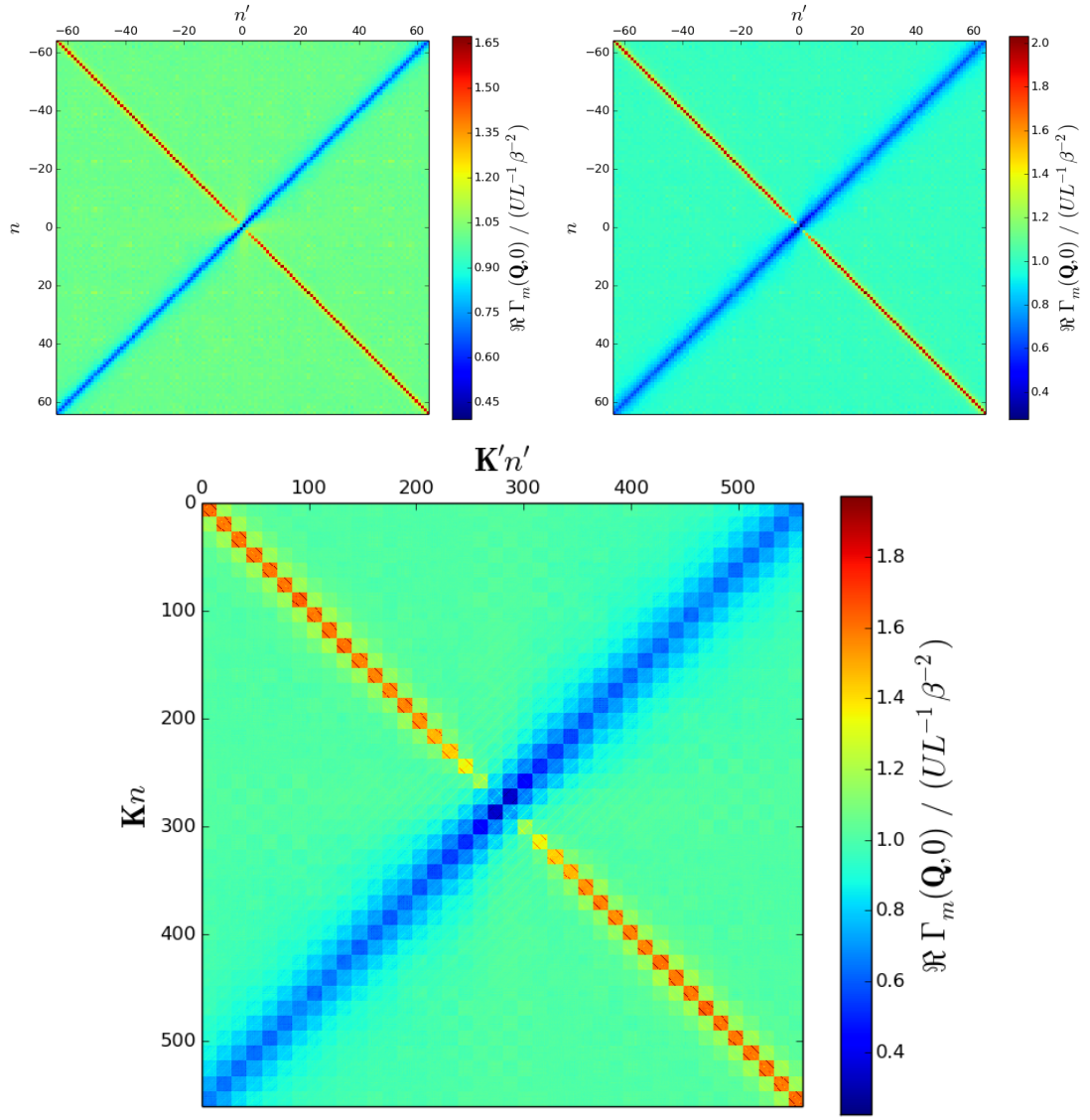

Figure 3.7: Displayed is the magnetic channel of the impurity irreducible particle-hole vertex function $\Gamma_m^{\mathrm{imp}}(\mathbf{Q}, i\nu = 0)$. In the top left color plot we show its components for $\mathbf{K} = \mathbf{K}' = \mathbf{0}$. The value $UL^{-1}\beta^{-2}$ is its unrenormalized value. The imaginary part of $\Gamma^{\mathrm{imp}}(\mathbf{Q}, i\nu = 0)$ was vanishingly small for all components, in agreement with [115]. The top right plot shows the same quantity for $\mathbf{K} = \mathbf{0}$ and $\mathbf{K}' = \mathbf{Q}$. The bottom plot shows $\Re\Gamma_m^{\mathrm{imp}}(\mathbf{Q}, i\nu = 0)$ as a color map with multi-indices $(\mathbf{K}n)$ and $(\mathbf{K}'n')$ displaying 20 positive and 20 negative frequencies for each $\mathbf{K}$, $\mathbf{K}'$. The multiindex is computed as $(n+20)L+k$, where k uniquely determines the cluster reciprocal vectors $\mathbf{K}$ as $\frac{2\pi k}{La}\left(-1\hat{\mathbf{e}}_1 + 3\hat{\mathbf{e}}_2 + 5\hat{\mathbf{e}}_3\right)$. The data was obtained for the Hubbard model on the isotropic cubic lattice at $U = 4t$, $\beta t = 4$, $t = t'$, and $\mu = U/2$. As the cluster was chosen a 14-site large bipartite cluster with bipartite imperfection equal to zero.

energy scales: T and t are of the same order but an order of magnitude larger than t'.

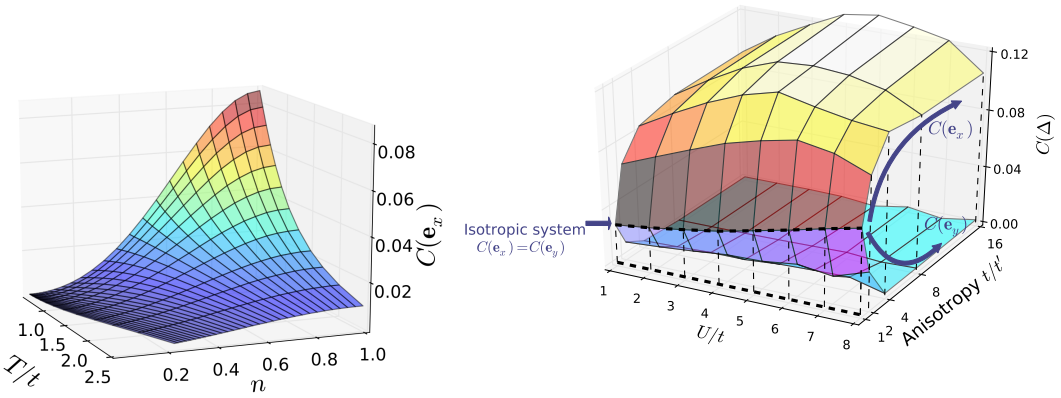

Figure 3.8: Left: N. n. spin correlation $C(\mathbf{e}_x)$ vs. filling and temperature for $t/t' = 7.36$, $U = 1.4375t$ in a homogeneous system. Right: N. n. spin correlation along the strong tunneling $C(\mathbf{e}_x)$ (upper surface) and in the transverse direction $C(\mathbf{e}_y)$ (lower surface) for a homogeneous system at half-filling and $T = 0.5t$ as a function of anisotropy and interaction strength.

3.5.2 Comparison with experiment

Fig. 3.9(a) shows the calculated and experimental n.n. spin correlation versus anisotropy t/t'; owing to the experimental realization, the interaction U/t decreases for larger anisotropies in this scan. We find good agreement between the DCA+LDA calculation and the experimental data assuming an entropy per particle S/N in the range of 1.4 to 1.8. For anisotropies $\gtrapprox 5$ the experiment enters a regime where corrections to the single band Hubbard model Eq. 3.1 may start to play a role in the shallow optical lattice [121]. Close to the isotropic limit, the second order HTSE with $S/N = 1.7$ describes the data well. For increasing anisotropies, the HTSE becomes unreliable as the expansion parameter βt reaches one. The inset of Fig. 3.9(a) shows that the introduction of the anisotropy leads to a situation where the temperature becomes comparable to or lower than the strong tunnel coupling t. The average $C(\mathbf{e}_x)$ increases monotonously with anisotropy, which is a consequence of both the enhancement of correlations for a given βt and additionally the increasing βt.

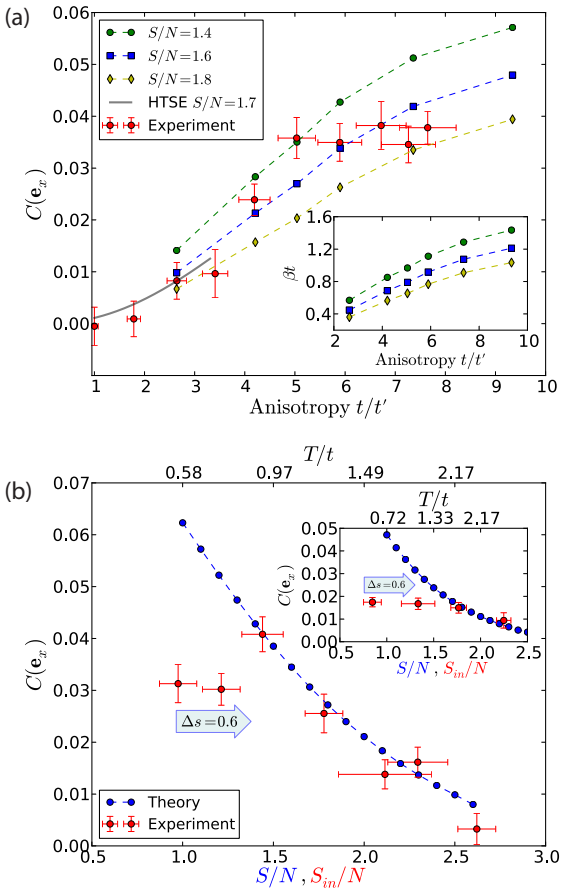

Figure 3.9: Comparison of the calculated spin correlations from DCA+LDA with the experiment. (a) N.n. spin correlation for different anisotropies and interaction strengths. The entropy per particle before loading into the lattice is below 1.0 in the experiment. For increasing anisotropy the interaction U/t decreases from 16.2 to 0.975. Detailed parameters are listed in the supplemental materials of [1]. Theoretical calculations with different entropies per particle are shown as symbols connected by dashed lines. The solid line shows HTSE results with $S/N = 1.7$. The inset shows the inverse temperature βt versus anisotropy used in the DCA+LDA calculations. (b) N.n. spin correlation as a function of entropy per particle for $t/t' = 7.36$ and $U = 1.4375t$. The experimental data is plotted as a function of the initial S/N before loading into the lattice, and the blue curve is the theoretical prediction. The upper axis denotes the corresponding temperature determined from the DCA+LDA calculation. For the lowest initial entropies the measured spin correlation deviates from the expected value. These experimental data points agree with an approximate entropy increase of 0.6 possibly caused by heating during lattice loading. The inset shows a comparison with the experiment at a different set of parameters ($t/t' = 4.21$, $U = 2.98t$). There, additional heating may have occurred below 1.8.

For a fixed anisotropy $t/t' = 7.36$, Fig. 3.9(b) shows the trap averaged $C(\mathbf{e}_x)$ versus entropy per particle (for the experimental data the horizontal axis denotes the initial entropy per particle measured before loading into the lattice). Without any free parameters and assuming no heating, we find very good agreement for entropies of $1.4k_\mathrm{B}$ and above, showing that magnetic effects in the Hubbard model can be accurately studied in this regime. For lower entropies, the experimentally measured spin correlation does not increase further, deviating from the theoretical prediction. This suggests that additional heating may have occurred during the optical lattice loading process, or the system may not have fully equilibrated in the lattice for the lowest initial entropies. This is an important outcome of this study not deducible from the experimental data alone. A similar situation is found in previous studies of dimerized and simple cubic optical lattices [97, 98]. The inset of Fig. 3.9(b) shows a comparison at a different anisotropy $t/t' = 4.21$, where similar agreement at high entropies and deviations at low entropies are found. The observed heating, which varies depending on the system parameters, may be caused by non-adiabaticity with respect to changes of the local Hamiltonian, or due to the expected long timescale of density redistribution within the harmonic trap [99].

The upper horizontal axis of Fig. 3.9(b) shows the temperature used in the DCA+LDA calculations. For the lowest entropy $S/N = 1.4$, where the experimentally measured spin correlator matches the theoretical value, the temperature is found to be $T \approx 0.88t$. An anisotropic 3D system prepared at temperatures between the strong and weak exchange energy along and between the chains effectively realizes an array of 1D systems in global thermodynamic equilibrium – in contrast to an array of decoupled 1D chains, where the thermalization is hindered by negligible tunneling between the 1D chains. It provides thus a viable system for an experimental study with controllable parameters of the low-temperature regime of the Hubbard model in effectively one dimension [122] at currently accessible experimental entropies.

3.5.3 DCA+LDA

Fig. 3.10(a) shows the calculated distribution of the density, entropy and n.n. spin correlation in the trap for the isotropic ($t/t' = 1$) and anisotropic ($t/t' = 7.36$) Hubbard model with the same U/t, particle number and entropy per particle. In order to display the density and entropy redistribution, we tune in each case the trapping potential to obtain the filling $n = 1$ in the trap center and to obtain the same total atom number. The profiles for the experimental setting may be found in Fig. 3.11. The corresponding temperatures are $T = 0.95t$ and $T =$

$0.58t$, respectively.[24] Owing to qualitatively similar equations of state between the isotropic and anisotropic case at fixed tunneling t, we find a very similar behavior for both the density and entropy distribution in the trap. This is in contrast with the dimerized lattice examined in [97], which has an energy gap. In Fig. 3.10(a) the n.n. spin correlations are more pronounced for large anisotropy when comparing to the isotropic case, similar to the results in Fig. 3.8 right. To further characterize the state realized in the experiment, we compute the spin correlation beyond n.n. along the x direction, shown in Fig. 3.10(b). It shows an alternating sign with distance, confirming the presence of antiferromagnetic spin correlations.[25] At large distances the spin correlations are expected to decay exponentially, as the chosen temperatures are above the critical value of the Néel transition. For the experimentally accessible temperatures, already the calculated values of next-nearest neighbor correlations are below the experimental resolution.

Fig. 3.11 shows the density, entropy and the n.n. spin-correlation in the trap using the same parameters as experiment with average entropy per particle $S/N = 1.4$.

3.5.4 Néel transition

Finally, we address the question of how the introduction of anisotropy affects the Néel transition in a 3D half-filled lattice. Fig. 3.12 shows the calculated critical entropy at the Néel transition for different anisotropies. The critical entropy at $U = 4t$ shows a nonmonotonic behavior as a function of anisotropy.[26] We explain this by the reduction of the total bandwidth $W = 4(t+2t')$ and thus by the effective increase of the interaction strength (U/W) towards the optimal value $U/W \approx 2/3$ for the isotropic system [102]. Consistent with our simple argument, the curve for $U = 8t$ decays monotonically. We find that the introduction of anisotropy does not enhance the critical entropy over the optimum value ($S/N \approx 0.487(23)$ in the present study) reached at $U = 8t$ for the isotropic case.

The estimate of the Néel temperature was obtained for a set of clusters within the DCA simulation by looking for the divergence of the static antiferromagnetic spin susceptibility [59]; see details in Subsec. 3.4.6. The $T_{\text{Néel}}$ was then obtained by

[24] T/t is lower in the anisotropic case because of reduction of the total bandwidth.

[25] In Fig. 3.10(b) we find $|C(3\mathbf{e}_x)| > |C(2\mathbf{e}_x)|$ for $T = 0.2t$, which is a feature inherited from the half-filled non-interacting system on the cubic lattice, where spin correlations at even Manhattan distances vanish; see Sec. C.2.

[26] Our particular interest was the search for the optimal parameters U/t and t/t' in terms of largest $S_{\text{Néel}}/N$. For that reason we did not study the low U/t regime, where $T_{\text{Néel}}$ in the isotropic case is much smaller than the critical temperature at $U/t = 8$.

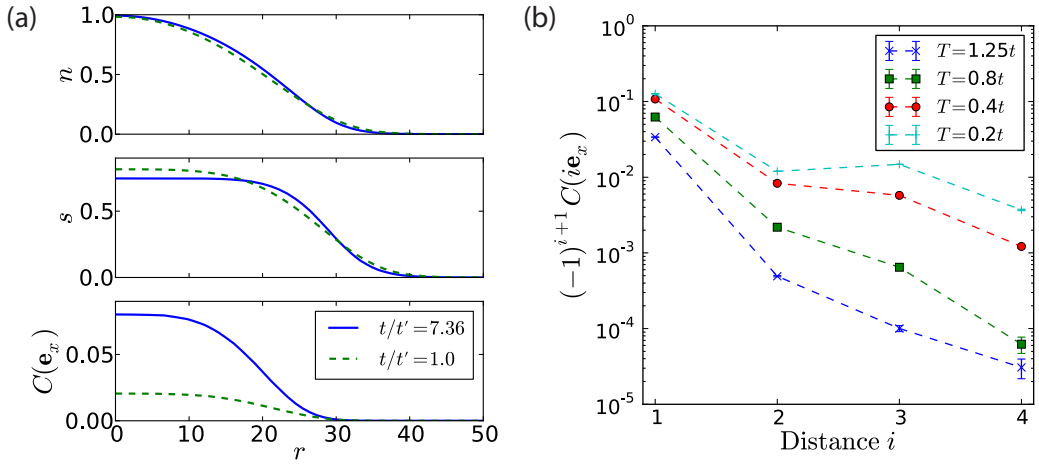

Figure 3.10: (a) The distribution of density, entropy and n.n. spin-correlation per site in the harmonic trap vs. distance from the center. The simulation is done with $U = 1.4375t$ with the trap averaged entropy $S/N = 1.6$. The chemical potential and trapping frequency are chosen such that the filling is $n = 1$ at the trap center and $N = 50000$ for both anisotropy ratios. (b) Extrapolated spin correlations as a function of distance along the x axis in the paramagnetic phase for $t/t' = 7.36$, $U = 1.44t$ and half-filling for different temperatures.

extrapolation in cluster size as suggested in [101].[27] The data with the extrapolated $T_{\text{Néel}}$ and the cluster estimates of $T_{\text{Néel}}$ can be found in the supplemental materials of [1]. Fig. 3.12 shows $s(T_{\text{Néel}})$ with curve $s(T)$ integrated within the paramagnetic phase. Our results for the isotropic case, $T_{\text{Néel}}/t = 0.1955(25)$ for $U = 4t$ and $T_{\text{Néel}}/t = 0.3595(83)$ for $U = 8t$, are consistent with previous studies [100, 101]. Both estimates are slightly above the estimates $T_{\text{Néel}}/t < 0.17$, $T_{\text{Néel}}/t = 0.3325(65)$ obtained by diagrammatic determinantal QMC calculations on larger lattices for $U = 4t$ and $U = 8t$, respectively [104].

[27] For $t = t'$ our model is part of the universality class of the 3D $S = 1/2$ Heisenberg model and for $t \neq t'$ it belongs to the classical 3D Heisenberg universality class, both of which have a critical exponent of $\nu \approx 0.71$ [118].

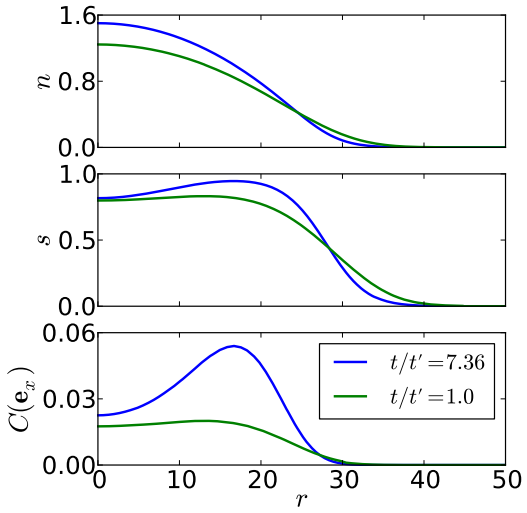

Figure 3.11: The distribution of density, entropy and n.n. spin-correlation per site in the harmonic trap vs. distance from the center. The simulation is done with $N = 66000$, the trap averaged entropy is $S/N = 1.4$. The trapping potential (defined by frequency $\bar{\omega}$ and N) is same as the experimental parameters in the Fig. 3.9(b) for $U = 1.4375t, t/t' = 7.36$.

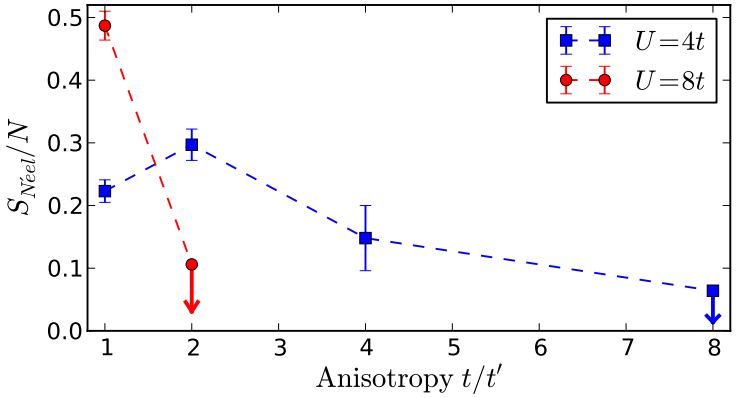

Figure 3.12: Critical entropy per particle $S(T_{\text{Néel}})/N$ at the Néel transition vs. anisotropy for two different interactions at half-filling. The data points shown with an arrow are upper bounds owing to the difficulty of obtaining the extrapolated $T_{\text{Néel}}$ or a reliable $s(T)$ down to the extrapolated transition temperature.

4 Stacked honeycomb and square lattice

We present a numerical study of the Hubbard model on a simply stacked honeycomb and square lattice, motivated by a recent experimental realization of such models with ultracold atoms in optical lattices. We perform simulations with different interlayer coupling and interaction strengths and obtain Néel transition temperatures and entropies. We provide data for the equation of state to enable comparison of experiment and theory, and for calibration of the experiment. We find an enhancement of the short-range correlations in the anisotropic lattices compared to the isotropic cubic lattice, in parameter regimes suitable for the interaction driven adiabatic cooling.

This chapter follows the study [2].

4.1 Model

We study weakly to moderately coupled stacked honeycomb and square lattices, as depicted in Fig. 4.1. The Hamiltonian of the Hubbard model on these lattices is

$$\begin{aligned} \hat{H} &= -t \sum_{\langle i,j\rangle,\sigma} \hat{c}^\dagger_{i\sigma}\hat{c}_{j\sigma} - t' \sum_{\langle i,j\rangle',\sigma} \hat{c}^\dagger_{i\sigma}\hat{c}_{j\sigma} \\ &\quad -\mu \sum_{i,\sigma} \hat{n}_{i\sigma} + U \sum_i \hat{n}_{i\uparrow}\hat{n}_{i\downarrow}, \end{aligned} \tag{4.1}$$

where $\hat{c}^\dagger_{i\sigma}$ ($\hat{c}_{i\sigma}$) creates (annihilates) a fermion at site i with spin $\sigma \in \{\uparrow,\downarrow\}$; $\hat{n}_{i\sigma} \equiv \hat{c}^\dagger_{i\sigma}\hat{c}_{i\sigma}$ denotes the occupation number operator, $U \geq 0$ is the repulsive on-site interaction, t the nearest-neighbor in-plane hopping, t' the inter-layer hopping, and μ the chemical potential. By $\langle i,j\rangle$ we denote nearest neighbors i, j within a plane and by $\langle i,j\rangle'$ nearest neighbor pairs in adjacent planes.

We investigate the case $t \geq t' \geq 0$. Both lattices are bipartite and the model is thus particle-hole symmetric with half filling corresponding to $\mu = U/2$. The

simply stacked square lattice in the regime of weakly coupled chains, $t' \geq t \geq 0$, was studied in Ref. [1] (previous chapter).[1] Note that the simply stacked honeycomb lattice does not correspond to the lattice of graphite, where adjacent layers are shifted relative to each other.

The non-interacting bandwidth of the studied lattices is $W = 2Z_t t + 4t'$, where Z_t denotes the in-plane coordination number $Z_t = 3$ for the stacked honeycomb lattice, and $Z_t = 4$ for the stacked square lattice.

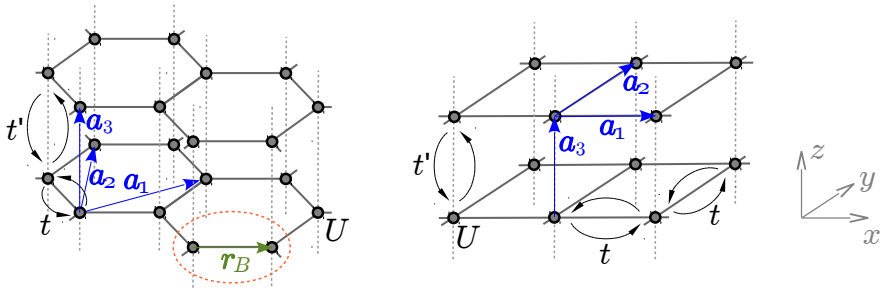

Figure 4.1: Left panel: simply stacked honeycomb lattice with interaction U, in-plane hopping t, and inter-plane hopping t'. The dashed ellipse denotes the unit cell, containing two sites, A and B. The intracell vector $\mathbf{r}_B$ is displayed in green, $\mathbf{r}_A$ is $\mathbf{0}$. The lattice basis vectors $\mathbf{a}_i$ are shown in blue. Right panel: stacked square lattice. Here, the unit cell consists of a single site.

4.2 Introduction

The single-orbital Hubbard model, originally introduced to describe correlation driven metal-insulator transitions [18], has been the subject of intensive study in recent years, as it is widely believed that its realization on a two-dimensional square lattice captures many of the salient features of high-temperature superconductivity [123, 124]. Apart from a Fermi liquid phase at weak interaction and large doping strength and a correlation driven insulating phase at half filling and large interaction strength, superconducting phases of various types [125, 126, 127, 128], pseudogap behavior in the absence of long-range order [129, 130, 131, 22], ferromagnetic [132, 133, 134], and antiferromagnetic (AF) phases [100], as well as different types of stripe phases [135, 136] have been proposed.

Theoretical and numerical studies of the low temperature properties of the Hubbard model have proven to be difficult, especially in the strongly correlated regime where the interaction strength is comparable to the bandwidth and many

[1] Notice that the role of t and t' is interchanged in [1].

low-lying degrees of freedom compete. Experimental realizations using cold atomic gas systems [94, 69], on various lattices in two and three dimensions, offer an alternative route to increase our understanding the physics of this model. While the temperatures accessible by these experiment are still far above the superconducting phase transitions, a range of phenomena, including long range AF order in three dimensions, may soon be accessible [103, 137, 97, 72][1].

One of the current challenges is the calibration of the precise parameters of experiments using ultracold atomic gases, and in particular their temperature or entropy. Numerical simulations of the model for a range of parameters have proven to be useful in this context, and especially quantities that show a strong dependence on temperature and are accessible both in simulation and experiment. An example are nearest neighbor the spin-correlations [97]. Comparison to numerics was able to identify unexpected heating effects and could pinpoint the temperature down to which the experimental realization of the model was accurate [1].

Motivated by the physics of graphene and by the search for a spin liquid state at low temperature [138, 139, 140], experimental realizations of the model on a honeycomb geometry have appeared [99] and provided results in agreement with numerical calculations of the $2d$ model [141, 142]. Complementary to studies on isotropic lattices, anisotropic lattices of various types, *e.g.* with couplings in the vertical axis chosen differently from in-plane couplings, can be realized [97, 99]. These models offer the possibility of studying a dimensional crossover between three, two and one dimensions and with this the possibility of tuning phase transitions to a more readily accessible regime.

From the experimental perspective, layered systems are a natural setup to investigate quasi-2d physics. The reduced dimensionality may give rise to interesting phenomena, but the presence of the third dimension will affect some of the low temperature properties – *e.g.* allowing for long range order at non-zero temperature which is absent in systems with continuous symmetries in two dimensions [143, 144].

For the purpose of quantitative comparisons to cold atoms experiments, numerical simulations need to provide results at comparatively high temperature. For much of the parameter regime accessible to experiment, high temperature series expansion and numerical linked cluster expansions seem to be sufficient. As the temperature is lowered outside of the convergence radius of these series, non-perturbative techniques are required. Cluster dynamical mean field methods [59] in particular are able to reach lower temperature in the thermodynamic limit both at and away from half filling and have been shown to be a reliable tool for this task [102].

4.3 Numerical simulation

The stacked square lattice has a single site per unit cell and may be simulated with the standard DCA method. The basis vectors of the stacked square lattice are the unit vectors in x, y, and z direction, $\mathbf{a}_1 = (1,0,0)$, $\mathbf{a}_2 = (0,1,0)$, $\mathbf{a}_3 = (0,0,1)$.

The simply stacked honeycomb lattice is simulated with the generalization of DCA formulated for an multi-site unit cell discussed in detail in Sec. 2.4. For simulations of the paramagnetic phase we use the 2-site unit cell depicted in the left panel of Fig. 4.1. The basis vectors of the simply stacked honeycomb lattice are $\mathbf{a}_1 = \left(\frac{3}{2}, \frac{\sqrt{3}}{2}, 0\right)$, $\mathbf{a}_2 = (0, \sqrt{3}, 0)$, $\mathbf{a}_3 = (0,0,1)$, and the intracell vectors are $\mathbf{r}_A = \mathbf{0}$, $\mathbf{r}_B = (1,0,0)$.

We locate the temperature of the Néel phase transition by measurement of the static antiferromagnetic susceptibility diverging at the transition. We find this method to be superior to direct order parameter measurement in the ordered phase, which requires allowing for translational symmetry breaking by doubling of the unit cell. The reason is a critical slowing down of the DCA self-consistency loop close to the phase transition. For the stacked square lattice we utilize the susceptibility measurement presented in Subsec. 3.4.6. For the stacked honeycomb we needed to generalize that measurement, enabling for multiple sites per unit cell. Details on that are presented in Subsec. 4.4.1.

The impurity solver employed in the study is the CT-AUX QMC solver [39] with sub-matrix updates [109]. The sign problem is absent at half filling and simulations away of the half-filled case show for the examined parameters only small reduction of the average sign.

Most of the clusters utilized in the study respect the three-fold (four-fold) rotational symmetry around the vertical axis of the stacked honeycomb (square) lattice. The aspect ratio of the clusters is chosen to be similar to the anisotropy t/t'. Since usage of non-bipartite clusters may cause artificial frustration at low temperature, we used them only for the calculations of equation of state (EOS) above the Néel temperature. In particular, we used simply stacked single and triple layered clusters, which are non-bipartite in the direction of the weak hopping t'. Tables listing the clusters are given in Appendix B of [2]. As a part of the cluster selection we performed DCA simulation with a large number of clusters for a small set of parameters to select a small set of clusters for the actual EOS calculations. In Figs. 4.2, 4.3, and 4.4 we see that:

1. Clusters containing rings of length 2 due to the periodical boundary conditions are outriders and therefore are not suitable for use in extrapolations.

2. Uniform scaling of the clusters in all dimensions is a necessary requirement for unbiased extrapolations of the energy (e) and the density (n) to the

thermodynamic limit.

3. The in-plane (xy) nearest neighbor spin-spin correlations, $\langle S^z_{\mathbf{r}A} S^z_{\mathbf{r}B} \rangle$ for the stacked honeycomb lattice,[2] and $\frac{1}{2}\left\langle S^z_{\mathbf{r}} S^z_{\mathbf{r}+\mathbf{a}_x} + S^z_{\mathbf{r}} S^z_{\mathbf{r}+\mathbf{a}_y} \right\rangle$ in the case of stacked square lattice, are in the examined parameter range practically independent from the z extent of the cluster. That applies at the half-filling and away from it.

Respecting the first point becomes hard for the anisotropic models, as abandoning the use of doubly layered clusters would render it impossible to find a set of reasonably small clusters with suitable aspect ratios. Therefore, we tried to circumvent the problem by choice of $\tilde{\mathbf{a}}_3 \neq 2\mathbf{a}_3$, particularly $\tilde{\mathbf{a}}_3 = 2\mathbf{a}_3 + \mathbf{a}_1 + \mathbf{a}_2$ fulfills the bipartite criterion.

A direct simulation in the AF phase is possible with accordingly enlarged unit cell. For the stacked square lattice we need the unit cell to be a cluster containing the reciprocal $\mathbf{Q} = \pi(\mathbf{e}_1 + \mathbf{e}_2 + \mathbf{e}_3)$ vector, see discussion in Sec. 2.5. For the stacked honeycomb lattice it is possible to take two unit cells on top of each other as the enlarged unit cell consisting of 4 sites: $\mathbf{r}_A$, $\mathbf{r}_B$, $\mathbf{a}_3 + \mathbf{r}_A$, and $\mathbf{a}_3 + \mathbf{r}_B$. For the present study we could have utilized this formulation for the $T_{\text{Néel}}$ estimate. However, slow convergence of the DCA selfconsistency loop close to phase transition causes difficulty in getting the solutions converged. Therefore, this approach leads to larger error bars, see in Fig. 4.8. The internal consistency of both approaches was shown in [78], numeric check of the consistency is offered in Figs. 4.8, 4.7.

For weak t' compared to t it is reasonable to obtain a rough estimate of $T_{\text{Néel}}$ by taking a single layered cluster with vertical couplings t' taken into account in a DMFT manner enabling AF order along that direction [55]. It has to be emphasized that this data is not suitable for extrapolation of $T_{\text{Néel}}$ and data using this approximation was not used in [2]. In particular, for this simplification we used doubled original cell, with sites $\mathbf{r}_\alpha$ in the bottom layer and sites $\mathbf{r}_{\alpha+\ell} \equiv \mathbf{a}_3 + \mathbf{r}_\alpha$ in the upper layer ($\alpha \in \{1, \ldots, \ell\}$). The cluster was chosen of the form,

$$\tilde{\mathbf{a}}_1 = n_{11}\mathbf{a}_1 + n_{12}\mathbf{a}_2\,, \qquad \tilde{\mathbf{a}}_2 = n_{21}\mathbf{a}_1 + n_{22}\mathbf{a}_2\,, \qquad \tilde{\mathbf{a}}_3 = 2\mathbf{a}_3\,, \tag{4.2}$$

i.e. the vertical extent $\tilde{\mathbf{a}}_3$ of the cluster is that of the doubled unit cell. Thus any cluster $\mathbf{K}$ vector can be expressed as an integer linear combination of $\tilde{\mathbf{b}}_1$ and $\tilde{\mathbf{b}}_2$.

[2] A symmetrization over all three in-plane nearest neighbors was needed in case of clusters lacking the three-fold rotational symmetry around the z-axis.

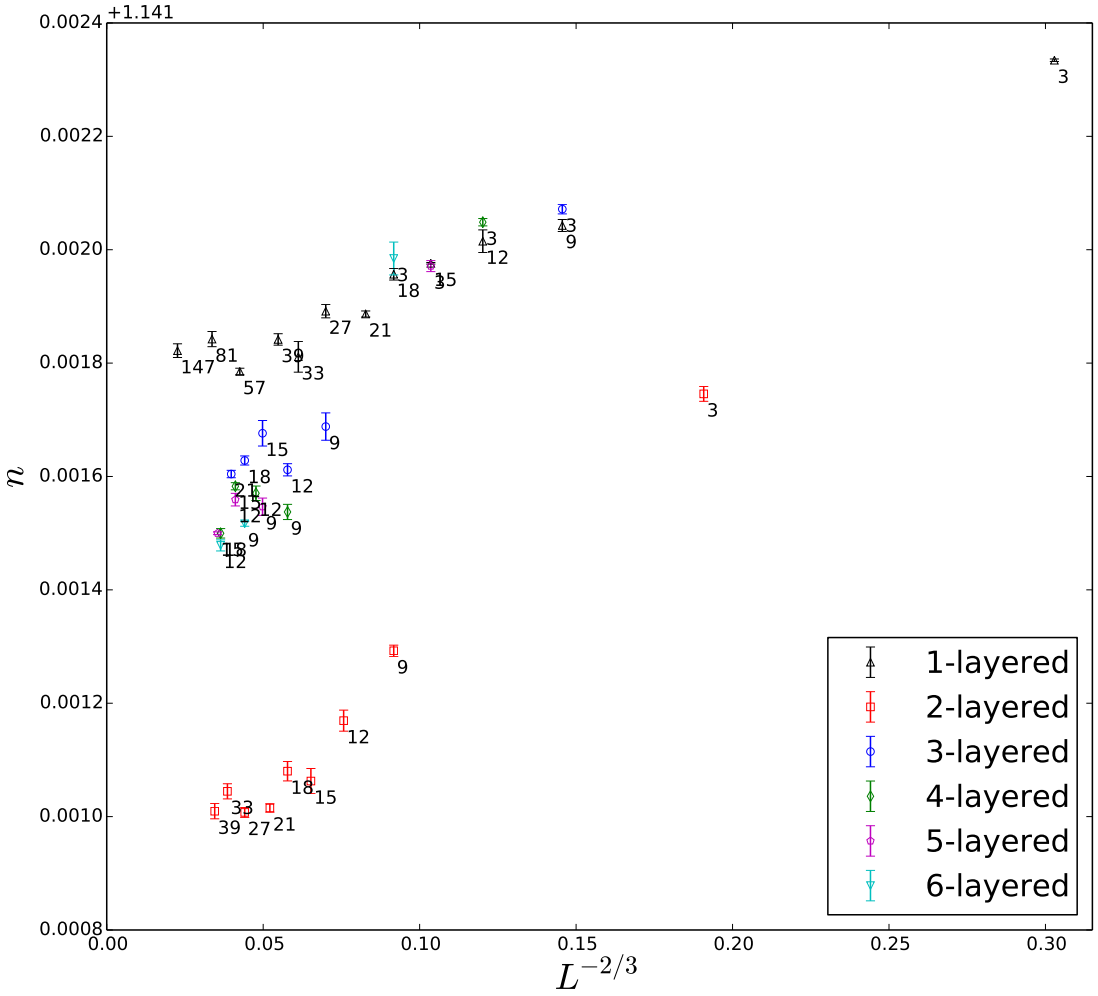

Figure 4.2: DCA density for the stacked honeycomb lattice at $t/t' = 1$, $U/t = 4$, $\beta t = 1$, $\mu = U/2 + t$ using clusters with up to $N = 294$ sites. All of them have the basis vectors of the form $\tilde{\mathbf{a}}_1 = n_{11}\mathbf{a}_1 + n_{12}\mathbf{a}_2$, $\tilde{\mathbf{a}}_2 = n_{21}\mathbf{a}_1 + n_{22}\mathbf{a}_2$, and $\tilde{\mathbf{a}}_3 = n_{33}\mathbf{a}_3$. The labels in the plot show the number of cells in a single layer. The legend shows the number n_{33} of layers of the cluster. Clusters with 3, 9, 12, 21, 27, and 39 cells per layer respect the 3-fold rotational symmetry around the z axis. The clusters with two layers (red open squares) show a bias, which we account to the periodical boundary condition causing doubled connection of each site with its vertical neighbor.

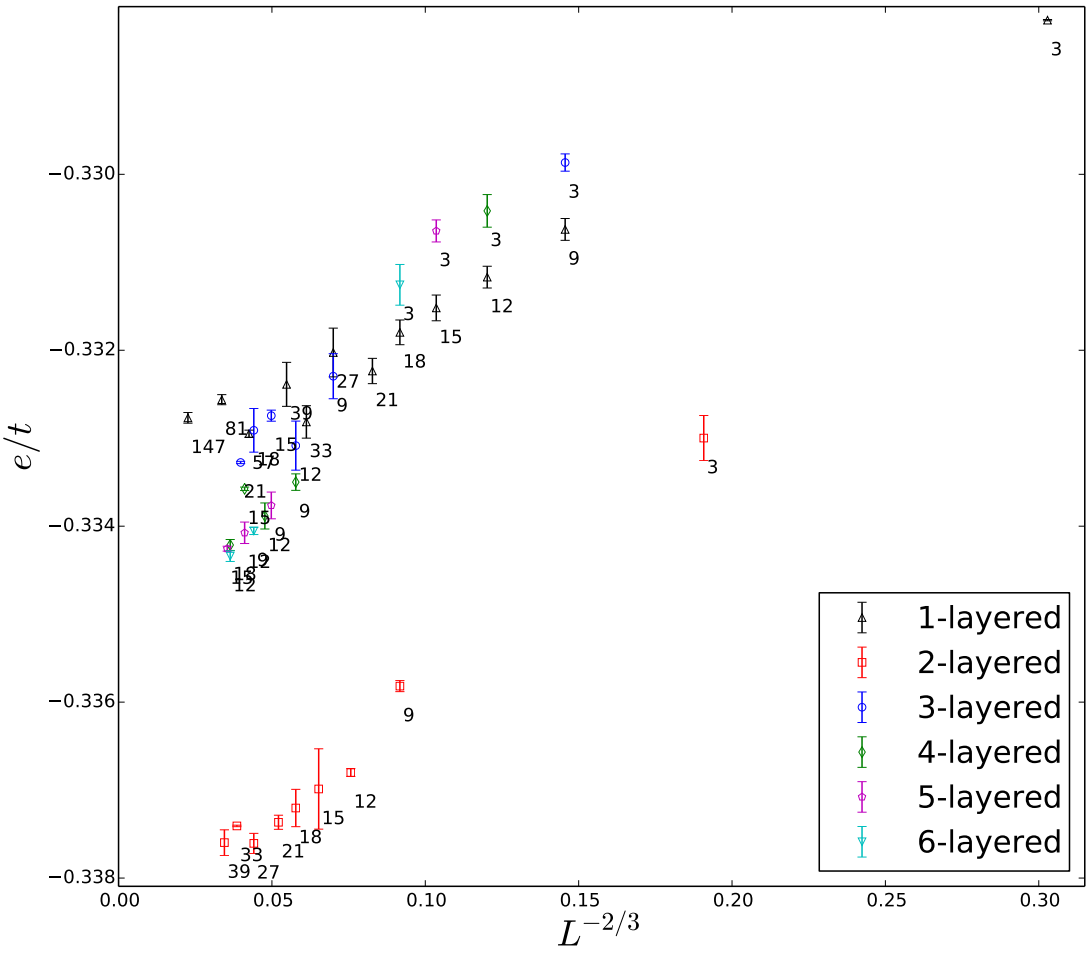

Figure 4.3: DCA energy per site for the stacked honeycomb lattice at $t/t' = 1$, $U/t = 4$, $\beta t = 1$, $\mu = U/2 + t$ using clusters with up to $N = 294$ sites. All of them have the basis vectors of the form $\tilde{\mathbf{a}}_1 = n_{11}\mathbf{a}_1 + n_{12}\mathbf{a}_2$, $\tilde{\mathbf{a}}_2 = n_{21}\mathbf{a}_1 + n_{22}\mathbf{a}_2$, and $\tilde{\mathbf{a}}_3 = n_{33}\mathbf{a}_3$. The labels in the plot show the number of cells in a single layer. The legend shows the number n_{33} of layers of the cluster. Clusters with 3, 9, 12, 21, 27, and 39 cells per layer respect the 3-fold rotational symmetry around the z axis. The clusters with two layers (red open squares) show a bias, which we account to the periodical boundary condition causing doubled connection of each site with its vertical neighbor.

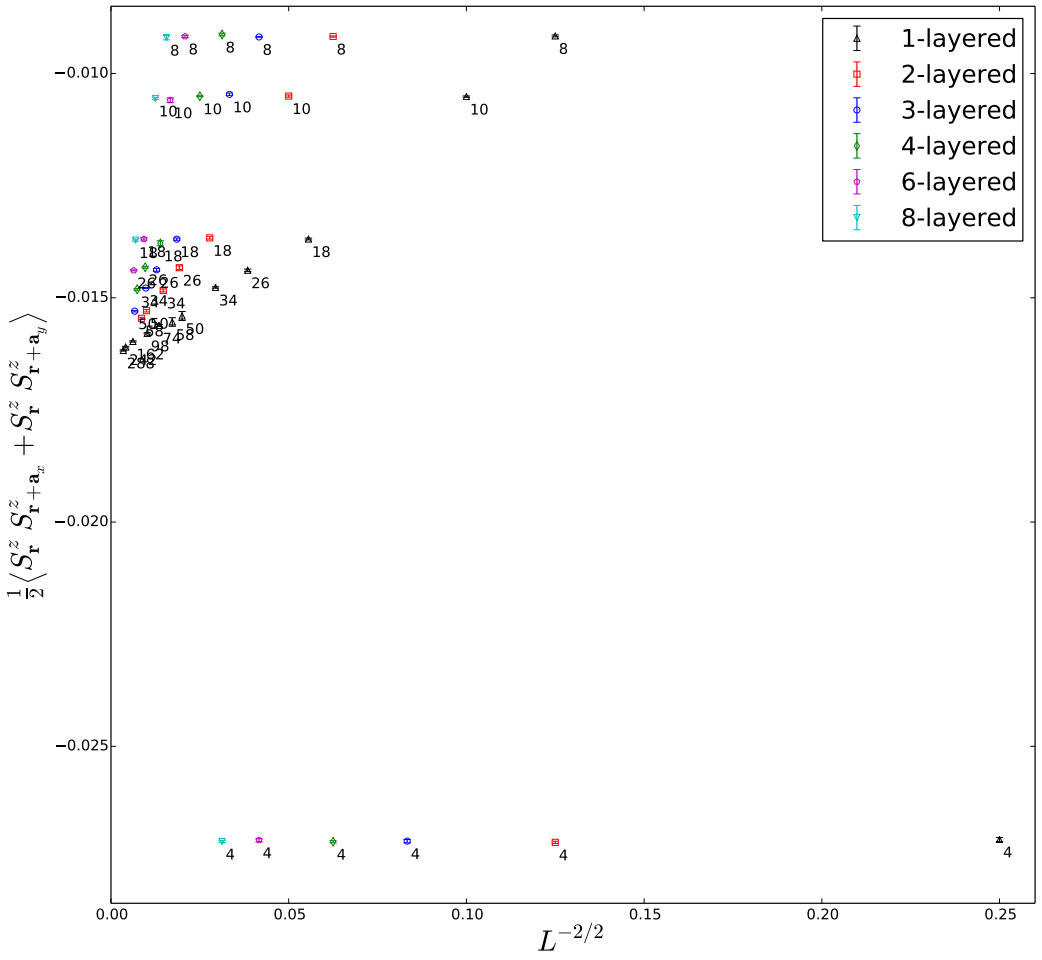

Figure 4.4: DCA spin-spin correlation for the stacked square lattice at $t/t' = 2$, $U/t = 4$, $\beta t = 1$, $\mu = U/2$ obtained with clusters of up to $N = 288$ sites. All of them have a form of a (possibly rotated) square in the xy plane, $\tilde{\mathbf{a}}_1 = n_{11}\mathbf{a}_1 + n_{12}\mathbf{a}_2$, $\tilde{\mathbf{a}}_2 = -n_{12}\mathbf{a}_1 + n_{11}\mathbf{a}_2$, and $\tilde{\mathbf{a}}_3 = n_{33}\mathbf{a}_3$. The labels in the plot display the square area $n_{11}^2 + n_{12}^2$ and the legend shows n_{33}. The cluster basis vectors $\tilde{\mathbf{a}}_1$ and $\tilde{\mathbf{a}}_2$ respect the criterion for a bipartite cluster, Eq. 2.23. The clusters with square area equal to 4, with $\tilde{\mathbf{a}}_1 = \tilde{\mathbf{a}}_2 = 2\mathbf{a}_1$ are clear outriders unsuitable for use in the extrapolation. The reason is the doubled connection of each site with both its neighbors in the xy plane due to the periodical boundary conditions. Further it is noticeable that for the in-plane spin-spin correlation, the z extent of the clusters does not play any role. That makes it possible to perform an extrapolation with clusters of fixed z extent and perform the extrapolation of $\frac{1}{2}\left\langle S^z_{\mathbf{r}} S^z_{\mathbf{r}+\mathbf{a}_x} + S^z_{\mathbf{r}} S^z_{\mathbf{r}+\mathbf{a}_y} \right\rangle$ with $L^{-2/2}$, *i.e.* as for an effectively 2-dimensional problem. Such extrapolations deliver $-0.0166(1)$, $-0.0166(1)$, $-0.0166(2)$, and $-0.0168(3)$ when done for the single layered, doubly layered, triple layered, and 4-layered clusters, respectively. These are consistent with extrapolation according to $L^{-2/3}$ performed with a set of approximatively uniformly scaled clusters.

In the DMFT treatment of the vertical coupling we approximate the self energy with a blocked form (using symmetry relation 1.61),

$$\Sigma_\sigma(\mathbf{K}, \alpha+\ell, \alpha'+\ell) = \Sigma_{\bar{\sigma}}(\mathbf{K}, \alpha, \alpha')\,, \tag{4.3}$$

$$\Sigma_\sigma(\mathbf{K}, \alpha+\ell, \alpha') = 0 = \Sigma_\sigma(\mathbf{K}, \alpha, \alpha'+\ell)\,, \qquad \text{for } \alpha, \alpha' \in \{1, \ldots, \ell\}\,. \tag{4.4}$$

The DCA patch averaging is done over patches corresponding to the cluster with doubled cells and since in the impurity solver we solve only the bottom layer of the cluster, ignoring the top layer, only the relevant $\ell \times \ell$ block of $\bar{G}^{\mathrm{lat}}(\mathbf{K})$ enters the Eq. 2.7.

4.4 Observables

Similarly to the anisotropic Hubbard model study on the cubic lattice presented in the Chap. 3, we measure the EOS, spin-spin correlations, and perform extrapolation to thermodynamic limit for those quantities. The real space observables, *i.e.* the density, the double occupation $\langle \hat{n}_{i\uparrow}\hat{n}_{i\downarrow}\rangle$ entering the potential energy, and the spin-spin correlation can be measured and extrapolated in the same way as it was described in Subsec. 3.4.1-3.4.3. The necessary modification concerns the quantities in reciprocal spaces. The kinetic energy was already in Subsec. 3.4.1 treated for the case of a general lattice. More careful revision is needed for the DCA compatible susceptibility measurement, which was for the Bravais lattice described in Subsec. 3.4.6. In the following subsection we generalize that approach for non-Bravais lattices.

4.4.1 DCA static AF susceptibility for non-Bravais lattices

This subsection contains the generalization of the DCA static AF susceptibility measurement for Bravais lattices described in Subsec. 3.4.6 for the case of non-Bravais lattices. To the best of our knowledge, this generalization was used for the first time in [2]. We stick to the naming and denotations used in the section of [59] on the susceptibility measurement.

DCA approximation on two-particle quantities, measurement

We assume a general case with ℓ sites per cell and L cells in the cluster, with $N = L\ell$ sites. The staggered magnetization operator is assumed to have the form,

$$\hat{m} = \frac{1}{L\ell} \sum_{\mathbf{r},\alpha,\sigma} e^{i\mathbf{Q}\cdot\mathbf{r}}\, (-1)^\alpha\, \sigma\, \hat{n}_{\mathbf{r}\alpha\sigma}\,, \qquad \sigma = \pm 1\,. \tag{4.5}$$

For the stacked honeycomb lattice we may take the 2-site honeycomb cell shown in Fig. 4.1(left) as the unit cell and $\mathbf{Q} = \frac{1}{2}\mathbf{b}_3$. For the 2D honeycomb lattice we would have $\mathbf{Q} = \mathbf{0}$ and a 2-site unit cell able to accommodate the AF state.

The Bethe–Salpeter equation has same form as given in Eq. 3.35, but the multiindices are composed of $\mathbf{k}$, n, σ and two additional sublattice indices $\alpha, \gamma \in \{1, 2, \ldots, \ell\}$, *i.e.* $k \equiv (\mathbf{k}\alpha\gamma n\sigma)$.[3] We approximate the (longitudinally) particle-hole irreducible lattice vertex function Γ^{lat} schematically shown in Fig. 4.5 by the corresponding vertex function Γ^{imp} on the cluster,

$$\Gamma^{\mathrm{lat}}_{(\mathbf{k}\alpha\gamma n\sigma)(\mathbf{k}'\alpha'\gamma'n'\sigma')}(\mathbf{Q}, i\nu_m) \approx \Gamma^{\mathrm{imp}}_{(\mathbf{K}\alpha\gamma n\sigma)(\mathbf{K}'\alpha'\gamma'n'\sigma')}(\mathbf{Q}, i\nu_m)\,. \tag{4.6}$$

The two-particle Green's function $\bar{\chi}$ is defined by

$$\begin{aligned}
&\chi_{(\mathbf{k}\alpha\gamma n\sigma)(\mathbf{k}'\alpha'\gamma'n'\sigma')}(\mathbf{Q}, i\nu_m = 0) = \\
&= \frac{1}{\beta}\int_0^\beta\int_0^\beta\int_0^\beta\int_0^\beta \mathrm{d}\tau_1\,\mathrm{d}\tau_2\,\mathrm{d}\tau_3\,\mathrm{d}\tau_4\, e^{-i(\omega_n\tau_1 - \omega_n\tau_2 + \omega_{n'}\tau_3 - \omega_{n'}\tau_4)} \\
&\quad \times \left\langle T_\tau c^\dagger_{\mathbf{k}+\mathbf{Q}\alpha\sigma}(\tau_1) c_{\mathbf{k}\gamma\sigma}(\tau_2) c^\dagger_{\mathbf{k}'\alpha'\sigma'}(\tau_3) c_{\mathbf{k}'+\mathbf{Q}\gamma'\sigma'}(\tau_4)\right\rangle\,.
\end{aligned} \tag{4.7}$$

Proceeding similarly as in Subsec. 3.4.6 we find the coarse-grained approximation for the lattice two-particle Green's function $\bar{\chi}_{KK'}(\mathbf{Q}, i\nu_m)$,

$$\bar{\chi}(\mathbf{Q}, i\nu_m)^{-1} = \chi_c(\mathbf{Q}, i\nu_m)^{-1} - \chi^0_c(\mathbf{Q}, i\nu_m)^{-1} + \bar{\chi}^0(\mathbf{Q}, i\nu_m)^{-1}\,, \tag{4.8}$$

analogous to the Eq. 3.42. All quantities in the above equation are matrices with multiindices $(\mathbf{K}\alpha\gamma n\sigma)$ and the bar indicates the patch-averaging according to Eq. 3.40.

The actual static AF susceptibility defined by Eq. 3.33 with inserted explicit form of the magnetization operator defined in Eq. 4.5 can be expressed using FT in terms of $\chi(\mathbf{Q}, i\nu_m)$ as

$$\chi_{\mathrm{AF}} = \frac{1}{L\ell\beta^2}\sum_{\substack{\mathbf{K},\mathbf{K}',\alpha,\alpha'\\ \sigma,\sigma',n,n'}} (-1)^{\alpha+\alpha'}\sigma\sigma' e^{-i\mathbf{Q}'\cdot\mathbf{r}_\alpha} e^{i\mathbf{Q}''\cdot\mathbf{r}_{\alpha'}} \bar{\chi}_{(\mathbf{K}\alpha\alpha n\sigma)(\mathbf{K}'\alpha'\alpha'n'\sigma')}(\mathbf{Q}, i\nu_m = 0)\,, \tag{4.9}$$

with phase factors,[4]

$$e^{-i\mathbf{Q}'\cdot\mathbf{r}_\alpha} = e^{i(K_{\mathrm{repr}}(\mathbf{K}) - K_{\mathrm{repr}}(\mathbf{K}+\mathbf{Q}))\cdot\mathbf{r}_\alpha}\,, \tag{4.10}$$

$$e^{i\mathbf{Q}''\cdot\mathbf{r}_{\alpha'}} = e^{i(K_{\mathrm{repr}}(\mathbf{K}'+\mathbf{Q}) - K_{\mathrm{repr}}(\mathbf{K}'))\cdot\mathbf{r}_{\alpha'}}\,, \tag{4.11}$$

where $K_{\mathrm{repr}}(\mathbf{K})$ is the function returning the representant of $\mathbf{K}$.[5]

[3] We need two sublattice indices are these are not conserved.

[4] These factors have their origin in the form of the FT 1.19. The vector $\mathbf{Q}'$ ($\mathbf{Q}''$) may differ from $\mathbf{Q}$ by a reciprocal lattice vector.

[5] Recall that the FT form 1.19 requires to work with a fixed set of $\mathbf{K}$ vectors as a translation by a reciprocal lattice vector influences the phase in a sublattice-dependent way.

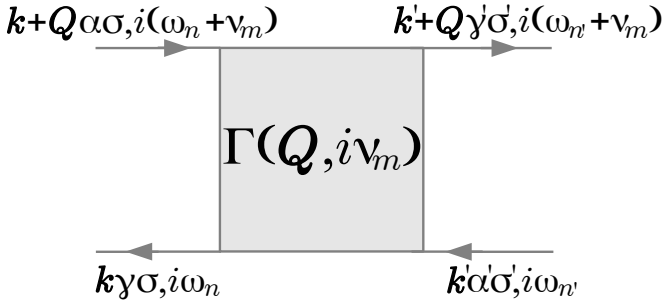

Figure 4.5: The (longitudinally) particle-hole irreducible vertex Γ^{lat} of the original lattice problem is in a DCA compliant susceptibility measurement approximated by the corresponding vertex Γ^{imp} on the impurity.

Estimators for the DCA susceptibility

Let us define an auxiliary two-momenta and two-frequencies Green's function

$$\begin{aligned}&\tilde{g}_\sigma(\mathbf{k}\alpha, \mathbf{k}'\alpha', i\omega_n, i\omega_{n'}) = \\ &\quad \equiv \frac{1}{\beta L}\int_0^\beta \int_0^\beta \mathrm{d}\tau\, \mathrm{d}\tau'\, e^{i\omega_n\tau} e^{-i\omega_{n'}\tau'} \sum_{\mathbf{r},\mathbf{r}'} e^{-i\mathbf{k}\cdot(\mathbf{r}+\mathbf{r}_\alpha)} e^{i\mathbf{k}'\cdot(\mathbf{r}'+\mathbf{r}_{\alpha'})} \tilde{g}_\sigma(\mathbf{r}\alpha\tau, \mathbf{r}'\alpha'\tau')\,, \end{aligned} \tag{4.12}$$

with ([39])

$$\begin{aligned}&\tilde{g}_\sigma(\mathbf{r}\alpha\tau, \mathbf{r}'\alpha'\tau') = \\ &\quad \equiv g^0_\sigma(\mathbf{r}\alpha', \mathbf{r}'\alpha', \tau-\tau') - \sum_{p,q} g^0_\sigma(\mathbf{r}\alpha, \mathbf{r}_p\alpha_p, \tau-\tau_p) M_{pq\sigma} g^0_\sigma(\mathbf{r}_q\alpha_q, \mathbf{r}'\alpha', \tau_q-\tau')\,. \end{aligned} \tag{4.13}$$

Eq. 4.12 can be rewritten as

$$\begin{aligned}&\tilde{g}_\sigma(\mathbf{k}\alpha, \mathbf{k}'\alpha', i\omega_n, i\omega_{n'}) = \\ &\quad = \delta_{\mathbf{k}\mathbf{k}'}\delta_{nn'} g^0_\sigma(\mathbf{k}\alpha\alpha', i\omega_n) - \frac{1}{\beta L}\sum_{\gamma,\gamma'} g^0_\sigma(\mathbf{k}\alpha\gamma, i\omega_n) M_{\mathbf{k}\gamma n\mathbf{k}'\gamma' n'\sigma} g^0_\sigma(\mathbf{k}'\gamma'\alpha', i\omega_{n'})\,, \end{aligned} \tag{4.14}$$

with

$$M_{\mathbf{k}\gamma n\mathbf{k}'\gamma' n'\sigma} = \sum_{\mathbf{r},\mathbf{r}'} e^{i\omega_n\tau_p} e^{-i\mathbf{k}\cdot(\mathbf{r}+\mathbf{r}_\gamma)} e^{-i\omega_{n'}\tau_q} e^{i\mathbf{k}'\cdot(\mathbf{r}'+\mathbf{r}_{\gamma'})} M_{\mathbf{r}\gamma\mathbf{r}'\gamma'\sigma}\,. \tag{4.15}$$

Using the Wick's theorem for the decoupled problem (with auxiliary spins or within the weak coupling expansion) we find

$$\begin{aligned}\chi_{(\mathbf{k}\alpha\gamma n\sigma)(\mathbf{k}'\alpha'\gamma' n'\sigma')}(\mathbf{Q},0) = \\ = \beta\,\langle \tilde{g}_\sigma(\mathbf{k}\alpha,\mathbf{k}+\mathbf{Q}\gamma,i\omega_n,i\omega_n)\tilde{g}_{\sigma'}(\mathbf{k}'+\mathbf{Q}\alpha',\mathbf{k}'\gamma',i\omega_{n'},i\omega_{n'}) \\ - \delta_{\sigma\sigma'}\tilde{g}_\sigma(\mathbf{k}\alpha,\mathbf{k}'\gamma',i\omega_n,i\omega_{n'})\tilde{g}_\sigma(\mathbf{k}'+\mathbf{Q}\alpha',\mathbf{k}+\mathbf{Q}\gamma,i\omega_{n'},i\omega_n)\rangle\ . \quad (4.16)\end{aligned}$$

The non-interacting two-particle susceptibility bubble equals to

$$\begin{aligned}\chi^0_{(\mathbf{k}\alpha\gamma n\sigma)(\mathbf{k}'\alpha'\gamma' n'\sigma')}(\mathbf{q},0) &= -\beta\delta_{\sigma\sigma'}\delta_{nn'}\delta_{\mathbf{k}\mathbf{k}'}G_\sigma(\mathbf{k}\alpha\gamma',i\omega_n)G_{\sigma'}(\mathbf{k}'+\mathbf{Q}\alpha'\gamma,i\omega_{n'}) \\ &\quad + \beta\delta_{\mathbf{Q}\mathbf{0}}G_\sigma(\mathbf{k}\alpha\gamma,i\omega_n)G_{\sigma'}(\mathbf{k}'\alpha'\gamma',i\omega_{n'})\,. \quad (4.17)\end{aligned}$$

For the non-interacting *cluster* susceptibility the G-s are the dressed *cluster* Green's functions, and for the non-interacting *lattice* susceptibility the G-s are the dressed *lattice* Green's functions $G^{\mathrm{lat}}(\mathbf{k},i\omega_n) = \left[G^{0,\mathrm{lat}}(\mathbf{k},i\omega_n)^{-1} - \Sigma(\mathbf{k},i\omega_n)\right]^{-1}$.

As we mentioned in Subsec. 3.4.6, the restriction to the PM phase ensures the symmetry in spin σ,

$$\chi_{(\mathbf{k}\alpha\gamma n\sigma)(\mathbf{k}'\alpha'\gamma' n'\sigma')}(\mathbf{Q},0) = \chi_{(\mathbf{k}\alpha\gamma n\bar{\sigma})(\mathbf{k}'\alpha'\gamma' n'\bar{\sigma'})}(\mathbf{Q},0)\,, \quad (4.18)$$

enabling decomposition into the charge and the spin channel.[6] Further properties of χ suitable for reduction of independent observables are

$$\chi_{(\mathbf{k}\alpha\gamma n\sigma)(\mathbf{k}'\alpha'\gamma' n'\sigma')}(\mathbf{Q},0) = \chi^*_{(-\mathbf{k}\alpha\gamma-(n+1)\sigma)(-\mathbf{k}'\alpha'\gamma'-(n'+1)\sigma')}(\mathbf{Q},0)\,, \quad (4.19)$$

$$\chi_{(\mathbf{k}\alpha\gamma n\sigma)(\mathbf{k}'\alpha'\gamma' n'\sigma')}(\mathbf{Q},0) = \chi_{(\mathbf{k}'+\mathbf{Q}\alpha'\gamma' n'\sigma')(\mathbf{k}+\mathbf{Q}\alpha\gamma n\sigma)}(\mathbf{Q},0)\,, \quad (4.20)$$

where the first property requires $M_{pq\sigma} \in \mathbb{R}$, which is given for the studied model with purely real real space Hamiltonian, and correspondingly chosen CT-AUX parameter K (Sec. B.1) such that $e^{\pm\gamma} \in \mathbb{R}$. Notice that the symmetry 4.20 implies that χ is symmetric in case $\mathbf{Q} = \mathbf{0}$.

Estimate of the critical point

For any practical use the frequencies ω_n, $\omega_{n'}$ need to be cut-off at some ω_c. The frequency cut-off is cured by fitting the $\frac{1}{\omega_n^2}$ tail and adding its contribution to the result [145], see in Fig. 4.6. The cut-off was validated by comparison of the tail-fitted impurity susceptibility obtained by Eq. 4.9, where we replaced $\bar{\chi}$ by χ_c, with the directly measured impurity susceptibility using estimator given in Eq. 3.26 with $\hat{m}$ given in Eq. 4.5; see Subsec. 3.4.5. Typically we use $\omega_c \approx 5U$.

[6] Note that the second (spin-independent) term in Eq. 4.17 is canceled in the spin channel.

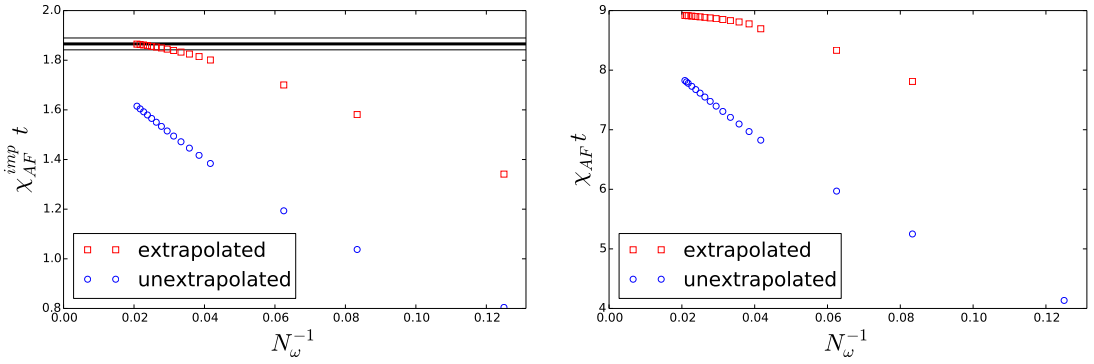

Figure 4.6: The left plot shows the unextrapolated impurity susceptibility obtained via Eq. 4.9 with χ_c in role of $\bar{\chi}$ as a function of the frequency cut-off N_ω. Next it displays its extrapolated values, which use fitting of the tail to $\frac{C}{\omega_n^2}$. The direct measurement of the impurity susceptibility via Eq. 3.26 with magnetization operator 4.5 is displayed by the horizontal lines – the thick line is the mean and the narrow lines show the standard deviation. The right plot shows the lattice susceptibility. As in the left plot, we show the extrapolated and unextrapolated χ_{AF}. The data was obtained for the Hubbard model on the honeycomb lattice at $U = 3t$, $\beta t = 20$, at half filling ($\mu = U/2$) using a cluster with 18 sites respecting the three-fold rotational symmetry of the model. Notice the difference of the scale on the vertical axes.

Notice that not all entries of $\bar{\chi}$ are summed to get χ_{AF} when $\ell > 1$. Therefore, the leading eigenvalue of $\Gamma\bar{\chi}^0$ may in principle be associated with a mode which is not relevant for χ_{AF}. Thus, instead of examination of the leading eigenvalue of $\Gamma\bar{\chi}^0$ we stick to the evaluation of χ_{AF}. DCA, as a mean-field based method, displays close to the second order phase transition the mean-field critical exponents. We utilize that for a precise location of the transition for each cluster – we search for the intersection of $\chi_{AF}^{-\gamma_{\mathrm{mf}}}(L)$ with zero, with the mean-field critical exponent $\gamma_{\mathrm{mf}} = 1$; see Fig. 4.7.

In Fig. 4.8 we display the extrapolations of the Néel temperature based on Néel temperatures obtained on several clusters both with the susceptibility measurement and with the order parameter measurement. The susceptibility measurement was conducted in the PM regime with enforced symmetrization. For the order parameter measurement we used a formulation with doubled unit cell (here with $\ell = 4$ sites per cell) allowing for AF ordering. The extrapolation in cluster size is done both with equally weighted $T_{\mathrm{N}}(L\ell)$ and also with weights inversely proportional to the square of the standard deviation of $T_{\mathrm{N}}(L\ell)$.

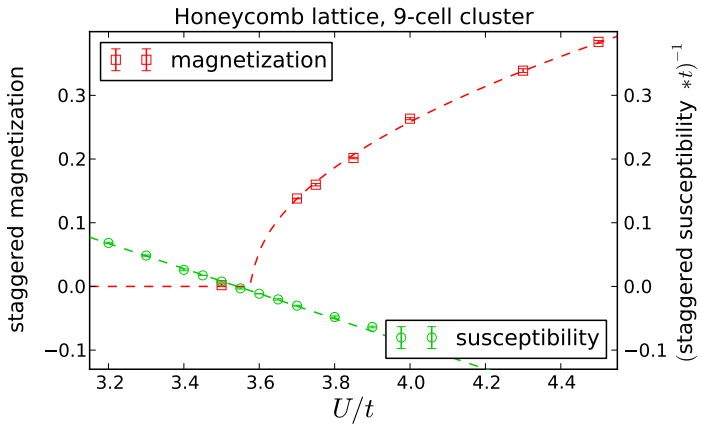

Figure 4.7: Plot of the static AF susceptibility obtained in a PM-restricted simulation along with the staggered magnetization (order parameter) obtained in a DCA simulation allowing for AF ordering. This plot demonstrates the consistency of both approaches. The investigated model was the Hubbard model on the honeycomb lattice with nearest neighbor hopping t, at half filling, $\beta t = 20$. The frequency cut-off for the susceptibility measurement was $N_\omega = 48$ and the data for the susceptibility was extrapolated to $N_\omega \to \infty$ using high-frequency tail fitting. The susceptibility and the order parameter are in the vicinity of the phase transition fitted with the mean-field critical exponents $\gamma_{\mathrm{mf}} = 1$ and $\beta_{\mathrm{mf}} = 0.5$, resp. Remark: the ordering at finite βt is a DCA artifact, showing up when the correlation length becomes comparable with the linear cluster size.

4.4.2 Structure of the particle-hole irreducible vertex Γ

As a model system we investigate the Hubbard model on the honeycomb lattice at $U = 3t$, $\beta t = 20$, at half-filling. The lattice susceptibility is close to $9\, t^{-1}$, a value that is roughly 5-times larger than the corresponding impurity susceptibility measured with Eq. 3.26. We measure $\chi_c(\mathbf{Q} = \mathbf{0}, i\nu = 0)$ and compute the particle-hole irreducible vertex Γ according to Eq. 3.35. The simulations are performed with two clusters: a 9-cell and a larger 39-cell cluster. The larger cluster is displayed in the Fig. 4.10(bottom right). It enables linear arrangement of the cluster reciprocal $\mathbf{K}$ momenta.

The vertex Γ has real-valued entries for particle-hole symmetric models defined on a Bravais lattice [115]. Since the model examined in the present subsection is not on a Bravais lattice the components of Γ might be complex.

The top row plots in Fig. 4.9 display the real and imaginary part of the low frequency entries of $\Gamma_m(\mathbf{0}, 0)$. The most obvious structure is that of the bare vertex,

$$\bar{\Gamma}^{0,\mathrm{lat}}_{(\mathbf{k}\alpha\gamma n\sigma)(\mathbf{k}'\alpha'\gamma' n'\sigma')}(\mathbf{Q}, i\nu_m) = -\frac{U}{L\beta^2}\delta_{\alpha\gamma}\delta_{\alpha'\gamma'}\delta_{\alpha\alpha'}\delta_{\bar{\sigma}\sigma'}\,. \tag{4.21}$$

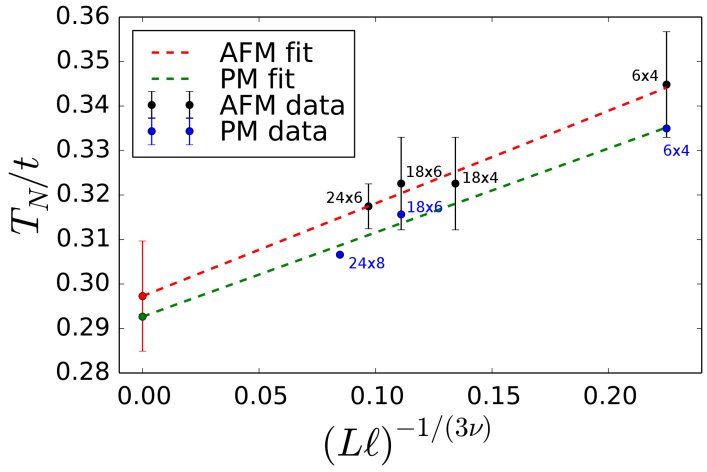

Figure 4.8: Extrapolation of the Néel temperature T_N for the stacked honeycomb lattice for $t/t' = 1$, $U/t = 6$. The critical exponent $\nu = 0.71$ was taken from the 3D Heisenberg model [118] in the same universality class. The error bars for the AF data show lower and upper bounds of the transition based on measurement of the staggered magnetization. The PM data points are susceptibility based measurement with error bars smaller than the symbol size. The labels show number of sites in a single plane times the number of layers of the used cluster.

The random phase approximation with the bare Γ^0 and χ^0 obtained as a product of the dressed Green's functions G (Eq. 4.17) yields for the investigated model $U_c/t \approx 2.65$ with G obtained on the 9-cell cluster.[7] That is to be compared with $U_c/t = 3.56(2)$ obtained in a fully DCA compliant procedure both with direct order parameter measurement in the AF phase and the susceptibility measurement with $\Gamma^\mathrm{lat} \approx \Gamma^\mathrm{imp}$, see in Fig. 4.7.

Structure in the different sublattice sectors

Apart from the model independent symmetry of Γ in the multiindices inherited from $\chi(\mathbf{0}, 0)$, see Eq. 4.20, the model has inversion symmetry (Subsec. 1.3.7), leaving 6 *independent* out of the total 16 sublattice blocks, $(\alpha, \gamma, \alpha', \gamma') = AAAA$, $ABAA$, $BAAA$, $BBAA$, $ABAB$, $ABBA$. The sector $AAAA$ is without surprise the dominant one, as the $UL^{-1}\beta^{-2}$ is its non-renormalized value for any frequency and $\mathbf{K}$ vector. Out of the other sectors, $ABBA$ and $ABAB$ seem to be significant, while the other sectors, $ABAA$, $BAAA$, $BBAA$, have entries with magnitude at most $0.1UL^{-1}\beta^{-2}$.

[7] The non-interacting 2-particle susceptibility χ^0 is in a typical random phase approximation obtained as a product of the bare lattice Green's functions G^0.

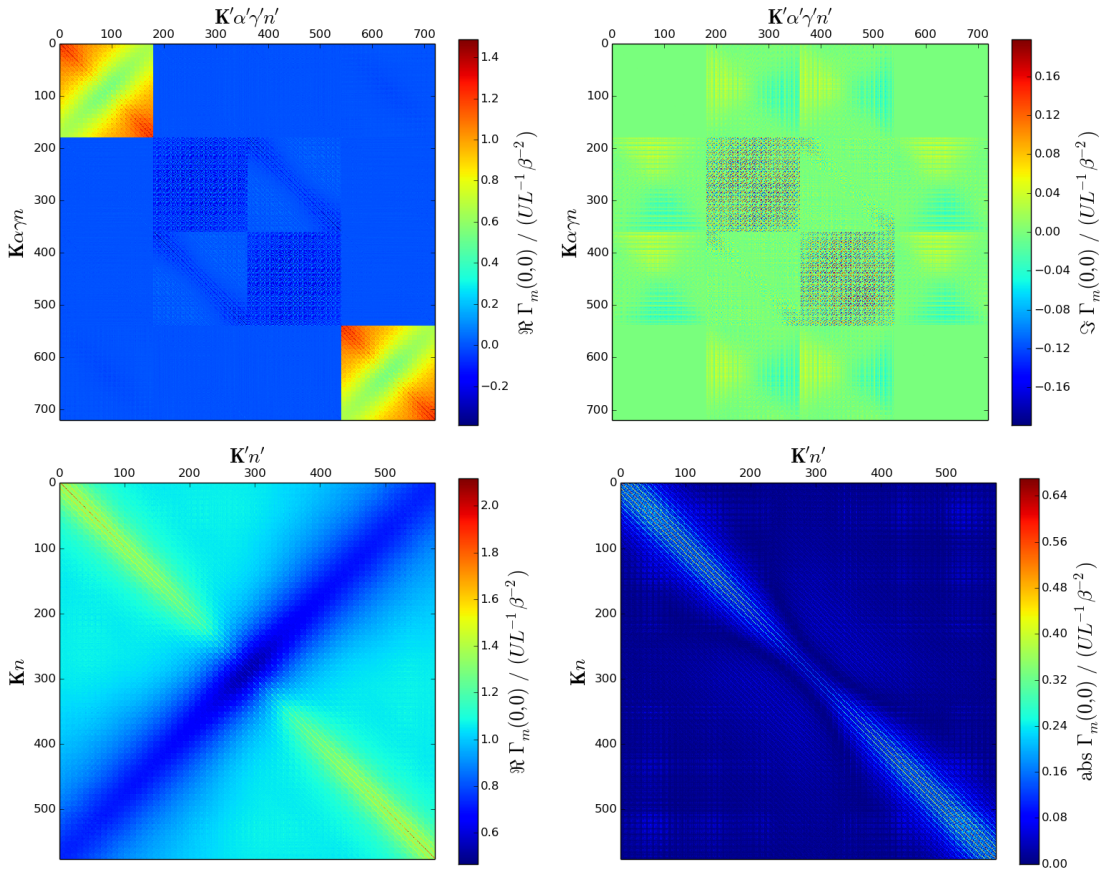

Figure 4.9: The magnetic channel of the impurity particle-hole irreducible vertex function $\Gamma_m^{\text{imp}}(\mathbf{0}, i\nu = 0)$ is displayed. In the top color plots we show its real and imaginary part. $UL^{-1}\beta^{-2}$ is its bare value. The multiindices $(\mathbf{K}\alpha\gamma n)$ and $(\mathbf{K}'\alpha'\gamma'n')$ are computed as $2\,(2\,(L(n+10)+k)+\alpha)+\gamma$, with index k for the cluster $\mathbf{K}$ points. The lower row shows the sector $AAAA$ in the left, and $ABBA$ in the right. There the indices are computed as $L(n+10)+k$. The data was obtained on a 9-cell cluster with 3-fold rotational symmetry.

Structure in the frequency space

The sector $AAAA$ of $\Gamma_m(\mathbf{0}, 0)$ has already in its bare limit non-vanishing elements for any frequencies $i\omega_n$, $i\omega_{n'}$ (and reciprocal vectors $\mathbf{K}$, $\mathbf{K}'$). In the bottom left plot of Fig. 4.10 there is evident an enhancement (suppression) around equal (opposite) frequencies. These most pronounced features were already observed within a DMFT treatment in [115].

In the sector $ABBA$ we find non-zero elements emerged along equal frequencies, saturating for large $n = n'$, see in Fig. 4.10.

The last sector with non-negligible entries in Γ_m is $ABAB$, whose contributions are restricted to low frequencies, for $|n|, |n'| \lessapprox 24$, with absolute values up to $0.4UL^{-1}\beta^{-2}$.

Structure in the reciprocal space

The most significant $\mathbf{K}$-structure of the vertex $\Gamma_m(\mathbf{Q}, 0)$ is visualized in Fig. 4.10, 4.11. The top row plots in Fig. 4.10 for sectors $AAAA$ and $ABBA$ at equal frequencies show that these are dominantly dependent on $\mathbf{K} - \mathbf{K}'$, hinting to low order diagram(s) being responsible for that structure. Two of the three second order (longitudinally) particle-hole irreducible diagrams, see in Fig. 4.12, have the desired structure, but they precisely cancel each other in the magnetic channel. All third order diagrams have different dependence on $\mathbf{K}$, $\mathbf{K}'$ (and n, n') [115], so one needs to go at least to the fourth order for the explanation.

The $\mathbf{K}$-dependence of the sector $AAAA$ at opposite frequencies, $i\omega_{n'} = -i\omega_n$, shows smaller variations than at equal frequencies, of approximatively 12.5% around the mean value. The $\mathbf{K}$-dependence there is, similarly as in the sector $ABAB$ at low frequencies (Fig. 4.11), dominantly on $\mathbf{K} + \mathbf{K}'$.

4.5 Results

We compute the EOS and further properties – the energy, entropy, density, nearest-neighbor spin correlation, and the double occupancy – of the model of Eq. 4.1 using DCA and extrapolating the results to the thermodynamic limit according to $L^{-2/3}$ (see [102, 110] for details). We restrict the calculations to fillings $n \leq 1$ per site, as the results for $1 < n \leq 2$ are related to those for $n \leq 1$ via particle-hole symmetry.

4.5.1 Spin correlations

We calculated the nearest-neighbor spin correlations, which capture the onset of magnetic ordering and have proven to be a suitable observable for estimate of the temperature of the system [102][1]. We specifically calculate the equal-time in-plane nearest-neighbor spin correlations

$$C_{nn} = -\frac{2}{Z_t L \ell} \sum_{\langle i,j \rangle} \left\langle \hat{S}_i^z \hat{S}_j^z \right\rangle , \tag{4.22}$$

where the sum runs over in-plane nearest-neighbor pairs (coupled by the strong hopping t), $\hat{S}_i^z = \frac{1}{2}(\hat{n}_{i\uparrow} - \hat{n}_{i\downarrow})$, L is the number of cells and the average $\left\langle \hat{S}_i^z \hat{S}_j^z \right\rangle$

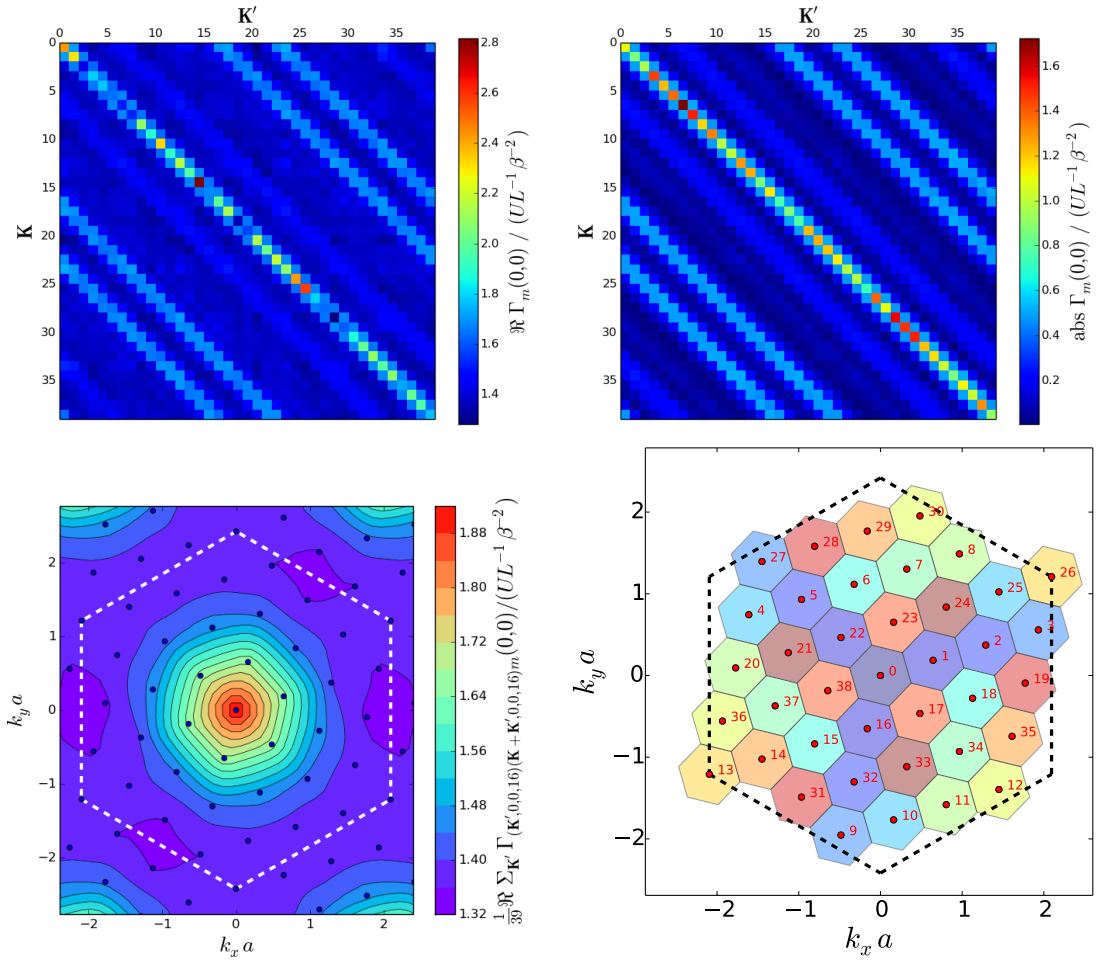

Figure 4.10: Plot of $\Gamma_m(\mathbf{0},0)$ at equal frequency, $n = n' = 16$. The top left plot is for sublattice sector $AAAA$, and the top right is for $ABBA$. Using white noise addition we checked that the "pattern" on both main diagonals in the top row plots is of noise origin. The bottom left plot shows the data of the top left plot symmetrized along the diagonals, reducing to a single K-vector dependency, interpolated in a Brillouin zone. For the simulation we used the 39-cell cluster shown in the bottom right plot in the reciprocal space. Its reciprocal $\mathbf{K}$ points are $k\,(7\mathbf{b}_1 + 2\mathbf{b}_2)\,/39$ shifted by suitable reciprocal lattice vector to the Brillouin zone, with k running from 0 to 38; $\mathbf{b}_1 = \frac{2\pi}{a}\left(\frac{2}{3}, 0\right)$, $\mathbf{b}_2 = \frac{2\pi}{a}\left(-\frac{1}{3}, \frac{1}{\sqrt{3}}\right)$; a denotes the nearest neighbor distance of the sites on the honeycomb lattice.

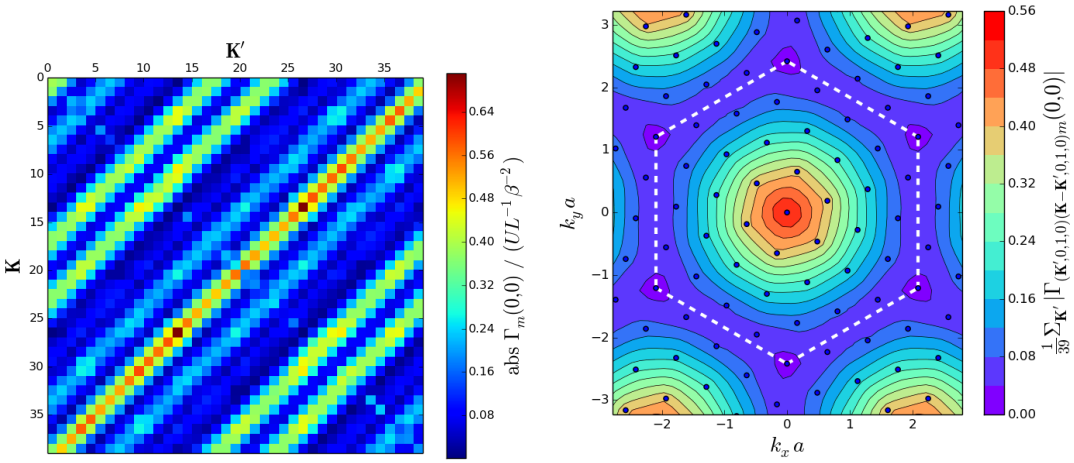

Figure 4.11: Left: $\Gamma_m(\mathbf{0}, 0)$ for $n = n' = 0$ and sector $ABAB$. Right: Here we show the data from the left plot symmetrized along the antidiagonals and subsequently interpolated in the reciprocal space. The simulation was the same as for Fig. 4.10.

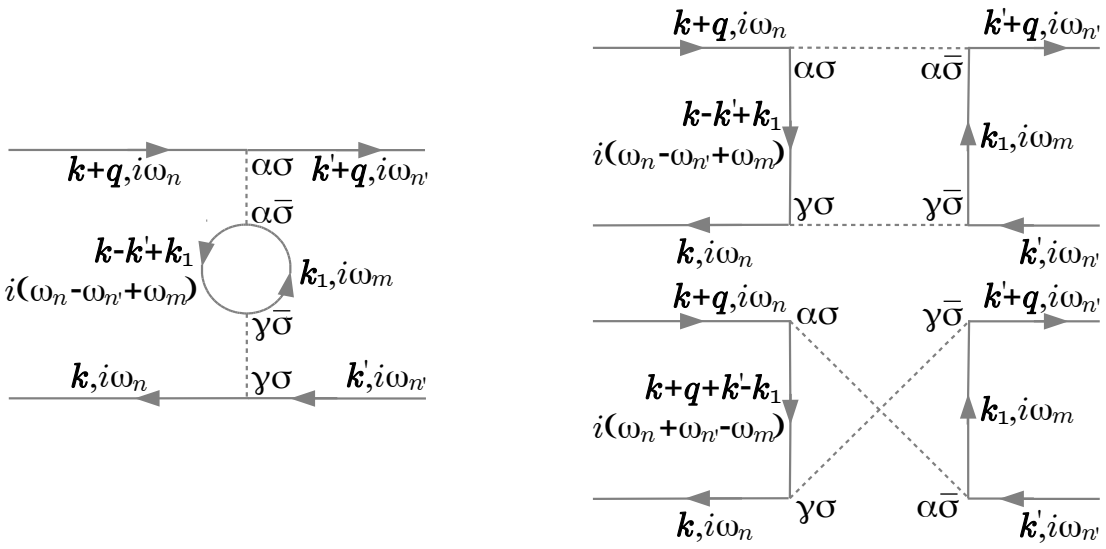

Figure 4.12: Second order contributions in U to the (longitudinally) particle-hole irreducible Γ. The left diagram contributes to $\Gamma_{\sigma\sigma}$, while the right diagrams contribute to $\Gamma_{\sigma\bar{\sigma}}$. Contribution of the left diagram and the top right diagram naively differs by a minus sign due to the extra fermionic loop in the left diagram, however these diagrams have to be closed on both sides, according to Eq. 3.35, which results in an additional fermionic loop for the right diagram. Thus their contribution equals and is canceled in the magnetic channel $\Gamma_m = \Gamma_{\uparrow\uparrow} - \Gamma_{\uparrow\downarrow}$. The right bottom diagram contributes to sectors $AAAA$ and $ABAB$. Its largest contribution is for $\omega_n \approx -\omega_{n'}$, its $\mathbf{k}$-dependence is only on $\mathbf{k} + \mathbf{q} + \mathbf{k}'$.

is measured directly on the cluster. The measurement was in detail described in Subsec. 3.4.3. Although there we described it for assuming a Bravais lattice, it is formulated in real space, so the formulas can be without modification used for any graph. We show the spin correlations for the stacked honeycomb and stacked square lattice in Fig. 4.13. The data shown was calculated for a homogeneous system at half filling and at a fixed entropy per particle. C_{nn} shows similar behavior with interaction strength and anisotropy for both lattices, with an approximative amplification by a factor 4/3 in the stacked honeycomb lattice. The factor 4/3 is the ratio of strong hopping coordination number Z_t on the stacked square lattice to that of the stacked honeycomb lattice. The maxima are at similar interaction strengths if interactions are measured in units of the bandwidth W. Qualitatively, the observed behavior is captured by the second order HTSE (Sec. D.3), which is at half filling given by

$$C_{nn}^{(2)}(s) = \frac{2(\ln 4 - s)t^2}{8(Z_t t^2 + 2t'^2) + U^2}. \tag{4.23}$$

Quantitatively, the second order high-temperature estimate of $C_{nn}(T)$ is reliable only for $T/t \gtrapprox 3$, corresponding to an entropy per site s well above 1. Note that Fig. 4.13 is calculated for $s = 0.7$, which is close the lowest experimentally realizable value at half filling [1]. Noticeably, the sum of $C_{nn}^{(2)}(s)$ over all bonds $\langle i, j\rangle$ is independent of the lattice properties if U is scaled according to the root of the second moment of the non-interacting density of states $D_2 = Z_t t^2 + 2t'^2$.

C_{nn}, as an experimentally measurable quantity [97], may serve as a sensitive thermometer in the temperature range $T/t \sim 1$ if compared with the EOS we provide. The enhancement due to anisotropy raises the signal and renders the measurement more precise.

4.5.2 Trap effects

In experiments, ultracold atoms are confined by a trapping potential, which may be modeled by a LDA at currently experimentally accessible temperatures [106, 107]. As confining potential we take a quadratic function $V(\mathbf{x})$ with minimum in the trap center. The chemical potential μ we choose such that the system is half-filled in the trap center. Assuming a large lattice, we use a continuous approximation instead of discrete summation over lattice sites and obtain a trap-averaged quantity Q as

$$Q = \int \mathrm{d}^3\mathbf{x}\; q\left(\mu - V(\mathbf{x}); T\right), \tag{4.24}$$

where q is the density of the quantity of interest in a homogeneous system. With this definition, the quantity Q per particle, Q/N, is independent on the specific

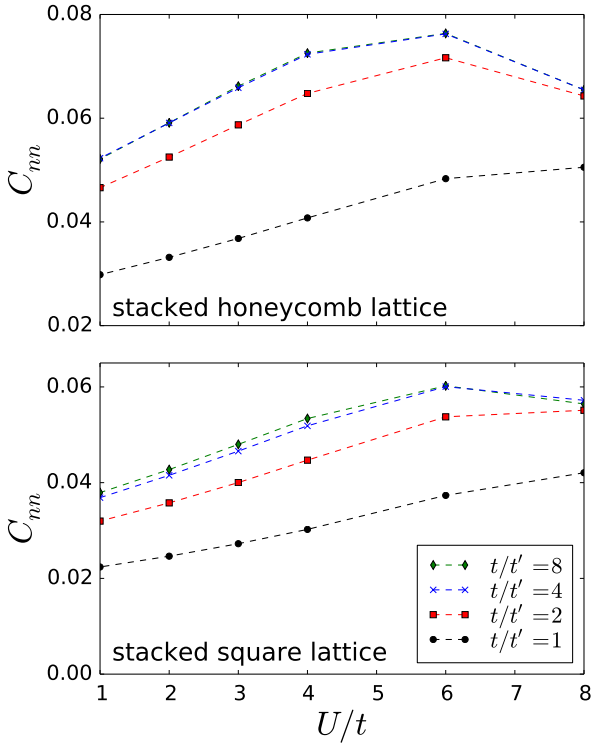

Figure 4.13: The nearest neighbor in-plane spin correlation C_{nn} for the stacked honeycomb lattice (top) and stacked square lattice (bottom) as a function of the interaction strength U/t for various anisotropies t'/t at half filling ($n = 1$, $\mu = U/2$) and at an entropy $s = 0.7$. C_{nn} shows an enhancement in the anisotropic case $t/t' > 1$. The curves for $t/t' = 4$ and 8 are on top of each other.

parameters of the quadratic potential. For the LDA calculations we need the EOS at low filling, which we approximate by the EOS of the corresponding non-interacting system (App. C). Fig. 4.14 shows the trap-averaged C_{nn}. Even in the trap, with contribution from sites at all fillings, the C_{nn} is at fixed entropy per site roughly proportional to Z_t^{-1}. This observation may be confronted with the experimental results presented in Fig.(2)a in [72], where *Greif et al.* present the trap-averaged nearest-neighbor spin correlations obtained in weakly coupled square stacks with varying ratio of in-plane hoppings. In particular, they find for $Z_t = 2$ almost doubled spin correlations when compared to $Z_t = 4$, which is consistent with our outcome. Their measurement is conducted after a nearly adiabatic ramp of the optical lattice, in a system with total entropy not significantly dependent on the chosen ratio of in-plane hoppings. In Fig. 4.15 we display profiles of density, entropy per site, and C_{nn} for the stacked honeycomb and square lattice and the 1D coupled chains. For Fig. 4.15 we assume isotropic $V(\mathbf{x})$. The distance from

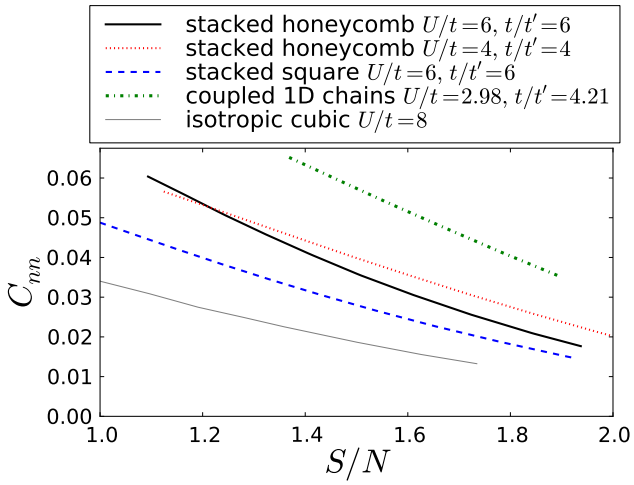

Figure 4.14: Average spin correlation C_{nn} per particle plotted as a function of the entropy per particle S/N in a quadratic trap with chemical potential adjusted to obtain half filling ($n = 1$) in the trap center. The data for the coupled 1D chains and isotropic cubic lattice is taken from Refs. [1][102].

the trap center we denote by r. In the studied temperature regime, coupled 1D chains [1] show the largest spin correlation.[8] The density and entropy distributions differ only marginally. Therefore, a dynamic change of topology of the lattice, as done in [72], is not accompanied by a substantial particle redistribution, which may cause unwanted heating [146]. In the lower panel of Fig. 4.15 we observe that C_{nn} at half filling ($r = 0$) is roughly proportional to the inverse strong hopping coordination number Z_t^{-1}. This effect might be qualitatively explained by the different energy scales of the hoppings – the simulations are performed at a high temperature relative to the weak hopping t', but the temperature is comparable with the strong hopping t. Thus the AF short-range correlations tend to build up in the strong hopping directions (in-plane) and the singlet formation is facilitated by lower Z_t.

4.5.3 Double occupancy and adiabatic cooling

Of further experimental interest are ways to cool the particles, to provide access to interesting low temperature phenomena. As discovered in Ref. [147], an analogue of the Pomeranchuk effect can be used to cool fermions in an optical lattice.

[8] For the 1D chain the C_{nn} is the nearest-neighbor spin correlation in direction of the strong hopping, see definition in Ref. [1].

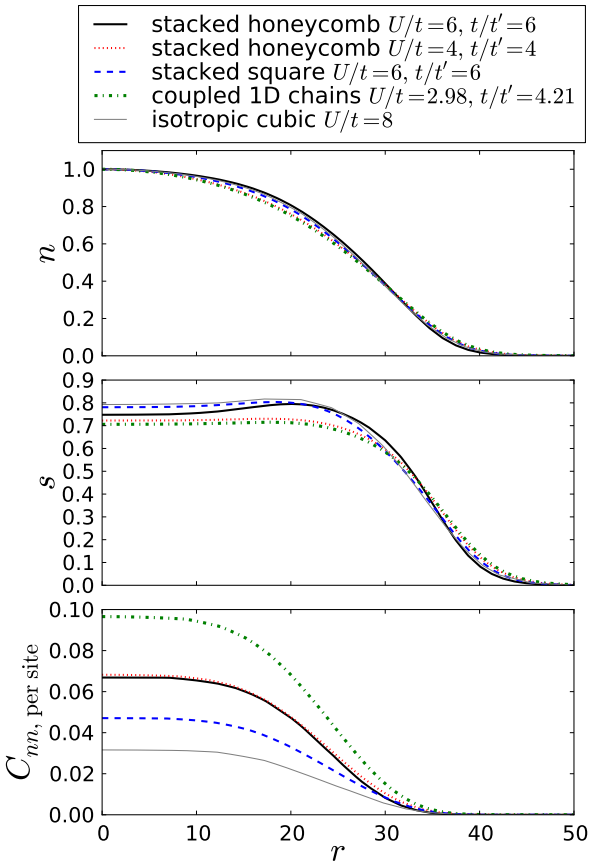

Figure 4.15: Density n, entropy s, and C_{nn} profile in a quadratic trap with the particle number fixed to $N = 10^5$ and half filling in its center. The radius r is given in units of lattice sites. The entropy per particle S/N is set to 1.4, which is an experimentally achievable value [1]. The data for the coupled 1D chains and isotropic cubic lattice is taken from Ref. [1][102].

These lower their temperature T in an adiabatic process of (slow) increase of the interaction strength if the double occupancy $D = \frac{1}{L\ell}\langle n_{i\uparrow} n_{i\downarrow}\rangle$ shows an increase upon cooling at fixed density n. The adiabatic cooling effect $\left(\frac{\partial T}{\partial U}\right)_{s,n}$ is proportional to the temperature, to the inverse of the specific heat, and to $\left(\frac{\partial D}{\partial T}\right)_{U,n}$.[147] The interaction driven adiabatic cooling was experimentally utilized for a $SU(6)$ Hubbard model [148]. For the Hubbard model in the context of optical lattice experiments, the presence of the effect was numerically observed both for square and honeycomb lattices [149, 141].

We here investigate this effect for the stacked lattices in a homogeneous system. Figure 4.16 shows the adiabatic cooling effect at half filling and at entropy per

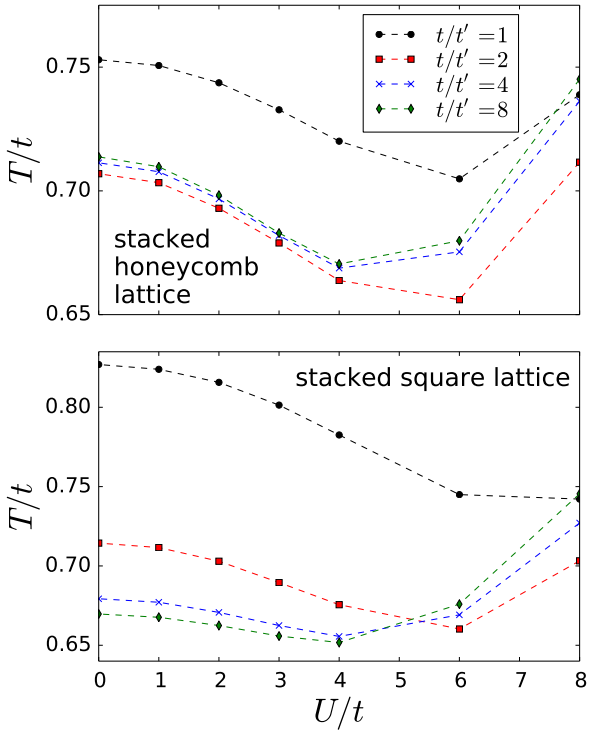

Figure 4.16: Temperature T/t plotted as a function of U/t for the stacked honeycomb (top) and stacked square lattice (bottom) at half filling and at entropy per site $s = 0.7$ for various anisotropies t/t'. An adiabatic increase of U/t from 0 up to a parameter-specific U induces cooling in all cases.

site $s = 0.7$ at a range of anisotropies, with cooling persisting up to $U/t \approx 6$. Alternatively it is possible to start from large interactions and decrease U; however, in that case T/U may increase. The cooling is present only at sufficiently low entropies, $s \lessapprox 0.8$, and it is accompanied by an approximate maximization of C_{nn} according to the Fig. 4.13(top). The stacked square lattice shows the largest effect in its isotropic limit, which is the cubic lattice.

Fig. 4.17 shows $\left(\frac{\partial D}{\partial T}\right)_{U,n}$ away from half filling. Cooling here appears at even higher temperature than in the half filled case. This might be utilized to transfer entropy from the region with half filling to less densely occupied regions in the trap. While realistic cooling design was discussed in Refs. [150, 151], we only note that the low density regions show large entropy per particle and thus they may store a large portion of the total entropy. Fig. 4.17 shows that there are no qualitative but only subtle quantitative differences in between the examined lattices with respect to the presence and strength of the cooling phenomenon. As

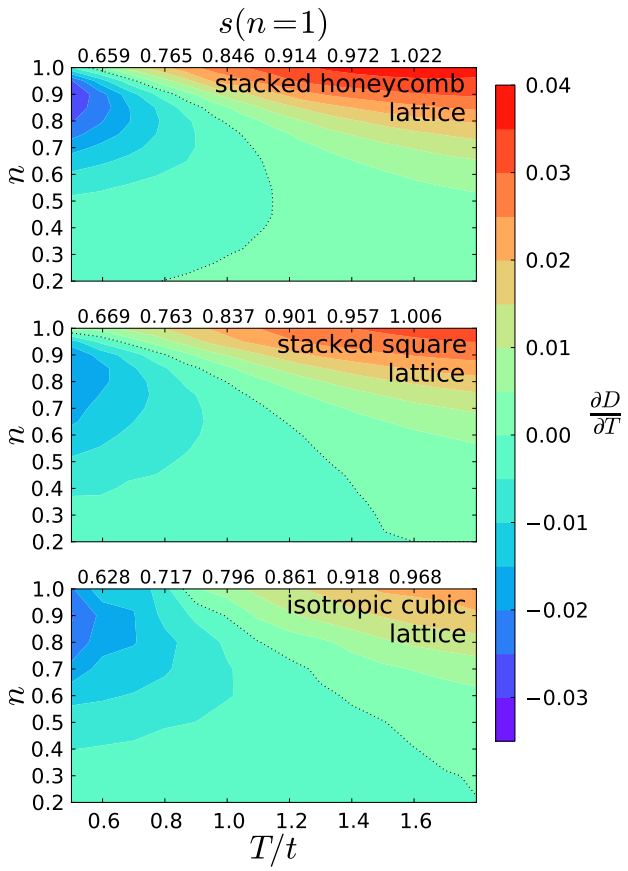

Figure 4.17: Negative values of $\left(\frac{\partial D}{\partial T}\right)_{U,n}$ indicate presence of the effect of adiabatic cooling upon interaction increase. The corresponding quantity is plotted as a function of T and n for the stacked honeycomb (top) and stacked square lattice (middle) at $U/t = 6$ and $t/t' = 6$. For comparison we show the same quantity for isotropic cubic lattice at $U/t = 6$ in the bottom panel, using data from Ref. [102]. The regions of positive and negative $\frac{\partial D}{\partial T}$ are separated by dotted line. For a fair comparison we add upper axis with entropy per site of half filled system, $s(n = 1)$, at temperature given by the temperature axis common to all plots.

the magnitude of $\left(\frac{\partial D}{\partial T}\right)_{U,n}$ does not show great differences among the investigated lattices, the cooling effect is of comparable strength with some enhancement in the case of stacked honeycomb lattice at density near to the half filling.

		stacked square		stacked honeycomb	
t/t'	U/t	T_N/t	s_N	T_N/t	s_N
1	4	0.1955(25)	0.223(18)	0.206(1)	
	6	0.324(2)	0.430(8)	0.292(4)	0.405(35)
	8	0.3595(83)	0.487(23)	0.299(2)	0.33(10)
2	4	0.206(2)	0.313(49)	0.173(4)	
	6	0.293(4)	0.438(39)	0.239(11)	0.28(8)
	8	0.294(8)	0.41(6)	0.205(21)	
4	4	0.200(2)	0.30(7)		
	6	0.245(7)	0.28(11)		
	8	0.219(8)			
8	4	0.185(2)			
	6	0.208(7)			

Table 4.1: Néel temperatures and entropies for both examined stacked lattices. For stacked square lattice we studied wide range of anisotropies as those may be of interest with respect to undoped high-T_c superconductor parent materials. Missing s_N entries indicate that we did not integrate the entropy down to T_N. The isotropic cubic lattice data for $U/t = 4, 8$ is from Ref. [1].

4.5.4 Néel transition

The entropy per particle at the Néel temperature T_N is expected to decrease for large anisotropies, in accordance with the Mermin–Wagner–Hohenberg theorem [143, 144]. We investigate the Néel transition for half filling only. In order to identify the lattice with the largest entropy per site at the Néel transition, s_N, we therefore focused on smaller anisotropies in this part. Since any mean-field theory overestimates ordering, the T_N and s_N for a specific cluster provides an upper bound of the corresponding quantities in the thermodynamic limit. For an unbiased estimate we localize the transition temperature for several clusters and extrapolate the transition temperature T_N as suggested in Ref. [101], using the critical exponent $\nu = 0.71$ for the 3D Heisenberg model [118]. For the stacked square lattice of anisotropy $t/t' = 4$ we managed to obtain the T_N estimate for a cluster with 384 sites. We checked that disregarding data for this largest cluster in the extrapolation, keeping data for clusters only up to 100 sites, changes T_N by about the error estimate. Example of the T_N extrapolation is provided in Fig. 4.8. The entropy s_N is obtained as $s(T_N)$. To its error estimate contribute both uncertainty of T_N and error of the numerical integration of s. T_N and s_N calculated for the different systems studied in this paper are summarized in the Tab. 4.1.

5 Haldane–Hubbard model

We study the interplay of topological band structure and conventional magnetic long-range order in spinful Haldane model with onsite repulsive interaction. Using the DCA with clusters of up to 24 sites we find evidence of a first order phase transition from a Chern insulator at weak coupling to a topologically trivial antiferromagnetic insulator at strong coupling. These results call into question a previously found intermediate state with coexisting topological character and antiferromagnetic long-range order. Experimentally measurable signatures of the first order transition include hysteretic behavior of the double occupancy, single-particle excitation gap and nearest neighbor spin-spin correlations. This first order transition is contrasted with a continuous phase transition from the conventional band insulator to the antiferromagnetic insulator in the ionic Hubbard model on the honeycomb lattice.

The findings described in this chapter were published in [3]. The CT-AUX impurity solver implementation was based on the solver provided by Emanuel Gull. Lei Wang supplied script for computation of the Chern number for a provided topological Hamiltonian H_{topo}.

5.1 Model

The Hamiltonian of the Haldane–Hubbard model reads

$$\begin{aligned} \hat{H} &= -t \sum_{\langle i,j\rangle,\sigma} \hat{c}^{\dagger}_{i\sigma}\hat{c}_{j\sigma} - \mathrm{i}\lambda \sum_{\langle\langle i,j\rangle\rangle,\sigma} v_{ij}\hat{c}^{\dagger}_{i\sigma}\hat{c}_{j\sigma} \\ &\quad + \Delta \sum_{i,\sigma} s_i \hat{n}_{i\sigma} + U \sum_i \left(\hat{n}_{i\uparrow} - \frac{1}{2}\right)\left(\hat{n}_{i\downarrow} - \frac{1}{2}\right), \end{aligned} \tag{5.1}$$

where $\hat{c}^{\dagger}_{i\sigma}$ ($\hat{c}_{i\sigma}$) creates (annihilates) a fermion at site i of the honeycomb lattice with spin $\sigma \in \{\uparrow,\downarrow\}$, $\hat{n}_{i\sigma} \equiv \hat{c}^{\dagger}_{i\sigma}\hat{c}_{i\sigma}$ denotes the occupation number operator, t

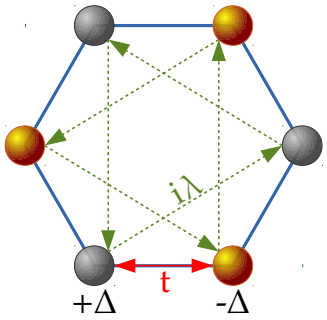

Figure 5.1: As unit cell of the model can be taken the displayed hexagon, with two sites belonging to it. The sketch visualizes all terms of the non-interacting part of the Hamiltonian Eq. 5.1: nearest neighbor hopping t, next nearest neighbor hopping iλ, and staggered potential, which is $+\Delta$ ($-\Delta$) on the sublattice with orange (gray) sites.

is the hopping amplitude between nearest neighbors $\langle i,j\rangle$, and iλ is the purely imaginary hopping between next-nearest-neighbor sites $\langle\langle i,j\rangle\rangle$. $v_{ij} = -1$ $(+1)$ for the hopping from site i to j in (anti-)clock-wise direction with respect to the center of the hexagon, illustrated in Fig. 5.1. The sign s_i is $+1$ on one sublattice of the honeycomb lattice and -1 on the other. The last term is the onsite repulsive interaction with strength $U > 0$. Without loss of generality we assume $\lambda \geq 0$.

The main focus of our study is the half-filled Haldane–Hubbard model with $\lambda \neq 0$ and $\Delta = 0$. Without interactions ($U = 0$), the ground state is a topologically non-trivial Chern insulator (CI) with Chern number 1 for both spin species and a band gap $\min(\sqrt{27}\lambda, t)$. For comparison, we also consider the ionic Hubbard model on the honeycomb lattice with staggered chemical potential $\Delta \neq 0$ and $\lambda = 0$. In this case the non-interacting system also has a finite band gap, determined by Δ, but it is topologically trivial. The full model (5.1) can be experimentally implemented with independent tunability of each term [73, 152].

The Hamiltonian 5.1 conserves the spin projection. Its form is left invariant (up to irrelevant constants) under particle-hole transformation (Subsec. 1.3.6) combined with space inversion (Subsec. 1.3.7),

$$\hat{h}_{\mathbf{r}A\sigma} = \hat{c}^\dagger_{-\mathbf{r}B\sigma}\,, \qquad \hat{h}_{\mathbf{r}B\sigma} = -\hat{c}^\dagger_{-\mathbf{r}A\sigma}\,. \tag{5.2}$$

That ensures half filling for any choice of the real-valued parameters U, Δ, λ, t. Moreover, the coupling to staggered magnetization, $h\sum_{i,\sigma} s_i(1-2\delta_{\sigma\uparrow})\hat{n}_{i\sigma}$, is also left invariant under the transformation, ensuring half filling even in case of emergence of a spontaneous AF order. This property constrains the Green's function as follows,

$$G_{\mathbf{k}\alpha\alpha'\sigma}(i\omega_n) = -s_\alpha s_{\alpha'} G^*_{\mathbf{k}\bar{\alpha}\bar{\alpha}'\sigma}(i\omega_n)\,, \tag{5.3}$$

where α, α' refer to sublattice (as introduced in Subsec. 1.2.2), $\bar{\alpha}$ means the other sublattice as α, s_α has same meaning as s_i (which depends on sublattice only).

The non-interacting dispersion of $\hat{H}$ is linear at the K and K' only for $\Delta = \lambda = 0$; the position of those can be seen in Fig. 5.3(right). The K and K' points remain the points of minimal non-interacting band gap for $\lambda/t \leq 1/\sqrt{27} \approx 0.192$ irrespective of Δ. At the M points (Fig. 5.3) there is the van Hove singularity for $\lambda/t \leq 1/\sqrt{32} \approx 0.177$ also irrespective on Δ. For $\lambda/t > 1/\sqrt{32}$ the M points become local gap minima and for $\lambda/t \leq 1/\sqrt{27}$ they become points of globally minimal non-interacting gap. K and K' points are local minima up to $\lambda/t = 1/\sqrt{18}$ and for larger λ they turn to points of local gap maxima.

5.2 Introduction

The Haldane model [153] describes non-interacting fermions hopping on a honeycomb lattice in a staggered magnetic field. Over the past decade, this prototypical model of a topologically non-trivial bandstructure has inspired numerous developments in the field of topological insulators [154, 155], and has recently been experimentally realized using ultracold fermions in an optical lattice [73]. Because of their high degree of controllability, ultracold atomic gases offer a unique opportunity to investigate the interplay of topological bandstructure and the strong interactions, where one expects a variety of fascinating phenomena [156].

To experimentally investigate the interaction effects on the Haldane model, one loads two-species of ultracold fermionic atoms into an optical lattice and tunes their onsite interaction. However, this Haldane–Hubbard model poses a theoretical challenge. The lack of the time-reversal symmetry gives rise to severe fermion sign problem [41] and limits the use of QMC methods [42]. This is in contrast with the time-reversal symmetric Kane–Mele–Hubbard (KMH) model, in which the two spin species experience opposite magnetic flux. The KMH model thus allows sign-problem free QMC simulations at half filling that show a continuous phase transition from the quantum spin Hall insulator into an antiferromagnetic insulator (AFI) as the interaction strength increases [157, 158, 159].

Similarly, in the Haldane–Hubbard model the local onsite interaction favors an AFI in the strong coupling regime [160, 161], which competes with the Chern insulating state at weak coupling. To find out how the two limiting cases are connected requires a non-perturbative treatment. Being hard to tackle, some of the previous studies used static mean-field approximations [162, 163, 164, 165, 166]. All these studies reported an additional phase with coexisting antiferromagnetic long-range order and non-trivial topological character at intermediate interaction strengths. This topologically non-trivial AFI state has a clear mean-field picture: in the vicinity of a putative second order quantum phase transition to the AFI,

the antiferromagnetic order parameter increases continuously so that there is a finite region where the topological band gap persists despite of the counteracting topologically trivial band gap due to the magnetic order. However, given the approximate nature of the static mean-field treatment, it is hard to assess whether this intermediate state really exists.

In this paper we study the ground state phase diagram of the Haldane–Hubbard model using the DCA. By using clusters embedded in a self-consistently determined bath, both short-range correlations within the cluster and long-range correlations are captured. Solving embedded cluster with up to 24 sites at low temperature we can go beyond static mean-field and exact diagonalization treatments. Our main result is a *first order* phase transition from a topologically non-trivial band insulating state to a magnetic long-range ordered state, preempting the intermediate "topological AFI" state. Observables such as the antiferromagnetic magnetization, double occupancy, all exhibit hysteretic behavior around the transition point, which are clear signatures of the first order phase transition [167].

5.3 Numerical simulation

To map out the ground state phase diagram of Eq. 5.1 using the DCA method, we solve a quantum impurity problem embedded selfconsistently into a bath using continuous-time auxiliary-field QMC method with sub-matrix updates. [39, 109] Details of the DCA method for multisite unit cells are described in Sec. 2.4. For most of this study we use the cluster shown in Fig. 5.3(left), which respects the three-fold rotational symmetry of the honeycomb lattice. Its reciprocal representation displayed in Fig. 5.3(right) contains all the high symmetry reciprocal lattice points of our model. We used smaller clusters, Fig. 5.4, to address differences found with respect to competing studies. These as well respect the three-fold rotational symmetry, but one of them contains the points Γ, K, K', while the other cluster contains $\Gamma, M_{1,2,3}$.

For $\lambda = 0$ and $\Delta = 0$, the model reduces to the honeycomb lattice Hubbard model where sign-problem free QMC simulations have shown a continuous phase transition from a Dirac semi-metal to an AFI [139, 140]. However, the model suffers from a sign problem [41, 42] for $\lambda \neq 0$ or $\Delta \neq 0$. Even though the sign problem is mitigated in the DCA approach compared to lattice QMC simulations, it still limits the accessible cluster size, temperature, and parameter ranges of λ or Δ. We perform simulations at a temperature $T/t = 1/16$, which corresponds to the bulk non-interacting gap of the Haldane model at $\lambda/t \approx 0.012$. This temperature is below all relevant energy scales and should thus exhibit ground state behavior of the model. The sign problem limits the accessible range of λ for the chosen cluster and temperature to $\lambda/t \leq 0.15$, which nevertheless lies in the experimentally

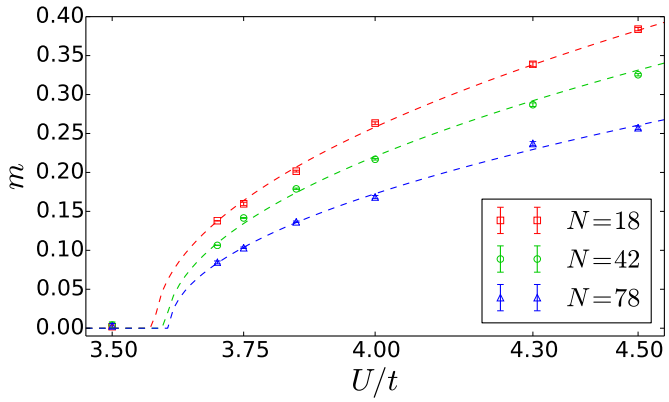

Figure 5.2: Staggered magnetization of the Hubbard model on the honeycomb lattice at half filling obtained by a DCA simulation performed with clusters with $N = 18$, 42, and 78 sites at $\beta t = 20$. The dashed lines are fits using mean-field exponent $\beta_{\mathrm{mf}} = 0.5$. All clusters were three-fold rotationally symmetric and all of them contained the K and K' point in their representation.

relevant region [73].

While the investigated two-dimensional model cannot spontaneously break the continuous symmetry at non-zero temperature [143, 144], the DCA solution at a low but non-zero temperature T may still develop magnetic long-range order as DCA treats long-range correlations in a mean-field fashion. Such ordered solution should be thought of as a DCA approximation of the ground state. By systematically increasing the cluster size the DCA result then becomes increasingly accurate.

For better understanding of this peculiar situation we provide data for the Hubbard model on the honeycomb lattice in Fig. 5.2. One clear feature in the plot is that all magnetization curves follow the mean-field critical behavior – thus these cannot be fully trusted in the ordered region. Secondly, we see that the magnetization value decreased for a fixed parameter set with growing cluster size N, consistent with vanishing magnetization at any $T > 0$ for $N \to \infty$.[1]

For $\lambda \neq 0$ the sign s becomes complex number of unit magnitude. Its average is purely real, as $\langle s \rangle = Z/\tilde{Z}$, where Z is the partition function of the studied system (real for hermitian $\hat{H}$, see Subsec. 1.3.2), and $\tilde{Z}$ is a sum of magnitudes of the sampled weights, *i.e.* it is positive. For an observable o which is purely real on a physical ground,[2] it is therefore sufficient to accumulate $\Re(o\, s)$, and at the end of

[1] In the ordered phase, m only weakly grows with β for given cluster at fixed U. For $N = 42$ at $U = 3.75t$ we find $m(\beta t = 20.0) = 0.1328 \pm 0.0004$, $m(\beta t = 30.55) = 0.1412 \pm 0.0003$, $m(\beta t = 46.67) = 0.1450 \pm 0.0004$.

[2] For example, density or instantaneous density-density correlations are guaranteed to be real;

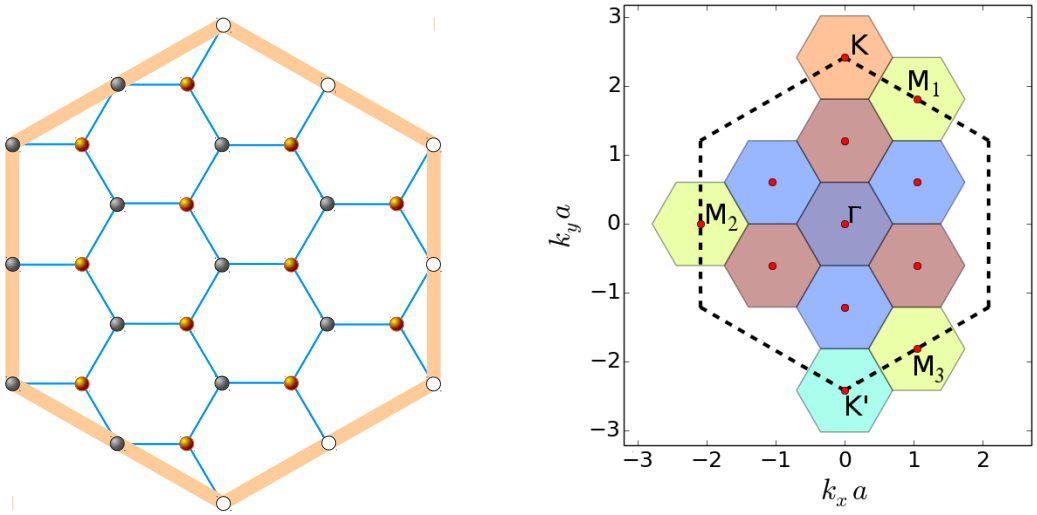

Figure 5.3: Left: The embedded cluster with 24 sites used to obtain the phase diagram. White sites on the border correspond via periodic boundary conditions to gray sites on the opposite border. Right: The DCA patches in the reciprocal space for the same 24-site cluster used throughout the study. The number of DCA patches, 12, equals to the number of unit cells contained by the cluster. The Brillouin zone of the lattice is the interior of the dashed hexagon. All high symmetry points of the Brillouin zone, Γ, K, K', and the three "time-reversal symmetric" points M_i, are located at a patch center. The nearest neighbor distance of sites in real space is denoted by a.

the simulation evaluate (*e.g.* by use of Jackknife analysis of binned decorrelated data) $\langle \Re(o\, s)\rangle \,/\, \langle \Re\, s\rangle$. For complex observable o, *e.g.* $M_{\mathbf{\Delta}\alpha_3\alpha_4\sigma}(i\omega_n)$ (Eq. B.18) that is used for evaluation of the Green's functions, we performed the Jackknife analysis of $\langle o\, s\rangle \,/\, \langle s\rangle$.

see Subsec. 1.3.2.

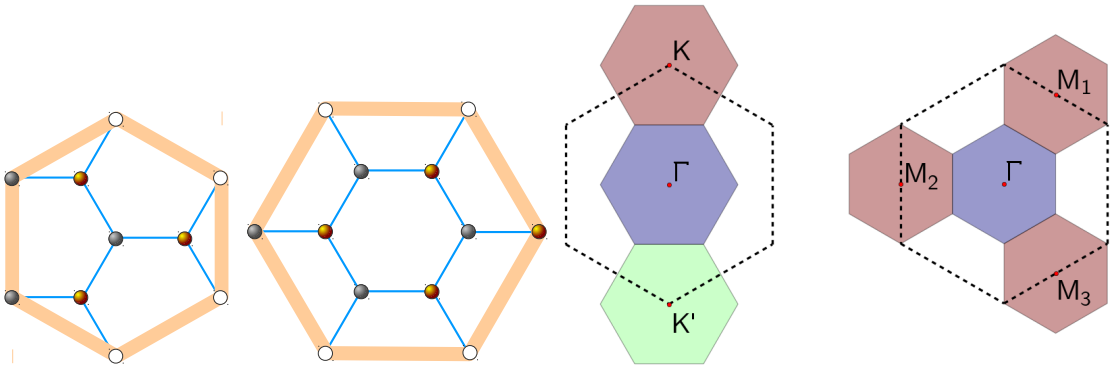

Figure 5.4: Smaller clusters with 3 and 4 cells shown in the real space (left) and reciprocal (right) representation.

5.4 Observables

5.4.1 Staggered magnetization

To characterize the magnetic property of the system we measure the staggered magnetization in the cluster,

$$m = \frac{1}{N} \left\langle \sum_i s_i (\hat{n}_{i\uparrow} - \hat{n}_{i\downarrow}) \right\rangle , \tag{5.4}$$

with $N = L\ell$ being the number of sites of the cluster. As explained in Subsec. 3.4.1, the density and thus as well the (staggered) magnetization can be measured directly on the impurity, while being the corresponding DCA lattice quantity. In Subsec. 4.4.1 we explained that if we are interested in the value of critical U (or β), we may utilize the susceptibility measurement. For this study we did not use that, as we were interested in the phase entered after the magnetic transition.

5.4.2 Estimate of the physical single-particle gap

Metalicity estimate

For a qualitative estimate of the physical single-particle gap Δ_{sp}, *i.e.* in order to distinguish gapped system from a metalic one, the estimate of the local density of states at the Fermi level, $\rho(0)$, may be used,

$$-\frac{1}{\pi} \lim_{\beta\to\infty} \beta \underbrace{\frac{1}{2L\ell} \sum_{\alpha,\mathbf{K},\sigma} G_{\alpha\alpha,\sigma}(\mathbf{K}, \tau = \beta/2)}_{G_{\text{local}}(\tau=\beta/2)} = A(\omega = 0; T = 0)\,. \tag{5.5}$$

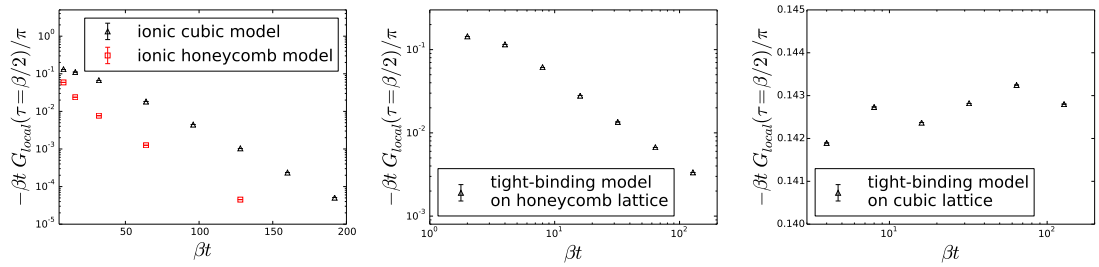

Figure 5.5: Behavior of the estimator for the density of states at the Fermi level, Eq. 5.5, tested on various non-interacting systems at half filling. Left: The gapped ionic models with staggered potential $\Delta = 0.1t$ ($\Delta_{\mathrm{sp}} = \Delta$) show exponential suppression of the estimator with growing β for $\beta\Delta \gg 1$. Since the DOS of the ionic cubic model diverges at the band gap edges as $\frac{1}{\varepsilon \pm \Delta}$, the exponential regime is entered at larger β when compared to the ionic honeycomb model with finite DOS at the band gap edges. Center: the semimetalic system shows decay proportional to β^{-1}, consistent with analytical result obtained with Sommerfeld expansion. Right: a metalic system with almost β-independent values of the estimator. Notice that for precise results it is needed to scale both the Matsubara frequency cut-off N_ω and the discretization of the Brillouin zone with β.

Tests on non-interacting models are shown in Fig. 5.5.

Another option is to perform simulation at fixed β and vary the chemical potential μ. The slope of density taken as a function of μ serves then as estimator of the spectral function $A(\omega = \mu; \beta)$. Fig. 5.6 illustrates the difficulty to distinguish a semimetalic system (center plot) from a system with small gap (left plot).

Gap value estimates

The single particle gap Δ_{sp} is obtained from the imaginary time lattice Green's function at chosen $\mathbf{k}$, $G^{\mathrm{lat}}(\mathbf{k}, \tau)$, by fitting to

$$f(\tau; A, \tau_c, \Delta_{\mathrm{sp}}) = A \cosh\left[\Delta_{\mathrm{sp}}(\tau - \tau_c)\right] \tag{5.6}$$

near $\tau = \beta/2$ with fit parameters A, τ_c, Δ_{sp}. In particular, we optimized

$$\chi^2(A, \tau_c, \Delta_{\mathrm{sp}}) = \int_0^\beta \mathrm{d}\tau \, \left(f(\tau; A, \tau_c, \Delta_{\mathrm{sp}}) - G^{\mathrm{lat}}(\mathbf{k}, \tau)\right)^2 e^{-(\tau-\beta/2)^2/\sigma^2}, \tag{5.7}$$

typically with $\sigma = \beta/10$. The fit may also be applied to local Green's function. In such a case the Green's function is symmetric in τ around $\beta/2$ for particle-hole symmetric models, see Subsec. 1.3.6, and we may set $\tau_c = \beta/2$.

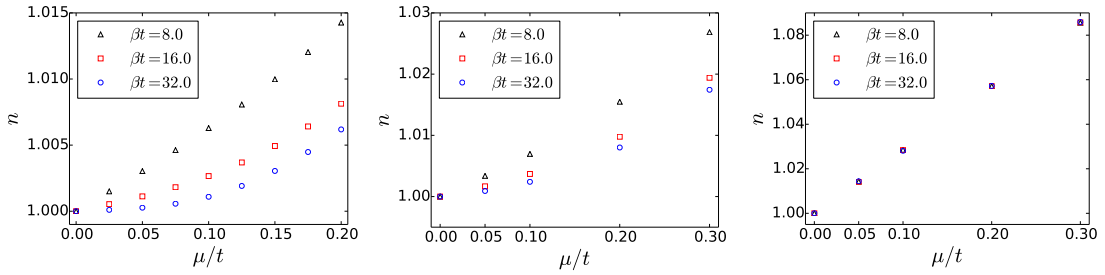

Figure 5.6: Behavior of the density as a function of chemical potential μ, tested on non-interacting systems close to half filling at various temperatures. Left: The gapped ionic model on honeycomb lattice with staggered potential $\Delta = 0.1t$ ($\Delta_{\mathrm{sp}} = \Delta$) shows exponential suppression of increase of n with β inside of the gap, where $n(\mu;\beta) \approx n(\mu = 0;\beta \to \infty) + \frac{c}{\beta^2} e^{-\beta\Delta} \sinh(\beta\mu)$ with a constant c. Center: the semimetalic system shows $n(\mu;\beta) \approx n(\mu = 0;\beta \to \infty) + c\left(\frac{\pi^2}{6\beta^2} + \frac{\mu^2}{2}\right) \mathrm{sign}(\mu)$ (Sommerfeld expansion). Right: a metalic system with almost β-independent results and n linear in μ.

To motivate the fitting form given in Eq. 5.6, we first consider the case of symmetric $G(\tau) = G(\beta - \tau)$, in which case a good way to extract the gap is via curvature of the Green's function at $\tau = \beta/2$,

$$\Delta_{\mathrm{sp}} \approx \sqrt{G^{-1}(\beta/2) \left.\frac{\mathrm{d}^2 G(\tau)}{\mathrm{d}\tau^2}\right|_{\tau=\beta/2}} \,. \tag{5.8}$$

However, in general, the examined Green's function may be asymmetric in τ,[3] in which case it is appropriate to fit $G(\tau)$ with an exponential decay $Ae^{-\Delta_{\mathrm{sp}}\tau}$ around $\tau = \beta/2$. The form of our fit comprises both needs in a single form.[4] Tests on non-interacting models are presented in Fig. 5.7.

A completely different approach for the gap estimate is the extraction of the spectral function $A(\mathbf{k},\omega;\beta)$ from the Green's function,

$$G(\mathbf{k},\tau;\beta) = -\int \mathrm{d}\omega A(\mathbf{k},\omega;\beta) \frac{e^{-\tau\omega}}{1+e^{-\beta\omega}} \,, \tag{5.9}$$

which is a numerically ill-posed task. A technique based on Bayesian statistics, in the context of QMC simulations commonly referred to as the "maximum entropy

[3] That is for instance the case for the local Green's function of the ionic models with staggered potential ($\Delta \neq 0$).

[4] The form of the fit is precisely the form of the Green's function $G_{11}(\tau)$ for $\hat{H} = -t(\hat{c}_1^\dagger \hat{c}_2 + \hat{c}_2^\dagger \hat{c}_1)$ with single-particle state eigenvalues equal to $\pm t$. With $\mu = 0$, the gap is $\Delta_{\mathrm{sp}} = t$.

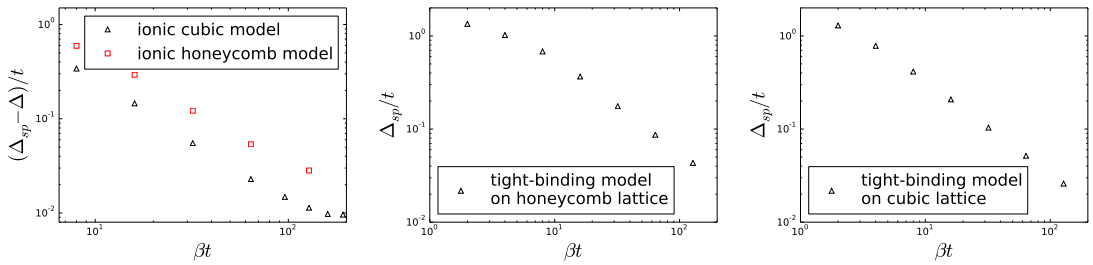

Figure 5.7: Gap estimates Δ_{sp} obtained via fitting of the local Green's function to form in Eq. 5.6 for different non-interacting models at half filling plotted as a function of β. Left: The gap of ionic models with staggered potential $\Delta = 0.1t$ approaches Δ for $\beta \to \infty$ roughly as β^{-1}. The decay is more rapid for the ionic cubic model due to diverging DOS at band gap edges. Center: the semimetal has vanishing gap, the decay is proportional to β^{-1}. Right: a (gapless) metal with decay β^{-1}.

method" [168], may be applied to the inversion of Eq. 5.9.[5] Fig. 5.8 displays ambiguity of the outcome depending on the choice of the initial model entering the Bayesian approach. We did not feel confident about results postprocessed with this technique, therefore we did not make use of this technique any further.

5.4.3 Chern number measurement

To reveal the topological nature of the phase we compute the Chern number, using the topological Hamiltonian of Ref. [170],

$$H_{\mathrm{topo}}(\mathbf{k}) \equiv -G^{-1}(i\omega = 0, \mathbf{k}) = H_0(\mathbf{k}) + \Sigma(i\omega = 0, \mathbf{k})\,, \tag{5.10}$$

where $H_0(\mathbf{k})$ is the non-interacting part of the Hamiltonian 5.1. Notice that $H_{\mathrm{topo}}(\mathbf{k})$ is a hermitian matrix in the sublattice indices thanks to the property of the Green's function, Eq. 1.41, ensuring hermiticity of $G(i\omega = 0, \mathbf{k})$. We obtain $\Sigma(i\omega = 0, \mathbf{K})$ by a cubic spline interpolation over 40 lowest (positive and negative) Matsubara frequency self energies $\Sigma(i\omega_n, \mathbf{K})$. In the DCA, the lattice self energy $\Sigma(\mathbf{k})$ is approximated by the impurity self energy $\Sigma(\mathbf{K})$ at the closest cluster momentum $\mathbf{K}$, *i.e.* it is a patch-wise constant function in reciprocal space. The Chern number calculation utilizing H_{topo} is performed by discretization of the Brillouin zone as in Ref. [171]. The results are robust with respect to different Brillouin zone

[5] The method can be applied straightforwardly if $G(\mathbf{k}, \tau)$ is purely real and negative, which is the case provided the Hamiltonian is hermitian and time-independent and the lattice is a Bravais lattice (Eq. 1.37).

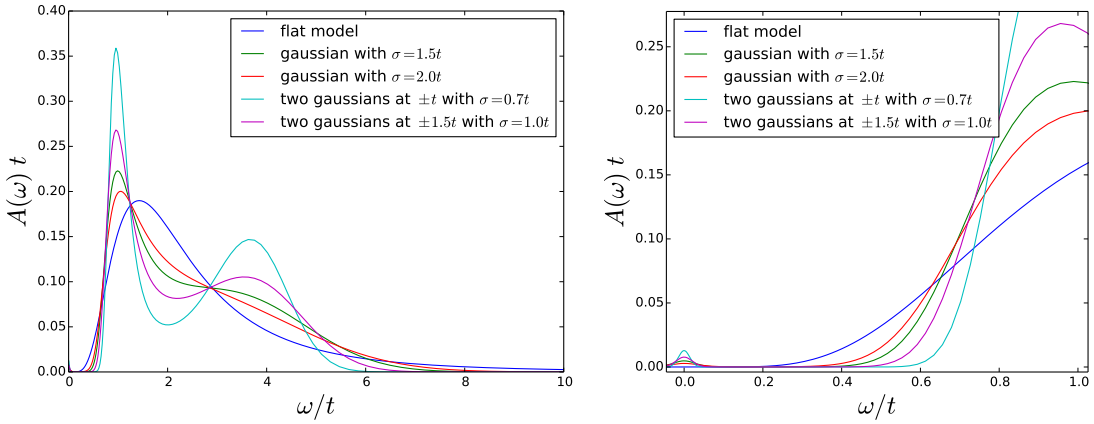

Figure 5.8: Spectral function $A(\omega)$ obtained with maximum entropy method using the local Green's function obtained in a DCA simulation of Hubbard model on the honeycomb lattice at $U = 5t$, $\beta t = 20$, at half filling, simulated with a cluster consisting of 42 sites. Each solution has in the legend specified the initial model of the spectral function. Right plot is a zoom in of the left plot at low ω. Only the solution for flat initial model does not show the little peak at $\omega = 0$. We plot $A(\omega)$ only for positive energies ω as it is symmetric for the investigated particle-hole symmetric model. The simulation was forced to be in the paramagnetic phase by symmetrization of the Green's functionsn. We used the maximum entropy implementation in ALPS [169].

discretization meshes. In addition we checked robustness of the results with respect to interpolation of the self energy in reciprocal space using natural neighbor interpolation.

The Chern number, being a topological invariant, may change only if the topological gap, *i.e.* the band gap of $H_{\text{topo}}(\mathbf{k})$, closes. This topological gap can be obtained by diagonalization of $H_{\text{topo}}(\mathbf{k})$. We checked that consistent results can be at the cluster $\mathbf{K}$ points obtained via (quadratic) extrapolation of the gap of $-\frac{1}{2}\left[G^{\text{lat}}(i\omega_n,\mathbf{K})^{-1} + \left(G^{\text{lat}}(i\omega_n,\mathbf{K})^{-1}\right)^{+}\right]$ for $n = 0, 1, 2$ to $i\omega = 0$. We find that for all examined values of λ, *i.e.* for $\lambda/t \leq 0.15$, the topological gap closes at the K and K' point,[6] while the single particle gap Δ_{sp} of the physical Hamiltonian (5.1) remains finite.

[6]In case of the discontinuities, the topological gap closes during the run of the selfconsistency, for a non-converged iteration.

5.5 Results

We first present the phase diagram of the Haldane–Hubbard model in Subsec. 5.5.1 with detailed analysis of the numerical data in different parameter regions in its subsubsections. Then we compare the phase diagram with the one of the ionic Hubbard model on honeycomb lattice in Subsec. 5.5.2. Finally we compare our results with recent quantum cluster studies employing smaller clusters [172, 173] in Subsec. 5.5.3.

5.5.1 Phase diagram

Figure. 5.9 shows our phase diagram of the Haldane–Hubbard model. For $\lambda/t \geq 0.075$, we find clear evidence of a first order transition from the CI to the topologically trivial AFI shown by the black solid line. This phase boundary is not extrapolated in cluster size. To assess the systematic error, we consider the $\lambda = 0$ limit where the model reduces to the honeycomb lattice Hubbard model where unbiased QMC methods predict a critical interaction to lie between $3.78t$ and $3.9t$ [139, 140]. The unextrapolated value $U_{\mathrm{HH}}(\lambda = 0)/t = 3.575 \pm 0.075$ based on our 24-site cluster underestimates this value by about $0.3t$, as the DCA transition occurs when the correlation length reaches the order of the cluster size. This difference provides an estimate of the systematic error. At the first order transition the systematic error is expected to be smaller. For $\lambda/t \leq 0.05$ DCA with 24-site cluster is consitent with a continuous phase transition with intermediate topological AFI. However we believe this to be due to insufficiently large cluster and that using larger clusters will again lead a first order transition.

First order transition for $\lambda/t \geq 0.075$

Figure 5.10 shows the staggered magnetization as a function of U/t for various values of λ. Noticeably, m shows a discontinuity for $\lambda/t \geq 0.075$, accompanied by hysteretic behavior. The simulation can converge to two different solutions depending on the initial bare cluster Green's function provided to the self-consistency loop. This provides a clear signature of a first order phase transition at $\lambda/t \geq 0.075$. In order to distinguish between slow convergence of the self-consistency procedure and (meta)stable solutions we perform about one to two hundred iterations.

Around the first order transition other observables also exhibit hysteretic behavior, as shown in Fig. 5.11. The two curves in each panel are obtained with self-consistent iterations either started from the CI or from the AFI state. Hysteresis behavior in these physical observables can also be measured experimentally

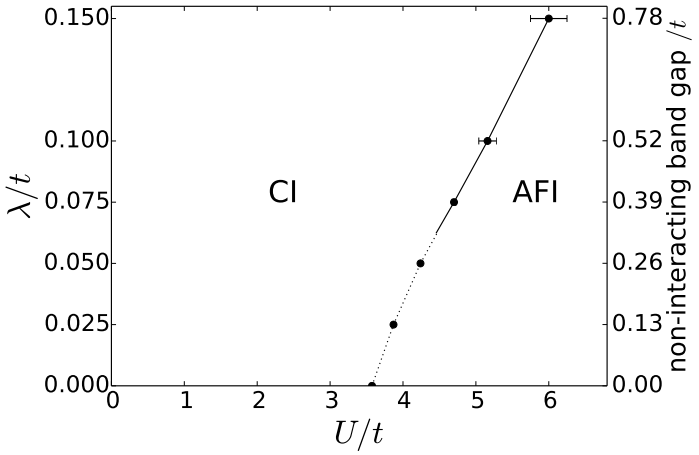

Figure 5.9: The phase diagram of the Haldane–Hubbard model on honeycomb lattice based on simulation at $T/t = 1/16$ using the 24-site cluster. The solid line is a first order phase transition in the Haldane–Hubbard model from the CI to the AFI. On the dotted line we do not have confidence about the character of the transition even though we observe continuous phase transition (see text for discussions). The error bars of the data points indicate the range of the hysteresis. The right vertical axis shows the size of the non-interacting band gap, $\sqrt{27}\lambda$.

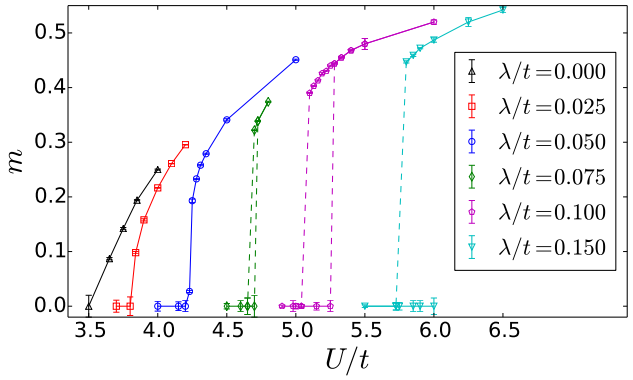

Figure 5.10: The staggered magnetization as a function of U/t for different λ/t obtained for a 24-site cluster at $T/t = 1/16$. The dashed lines indicate a discontinuity of the staggered magnetization, and the region between the dashed lines indicates the hysteretic region where it is possible to converge to either a paramagnetic or an antiferromagnetically ordered solution. The hysteresis is visible for $\lambda/t = 0.075$, 0.1, 0.15. For $\lambda = 0.15t$ we do not provide the upper bound for stability of the paramagnetic phase due to a too large sign problem.

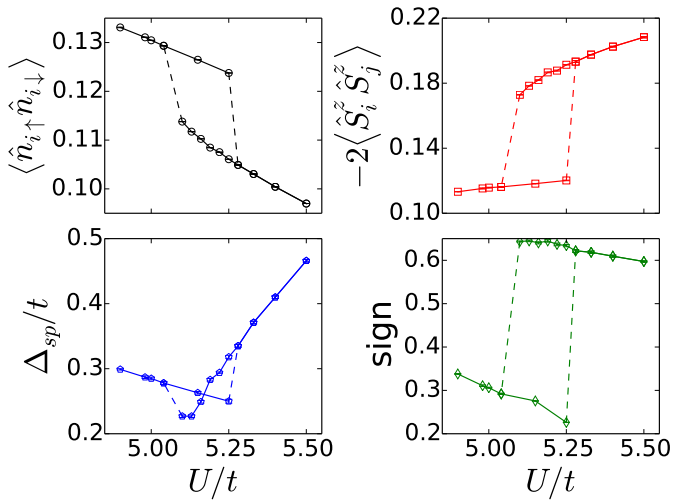

Figure 5.11: Double occupancy $\langle \hat{n}_{i\uparrow}\hat{n}_{i\downarrow} \rangle$, nearest neighbor spin-spin correlation function $-2\left\langle \hat{S}_i^z \hat{S}_j^z \right\rangle$, single particle gap Δ_{sp}, and the average sign in the simulation are shown as a function of U at $\lambda/t = 0.1$. The dashed line segments show the discontinuity at the first order phase transition.

as a signature of a first order phase transition. Note that in this case the temperature $T/t = 1/16$ is for all values of U at least four times smaller than the single particle gap, and thus low enough to capture ground state behavior. The average sign of the impurity solver is also notably different in the two phases and exhibits a jump at the transition point. The Chern number (not plotted) equals to 1 for the non-magnetic solutions and to 0 for the magnetic solutions.

This clear evidence of a first order phase transition is different than the continuous phase transition transition found in the static mean-field [162, 163, 164, 165, 166] and two-site cellular DMFT (CDMFT) studies [172]. Since our DCA calculation on a 24-site cluster incorporates short-range correlation effects and we can reproduce some of the continuous transition character by using small clusters (see Sec. 5.5.3), we believe the first order transition found in the Haldane–Hubbard model is real.

Phase transition for $\lambda/t < 0.075$

For $\lambda/t \leq 0.05$, we find a continuous increase of the staggered magnetization, as shown in Fig. 5.10. As a consequence of the smooth increase of the magnetic order parameter, an intermediate topologically non-trivial AFI appears in between the CI for low U and the AFI for large U. The simulation results at $\lambda/t = 0.025$ are depicted in terms of the topological gap at the K point, the staggered

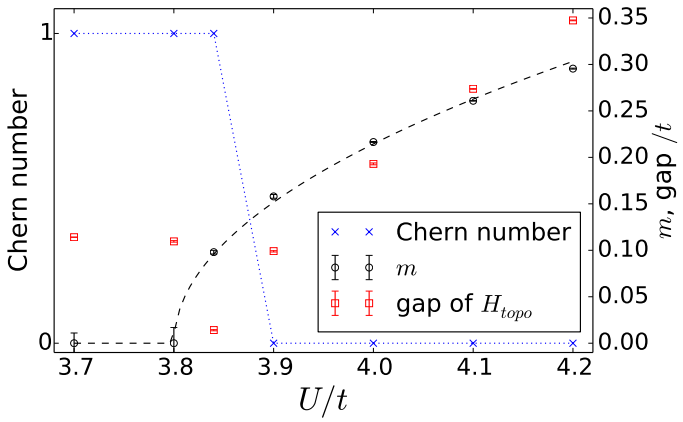

Figure 5.12: The staggered magnetization and the topological gap at the K point as a function of U/t for $\lambda/t = 0.025$. The fit of the staggered magnetization in range $U/t \in [3.7, 4.1]$ uses the mean-field critical exponent $\beta_{\text{mf}} = 0.5$. The Chern numbers of the occupied bands drop in between $3.84 < U/t < 3.9$, consistent with closing of the gap of H_{topo} in the same range. The dotted line is a guide for eye.

magnetization m, and the Chern number as a function of U in Fig. 5.12. The Chern number drops from 1 to 0 inside the magnetic ordered phase. The same scenario is found at $\lambda/t = 0.05$.

Even though our DCA results are consistent with an intermediate topological AFI state in a small portion of the parameter space, the data is also consistent with the scenario of a first order phase transition for any non-zero λ, and a diverging correlation length as $\lambda \to 0$. In this scenario, the correlation length at the first order transition remains finite at any non-zero λ, but is larger than the 24-site cluster employed here, thus resulting in an apparent continuous phase transition for $\lambda/t \leq 0.05$ region. Larger clusters would thus be required to resolve the phase transition character in the small λ region, but are intractable because of the sign problem.

Finally, for $\lambda = 0$, the model reduces to the Hubbard model on the honeycomb lattice, where there is a firm evidence that the model undergoes a direct second order phase transition from the paramagnetic semimetal to the AFI [139, 140]. A DCA study of that model predicts in agreement with the latter studies the direct second order phase transition [174].[7] In the vicinity of a second order phase

[7]The DCA study [174] by Wu and Tremblay utilized as the impurity solver a determinantal QMC, for which the bath needed to be discretized and fitted. Their bath consisted of about 200 sites. We tried to reproduce their results using CT-AUX impurity solver working with effective action and thus without need of bath discretization. We found discrepancy in results for the 24-site cluster (Fig. 5.3) shown in their Fig. 6a, where we see the change of low frequency behavior

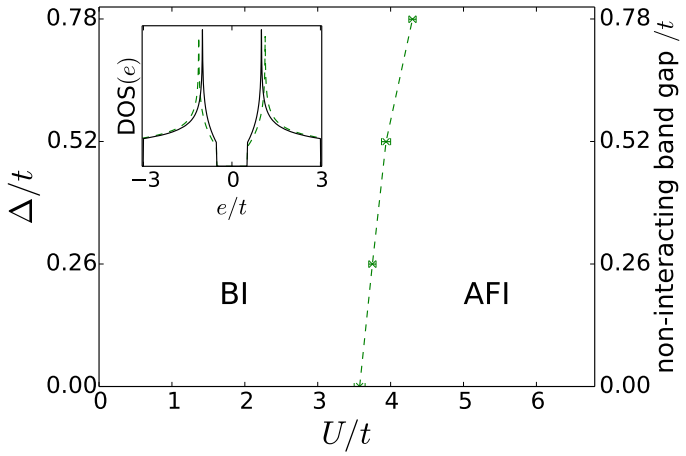

Figure 5.13: The phase diagram of the ionic Hubbard model on the honeycomb lattice based on simulation at $T/t = 1/16$. The dashed line denotes the critical interaction strength U_{IH} of a second order phase transition from a band insulator to an AFI. The error bars show the bounds for the onset of ordering for a 24-site cluster. The inset shows the density of states of the non-interacting Haldane model at $\lambda/t = 0.1$ as a solid black line, and that of the non-interacting ionic model for $\Delta = 0.52t$ as a dashed green line. Both models have a band gap of $0.52t$.

transition the correlation length extends the cluster size and then the mean-field behavior appears in the DCA solution.

As the sign problem is reduced at small λ, at $\lambda/t = 0.025, 0.05$ we could perform simulations with a larger cluster with 72 sites, at the same temperature $T = t/16$. That possessed the three-fold rotational symmetry and contained all high symmetry reciprocal points (Γ, K, K', M_i). We searched for traces of hysteresis in m, but we did not find any.

5.5.2 Comparison with ionic Hubbard model on honeycomb lattice

To further reveal role of the topological band gap, we compare the phase diagram of the Haldane–Hubbard model with that of the ionic Hubbard model on honeycomb lattice. The latter model is defined by $\lambda = 0$ and a staggered sublattice potential $\pm\Delta$, which opens a topologically trivial band gap. The non-interacting dispersion of the Haldane and the ionic models are similar if the non-interacting band gaps

of the self energy between $U = 4.5t$ and $U = 5t$, whereas Wu and Tremblay find it in range $4.2 < U/t < 4.4$. This difference may be due to insufficient number of discrete bath states they used.

are adjusted to match each other. The density of states for both models with non-interacting band gap $0.52t$ is shown in the inset of Fig. 5.13.[8] Thus, in a crude theoretical treatment which only cares about the band gap or density of states, these two models should have similar phase diagrams. However, the phase diagram of the ionic honeycomb model shown in Fig. 5.13 differs substantially from that of the Haldane–Hubbard model in Fig. 5.9. The dependence of the critical interaction strength on the non-interacting band gap in the ionic model is weaker than in the Haldane–Hubbard model. More importantly, the character of the transition is second order in the ionic Hubbard model for all simulated parameters.

While the ionic Hubbard model on the square lattice exhibits an intermediate metallic phase between the ionic band insulator (BI) and AFI [175, 176, 177], our simulations find no indication of such phase on the honeycomb lattice.[9] A reason for this difference may be different position of the van Hove singularities, which are at the band edges for the square lattice, but not for the honeycomb lattice. A similar observation was made in Ref. [178]. A charge imbalance due to the staggered sublattice potential Δ is present both in the BI and in the AFI.

5.5.3 Comparison with recent small cluster calculations

Both static mean-field calculations [162, 163, 164, 165, 166] and CDMFT on 2-site clusters [172] predict a continuous phase transition from CI to the AFI, with an intermediate topologically non-trivial AFI phase for a wide range of λ. Our Hartree approximation results are in Fig. 5.14. Also results of a variational cluster approximation calculation on 6-site clusters [172, 173] indicate an indirect transition from CI to AFI, but via a topologically non-trivial non-magnetic insulating phase with opposite Chern number as the CI. Another recent study using 6-site DCA and CDMFT calculations [179] reports, similar to our findings, a signature of a first order transition for $\lambda/t = 0.2$. Since all studies mentioned above employ quantum cluster approaches of a similar nature, these discrepancies may either be due to insufficiently large clusters or due to subtleties in the cluster embeddings which break the spatial symmetries [180, 181].

[8] The largest difference between the non-interacting dispersions of the two compared models is at the M points, $\sqrt{t^2 - 27\lambda^2} - t$, where this is the shift of the van Hove peaks in the non-interacting density of states.

[9] For that we focused on $\Delta = 0.52t$. We performed simulations at $\beta t = 8.0$, 11.3, 16.0, 22.6, 32.0, which we used for the DOS estimate (Eq. 5.5) and gap fitting. In addition we simulated at $\beta t = 16.0$ two larger clusters, of 42 and 72 sites, to get the dependence on cluster size. Using the 24-site cluster at $\beta t = 16$ we scanned the density away from half-filling. For $U/t = 3.4$, 3.6, 3.75 ($U^*(\Delta = 0.52t)/t = 3.94 \pm 0.06$) we found vanishing DOS at the Fermi level. The gap estimate after extrapolation in cluster size and β is $0.12t$, $0.10t$, and $0.09t$ for $U/t = 3.4$, 3.6, and 3.75, resp. The cluster size dependence is stronger here than the temperature dependence.

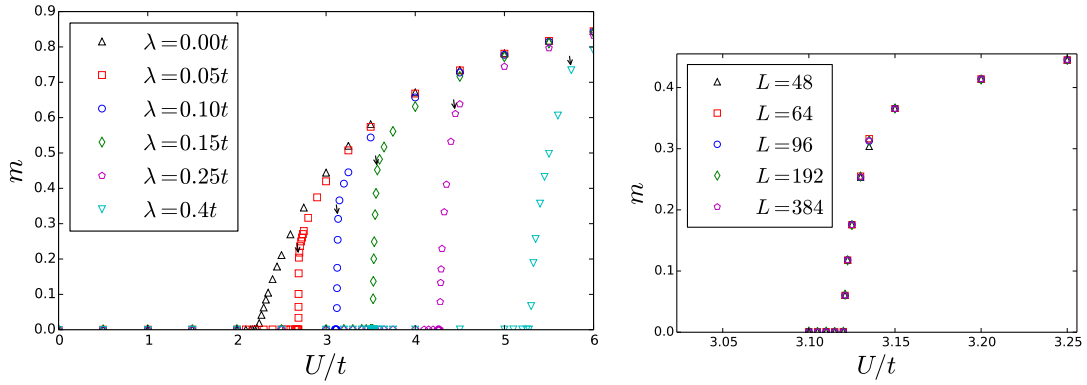

Figure 5.14: The staggered magnetization of the Haldane–Hubbard model obtained using Hartree approximation at zero temperature. Left: m shown for various λ, computed with a mesh of L^2 points in the Brillouin zone, $L = 192$. For $\lambda \neq 0$, the small arrows show U/t with vanishing gap Δ_{sp}, which in the Hartree approximation is the same as the topological gap. Thus the arrows show the location of the topological transition from the topological AFI to the topologically trivial AFI. Apparent is the steepening of the magnetization onset for small λ, but all curves remain continuousa and no first order transition with a discontinuity is found within the Hartree approximation. Right: Discretization mesh effect on m is negligible for $L \geq 96$ at $\lambda = 0.1t$.

To shed light on this issue we examined the Haldane–Hubbard model using two additional clusters of different size, shown in Fig. 5.4. The 6-site cluster contains the K and K' point in its reciprocal representation, while the 8-site cluster does not. Both of them respect the three-fold rotational symmetry. The staggered magnetization obtained using these clusters at $\lambda/t = 0.1$ are shown in Fig. 5.15. The 6-site cluster displays similar hysteresis as observed above for the 24-site cluster,[10] with a difference in transition point U/t of at most 0.1. The value of m in the ordered phase is larger than for the 24-site cluster, which is expected, as DCA becomes exact for $N \to \infty$ and m has to vanish in the thermodynamic limit at $T \neq 0$. In contrast, using the 8-site cluster we observe a sharp but continuous increase of m at a strongly shifted transition point $U_{\mathrm{HH}}/t = 5.40 \pm 0.03$ for $\lambda/t = 0.1$, without any trace of hysteresis. These findings are similar to those obtained for Haldane model of spinless fermions [182, 183, 184], where Varney *et al.* using exact diagonalization, observed first order or continuous transition depending on the presence of the K and K' points in the cluster reciprocal representation. Our findings in DCA support their conclusion that the choice of the cluster is

[10] We performed simulation utilizing the 6-site cluster as well for $\lambda = 0.075t$, where we found tiny hysteresis, at same U as for the 24-site cluster.

significant and that reliable clusters need to contain the K and K' points. That hints as well on the importance of preserving translational invariance at all levels of the applied method.

Examining the model within the single-site DMFT yields further insight. For this we simulate single site from in sublattice A. The form of the **k**-independent DMFT self energy for a single unit cell (containing two sites) is obtained only from the self energy of the simulated site. Its form has to respect the symmetry Eq. 5.2 of the studied Hamiltonian 5.1. The DMFT self energy is approximated by

$$\Sigma_\sigma(i\omega_n) = \begin{pmatrix} \Sigma_{AA\sigma}(i\omega_n) & 0 \\ 0 & -\Sigma^*_{AA\sigma}(i\omega_n) \end{pmatrix} , \tag{5.11}$$

neglecting the off-diagonal components, motivated by the dominantly local character of the self energy for a Hubbard interaction, see Subsec. A.4.3.[11] The DMFT mapping is conveniently formulated with 2×2 matrices, comprising the sublattice indices,

$$G_{AA\sigma}(i\omega_n) = \frac{1}{\Omega_{\mathrm{BZ}}} \int_{\mathrm{BZ}} \mathrm{d}\mathbf{k} \, \left[\left(G^0_\sigma(i\omega_n, \mathbf{k}) \right)^{-1} - \Sigma_\sigma(i\omega_n) \right]^{-1}_{AA} . \tag{5.12}$$

Surprisingly, the magnetization curve for the Haldane–Hubbard model at $\lambda/t = 0.1$ shows discontinuities and hysteresis, Fig. 5.15 and 5.16, even in the DMFT simulation. This apparent contradiction to our conclusion about the necessity of the K and K' point in the cluster reciprocal representation can be explained by the prescribed form of the DMFT self energy in Eq. 5.11, which *coincidentally* obeys the same constraints, of vanishing AB components, as those due to the symmetry of the self energy at the K and K' point, arising from the three-fold rotational symmetry of the model.[12] For the ionic honeycomb model simulated by DMFT at $\Delta/t = 0.52$, m is continuous. Note that the next-nearest neighbor hoppings on the same sublattice ($\lambda \neq 0$) do not allow to rewrite the mapping Eq. 5.12 as an integral over the DOS,[13] which explains the possibility of finding qualitatively different magnetization in the Haldane–Hubbard and ionic honeycomb model despite their very similar non-interacting DOS.

Finally, the 6-site cluster enable simulations at lower temperature since the sign problem is less severe than for the 24-site cluster. Results obtained at twice lower temperature differ only by an enlarged ordered phase (see Fig. 5.4), while the first order characteristics remains unchanged.

[11] The other reason is that a single-site DMFT does not provide a suitable quantity which we could relate to $\Sigma_{AB\sigma}(i\omega_n)$. Note that for $\Delta = 0$, the model becomes inversion symmetric, resulting in $\Sigma_{BB\sigma}(i\omega_n) = -\Sigma^*_{AA\sigma}(i\omega_n) = \Sigma_{AA\bar{\sigma}}(i\omega_n)$, valid both in the paramagnetic and the (spontaneously) antiferromagnetically ordered case. Since $\Sigma_{AB\sigma} = 0 = \Sigma_{BA\sigma}$, the presence or

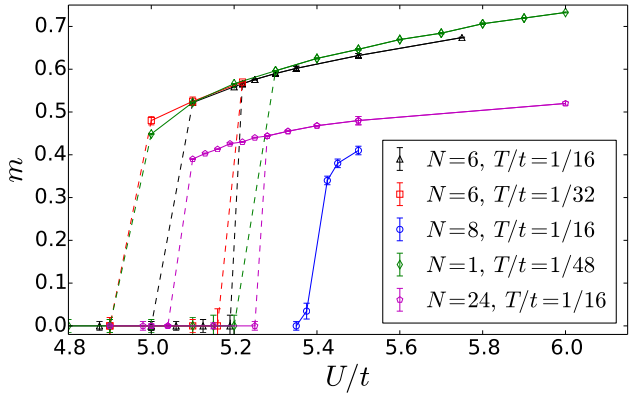

Figure 5.15: The staggered magnetization of the Haldane–Hubbard model at $\lambda/t = 0.1$ obtained with various clusters shown in Fig. 5.4 simulated at temperature T. The single-site DMFT data ($N = 1$) is presented as well. The magnetization curve for the 8-site cluster is qualitatively different from the other curves. The lower value of m for $N = 24$ compared to $N = 1, 6$ is consistent with the observation on the honeycomb lattice Hubbard model (Fig. 5.2).

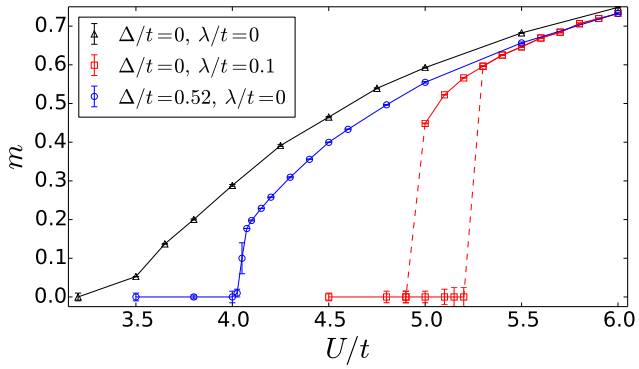

Figure 5.16: The staggered magnetization obtained with a single-site DMFT simulation for the model defined by Eq. 5.1 with different choices of parameters Δ and λ: in particular for the Hubbard model on the honeycomb lattice ($\Delta = \lambda = 0$), the Haldane model ($\Delta = 0$, $\lambda \neq 0$), and the ionic honeycomb model ($\Delta \neq 0$, $\lambda = 0$). The temperature was in all cases $T/t = 1/48$. The magnetization curve for the Haldane model shows a first order discontinuity and hysteresis, while the other curves are continuous.

5.6 Summary and Outlook

Out predictions can be checked by the experiments on the Haldane–Hubbard model in optical lattice simulators [152, 167]. The first order phase transition can be detected as a hysteresis of spatially averaged local observables. By tuning the interaction strength to the coexisting region one may also find coexisting domains of CI and AFI phases. Each AFI domain is of the size of the magnetic correlation length at the first order transition point. Interestingly, the topological nature of the CI would imply presence of chiral edge states around the domain walls which may be revealed by an in-situ measurement of the domains in the ultracold atomic gas.

absence of the intracell phase factors in FT (Eq. 1.19) does not influence the solution.

[12]This property was discussed in caption of Fig. 2.8.

[13]As done in Eq. 97 of section V.B of [55].

6 Conclusion and outlook

In this thesis we present several applications where the use of DCA is advantageous over competing methods. DCA is well suited for obtaining thermal averages of physical observables at moderate temperatures. Another field of application of the method are models which cannot be studied directly with a finite lattice simulation due to the sign problem. As this is reduced in DCA, it permits simulations using moderately sized clusters. Our Haldane–Hubbard model study in Chap. 5 is an example of such a case. However, the sign problem is not absent in DCA and thus we were not able to firmly determine the character of the phase transition at small values of λ. Solving the Haldane–Hubbard model with DCA$^+$ [185], where the sign problem was reported to be reduced even more than in DCA, may be subject of future work.

We attempted at a global update for the CT-AUX solver with the aim to reduce the autocorrelation times. As described in Sec. B.4, the proposed update based on Langevin evolution of the imaginary time positions of the auxiliary spins missed the goal. The obstacle is that reasonable acceptance rate was given only for relatively short evolution time, which does not significantly change the auxiliary field configuration. Longer evolution time has to be achieved, even if the evolution is only approximate.[1]

The structure of the vertex function investigated in Subsec. 3.4.6 and 4.4.2 can be used for further development of approximations utilizing the vertex function: DMFT with vertex corrections [187], dynamical vertex approximation (DΓA) [188, 189], dual fermion approach [190], multi-scale extension to quantum cluster method [191]. DΓA pushes the locality assumption in DMFT from the self energy to the fully irreducible two-particle vertex,[2] which can be justified by the use of DCA.

[1] A related update is applied in the so-called *hybrid QMC* [186] with continuous Hubbard–Stratonovich fields, where the evolved degrees of freedom are the auxiliary field strengths.

[2] Notice that in Subsec. 3.4.6 and 4.4.2 we work with the longitudinally particle-hole irreducible vertex Γ, as opposed to the fully irreducible two-particle vertex Γ_{fir} that plays the central role in the DΓA. The former contains contribution of diagrams that may be reducible in the transverse

This would require measurement of the susceptibility in all channels and for all cluster reciprocal vectors $\mathbf{Q}$ and multiple bosonic frequencies ν with total memory requirement proportional to $(LN_\omega)^3$. With similar computational resources as those used for largest clusters simulated in [2], where it was sufficient to accumulate the susceptibility measurements for a single $\mathbf{Q}$ vector and for $\nu = 0$, one may anyhow reach $LN_\omega \approx 400$.

The scaling $(\beta U)^3$ of the action-based impurity solvers (CT-AUX [39], CT-INT [113]) needed for the DCA is a clear disadvantage for reaching low temperature or large interaction when compared to the linearly scaling Hamiltonian-based LCT-INT [40]. In order to exploit the linear scaling of LCT-INT, one may fit the DCA bath with n_{bath} bath sites coupling to the physical sites as in [174]. The scaling of n_{bath} with respect to β and U in order to keep constant fit precision is *a priori* unknown. Further investigation along this line is needed to find the overall complexity of this approach.

While a truly *ab initio* numerical simulation of the experimental realization of the Bose–Hubbard model in an optical lattice was done several years ago [74], analogous studies for fermionic systems [75][1] rely on the LDA. For anisotropic models like the stacked lattices examined in Chap. 4, it is reasonable to treat the weak coupling t' in vertical direction within DMFT, provided the temperature is much larger than t'. This suggests simulation of independent layers with strong in-plane hoppings t and DMFT-treated out-of-plane hoppings t'. Such simulation with a realistic experimental extent of the simulated layer and realistic site potentials is feasible.[3] This proposal may be especially useful in presence of large potential gradients, in which case the in-plane use of LDA may be unreliable.

particle-hole or in the particle-particle channel. Therefore, Γ_{fir} is assumed to show even weaker variations in the reciprocal space than Γ.

[3] As a feasibility test we performed a finite lattice simulation of a 20×20 site open boundary cluster with a quadratic potential $V(r) = U/2 - r^2/40$, where the radius r is given in units of lattice sites. The temperature was $T = 0.5t$, interaction $U = 4t$, where t is the (strong) in-plane hopping. We set the out-of-plane hopping $t' = 0$. With an expansion order around 950 and an average sign of 0.99 in the CT-AUX solver the simulation was not very demanding. Notice that with DMFT along the weak coupling direction for the case $t' > 0$ the sign is expected to be even closer to 1.0.

A Fourier transformation in imaginary time

A.1 Fourier transformation $G_{ij}(i\omega_n) \to G_{ij}(\tau)$

We want to calculate the FT from Matsubara frequency to imaginary time representation,

$$G_{ab}(\tau) = \frac{1}{\beta} \sum_{n=-\infty}^{\infty} G_{ab}(i\omega_n)\, e^{-i\omega_n \tau}\,, \qquad \omega_n = \frac{(2n+1)\pi}{\beta}\,, \tag{A.1}$$

for $0 < \tau < \beta$ valid for systems with hermitian Hamiltonian $\hat{H}$ independent on time. Clearly, for any practical calculation we need to introduce some cut-off in the sum over n in Eq. (A.1). The Green's function definition in imaginary time,

$$G_{ab}(\tau) = -T_\tau \left\langle \hat{c}_a(\tau)\, \hat{c}_b^\dagger(0) \right\rangle\,, \qquad -\beta < \tau < \beta\,, \tag{A.2}$$

reveals the source of difficulty – $G_{ab}(\tau)$ is in general discontinuous at $\tau = 0$, causing long tailed $G_{ab}(i\omega_n)$. We will show that the contribution of the high frequency terms therefore needs to be taken into account, at least perturbatively. This issue is extremely important if using impurity solvers working with discretized imaginary time axis, like the Hirsch–Fye impurity solver [37]. It can be cured by usage of high-frequency expansions, which were for this purpose developed in [192, 193, 194]. In what follows we present this standard approach adapted for the case of general lattice Hamiltonians.

We start the derivation with a generic case, without assumption of any particular (real space, reciprocal, mixed, ...) representation, using a multiindex $\iota = (ab)$ labeling the Green's function.[1] We expand $G_\iota(i\omega_n)$ for large ω_n by successive use

[1] The multiindex may correspond for example to two site labels and spin ($\mathbf{r}\alpha$, $\mathbf{r}'\alpha'$, σ), or to two reciprocal quasimomenta, sublattice indices, and spin ($\mathbf{k}\alpha$, $\mathbf{k}'\alpha'$, σ).

of integration by parts,

$$
\begin{aligned}
&G_\iota(i\omega_n) = \\
&= \int_0^\beta \mathrm{d}\tau\, e^{i\omega_n\tau} G_\iota(\tau)\,, && \text{(A.3)}\\
&= \left[\frac{e^{i\omega_n\tau}}{i\omega_n} G_\iota(\tau)\right]_0^\beta - \frac{1}{i\omega_n}\int_0^\beta \mathrm{d}\tau\, e^{i\omega_n\tau} G'_\iota(\tau)\,, && \text{(A.4)}\\
&= \frac{-G_\iota(\beta^-) - G_\iota(0^+)}{i\omega_n} + \frac{G'_\iota(\beta^-) + G'_\iota(0^+)}{(i\omega_n)^2} + \frac{-G''_\iota(\beta^-) - G''_\iota(0^+)}{(i\omega_n)^3} + \dots\,, && \text{(A.5)}\\
&= \sum_{m=1}^{\infty} \frac{c^\iota_m}{(i\omega_n)^m}\,. && \text{(A.6)}
\end{aligned}
$$

If $\iota = (ab)$ and a, b label an orthonormal basis, *i.e.* $\left\{\hat{c}_a, \hat{c}_b^\dagger\right\} = \delta_{ab}$, then with cyclic permutation under the trace in Eq. A.2 we obtain[2]

$$
G_{ab}(\tau = 0^+) + G_{ab}(\tau = \beta^-) = -\delta_{ab} \qquad \Rightarrow \qquad c^\iota_1 = \delta_{ab}\,. \tag{A.7}
$$

Further spectral moments c^ι_m are Hamiltonian dependent. Specific examples are worked out in Sec. A.4. In general, since $G_{ab}(i\omega_n) = G^*_{ba}(-i\omega_n)$, see Eq. 1.36, we get $c^{ab}_m = \left(c^{ba}_m\right)^*$ for any m.

We proceed and use the high frequency asymptotics of $G_\iota(i\omega_n)$ for $|n| \geq N_\omega$ in the formula for $G_\iota(\tau)$,

$$
\begin{aligned}
G_\iota(\tau) &= \frac{1}{\beta}\sum_{n=0}^{\infty}\left[G_\iota(i\omega_n)e^{-i\omega_n\tau} + G_\iota(-i\omega_n)e^{i\omega_n\tau}\right], && \text{(A.8)}\\
&= \frac{1}{\beta}\sum_{n=0}^{N_\omega-1}\left[G_\iota(i\omega_n)e^{-i\omega_n\tau} + G_\iota(-i\omega_n)e^{i\omega_n\tau}\right] \\
&\quad - \frac{2}{\beta}\sum_{n=N_\omega}^{\infty}\sin(\omega_n\tau)\sum_{q=0}^{\infty}\left(\frac{c^\iota_{4q+1}}{\omega_n^{4q+1}} - \frac{c^\iota_{4q+3}}{\omega_n^{4q+3}}\right) \\
&\quad - \frac{2}{\beta}\sum_{n=N_\omega}^{\infty}\cos(\omega_n\tau)\sum_{q=0}^{\infty}\left(\frac{c^\iota_{4q+2}}{\omega_n^{4q+2}} - \frac{c^\iota_{4q+4}}{\omega_n^{4q+4}}\right). && \text{(A.9)}
\end{aligned}
$$

The infinite sums can be evaluated using special functions. For practical purpose

[2]Notice that the FT in Eq. A.1 ensures $G_{ab}(\tau = 0) + G_{ab}(\tau = \beta) = 0$. In practice, $G_{ab}(\tau = 0^+)$ can be obtained as $G_{ab}(\tau = 0) = \frac{1}{\beta}\sum_n G_{ab}(i\omega_n)$ and $G_{ab}(\tau = \beta^-)$ is set according to the Eq. A.7.

we truncate the sums over q, which allows us to come to this useful expression,[3]

$$\begin{aligned} G_\iota(\tau) &= \frac{1}{\beta}\sum_{n=0}^{N_\omega-1}\left(G_\iota(i\omega_n)+G_\iota(-i\omega_n)+\frac{2c_2^\iota}{\omega_n^2}\right)\cos\omega_n\tau \\ &\quad+\frac{1}{\beta}\sum_{n=0}^{N_\omega-1}\left(iG_\iota(-i\omega_n)-iG_\iota(i\omega_n)+\frac{2c_1^\iota}{\omega_n}-\frac{2c_3^\iota}{\omega_n^3}\right)\sin\omega_n\tau \\ &\quad-\frac{2c_1^\iota+\beta c_2^\iota}{4}+\frac{\tau}{4}(2c_2^\iota+\beta c_3^\iota)-\frac{\tau^2 c_3^\iota}{4}+\mathcal{O}\left(\frac{\beta^3}{N_\omega^3}\right), \end{aligned} \tag{A.10}$$

where we used analytic results,

$$\sum_{n=0}^{\infty}\frac{\sin\left[(2n+1)x\right]}{2n+1} = \frac{\pi}{4}, \tag{A.11}$$

$$\sum_{n=0}^{\infty}\frac{\cos\left[(2n+1)x\right]}{(2n+1)^2} = \frac{\pi^2}{8}-\frac{\pi}{4}x, \tag{A.12}$$

$$\sum_{n=0}^{\infty}\frac{\sin\left[(2n+1)x\right]}{(2n+1)^3} = \frac{\pi^2}{8}x-\frac{\pi}{8}x^2, \tag{A.13}$$

valid for $0<x<\pi$. To remove the explicit dependency on negative Matsubara frequencies in Eq. A.10, we use the relation $G_{ab}(i\omega_n)=G^*_{ba}(-i\omega_n)$ valid for any system with hermitian time-independent $\hat{H}$, see Eq. 1.36.

Further simplification is possible in the case of purely real imaginary-time $G_\iota(\tau)$.[4] That ensures $c_m^\iota\in\mathbb{R}$ and $G_\iota(-i\omega_n)=G_\iota(i\omega_{-n-1})=G^*_\iota(i\omega_n)$. In such case,

$$\begin{aligned} G_\iota(\tau) &= \frac{2}{\beta}\sum_{n=0}^{N_\omega-1}\left\{\left[\Re G_\iota(i\omega_n)+\frac{c_2^\iota}{\omega_n^2}\right]\cos\omega_n\tau+\left[\Im G_\iota(i\omega_n)+\frac{c_1^\iota}{\omega_n}-\frac{c_3^\iota}{\omega_n^3}\right]\sin\omega_n\tau\right\} \\ &\quad-\frac{2c_1^\iota+\beta c_2^\iota}{4}+\frac{\tau}{4}(2c_2^\iota+\beta c_3^\iota)-\frac{\tau^2 c_3^\iota}{4}+\mathcal{O}\left(\frac{\beta^3}{N_\omega^3}\right). \end{aligned} \tag{A.14}$$

[3] In this expression we omit usage of special functions, as it would provide real benefit only if using FFT. Since this FT is not performance critical part, we performed it with discrete FT. The sums over $n\in\{0,\dots,N_\omega-1\}$ are for numerical reasons to be evaluated with decreasing n starting from $N_\omega-1$.

[4] For $\iota=(ab)$ and $a=b$, assuming orthonormal basis, it is always the case – notable examples are local Green's function, $G_{\mathbf{rr}}(\tau)$, and the reciprocal space Green's function of a Bravais lattice, $G_{\mathbf{k}}(\tau)$. In general, for $a\neq b$, $G_{ab}(\tau)$ is certainly purely real if the Hamiltonian is real with respect to the basis labeled by a,b. That is often the case in the real space representation, in which case we obtain $G_{\mathbf{k}\alpha\alpha'}(i\omega_n)=G^*_{-\mathbf{k}\alpha\alpha'}(-i\omega_n)$, implying $c_m^{\mathbf{k}\alpha\alpha'}=\left(c_m^{-\mathbf{k}\alpha\alpha'}\right)^*$.

A.2 Fourier transformation $G_{ij}(\tau) \to G_{ij}(i\omega_n)$

We avoided need of this Fourier transformation via direct measurement of the Green's function in frequency domain. Performation of this transformation needs to be handled with care, as $G_\iota(\tau)$ is typically known only at some (regular) mesh.[5] To get the high frequency tail of $G_{ij}(i\omega_n)$ correctly, a spline of $G_{ij}(\tau)$ with prescribed spectral moments c_m^ι (this technique is called oversampling) comes into play. For more details see [195].

A.3 Density estimation solely from the Matsubara measurements

The density at the single particle state j, which may be a site in real space or a delocalized wave in the reciprocal space, is related to the imaginary-time Green's function at the given state j. Eq. 1.37 ensures that $G_{jj}(\tau)$ is purely real. Direct measurement of the density, which is an instantaneous 2-point correlation measurement, is typically simple and for most of the calculations we perform it. In case we measure only the $G_{jj}(i\omega_n)$, the density may be obtained as follows,

$$\langle n_{j\sigma}\rangle = -G_{jj\sigma}(\beta^-) = 1 + G_{jj\sigma}(0^+) \tag{A.15}$$

$$= \frac{1}{2} + \underbrace{\frac{2}{\beta}\sum_{n\geq 0}^{N_\omega} \Re\left[G_{jj\sigma}(i\omega_n)\right]}_{s_{j\sigma}} + c_2^{jj}\left(\frac{2}{\beta}\sum_{n\geq 0}^{N_\omega}\frac{1}{\omega_n^2} - \frac{\beta}{4}\right) + \mathcal{O}\left(N_\omega^{-3}\right) . \tag{A.16}$$

Using the expression $c_2^{jj} = -\tilde{t}_{jj\sigma} + U_j\left(\langle n_{j\bar{\sigma}}\rangle - 1/2\right)$ for a model with onsite interaction U_j, see Eq. A.29 and Eq. A.30, and solving the coupled linear equations for σ and $\bar{\sigma}$ we find

$$\langle n_{j\sigma}\rangle = \frac{1}{2} + \frac{s_{j\sigma} - U_j\beta\alpha(N_\omega)s_{j\bar{\sigma}} + \beta\alpha(N_\omega)\left(\tilde{t}_{jj\sigma} - U_j\beta\alpha(N_\omega)\tilde{t}_{jj\bar{\sigma}}\right)}{1 - \left(U_j\beta\alpha(N_\omega)\right)^2} + \mathcal{O}\left(N_\omega^{-3}\right) , \tag{A.17}$$

with

$$\alpha(N) = \frac{1}{4} - \frac{2}{\beta^2}\sum_{n\geq 0}^{N_\omega}\frac{1}{\omega_n^2} = \frac{1}{4} - \frac{2}{\pi^2}\sum_{n\geq 0}^{N_\omega}\frac{1}{(2n+1)^2} = \frac{2}{\pi^2}\sum_{n>N_\omega}^{\infty}\frac{1}{(2n+1)^2} > 0 . \tag{A.18}$$

Asymptotically, $\alpha(N_\omega) = \frac{1}{2\pi^2 N_\omega} + \mathcal{O}\left(N_\omega^{-2}\right)$. In order to keep constant precision, one thus needs to scale the cut-off N_ω linearly with β and the energy scales (U, t,

[5] The dependence of $G_\iota(\tau)$ on τ may be strong for $\tau \to 0^+$ and $\tau \to \beta^-$, which suggests use of irregular imaginary time meshes.

$V_{\alpha\sigma}$) in the Hamiltonian. For a typical frequency cut-off $N_\omega = 500$ we get $\alpha \approx \frac{1}{10^4}$, which provides sufficient precision for simulations at $\beta U \lessapprox 100$ and $t \lessapprox U$. For j being a real space site we have according to Eq. A.29 $\tilde{t}_{jj\sigma} = -(V_{j\sigma} - \mu)$.

A.4 Spectral moments

In the previous sections we explained that for reliable FT of $G_\iota(i\omega_n)$ to $G_\iota(\tau)$ we need to know the high-frequency asymptotics of $G_\iota(i\omega_n)$ given by the spectral moments c_m^ι. In this section we find explicit forms for these in some model systems.

A.4.1 Spectral moments of the non-interacting Green's function

For the non-interacting Green's function G_ι^0 the spectral moments c_m^ι are obtained effortless from the analytic form of the Green's function given in Eq. 1.14, 1.24, 1.25. For the non-interacting lattice Green's function in the reciprocal representation in matrix form with respect to the intracell sites we find

$$G_\sigma^{0,\mathrm{lat}}(\mathbf{k}, i\omega_n) = (i\omega_n \mathbb{1}_\ell + \tilde{T}_{\mathbf{k}\sigma})^{-1} = \frac{\mathbb{1}_\ell}{i\omega_n} - \frac{\tilde{T}_{\mathbf{k}\sigma}}{(i\omega_n)^2} + \frac{(\tilde{T}_{\mathbf{k}\sigma})^2}{(i\omega_n)^3} + \dots\,, \tag{A.19}$$

i.e. $c_m^{\mathbf{k}\alpha\alpha'\sigma} = \left[\left(-\tilde{T}_{\mathbf{k}\sigma}\right)^{m-1}\right]_{\alpha\alpha'}$.

A.4.2 Spectral moments of the full lattice Green's function for a model with onsite interaction

We work out the forms of the spectral moments for a model on a general non-Bravais lattice with Hubbard interaction. Formulas for a Bravais lattice might be obtained from these easily, or these can be found in the App. B of [195]. We aim finding the spectral moments c_m^{ij} in a real space basis labeled by i, j for a model with Hubbard interaction $\hat{H}_U$ and total Hamiltonian $\hat{H} = \hat{H}_0 + \hat{H}_U$, with

$$\hat{H}_0 = -\sum_{i,j,\sigma} \tilde{h}_{ij\sigma} \hat{c}_{i\sigma}^\dagger \hat{c}_{j\sigma}\,, \qquad \hat{H}_U = \sum_i U_i \hat{n}_{i\uparrow} \hat{n}_{i\downarrow}\,, \tag{A.20}$$

$$\tilde{h}_{ij}^\sigma = \tilde{t}_{ij\sigma} + U_i \delta_{ij}/2 = t_{ij\sigma} + (-V_{i\sigma} + \mu + U_i/2)\delta_{ij}\,, \tag{A.21}$$

assuming $U_i, V_{i\sigma}, \mu \in \mathbb{R}$, $t_{ii\sigma} = 0$, $t_{ij\sigma} = t_{ji\sigma}^*$. We made the chemical potential shift by $U_i/2$ a part of $\hat{H}_0$, as it is suitable to handle separately single particle terms

and the density-density interaction terms.[6]

Recall that so far we identified

$$c_m^{ij\sigma} = (-1)^m \left[G_{ij\sigma}^{(m-1)}(\beta^-) + G_{ij\sigma}^{(m-1)}(0^+) \right] . \tag{A.22}$$

To get the Green's function derivatives, we use

$$\hat{c}_\iota(\tau) = e^{\tau \hat{H}}\, \hat{c}_\iota\, e^{-\tau \hat{H}} \qquad \Rightarrow \qquad \partial_\tau\, \hat{c}_\iota(\tau)\big|_{\tau_0} = e^{\tau_0 \hat{H}} [\hat{H}, \hat{c}_\iota] e^{-\tau_0 \hat{H}} . \tag{A.23}$$

For the second order ($m = 2$) we thus get

$$\left.\begin{aligned} \partial_\tau\, G_{ij\sigma}(\beta^-) &= -\tfrac{1}{Z}\, \mathrm{Tr} \left\{ \hat{c}_{j\sigma}^\dagger\, [\hat{H}, \hat{c}_{i\sigma}]\, e^{-\beta \hat{H}} \right\} \\ \partial_\tau\, G_{ij\sigma}(0^+) &= -\tfrac{1}{Z}\, \mathrm{Tr} \left\{ [\hat{H}, \hat{c}_{i\sigma}]\, \hat{c}_{j\sigma}^\dagger\, e^{-\beta \hat{H}} \right\} \end{aligned} \right. \quad \Rightarrow \quad c_2^{ij\sigma} = -\left\langle \left\{ [\hat{H}, \hat{c}_{i\sigma}], \hat{c}_{j\sigma}^\dagger \right\} \right\rangle . \tag{A.24}$$

Here we list commutators useful to find the explicit form of $c_2^{ij\sigma}$, which are not listed in the App. B of [195],

$$[\hat{n}_{a\uparrow} \hat{n}_{a\downarrow}, \hat{c}_{i\sigma}] = -\delta_{ia} \hat{n}_{i\bar{\sigma}} \hat{c}_{i\sigma} , \tag{A.25}$$

$$[\hat{n}_{a\uparrow} \hat{n}_{a\downarrow}, \hat{n}_{i\bar{\sigma}} \hat{c}_{i\sigma}] = -\delta_{ia} \hat{n}_{i\bar{\sigma}} \hat{c}_{i\sigma} , \tag{A.26}$$

$$\left[\hat{c}_{a\sigma'}^\dagger \hat{c}_{b\sigma'}, \hat{n}_{i\bar{\sigma}} \hat{c}_{i\sigma} \right] = -\delta_{ia} \delta_{\sigma\sigma'} \hat{n}_{i\bar{\sigma}} \hat{c}_{b\sigma} - \delta_{ia} \delta_{\bar{\sigma}\sigma'} \hat{c}_{i\bar{\sigma}}^\dagger \hat{c}_{b\bar{\sigma}} \hat{c}_{i\sigma} + \delta_{ib} \delta_{\bar{\sigma}\sigma'} \hat{c}_{a\bar{\sigma}}^\dagger \hat{c}_{i\bar{\sigma}} \hat{c}_{i\sigma} . \tag{A.27}$$

Utilizing them we find

$$\left[\hat{H}_0, \hat{c}_{i\sigma} \right] = \sum_k \tilde{h}_{ik}^\sigma \hat{c}_{k\sigma} , \qquad \left[\hat{H}_U, \hat{c}_{i\sigma} \right] = -U_i \hat{n}_{i\bar{\sigma}} \hat{c}_{i\sigma} . \tag{A.28}$$

Then the second order spectral moments of the full Green's function can be expressed by

$$c_2^{ij\sigma} = -\left\langle \left\{ \left[\hat{H}, \hat{c}_{i\sigma} \right], \hat{c}_{j\sigma}^\dagger \right\} \right\rangle = -\tilde{h}_{ij\sigma} + U_i \delta_{ij} \langle \hat{n}_{i\bar{\sigma}} \rangle = -\tilde{t}_{ij\sigma} + U_i \delta_{ij} \left(\langle \hat{n}_{i\bar{\sigma}} \rangle - 1/2 \right) , \tag{A.29}$$

or in the reciprocal space representation

$$c_2^{\mathbf{k}\alpha\alpha'\sigma} = e^{-i\mathbf{k}\cdot(\mathbf{r}_\alpha - \mathbf{r}_{\alpha'})} \sum_{\mathbf{\Delta}} e^{i\mathbf{k}\cdot\mathbf{\Delta}} c_2^{\mathbf{\Delta}\alpha\alpha'} = -\tilde{t}_{\mathbf{k}\alpha\alpha'\sigma} + U_\alpha \delta_{\alpha\alpha'} \left(\langle \hat{n}_{\alpha\bar{\sigma}} \rangle - 1/2 \right) . \tag{A.30}$$

In complete analogy with Eq. A.24 we obtain the formula for the third order,

$$c_3^{ij\sigma} = \left\langle \left\{ \left[\hat{H}, \left[\hat{H}, \hat{c}_{i\sigma} \right] \right], \hat{c}_{j\sigma}^\dagger \right\} \right\rangle . \tag{A.31}$$

[6] The shift of the chemical potential results in half-filling at $\mu = 0$ for any interaction U if the problem to be solved is particle-hole symmetric, see Subsec. 1.3.6.

We list the partial results,

$$\left\{\left[\hat{H}_0,\left[\hat{H}_0,\hat{c}_{i\sigma}\right]\right],\hat{c}^\dagger_{j\sigma}\right\} = \sum_l \tilde{h}_{il\sigma}\tilde{h}_{lj\sigma}\,, \tag{A.32}$$

$$\left\{\left[\hat{H}_U,\left[\hat{H}_U,\hat{c}_{i\sigma}\right]\right],\hat{c}^\dagger_{j\sigma}\right\} = U_i^2\delta_{ij}\hat{n}_{i\bar{\sigma}}\,, \tag{A.33}$$

$$\left\{\left[\hat{H}_U,\left[\hat{H}_0,\hat{c}_{i\sigma}\right]\right],\hat{c}^\dagger_{j\sigma}\right\} = -U_j\tilde{h}_{ij\sigma}\hat{n}_{j\bar{\sigma}}\,, \tag{A.34}$$

$$\left\{\left[\hat{H}_0,\left[\hat{H}_U,\hat{c}_{i\sigma}\right]\right],\hat{c}^\dagger_{j\sigma}\right\} = -U_i\tilde{h}_{ij\sigma}\hat{n}_{i\bar{\sigma}} + U_i\delta_{ij}\sum_a\left(\tilde{h}_{ai\bar{\sigma}}\hat{c}^\dagger_{a\bar{\sigma}}\hat{c}_{i\bar{\sigma}} - \text{h.c.}\right)\,. \tag{A.35}$$

The third order spectral moments expression reads[7]

$$c_3^{ij\sigma} = \sum_l \tilde{h}_{il\sigma}\tilde{h}_{lj\sigma} - \tilde{h}_{ij\sigma}\Big(U_i\left\langle\hat{n}_{i\bar{\sigma}}\right\rangle + U_j\left\langle\hat{n}_{j\bar{\sigma}}\right\rangle\Big) + U_i^2\delta_{ij}\left\langle\hat{n}_{i\bar{\sigma}}\right\rangle\,, \tag{A.37}$$

$$= \sum_l \tilde{t}_{il\sigma}\tilde{t}_{lj\sigma} - \tilde{t}_{ij\sigma}\left[U_i\left(\left\langle\hat{n}_{i\bar{\sigma}}\right\rangle - 1/2\right) + U_j\left(\left\langle\hat{n}_{j\bar{\sigma}}\right\rangle - 1/2\right)\right] + U_i^2\delta_{ij}/4\,, \tag{A.38}$$

and in the reciprocal representation,

$$c_3^{\mathbf{k}\alpha\alpha'\sigma} = \sum_\beta \tilde{t}_{\mathbf{k}\alpha\beta\sigma}\tilde{t}_{\mathbf{k}\beta\alpha'\sigma} - \tilde{t}_{\mathbf{k}\alpha\alpha'\sigma}\Big(U_\alpha(\left\langle\hat{n}_{\alpha\bar{\sigma}}\right\rangle - 1/2) + U_{\alpha'}(\left\langle\hat{n}_{\alpha'\bar{\sigma}}\right\rangle - 1/2)\Big) + U_\alpha^2\delta_{\alpha\alpha'}/4\,. \tag{A.39}$$

A.4.3 Spectral moments of the lattice self energy

At this stage we are ready to calculate the tail of the lattice self energy via Dyson equation. In the following we use $\ell\times\ell$ matrices $\left(C_m^{\mathbf{k}\sigma}\right)_{\alpha\alpha'} = c_m^{\mathbf{k}\alpha\alpha'\sigma}$ for the spectral

[7] For $i\neq j$ it is straightforward to obtain the expression. For $i=j$ we need some additional tricks to get there – we use the general property $G_{ij}(\tau) = G^*_{ji}(\tau)$ (Eq. 1.35),

$$\left\langle\tilde{h}_{ai\bar{\sigma}}\hat{c}^\dagger_{a\bar{\sigma}}\hat{c}_{i\bar{\sigma}} - \tilde{h}_{ia\bar{\sigma}}\hat{c}^\dagger_{i\bar{\sigma}}\hat{c}_{a\bar{\sigma}}\right\rangle = \tilde{h}_{ai\bar{\sigma}}G_{ia\bar{\sigma}}(\beta^-) - \tilde{h}_{ia\bar{\sigma}}G_{ai\bar{\sigma}}(\beta^-) = 2i\Im\left[\sum_a \tilde{h}_{ai\bar{\sigma}}G_{ia\bar{\sigma}}(\beta^-)\right]\,. \tag{A.36}$$

Being purely imaginary, it cannot contribute to the purely real c_3^{ii}. The other terms are for $i=j$ purely real, thus we get a necessary condition $\Im\left[\sum_a \tilde{t}_{ai\bar{\sigma}}G_{ia\bar{\sigma}}(0^+)\right] = 0,\ \forall i,\sigma$.

moments of the interacting lattice Green's function,

$$\begin{aligned}
&\Sigma^{\mathrm{lat}}_{\alpha\alpha'\sigma}(\mathbf{k}, i\omega_n; U, \mu) = \\
&= \left[G^{0,\mathrm{lat}}_{\sigma}(\mathbf{k}, i\omega_n; 0, \mu)\right]^{-1}_{\alpha\alpha'} - \left[G^{\mathrm{lat}}_{\sigma}(\mathbf{k}, i\omega_n; U, \mu)\right]^{-1}_{\alpha\alpha'} && \text{(A.40)}\\
&= \left[i\omega_n \mathbb{1}_\ell + \tilde{T}_{\mathbf{k}\sigma}\right]_{\alpha\alpha'} - i\omega_n \left[\mathbb{1}_\ell - \left(\frac{-C_2^{\mathbf{k}\sigma}}{i\omega_n} + \frac{-C_3^{\mathbf{k}\sigma}}{(i\omega_n)^2} + \ldots\right)\right]^{-1}_{\alpha\alpha'} && \text{(A.41)}\\
&= \tilde{t}_{\mathbf{k}\alpha\alpha'\sigma} + c_2^{\mathbf{k}\alpha\alpha'\sigma} - \frac{1}{i\omega_n}\left(\sum_\beta c_2^{\mathbf{k}\alpha\beta\sigma} c_2^{\mathbf{k}\beta\alpha'\sigma} - c_3^{\mathbf{k}\alpha\alpha'\sigma}\right) + \ldots && \text{(A.42)}\\
&= U_\alpha \delta_{\alpha\alpha'}\big(\langle \hat{n}_{\alpha\bar{\sigma}}\rangle - 1/2\big) - \frac{\delta_{\alpha\alpha'}}{i\omega_n} U_\alpha^2 \left(\langle \hat{n}_{\alpha\bar{\sigma}}\rangle^2 - \langle \hat{n}_{\alpha\bar{\sigma}}\rangle\right) + \ldots . && \text{(A.43)}
\end{aligned}$$

Recall that G^{lat}_σ is according to Eq. A.21 at chemical potential shifted by $U/2$. That cancels the zeroth order, *i.e.* the Hartree part of self energy, in the half filled case.

A.4.4 Asymptotics of the impurity Green's function

In the DCA selfconsistency in combination with the CT-AUX solver [39] we need to perform FT of the bare impurity Green's function $G^{0,\mathrm{imp}}(i\omega_n)$ to $G^{0,\mathrm{imp}}(\tau)$, which is needed as the input for the solver. In this subsection we show that the 3 lowest spectral moments of $G^{0,\mathrm{imp}}(i\omega_n)$ are the same as the spectral moments of the patch-averaged $G^{0,\mathrm{lat}}(i\omega_n)$.

According to the DCA mapping (Eq. 2.4), the asymptotics of the full impurity Green's function $G^{\mathrm{imp}}(\mathbf{K})$ is the same as of the patch-averaged full lattice Green's function,

$$G^{\mathrm{imp}}_\sigma(\mathbf{K}, i\omega_n) = \left\langle G^{\mathrm{lat}}_\sigma(\mathbf{k}, i\omega_n)\right\rangle_{\mathbf{K}} = \left\langle \left(i\omega_n \mathbb{1}_\ell + \tilde{T}_{\mathbf{k}\sigma} - \Sigma^{\mathrm{lat}}_\sigma(\mathbf{K}, i\omega_n)\right)^{-1}\right\rangle_{\mathbf{K}}, \quad \text{(A.44)}$$

where we inserted the explicit form of $G^{0,\mathrm{lat}}_\sigma(\mathbf{K}, i\omega_n)$ from Eq. A.19. The patch averaging is denoted by $\langle \ldots \rangle_{\mathbf{K}}$. Plugging in the expansion of self energy,

$$\Sigma(i\omega_n) = \Sigma_0 + \Sigma_1/(i\omega_n) + \ldots \quad \text{(A.45)}$$

from the previous subsection, and using the $\mathbf{k}$-independence of Σ_0 and Σ_1, $\langle \Sigma_{0,1}\rangle_{\mathbf{K}} = \Sigma_{0,1}$, we get

$$\begin{aligned}
&G^{\mathrm{imp}}_\sigma(\mathbf{K}, i\omega_n) = \\
&= \frac{\mathbb{1}_\ell}{i\omega_n} + \frac{-\left\langle \tilde{T}_{\mathbf{k}\sigma}\right\rangle_{\mathbf{K}} + \Sigma_0}{(i\omega_n)^2} \\
&\quad + \frac{\Sigma_0^2 + \Sigma_1 - \Sigma_0\left\langle \tilde{T}_{\mathbf{k}\sigma}\right\rangle_{\mathbf{K}} - \left\langle \tilde{T}_{\mathbf{k}\sigma}\right\rangle_{\mathbf{K}}\Sigma_0 + \left\langle \tilde{T}^2_{\mathbf{k}\sigma}\right\rangle_{\mathbf{K}}}{(i\omega_n)^3} + \mathcal{O}\left((i\omega_n)^{-4}\right) . \quad \text{(A.46)}
\end{aligned}$$

The asymptotic behavior of the bare impurity Green's function $G^{\mathrm{imp},0}(\mathbf{K})$ can be obtained via the Dyson equation,

$$G_\sigma^{0,\mathrm{imp}}(\mathbf{K}, i\omega_n) = \left(G_\sigma^{\mathrm{imp}}(\mathbf{K}, i\omega_n)^{-1} + \Sigma_\sigma^{\mathrm{lat}}(\mathbf{K}, i\omega_n)\right)^{-1} , \tag{A.47}$$

where we utilized the DCA approximation of the self energy, $\Sigma_\sigma^{\mathrm{lat}}(\mathbf{K}, i\omega_n) = \Sigma_\sigma^{\mathrm{imp}}(\mathbf{K}, i\omega_n)$. Working that out we arrive at

$$G_\sigma^{0,\mathrm{imp}}(\mathbf{K}, i\omega_n) = \frac{\mathbb{1}_\ell}{i\omega_n} - \frac{\left\langle \tilde{T}_{\mathbf{k}\sigma} \right\rangle_{\mathbf{K}}}{(i\omega_n)^2} + \frac{\left\langle \tilde{T}_{\mathbf{k}\sigma}^2 \right\rangle_{\mathbf{K}}}{(i\omega_n)^3} + \mathcal{O}\left((i\omega_n)^{-4}\right) , \tag{A.48}$$

which is up to the shown order equivalent to the patch-averaged lattice non-interacting Green's function.

B Effective use of the CT-AUX impurity solver

B.1 Choice of the parameter K

The parameter K in the CT-AUX impurity solver [39] controls the expansion order N_s, which behaves like

$$\frac{\langle N_s \rangle}{N} = K + \beta U \left\langle \frac{n_\downarrow + n_\uparrow}{2} + n_\uparrow n_\downarrow \right\rangle , \tag{B.1}$$

thus it is advantageous to keep K low. However, K appears as well in the acceptance probability of the Monte Carlo updates, so it influences as well the autocorrelation times. Conventionally it is chosen positive to get real γ,

$$\cosh \gamma = 1 + \frac{\beta U}{2K} . \tag{B.2}$$

Another less obvious, but nevertheless useful option is the choice $K \in (-\beta U/4, 0)$, which results in $\Im\gamma = \pi$. As γ enters all formulas via $\exp(\pm\gamma)$, all of them remain purely real. Negative K raises suspicion that it may cause severe sign problem, as the configuration weight w is proportional to K^{N_s}. However, w is as well proportional to determinants of N_σ^{-1}, which depend on $\exp(\pm\gamma)$. Empirically we found that problems which are sign-problem free at $K > 0$ can be simulated with $K \in (-\beta U/4, 0)$ without introduction of artificial sign problem and with smaller computational effort, see in Fig. B.1. For production runs of sign-problem free problems we choose $K = -0.95\,\frac{\beta U}{4}$, unless the simulation is in weakly coupled regime, *i.e.* for small βU, as that would make the expansion order N_s close to 0, rendering the measurements inefficient.

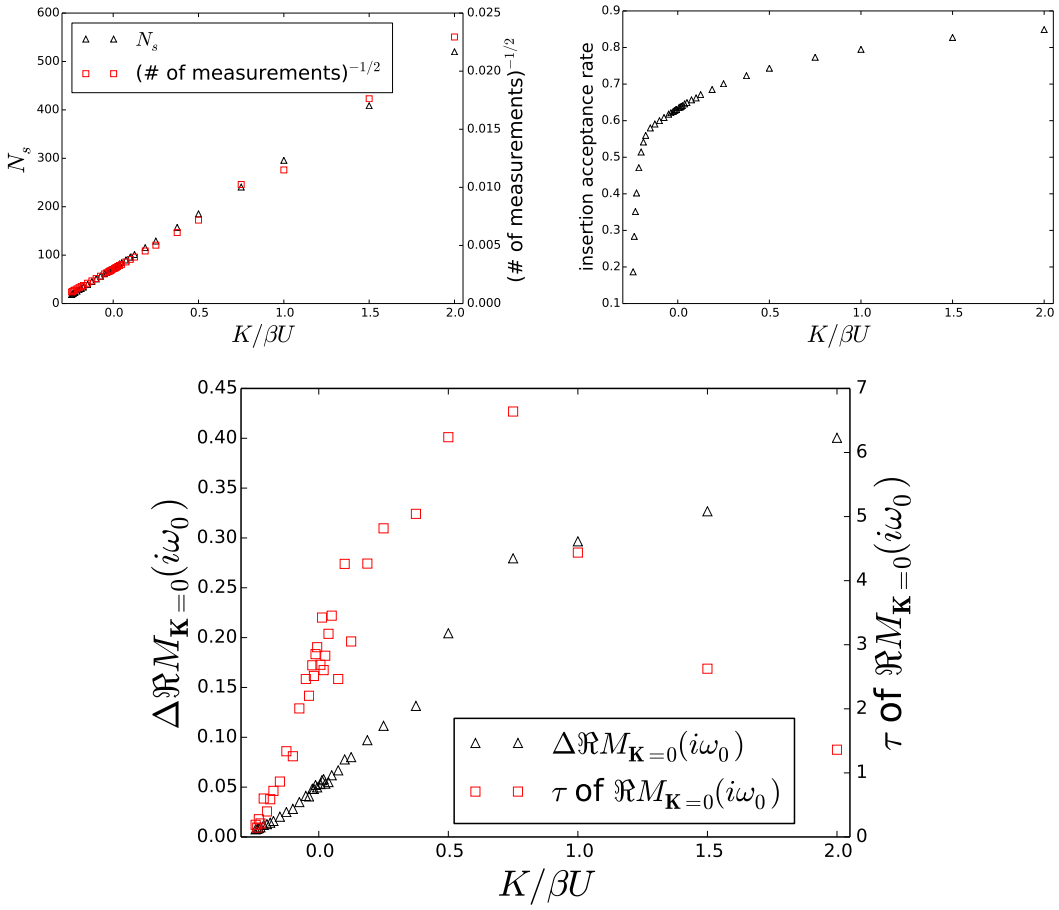

Figure B.1: Analysis of the role of the parameter K on the performance of CT-AUX impurity solver applied on a model problem. Each data point was obtained with same amount of resources. The top left plot shows linear dependence of $\langle N_s \rangle$ on K, in agreement with Eq. B.1. The total number of measurements affirms that the time per single update scales quadratically with N_s, as the measurement was performed once after 64 single update attempts. The top right plot shows the non-trivial dependence of the auxiliary spin insertion acceptance rate on K. The lower plot shows the error estimate and the autocorrelation time of the real part of $M_{\mathbf{K}=\mathbf{0}}(i\omega_0)$, which is related to the $G_{\mathbf{K}=\mathbf{0}}(i\omega_0)$, see Eq. B.16. The problem to be solved was the half filled Hubbard model on a cubic lattice with nearest neighbor hopping t, at $\beta t = 4$, ant $U/t = 4$. The DCA method with a 14-site cluster was used. Submatrix updates [109] with $k_{\max} = 32$ were used. Paramagnetic solution was enforced. The bare impurity Green's function on the input of CT-AUX was taken from a converged DCA simulation. The time needed for thermalization was in all runs lower than 12.5% of the total runtime.

B.2 Effective measurements of single particle Green's function

This section contain formulas for efficient measurement of the single particle Green's function in various representations. For time-independent and translationally invariant problems, the measurement described in Subsec. B.2.3 is the optimal choice. However it may be convenient to measure the instantaneous Green's function directly on the imaginary time axis, as discussed in Subsec. B.2.1. The usage of non-equidistant FFT for the FT from τ to $i\omega_n$ described in Subsec. B.2.2 was already mentioned in [119, 196, 185].

B.2.1 real space Green's function in imaginary time representation

The estimator of the imaginary time real space Green's function in the CT-AUX impurity solver [39], in a state with configuration $\{s_i, r_i, \tau_i\}$ of N_s auxiliary spins ($i \in \{1, 2, \ldots, N_s\}$) is given by

$$G_{ij\sigma}(\tau - \tau') = G^0_{ij\sigma}(\tau - \tau') - \sum_{p,q} G^0_{ir_p\sigma}(\tau - \tau_p)\, M_{pq\sigma}\, G^0_{r_qj\sigma}(\tau_q - \tau')\,, \qquad \text{(B.3)}$$

where p and q run over the auxiliary spins ($s_p = \pm 1$) at imaginary time τ_p and at site positions r_p. The matrix $M_{pg\sigma}$ of size $N_s \times N_s$ depends on the configuration $\{s_i, r_i, \tau_i\}$ and may be in easily obtained in N_s^2 operations if knowing N_σ, details may be found in [39]. Notice that unlike in the original paper [39], here we use the convention $G_{ii\sigma}(\tau) < 0$ for $\tau \in (0, \beta)$, consistent with rest of the thesis. The second term in Eq. B.3 has the form of product of three matrices, $G^0 \cdot M \cdot G^0$. Thus $G_{ij\sigma}(\tau - \tau')$ may be evaluated at all pairs of sites ij in $O\left(NN_s(N + N_s)\right)$ operations, where $N = L\ell$ denotes the number of sites of the impurity cluster.

B.2.2 real space Green's function in frequency representation

Fourier transformation of Eq. B.3 yields the expression[1]

$$G_{ij\sigma}(i\omega_n) = G^0_{ij\sigma}(i\omega_n) - \frac{1}{\beta}\sum_{p,q} G^0_{ir_p\sigma}(i\omega_n)\, M_{pq\sigma}\, e^{i\omega_n(\tau_p-\tau_q)}\, G^0_{r_qj\sigma}(i\omega_n)\,, \quad \text{(B.6)}$$

$$= G^0_{ij\sigma}(i\omega_n) - \frac{1}{\beta}\sum_{r,r'} G^0_{ir\sigma}(i\omega_n)\, M_{rr'\sigma}(i\omega_n)\, G^0_{r'j\sigma}(i\omega_n)\,, \quad \text{(B.7)}$$

again having a form of matrix products $G^0 \cdot M \cdot G^0$, with

$$M_{rr'\sigma}(i\omega_n) = \sum_{p:r_p=r,q:r_q=r'} M_{pq\sigma}\, e^{i\omega_n(\tau_p-\tau_q)}\,, \quad \text{(B.8)}$$

of size $N \times N$.[2] As $G^0_\sigma(i\omega_n)$ is a constant matrix, it suffices to accumulate $M_{rr'\sigma}(i\omega_n)$. $G_{ij\sigma}(i\omega_n)$ is then obtained via Eq. B.7 at the end of the simulation, performing the matrix operations only once. For translationally symmetric problems we may reduce the number of independent indices in $M_{rr'\sigma}(i\omega_n)$ by symmetrizing over the same relative distance $\mathbf{\Delta}$,

$$M_{\mathbf{\Delta}\sigma}(i\omega_n) = \sum_{p,q:\mathbf{r}_p-\mathbf{r}_q=\mathbf{\Delta}} M_{pq\sigma}\, e^{i\omega_n(\tau_p-\tau_q)}\,. \quad \text{(B.9)}$$

The key quantity, $M_{rr'\sigma}(i\omega_n)$ or $M_{\mathbf{\Delta}\sigma}(i\omega_n)$, may be efficiently evaluated using the NFFT library performing non-equidistant fast Fourier transformation [116]. For

[1] Perform integration $\frac{1}{\beta}\int_0^\beta \mathrm{d}\tau\, e^{i\omega_n\tau} \int_0^\beta \mathrm{d}\tau'\, e^{-i\omega_n\tau'}$ on both sides of Eq. B.3 and use the definition

$$G(i\omega_n) = \int_0^\beta \mathrm{d}\tau\, e^{i\omega_n\tau} G(\tau) = \int_x^{x+\beta} \mathrm{d}\tau\, e^{i\omega_n\tau} G(\tau)\,, \qquad \text{for } x \in (-\beta, 0)\,, \quad \text{(B.4)}$$

to recover the left hand side and the first term on the right hand side of Eq. B.6. Further plug in the definition

$$G(\tau) = \frac{1}{\beta}\sum_{n=-\infty}^{\infty} e^{-i\omega_n\tau} G(i\omega_n)\,, \qquad \omega_n = \frac{(2n+1)\pi}{\beta}\,, \quad \text{(B.5)}$$

for the two other G^0-s on the the right hand side and utilizing $\int_0^\beta e^{i(\omega_n-\omega_m)\tau}\,\mathrm{d}\tau = \beta\delta_{mn}$ recover the Eq. B.6.

[2] High-frequency tail of the interacting Green's function shows that $M_{rr'\sigma}(i\omega_n)$ may approach a non-zero constant. In the case of Hubbard interaction that may happen only for $r = r'$, see Eq. A.29. In that case, the Fourier transformed $M_{rr'\sigma}(\tau)$ may be ill-defined.

measurements of frequencies $\omega_n = \frac{(2n+1)\pi}{\beta}$ for $n = 0, 1, \ldots, N_\omega - 1$ with even N_ω, we perform

$$M_{rr'\sigma}(i\omega_n) = \sum_\iota e^{i\pi(2n+1)\chi_\iota} M_{\iota\sigma} \tag{B.10}$$

$$= \sum_\iota e^{i\pi 2(n-N_\omega/2)\chi_\iota} \underbrace{e^{i\pi(N_\omega+1)\chi_\iota} M_{\iota\sigma}}_{\tilde{M}_{\iota\sigma}} \tag{B.11}$$

$$= \sum_\iota e^{i\pi 2n'\tilde{\chi}_\iota} \tilde{M}_{\iota\sigma}\,, \tag{B.12}$$

with $\chi_\iota = \frac{\tau_p - \tau_q}{\beta}$ with a multiindex $\iota \equiv (p,q)$ for (p,q) satisfying the conditions $r_p = r$, $r_q = r'$. $\tilde{\chi}_\iota$ denotes χ_ι shifted by an integer to the range $[-0.5, 0.5)$ to match the requirements of the NFFT library. The effective frequencies to be computed are $n' \equiv n - \frac{N_\omega}{2} \in \left\{-\frac{N_\omega}{2}, \ldots, \frac{N_\omega}{2} - 1\right\}$, as needed by NFFT. In the actual implementation it is worth to precompute $e^{i\pi(N_\omega+1)\tau_p/\beta}$ at the begin of the measurement. The quantity $M_{rr'\sigma}(i\omega_n)$ can be obtained in $O\left(N_s^2 + N^2 N_\omega \ln(N_\omega)\right)$.

B.2.3 Reciprocal Green's function in frequency representation

In the case of translationally symmetric problems (with multisite unit cells) we use FT of form

$$f_{\alpha_1\alpha_2}(\mathbf{r}_1, \mathbf{r}_2) = \frac{1}{L}\sum_{\mathbf{k}} e^{-i\mathbf{k}\cdot(\mathbf{r}_2 - \mathbf{r}_1)}\, e^{-i\mathbf{k}\cdot(\alpha_2 - \alpha_1)}\, f_{\alpha_1\alpha_2}(\mathbf{k})\,, \tag{B.13}$$

$$f_{\alpha_1\alpha_2}(\mathbf{k}) = \frac{1}{L}\sum_{\mathbf{r}_1,\mathbf{r}_2} e^{i\mathbf{k}\cdot(\mathbf{r}_2 - \mathbf{r}_1)}\, e^{i\mathbf{k}\cdot(\alpha_2 - \alpha_1)}\, f_{\alpha_1\alpha_2}(\mathbf{r}_1, \mathbf{r}_2)\,, \tag{B.14}$$

where α_i denotes the intracell site label and the intracell position vector in the scalar product with $\mathbf{k}$ vector, *e.g.* in $e^{-i\mathbf{k}\cdot(\alpha_2-\alpha_1)}$.[3] The real space site position r_p of an auxiliary spin p is then encoded by unit cell position vector $\mathbf{r}_p$ and the intracell site (vector) α_p. Then, the Fourier transformed Green's function estimator in Eq. B.6 reads

$$G_{\mathbf{k}\alpha_1\alpha_2\sigma}(i\omega_n) = G^0_{\mathbf{k}\alpha_1\alpha_2\sigma}(i\omega_n) - \frac{1}{\beta L}\sum_{p,q} G^0_{\mathbf{k}\alpha_1\alpha_p\sigma}(i\omega_n)\, G^0_{\mathbf{k}\alpha_q\alpha_2\sigma}(i\omega_n) \times M_{pq\sigma}\, e^{i\omega_n(\tau_p - \tau_q)}\, e^{-i\mathbf{k}\cdot(\mathbf{r}_p - \mathbf{r}_q)}\, e^{-i\mathbf{k}\cdot(\alpha_p - \alpha_q)}\,, \tag{B.15}$$

[3] In the rest of the thesis is the intracell site vector denoted by $\mathbf{r}_\alpha$. Here we break the convention to avoid notation $\mathbf{r}_{\alpha_1}$ or $\mathbf{r}_{\alpha_p}$.

where we used the Bravais sum over cell vectors $\mathbf{r}$, $\sum_{\mathbf{r}} e^{-i(\mathbf{k}-\mathbf{k}')\cdot\mathbf{r}} = L\delta_{\mathbf{k}\mathbf{k}'}$. Rewriting it to a form with matrix multiplication we get

$$G_{\mathbf{k}\alpha_1\alpha_2\sigma}(i\omega_n) = G^0_{\mathbf{k}\alpha_1\alpha_2\sigma}(i\omega_n) - \frac{1}{\beta L}\sum_{\alpha_3,\alpha_4} G^0_{\mathbf{k}\alpha_1\alpha_3\sigma}(i\omega_n)\, M_{\mathbf{k}\alpha_3\alpha_4\sigma}(i\omega_n)\, G^0_{\mathbf{k}\alpha_4\alpha_2\sigma}(i\omega_n)\,, \tag{B.16}$$

with

$$M_{\mathbf{k}\alpha_3\alpha_4\sigma}(i\omega_n) = \sum_{\boldsymbol{\Delta}} M_{\boldsymbol{\Delta}\alpha_3\alpha_4\sigma}(i\omega_n)\, e^{-i\mathbf{k}\cdot\boldsymbol{\Delta}}\, e^{-i\mathbf{k}\cdot(\alpha_3-\alpha_4)}\,, \tag{B.17}$$

$$M_{\boldsymbol{\Delta}\alpha_3\alpha_4\sigma}(i\omega_n) = \sum_{p,q:\alpha_p=\alpha_3,\alpha_q=\alpha_4,\mathbf{r}_p-\mathbf{r}_q=\boldsymbol{\Delta}} M_{pq\sigma}\, e^{i\omega_n(\tau_p-\tau_q)}\,. \tag{B.18}$$

An effective implementation accumulates $M_{\boldsymbol{\Delta}\alpha_3\alpha_4\sigma}(i\omega_n)$ using the NFFT library [116], described in Subsec. B.2.2, and performs Eq. B.17 and B.16 at the end of the simulation. The accumulation of $M_{\boldsymbol{\Delta}\alpha_3\alpha_4\sigma}(i\omega_n)$ runs in $O\left(N_s^2 + L\ell^2 N_\omega \ln(N_\omega)\right)$. The above expressions simplify considerably in the case of unit cell consisting of a single site, as all intracell site labels α_i are trivial in that case and may be ignored. If the studied model possesses spatial symmetries, it may be advantageous to perform Eq. B.17 with FFT immediately after the measurement, symmetrize $M_{\mathbf{k}\alpha_3\alpha_4\sigma}(i\omega_n)$ in the model symmetry subspace and by that reduce the number of observables to be accumulated.

B.3 Fidelity susceptibility estimator for CT-AUX

As a part of the study [4] dealing with new fidelity susceptibility estimator invented by Lei Wang, the author of the thesis conducted several tests with the CT-AUX impurity solver in the role of a finite lattice QMC solver, *i.e.* without any selfconsistency condition. The main finding of [4] was the fidelity susceptibility estimator,

$$\chi_F^{T\neq 0} = \frac{\langle k_L k_R\rangle - \langle k_L\rangle\langle k_R\rangle}{2\lambda^2}\,, \tag{B.19}$$

valid for any Hamiltonian of form,

$$\hat{H} = \hat{H}_0 + \lambda\hat{H}_1\,, \tag{B.20}$$

simulated with a QMC perturbatively around $\hat{H}_0$, *i.e.* expanding in λ,

$$Z = \mathrm{Tr}\left\{e^{-\beta\hat{H}}\right\} = \sum_{k=0}^{\infty}\lambda^k \int_0^\beta \mathrm{d}\tau_1 \ldots \int_{\tau_{k-1}}^\beta \mathrm{d}\tau_k \sum_{\mathcal{C}_k} w(\mathcal{C}_k, \{\tau\})\,, \tag{B.21}$$

where $\mathcal{C}_k$ are configurations of the order k to be sampled from, and $w(\mathcal{C}_k, \{\tau\})$ are their corresponding weights. The k_L in the estimator B.19 denotes the number of τs in an arbitrarily chosen window of size $\beta/2$ in the periodic imaginary time domain $[0, \beta)$, and $k_R = k - k_L$.[4] Clearly, $\langle k_L \rangle = \langle k_R \rangle = \langle k \rangle /2$.

The CT-AUX solver, applied on a model with Hubbard interaction,

$$\hat{H} = \hat{H}_0 + U \sum_i \left(\hat{n}_{i\uparrow} - \frac{1}{2} \right) \left(\hat{n}_{i\downarrow} - \frac{1}{2} \right) , \tag{B.22}$$

expands the partition function to form

$$Z = \sum_{k=0}^{\infty} \left(\frac{K}{2\beta} \right)^k \int_0^\beta \mathrm{d}\tau_1 \ldots \int_{\tau_{k-1}}^\beta \mathrm{d}\tau_k \sum_{\mathcal{C}_k} w\left(\mathcal{C}_k, \{\tau\}; \gamma\right) , \qquad \cosh\gamma = 1 + \frac{\beta U}{2K} , \tag{B.23}$$

where K is a non-physical simulation parameter (Sec. B.1), and $\mathcal{C}_k = (\{r\}, \{s\})$ is a set of k auxiliary spins, at space and time position (r_i, τ_i) with strength $s_i = \pm 1$.[5] Importantly, w depends on K only via γ (Eqs. 6a,6b of [39]). Choosing $K = \alpha\beta U/2$ with a non-zero constant α we get,

$$Z = \sum_{k=0}^{\infty} U^k \int_0^\beta \mathrm{d}\tau_1 \ldots \int_{\tau_{k-1}}^\beta \mathrm{d}\tau_k \sum_{\mathcal{C}_k} \underbrace{\alpha^k \, w\left(\mathcal{C}_k, \{\tau\}; \mathrm{acosh}(1 + \alpha^{-1})\right)}_{\tilde{w}(\mathcal{C}_k, \{\tau\})} , \tag{B.24}$$

where the new weights $\tilde{w}$ are U-independent. By that we matched the form of Z to Eq. B.21, justifying the use of the fidelity susceptibility estimator found in [4] within CT-AUX.[6]

In [4] the studied fermionic system was the Hubbard model on the honeycomb lattice at half filling, where sign-problem free QMC enable large finite lattice studies [138, 139, 140]. In [4] the simulations were performed with LCT-INT [40], but for the investigated model parameters the advantage of linear scaling in βU with respect to cubically scaling CT-AUX did not make the CT-AUX solver with submatrix updates [109] outperformed. We found out that for reasonable precision of χ_F large number of measurements need to be conducted. That is not surprising, as the estimator measures the correlation of k_L and k_R. In both solvers, LCT-INT

[4] For the accumulation of $k_L k_R$ we need to find k_L. That can obviously be done in linear time with k for a fixed position of the window in imaginary time and given configuration ($\{\tau\}$). It is however possible to find $k_L k_R = k_L(k - k_L)$ averaged over all positions of the window with the same complexity if $\{\tau\}$ is sorted.

[5] In Secs. B.1, B.2 the expansion order k was denoted by N_s.

[6] Notice that we did not add any contraint to K, this was just a trick to make the form of Z to match the starting point of the derivation used in [4]. Direct derivation of the fidelity susceptibility estimator without assumptions on K leads naturally to the same estimator.

and CT-AUX, the updates are local, rendering autocorrelation times of observables proportional to k local updates. In CT-AUX, the autocorrelation time of $\langle k_L k_R \rangle$ was practically identical with that of $\langle k \rangle$. For clusters of $2L^2$ sites simulated at $\beta t = L$ for $L = 6$, 9, 12 at $U/t = 4.1$ both autocorrelation times were roughly $15 \langle k \rangle$.[7] That opened question, if a non-local update, even at cost $\mathcal{O}(k^3)$,[8] could not reduce the autocorrelation times to $\alpha \langle k \rangle$ with $\alpha \sim 1$.

B.4 Attempt for a global update

We experimented with a global update performing move of the auxiliary spin along the imaginary axis. In CT-AUX, the auxiliary spin positions on the imaginary axis are the only auxiliary field parameters enabling continuous evolution. The secondary reason for such a global move originates in the form of the fidelity susceptibility estimator described in the previous section, of which the part $\langle k_L k_R \rangle$ depends on the auxiliary spin imaginary time positions τ_i. Conceptually we followed the work [197] utilizing Langevin dynamics with damped motion.[9]

For this update we propose normally distributed velocities v_i ($N(\mu = 0, \sigma = 1)$) of the k auxiliary spins along the (periodical) imaginary time axis. We further evaluate the force $f_i = \frac{1}{w} \frac{\partial w}{\partial \tau_i}$ on each spin, and propose its move to[10]

$$\tilde{\tau}_i = \tau_i + v_i t + f_i t^2/2 \,. \tag{B.25}$$

The evolution time t was set to fixed value proportional to $\beta N/k$, which is the average imaginary time difference between neighboring auxiliary spins at the same real space position.[11] This is self-balanced. The proposal probability for the move from $\{\tau\}$ is $(2\pi)^{-k/2} \exp\left(-\frac{1}{2}\sum_i v_i^2\right)$, which can be expressed in terms of τ_i, $\tilde{\tau}_i$, and f_i via Eq. B.25. For the proposal probability of the backward move needed to compute the Metropolis [35] acceptance rate R we need to evaluate the forces $\tilde{f}_i$ at the final positions $\tilde{\tau}_i$ as those enable determination of the velocities to get from

[7] The parameter K was chosen here close to $-0.975\,\frac{\beta U}{4}$; recall Sec. B.1.

[8] The cost of local update in CT-AUX is $\mathcal{O}(k^2)$.

[9] In [198], the authors propose to evolve the continuous Hubbard–Stratonovich fields with the molecular dynamics move. In CT-AUX, the auxiliary spins have discrete values, so the only continuous degree of freedom to move are the imaginary time positions of the auxiliary spins.

[10] Since we do Langevin dynamics, v_i fluctuates in time and therefore our time evolution is modeled as a sequence of steps with small t. This is different from the molecular dynamics approach, where with single v_i one tries to evolve over $\tau \sim \beta$ according to $\dot{\tau}_i = v_i$, $\dot{v}_i = f_i$, which is then to be solved by numeric integration using composite integration rule.

[11] This is motivated by the assumption of exponentially decreasing G^0 with real space distance, see the form of the force in Eq. B.28.

$\tilde{\tau}$ to τ.[12] The acceptance rate is given by

$$R = \min\left\{1,\ \frac{\tilde{w}}{w}\ \exp\left(-\frac{1}{2}\sum_i\left[\frac{t^2}{4}\left(\tilde{f}_i^2 - f_i^2\right) - (\tau_i - \tilde{\tau}_i)\left(\tilde{f}_i - f_i\right)\right]\right)\right\}\ , \quad \text{(B.26)}$$

where $\tilde{w}$ denotes $w\left(\mathcal{C}_k, \{\tilde{\tau}\}\right)$.

For the evaluation of the force f_i we need the explicit form of $w\left(\mathcal{C}_k, \{\tau\}\right)$, for the CT-AUX [39]

$$w\left(\mathcal{C}_k, \{\tau\}\right) = e^{-KN}\,\mathrm{Tr}\left\{e^{-\beta\hat{H}_0}\right\}\prod_\sigma \det N_\sigma^{-1}\left(\mathcal{C}_k, \{\tau\}\right)\ . \quad \text{(B.27)}$$

Using the form of N_σ^{-1} given in Eqs. 8,7 of [39] we find

$$\begin{aligned} f_i \ = \ \sum_{\sigma, j\neq i}\Bigg[& \left(N_\sigma\right)_{ij}\left(1 - e^{-\gamma(-1)^\sigma s_i}\right)\frac{\partial G^0_{r_j r_i \sigma}(\tau_j - \tau_i)}{\partial \tau_i} \\ & + \left(N_\sigma\right)_{ji}\left(1 - e^{-\gamma(-1)^\sigma s_j}\right)\frac{\partial G^0_{r_i r_j \sigma}(\tau_i - \tau_j)}{\partial \tau_i}\Bigg]\ . \end{aligned} \quad \text{(B.28)}$$

The G^0 are the non-interacting impurity Green's function on the input of the solver, in the DMFT or DCA context these would be $G^{0,\mathrm{imp}}$.

The complexity of this update is $\mathcal{O}\left(k^3\right)$, as we need to compute the determinant and the inverse of N_σ^{-1}. That limits the reasonable frequency of this type of update to once per $\mathcal{O}(k)$ local updates.[13] For the Langevin dynamics the evolution time t cannot be very long, as that would negatively influence the acceptance rate R. A composition of these steps is desirable. For a practical use one would have to overcome the need of the $\mathcal{O}\left(k^3\right)$ operations at every single time step.

Unfortunately, the gain in reduction of the autocorrelation times of $\langle k\rangle$ and $\langle k_L k_R\rangle$ (entering the fidelity susceptibility measurement) due to this type of global update did not outweigh its high cost, reducing the rate of effectively independent measurements.[14]

[12] This would not be needed if we would use reversible integrator within a molecular dynamics approach (see footnote 10) as that would directly compute the final velocities $\tilde{v}_i$ at the end of the time evolution.

[13] The proposed global update cannot be the only type of update, as that would break ergodicity – neither it changes the real space position r_i of the auxiliary spins, nor does it alter their count k.

[14] For the test, we performed a single global update attempt per q local update attempts, with q fixed to a value of expected $\langle k\rangle$. We ran the test for the finite lattice simulation of the Hubbard model on the honeycomb lattice, using a cluster of $N = 72$ sites, at $\beta t = 6$ and $U = 4.3t$.

C Free fermions

This appendix contains results for free fermions on a (general) lattice. The energy per site, density, and entropy per site can be computed for free fermions based on the DOS $\rho(\varepsilon)$,

$$n_0 = 2\int \mathrm{d}\varepsilon\, \rho(\varepsilon)\, f(\varepsilon-\mu;\beta)\,, \tag{C.1}$$

$$e_0 = 2\int \mathrm{d}\varepsilon\, \rho(\varepsilon)\, \varepsilon\, f(\varepsilon-\mu;\beta)\,, \tag{C.2}$$

$$\begin{aligned} s_0 = -2\int \mathrm{d}\varepsilon\, \rho(\varepsilon)\, &[f(\varepsilon-\mu;\beta)\ln f(\varepsilon-\mu;\beta) \\ &+ (1-f(\varepsilon-\mu;\beta))\ln\left(1-f(\varepsilon-\mu;\beta)\right)]\,, \end{aligned} \tag{C.3}$$

where the prefactor 2 accounts for the spin degeneracy, and $f(\epsilon;\beta) = \left(1+e^{\epsilon\beta}\right)^{-1}$ is the Fermi–Dirac distribution.

The 2-particle properties, in general, cannot be obtained purely from the knowledge of DOS. The double occupation is an exception, as for the case when σ is a good quantum number, it reduces to the density product for the two spin flavors,

$$\frac{1}{L}\sum_{\mathbf{r},\alpha}\langle \hat{n}_{\mathbf{r}\alpha\uparrow}\hat{n}_{\mathbf{r}\alpha\downarrow}\rangle_0 = \frac{1}{L^2}\sum_{\mathbf{r},\mathbf{r}',\alpha}\langle \hat{n}_{\mathbf{r}\alpha\uparrow}\rangle_0 \langle \hat{n}_{\mathbf{r}'\alpha\downarrow}\rangle_0\,, \tag{C.4}$$

where $\langle\ldots\rangle_0$ is the thermal average with index 0 indicating absence of interactions. In the above equation we used translational invariance of the lattice, $\langle \hat{n}_{\mathbf{0}\alpha}\rangle_0 = \frac{1}{L}\sum_{\mathbf{r}}\langle \hat{n}_{\mathbf{r}\alpha}\rangle_0$. For quantification of the spin-spin correlations of free fermions we need to know the dispersion, as it is shown in subsequent sections.

The free fermion results are clearly suitable for checks of this limit case of interacting fermions obtained by numerical methods capable to deal with interacting problems. Apart from that we used the EOS obtained for free fermions in the LDA calculations for the dilute limit (subsec. 3.4.1), in which density-density interactions can be neglected.[1]

[1] Another alternative for cheap calculation of the properties in the dilute case is the Hartree

C.1 Spin-spin correlations of free fermions on a Bravais lattice

In the present section we calculate the spin-spin correlation,

$$\left\langle \hat{C}_{\mathbf{\Delta}} \right\rangle_0 \equiv \frac{2}{L} \sum_{\mathbf{r}} \left\langle \hat{S}^z_{\mathbf{r}} \hat{S}^z_{\mathbf{r}+\mathbf{\Delta}} \right\rangle_0 , \tag{C.5}$$

$$= \frac{1}{2L} \sum_{\mathbf{r}} \langle \hat{n}_{\mathbf{r}\uparrow} \hat{n}_{\mathbf{r}+\mathbf{\Delta}\uparrow} + \hat{n}_{\mathbf{r}\downarrow} \hat{n}_{\mathbf{r}+\mathbf{\Delta}\downarrow} - \hat{n}_{\mathbf{r}\uparrow} \hat{n}_{\mathbf{r}+\mathbf{\Delta}\downarrow} - \hat{n}_{\mathbf{r}\downarrow} \hat{n}_{\mathbf{r}+\mathbf{\Delta}\uparrow} \rangle_0 , \tag{C.6}$$

of non-interacting (free) fermions at real space relative position $\mathbf{\Delta}$ for the case of a Bravais lattice.[2] The single particle eigenstates are labeled by $\mathbf{k}$ and spin projection σ (which is assumed to be a conserved quantity and thus it is a good quantum number). We denote the multiparticle eigenstates by $|\{n_{\mathbf{k}\sigma}\}\rangle = \prod_{\mathbf{k},\sigma} {c^\dagger_{\mathbf{k}\sigma}}^{n_{\mathbf{k}\sigma}} |0\rangle$.

Let us transform the spin-spin correlation operator $\hat{C}_{\mathbf{\Delta}}$ to the $\mathbf{k}$-space,

$$\frac{1}{2L} \sum_{\mathbf{r},\sigma,\sigma'=\pm 1} \sigma\sigma' \hat{n}_{\mathbf{r}\sigma} \hat{n}_{\mathbf{r}+\mathbf{\Delta}\sigma'} = \frac{1}{2L^2} \sum_{\mathbf{k},\mathbf{k}',\mathbf{q},\sigma,\sigma'} \sigma\sigma' e^{i\mathbf{\Delta}\cdot\mathbf{q}} \hat{c}^\dagger_{\mathbf{k}\sigma} \hat{c}_{\mathbf{k}-\mathbf{q}\sigma} \hat{c}^\dagger_{\mathbf{k}'\sigma'} \hat{c}_{\mathbf{k}'+\mathbf{q}\sigma'} . \tag{C.7}$$

Thus $\langle \{n_{\mathbf{k}\sigma}\}| \hat{C}_{\mathbf{\Delta}} |\{n_{\mathbf{k}\sigma}\}\rangle$ equals to[3]

$$\frac{1}{2L^2} \sum_{\mathbf{k},\mathbf{k}',\mathbf{q},\sigma,\sigma'} \sigma\sigma' e^{i\mathbf{\Delta}\cdot\mathbf{q}} \left[\delta_{\mathbf{q},\mathbf{0}} n_{\mathbf{k}\sigma} n_{\mathbf{k}'\sigma'} + \delta_{\sigma\sigma'} \delta_{\mathbf{k},\mathbf{k}'+\mathbf{q}} n_{\mathbf{k}\sigma} (1 - n_{\mathbf{k}'\sigma}) \right] . \tag{C.8}$$

We compute the thermal average using the above expression[4]

$$\sum_{|e\rangle} \frac{e^{-\beta\varepsilon}}{Z} \langle e| \hat{C}_{\mathbf{\Delta}} |e\rangle = \tag{C.9}$$

$$= \prod_{\mathbf{q}} \left[\sum_{n_{\mathbf{q}\uparrow}=0,1} \frac{e^{-\beta\varepsilon_{\mathbf{q}\uparrow}}}{1+e^{-\beta\varepsilon_{\mathbf{q}\uparrow}}} \sum_{n_{\mathbf{q}\downarrow}=0,1} \frac{e^{-\beta\varepsilon_{\mathbf{q}\downarrow}}}{1+e^{-\beta\varepsilon_{\mathbf{q}\downarrow}}} \right] \langle e| \hat{C}_{\mathbf{\Delta}} |e\rangle , \tag{C.10}$$

$$= \frac{1}{2L^2} \sum_{\mathbf{k},\mathbf{k}',\mathbf{q},\sigma,\sigma'} \sigma\sigma' e^{i\mathbf{\Delta}\cdot\mathbf{q}} \left[\delta_{\mathbf{q},\mathbf{0}} f_{\mathbf{k}\sigma} f_{\mathbf{k}'\sigma'} + \delta_{\sigma\sigma'} \delta_{\mathbf{k},\mathbf{k}'+\mathbf{q}} f_{\mathbf{k}\sigma} (1 - f_{\mathbf{k}'\sigma}) \right] + \mathcal{O}\left(L^{-1}\right) , \tag{C.11}$$

approximation, with additional cost due to the selfconsistent condition on densities.

[2] The onsite spin-spin correlation needs to be handled differently, since $\hat{n}_{\mathbf{r}\sigma}\hat{n}_{\mathbf{r}\sigma} = \hat{n}_{\mathbf{r}\sigma}$. We find $\left\langle \hat{C}_{\mathbf{\Delta}=\mathbf{0}} \right\rangle = \frac{n}{2}\left(1 - \frac{n}{2}\right)$, where n is the density (per site).

[3] Note that the term with $\mathbf{q} = \mathbf{0}$ and $\mathbf{k} = \mathbf{k}'$ is double counted. However, as it is proportional to $n_{\mathbf{k}\sigma}(1 - n_{\mathbf{k}\sigma})$, and $n_{\mathbf{k}\sigma} \in \{0, 1\}$, it vanishes.

[4] Note that in Eq. C.11, unlike in Eq. C.8, the term for the case $\mathbf{q} = 0 \wedge \mathbf{k} = \mathbf{k}'$ does not vanish, which is the reason for the presence of the subleading term of order L^{-1}.

where the last line was evaluated in the occupation basis $n_{\mathbf{q}\sigma}$; $f_{\mathbf{k}\sigma}$ is the short notation for the Fermi–Dirac distribution function $\left(1+e^{\beta(\varepsilon_{\mathbf{k}\sigma}-\mu)}\right)^{-1}$. The expression above may be written as (assuming $\boldsymbol{\Delta} \neq \mathbf{0}$),

$$\left\langle \hat{C}_{\boldsymbol{\Delta}} \right\rangle_0 = \frac{1}{2}(n_\uparrow - n_\downarrow)^2 - \frac{1}{2L^2} \sum_{\mathbf{k},\mathbf{q},\sigma} e^{i\boldsymbol{\Delta}\cdot\mathbf{q}} f_{\mathbf{k}\sigma} f_{\mathbf{k}-\mathbf{q}\sigma} \,. \tag{C.12}$$

For spin-independent energies ($\forall \mathbf{q}:\ \varepsilon_{\mathbf{q}\uparrow} = \varepsilon_{\mathbf{q}\downarrow}$) $n_\uparrow = n_\downarrow$, so we get

$$\frac{2}{L} \sum_{\mathbf{r}} \left\langle \hat{S}^z_{\mathbf{r}} \hat{S}^z_{\mathbf{r}+\boldsymbol{\Delta}} \right\rangle_0 = -\frac{1}{L^2} \sum_{\mathbf{k},\mathbf{q}} e^{i\boldsymbol{\Delta}\cdot\mathbf{q}} f_{\mathbf{k}} f_{\mathbf{k}-\mathbf{q}} = -\left| \frac{1}{L} \sum_{\mathbf{k}} e^{i\boldsymbol{\Delta}\cdot\mathbf{k}} f_{\mathbf{k}} \right|^2 . \tag{C.13}$$

C.2 Spin-spin correlations of free fermions on a general lattice

Here we deal with spin-spin correlations on a general lattice with 2 or more sublattices indexed with capital letters, $A, B, \ldots$. Greek letters α, γ stand for some sublattice index. The goal is to derive expression for

$$\left\langle \hat{C}_{\boldsymbol{\Delta}\alpha\gamma} \right\rangle \equiv \frac{2}{L} \sum_{\mathbf{r}} \left\langle \hat{S}^z_{\mathbf{r}\alpha} \hat{S}^z_{\mathbf{r}+\boldsymbol{\Delta}\gamma} \right\rangle = \frac{1}{2L} \sum_{\mathbf{r},\sigma,\sigma'=\pm1} \sigma\sigma' \left\langle \hat{n}_{\mathbf{r}\alpha\sigma} \hat{n}_{\mathbf{r}+\boldsymbol{\Delta}\gamma\sigma'} \right\rangle \,, \tag{C.14}$$

where $\mathbf{r}$ denotes the real space position of the unit cell and $\boldsymbol{\Delta}$ is the unit cell relative position. Transformation to reciprocal space yields expression,

$$\hat{C}_{\boldsymbol{\Delta}\alpha\gamma} = \frac{1}{2L^2} \sum_{\mathbf{k},\mathbf{k}',\mathbf{q},\sigma,\sigma'} \sigma\sigma' e^{i\boldsymbol{\Delta}\cdot\mathbf{q}}\, \hat{c}^\dagger_{\mathbf{k}\alpha\sigma} \hat{c}_{\mathbf{k}-\mathbf{q}\alpha\sigma} \hat{c}^\dagger_{\mathbf{k}'\gamma\sigma'} \hat{c}_{\mathbf{k}'+\mathbf{q}\gamma\sigma'} \,. \tag{C.15}$$

Now we need to specify the Hamiltonian, which we consider to be of the form,

$$\hat{H} = \sum_{\mathbf{k},\alpha,\gamma,\sigma} \hat{c}^\dagger_{\mathbf{k}\alpha\sigma} h_{\mathbf{k}\alpha\gamma\sigma} \hat{c}_{\mathbf{k}\gamma\sigma} \,, \tag{C.16}$$

with α and γ running over the sublattices. We diagonalize $h_{\mathbf{k}\alpha\gamma\sigma}$ with a unitary transformation in the sublattice space at each $\mathbf{k}$ and σ,

$$\hat{H} = \sum_{\mathbf{k},n,\sigma} = \hat{d}^\dagger_{\mathbf{k}n\sigma} \varepsilon_{\mathbf{k}n\sigma} \hat{d}_{\mathbf{k}n\sigma} \,, \tag{C.17}$$

with transformation given by

$$\hat{c}^\dagger_{\mathbf{k}\alpha\sigma} = \sum_n U^*_{n\alpha}(\mathbf{k},\sigma)\, \hat{d}^\dagger_{\mathbf{k}n\sigma} \,, \qquad \hat{c}_{\mathbf{k}\alpha\sigma} = \sum_n U_{n\alpha}(\mathbf{k},\sigma)\, \hat{d}_{\mathbf{k}n\sigma} \,. \tag{C.18}$$

For the evaluation of $\left\langle \hat{C}_{\mathbf{\Delta}\alpha\gamma} \right\rangle$ for free fermions it is suitable to express the operator $\hat{C}_{\mathbf{\Delta}\alpha\gamma}$ in the free fermions eigenstate operators $d_{\mathbf{k}n\sigma}$, $d^\dagger_{\mathbf{k}n\sigma}$,

$$\begin{aligned}\hat{C}_{\mathbf{\Delta}\alpha\gamma} = \\ = \frac{1}{2L^2}\sum_{\sigma,\sigma'}\sigma\sigma' \sum_{\mathbf{k},\mathbf{k}',\mathbf{q},,n,n',m,m'} e^{i\mathbf{\Delta}\cdot\mathbf{q}} U^*_{n\alpha}(\mathbf{k},\sigma)U_{m\alpha}(\mathbf{k}-\mathbf{q},\sigma)U^*_{n'\gamma}(\mathbf{k}',\sigma') \\ U_{m'\gamma}(\mathbf{k}'+\mathbf{q},\sigma')\,\hat{d}^\dagger_{\mathbf{k}n\sigma}\hat{d}_{\mathbf{k}-\mathbf{q}m\sigma}\hat{d}^\dagger_{\mathbf{k}'n'\sigma'}\hat{d}_{\mathbf{k}'+\mathbf{q}m'\sigma'}\,. \qquad \text{(C.19)}\end{aligned}$$

Thus $\langle\{n_{\mathbf{k}n\sigma}\}|\,\hat{C}_{\mathbf{\Delta}\alpha\gamma}\,|\{n_{\mathbf{k}n\sigma}\}\rangle$ equals to

$$\begin{aligned}&\frac{1}{2L^2}\sum_{\mathbf{k},\mathbf{k}',n,n',\sigma} U^*_{n\alpha}(\mathbf{k},\sigma)U_{n'\alpha}(\mathbf{k}',\sigma)U^*_{n'\gamma}(\mathbf{k}',\sigma)U_{n\gamma}(\mathbf{k},\sigma)\,e^{i\mathbf{\Delta}\cdot(\mathbf{k}-\mathbf{k}')}\,n_{\mathbf{k}n\sigma}(1-n_{\mathbf{k}'n'\sigma}) \\ &+\frac{1}{2L^2}\sum_{\sigma,\sigma'}\sigma\sigma'\sum_{\mathbf{k},\mathbf{k}',n,n'}|U_{n\alpha}(\mathbf{k},\sigma)|^2\,|U_{n'\gamma}(\mathbf{k}',\sigma')|^2\,n_{\mathbf{k}n\sigma}n_{\mathbf{k}'n'\sigma'}\,. \qquad \text{(C.20)}\end{aligned}$$

Under assumption of σ independence of $h_{\mathbf{k}\alpha\gamma\sigma}$ the second term does not contribute at zero (finite) temperature, as the unitary matrices and occupation numbers (Fermi–Dirac distributions) will in that case be σ independent as well. In the rest we assume the σ independence of $\hat{H}$. Thus we have to deal only with the first term. Using the property of the unitary matrices $U(\mathbf{k},\sigma)$,

$$\sum_n U_{n\alpha}(\mathbf{k},\sigma)U^*_{n\gamma}(\mathbf{k},\sigma) = \delta_{\alpha\gamma}\,, \qquad \text{(C.21)}$$

and the Bravais sum over $\mathbf{k}'$ we see that the part independent on $n_{\mathbf{k}'n'\sigma}$ contributes only in the case of onsite spin-spin correlations, for $\mathbf{\Delta}=\mathbf{0}$ and $\alpha=\gamma$.[5] In the other case we find for a thermal ensemble the expression,

$$\left\langle \hat{C}_{\mathbf{\Delta}\alpha\gamma} \right\rangle = -\left|\frac{1}{L}\sum_{\mathbf{k},n} U^*_{n\alpha}(\mathbf{k})U_{n\gamma}(\mathbf{k})\,e^{i\mathbf{\Delta}\cdot\mathbf{k}}\,f_{\mathbf{k}n}\right|^2 + \mathcal{O}\left(L^{-1}\right)\,. \qquad \text{(C.22)}$$

For a bipartite lattice with two sublattices A, B,[6] *i.e.* with hoppings only between sites on different sublattices, $h_{\mathbf{k}\alpha\alpha}=0$ at half filling. Consequently $\varepsilon_{\mathbf{k}n} = \pm|h_{\mathbf{k}AB}|$, $|U_{n\alpha}(\mathbf{k})|^2 = 1/2$, and $\sum_n f_{\mathbf{k}n} = 1$, implying that $\left\langle \hat{C}_{\mathbf{\Delta}\alpha\alpha} \right\rangle$ vanishes for $\mathbf{\Delta}\neq 0$.

[5] For onsite spin-spin correlation the formula in footnote 2 applies.

[6] Example lattices: honeycomb lattice nearest neighbor hoppings, (anisotropic) cubic or square lattice with nearest neighbor hoppings.

D High-temperature series expansion

For various tasks, *e.g.* for entropy estimates, it is important to know the analytic behavior of various observables, valid at least in some parameter range. High-temperature series expansion (HTSE) provides such estimate for temperature larger than any other energy scales involved in the problem. We assume the Hamiltonian $\hat{H} = \hat{H}_0 + \hat{H}_U$ be of this form,

$$\hat{H}_U = \sum_i U_i \hat{n}_{i\uparrow}\hat{n}_{i\downarrow}\,, \qquad \hat{H}_0 = -\sum_{i,j,\sigma} \tilde{h}_{ij\sigma}\hat{c}^\dagger_{i\sigma}\hat{c}_{j\sigma}\,, \tag{D.1}$$

with

$$\tilde{h}_{ij\sigma} = t_{ij\sigma} + (\tilde{\mu} - V_{i\sigma})\delta_{ij}\,. \tag{D.2}$$

Notice that we included the chemical potential $\tilde{\mu}$ into the non-interacting Hamiltonian $\hat{H}_0$. As $\hat{N}$ we denote the total particle number operator,

$$\hat{N} = \sum_{i,\sigma} \hat{n}_{i\sigma}\,. \tag{D.3}$$

Since it is particularly convenient to perform the HTSE in real space basis, we do not explicitly adapt the site notation $\mathbf{r}\alpha$ used in the rest of the thesis. We nevertheless assume that U_i and $\tilde{h}_{ij\sigma}$ are translationally invariant.

D.1 High-temperature expansion in general

Let's assume an operator $\hat{O}$ and some Hamiltonian $\hat{H}$. Its high-temperature, *i.e.* low β, expansion is given by,

$$\begin{aligned}
\left\langle \hat{O} \right\rangle &= \frac{\sum_i \langle i| \hat{O} e^{-\beta \hat{H}} |i\rangle}{\sum_i \langle i| e^{-\beta \hat{H}} |i\rangle} && \text{(D.4)} \\
&= \beta^0 \left[\frac{1}{\Theta} \operatorname{Tr}\left\{ \hat{O} \right\} \right] - \beta^1 \left[\frac{1}{\Theta} \operatorname{Tr}\left\{ \hat{O}\hat{H} \right\} - \frac{1}{\Theta^2} \operatorname{Tr}\left\{ \hat{O} \right\} \operatorname{Tr}\left\{ \hat{H} \right\} \right] \\
&\quad + \beta^2 \left[\frac{1}{2\Theta} \operatorname{Tr}\left\{ \hat{O}\hat{H}^2 \right\} - \frac{1}{\Theta^2} \operatorname{Tr}\left\{ \hat{O}\hat{H} \right\} \operatorname{Tr}\left\{ \hat{H} \right\} \right. \\
&\qquad \left. - \frac{1}{2\Theta^2} \operatorname{Tr}\left\{ \hat{O} \right\} \operatorname{Tr}\left\{ \hat{H}^2 \right\} + \frac{1}{\Theta^3} \operatorname{Tr}\left\{ \hat{O} \right\} \operatorname{Tr}\left\{ \hat{H} \right\}^2 \right] \\
&\quad + \mathcal{O}(\beta^3) , && \text{(D.5)}
\end{aligned}$$

with traces over the multiparticle states $|i\rangle$; $\Theta \equiv \operatorname{Tr}\left\{ \hat{\mathbb{1}} \right\}$ is the dimension of the problem. For our $\hat{H} = \hat{H}_0 + \hat{H}_U$ as defined in Eq. D.1 it is convenient to evaluate the traces using the real space basis $|\{n_{\mathbf{r}\alpha\sigma}\}\rangle = \Pi_{\mathbf{r},\alpha,\sigma} \left(c^\dagger_{\mathbf{r}\alpha\sigma} \right)^{n_{\mathbf{r}\alpha\sigma}} |0\rangle$. We assume that the system contains L cells labeled by $\mathbf{r}$, each with ℓ sites denoted by α, and two flavors $\sigma \in \{\uparrow, \downarrow\}$.

Here we list traces which appear in Eq. D.5 and are $\hat{O}$-independent,

$$\begin{aligned}
\sum_i \langle i| \mathbb{1} |i\rangle &= 2^{\sum_{\mathbf{r},\alpha,\sigma} 1} = 2^{2\ell L} \equiv \Theta , && \text{(D.6)} \\
\sum_i \langle i| \hat{H} |i\rangle &= L\Theta \left[\frac{1}{2} \sum_{\alpha,\sigma} (V_{\alpha\sigma} - \tilde{\mu}) + \frac{1}{4} \sum_\alpha U_\alpha \right] , && \text{(D.7)} \\
\sum_i \langle i| \hat{H}^2 |i\rangle &= \frac{L\Theta}{4} \left[L \left(\sum_{\alpha,\sigma} (V_{\alpha\sigma} - \tilde{\mu} + U_\alpha/2) \right)^2 \right. \\
&\qquad + \sum_{\alpha,\sigma} (V_{\alpha\sigma} - \tilde{\mu})^2 + \sum_{\alpha,\sigma} (V_{\alpha\sigma} - \tilde{\mu}) U_\alpha + \frac{3}{4} \sum_\alpha U_\alpha^2 \\
&\qquad \left. + \sum_{\alpha,\alpha',\mathbf{\Delta},\sigma:(\alpha,\mathbf{0}) \neq (\alpha',\mathbf{\Delta})} |t^\sigma_{\mathbf{\Delta}\alpha\alpha'}|^2 \right] . && \text{(D.8)}
\end{aligned}$$

These were obtained via traces, evaluated with simple combinatorics,

$$\mathrm{Tr}\left\{\hat{c}_i^\dagger \hat{c}_j\right\} = \frac{\Theta}{2}\delta_{ij}\,, \tag{D.9}$$

$$\mathrm{Tr}\left\{\hat{n}_a \hat{c}_i^\dagger \hat{c}_j\right\} = \frac{\Theta}{4}\delta_{ij}\left(1+\delta_{ai}\right)\,, \tag{D.10}$$

$$\mathrm{Tr}\left\{\hat{c}_a^\dagger \hat{c}_{a'} \hat{c}_b^\dagger \hat{c}_{b'}\right\} = \frac{\Theta}{4}\delta_{ab'}\delta_{a'b}\,, \qquad \text{for } a\neq a',\ b\neq b'\,, \tag{D.11}$$

$$\mathrm{Tr}\left\{\hat{n}_a \hat{n}_b \hat{c}_i^\dagger \hat{c}_j\right\} = \frac{\Theta}{8}\delta_{ij}\left(1+\delta_{ab}+\delta_{bi}+\delta_{ai}\right)\,, \tag{D.12}$$

$$\mathrm{Tr}\left\{\hat{n}_{a\sigma}\hat{n}_{b\sigma'}\hat{n}_{c\uparrow}\hat{n}_{c\downarrow}\right\} = \frac{\Theta}{16}\left[1+\delta_{ac}+\delta_{bc}+\delta_{ab}\delta_{\sigma\sigma'}+\delta_{ab}\delta_{bc}\delta_{ac}\left(1-\delta_{\sigma\sigma'}\right)\right]\,. \tag{D.13}$$

It is noticeable that expression D.8 contains terms with different behavior with respect to the size L. That is the consequence of not excluding disconnected graphs at evaluation of the traces D.9-D.13. Since we assume $L\to\infty$, boundary terms do not play a role and any intensive physical quantity has to be proportional to L^0.

D.2 Equation of states

Now we calculate the HTSE of the average density per site, called as well filling, $\frac{1}{\ell L}\left\langle \hat{N}\right\rangle$. For that we need further traces,

$$\mathrm{Tr}\left\{\hat{c}_{a\sigma}^\dagger \hat{c}_{b\sigma}\hat{n}_{c\sigma'}\hat{c}_{b\sigma}^\dagger \hat{c}_{a\sigma}\right\} = \frac{\Theta}{8}\left(1+\delta_{bc}\delta_{\sigma\sigma'}-\delta_{ac}\delta_{\sigma\sigma'}\right)\,, \qquad \text{for } a\neq b\,, \tag{D.14}$$

$$\mathrm{Tr}\left\{\hat{n}_{a\sigma}\hat{n}_{b\uparrow}\hat{n}_{b\downarrow}\hat{n}_{c\uparrow}\hat{n}_{c\downarrow}\right\} = \frac{\Theta}{32}\left(1+\delta_{ab}+\delta_{ac}+3\delta_{bc}+2\delta_{ab}\delta_{bc}\delta_{ac}\right)\,. \tag{D.15}$$

The HTSE of density is given by

$$n(\beta) = 1-\frac{\beta}{4\ell}\sum_{\alpha,\sigma}\left(V_{\alpha\sigma}-\mu\right)+\frac{\beta^2}{16\ell}\sum_{\alpha,\sigma}\left(V_{\alpha\sigma}-\mu\right)U+\mathcal{O}(\beta^3)\,. \tag{D.16}$$

In the above expression we set $\tilde{\mu}=\mu+U/2$, and $U_\alpha = U$.

Analogously we would get for the magnetization $m=\frac{1}{\ell L}\left\langle\sum_i\left(\hat{n}_{i\uparrow}-\hat{n}_{i\downarrow}\right)\right\rangle$,

$$m = -\frac{\beta}{4\ell}\sum_{\alpha,\sigma}\sigma V_{\alpha\sigma}-\frac{\beta^2}{16\ell}\sum_{\alpha,\sigma}\sigma V_{\alpha\sigma}U+\mathcal{O}(\beta^3)\,, \tag{D.17}$$

with $\sigma=\pm 1$.

For the energy per site, $e = \frac{1}{\ell L}\left\langle \hat{H} + \tilde{\mu}\hat{N} \right\rangle$, we need further traces,

$$\begin{aligned}
\mathrm{Tr}\left\{\hat{c}^\dagger_a \hat{c}_{a'} \hat{c}^\dagger_b \hat{c}_{b'} \hat{c}^\dagger_c \hat{c}_{c'}\right\} &= \frac{\Theta}{8}\left(\delta_{a'b}\delta_{b'c}\delta_{c'a} - \delta_{a'c}\delta_{b'a}\delta_{c'b}\right) , \\
&\qquad \text{for } a \neq a',\ b \neq b',\ c \neq c' , \qquad \text{(D.18)} \\
\mathrm{Tr}\left\{\hat{c}^\dagger_{a\sigma} \hat{c}_{b\sigma} \hat{n}_{c\uparrow} \hat{n}_{c\downarrow} \hat{c}^\dagger_{b\sigma} \hat{c}_{a\sigma}\right\} &= \frac{\Theta}{16}\left(1 + \delta_{bc} - \delta_{ac}\right) , \qquad \text{for } a \neq b , \qquad \text{(D.19)} \\
\mathrm{Tr}\left\{\hat{n}_{a\uparrow}\hat{n}_{a\downarrow}\hat{n}_{b\uparrow}\hat{n}_{b\downarrow}\hat{n}_{c\uparrow}\hat{n}_{c\downarrow}\right\} &= \frac{\Theta}{64}\left(1 + 3\delta_{ab} + 3\delta_{bc} + 3\delta_{ac} + 6\delta_{ab}\delta_{bc}\delta_{ac}\right) . \qquad \text{(D.20)}
\end{aligned}$$

The HTSE of e up to second order in β equals to

$$\begin{aligned}
e(\beta) &= \frac{1}{2\ell}\sum_{\alpha,\sigma} V_{\alpha\sigma} + \frac{U}{4} \\
&\quad - \beta\left\{\frac{1}{4\ell}\sum_{\alpha,\sigma}\left(V_{\alpha\sigma} - \mu\right)\left(V_{\alpha\sigma} + \frac{U}{2}\right) + \frac{U^2}{16} + \frac{1}{4\ell}\sum_{\alpha,\alpha',\boldsymbol{\Delta},\sigma}\left|t_{\boldsymbol{\Delta}\alpha\alpha'\sigma}\right|^2\right\} \\
&\quad + \frac{\beta^2 U}{32\ell}\sum_{\alpha,\sigma}\left[\mu^2 + UV_{\alpha\sigma} + 3V_{\alpha\sigma}V_{\alpha\bar{\sigma}} - \mu U - 4\mu V_{\alpha\sigma}\right] + \mathcal{O}(\beta^3) . \qquad \text{(D.21)}
\end{aligned}$$

The HTSE for entropy per site may be estimated using Eq. 3.2,

$$s(\beta) = \ln 4 + \frac{f'(\beta=0)}{2}\beta^2 + \frac{f''(\beta=0)}{3}\beta^3 + \mathcal{O}\left(\beta^4\right) , \qquad \text{(D.22)}$$

with $f(\beta) = e(\beta) - \tilde{\mu}n(\beta = 0)$.

For a model with $V_{\alpha\sigma} = (\pm 1)^\alpha h\sigma$, *e.g.* with homogeneous or staggered magnetic field, and $t_{\boldsymbol{\Delta}\alpha\alpha'\sigma} = t_{\boldsymbol{\Delta}\alpha\alpha'}$ we get the following simpler expressions,

$$e(\beta) = \frac{U}{4} - \beta\left(\frac{U^2}{16} + \frac{h^2}{2} - \frac{U\mu}{4} + \frac{W_2}{2}\right) + \frac{\beta^2 U}{16}\left(\mu^2 - U\mu - 3h^2\right) + \mathcal{O}(\beta^3) , \qquad \text{(D.23)}$$

$$n(\beta) = 1 + \frac{\beta\mu}{2} - \frac{\beta^2 U\mu}{8} + \mathcal{O}(\beta^3) , \qquad \text{(D.24)}$$

$$s(\beta) = \ln 4 - \frac{\beta^2}{4}\left[\frac{U^2}{8} + \mu^2 + h^2 + W_2\right] + \frac{\beta^3 U}{8}\left(\mu^2 - h^2\right) + \mathcal{O}(\beta^4) , \qquad \text{(D.25)}$$

with W_2 standing for the second moment of the non-interacting density of states, under the present restrictions $W_2 = \frac{1}{\ell}\sum_{\boldsymbol{\Delta},\alpha,\alpha'}\left|t_{\boldsymbol{\Delta}\alpha\alpha'}\right|^2$.[1] The magnetization is in this case

$$|m| = \frac{\beta h}{2} + \frac{\beta^2 U h}{8} + \mathcal{O}\left(\beta^3\right) , \qquad \text{(D.26)}$$

[1] For single site per cell, W_2 reduces to $\sum_{\boldsymbol{\Delta}\neq\mathbf{0}}\left|t_{\mathbf{0}\boldsymbol{\Delta}}\right|^2$.

thus the (staggered) susceptibility is asymptotically equal to $(2T)^{-1}$.

As explained at the begin of Chap. D, HTSE is capable to capture the physics for temperatures $T = 1/\beta$ much larger than $U, t, |\mu|, h$. Notice, that μ as well enters the HTSE expressions for EOS and therefore influences useful range of β in the above HTSEs.[2]

D.3 Spin-spin correlations

The (z component of) spin-spin correlation is defined as

$$\left\langle \hat{S}_i^z \hat{S}_j^z \right\rangle = \frac{1}{4} \sum_{\sigma,\sigma'=\pm 1} \sigma\sigma' \left\langle \hat{n}_{i\sigma} \hat{n}_{j\sigma'} \right\rangle , \qquad \text{for } i \neq j . \tag{D.27}$$

For the HTSE of the spin-spin correlation we need to evaluate $\mathrm{Tr}\left\{\hat{n}_{i\sigma}\hat{n}_{j\sigma'}\hat{H}^n\right\}$ for $n = 0, 1, 2, \ldots$. Thanks to the factor $\sigma\sigma'$ in its definition, only those terms may contribute to it, which depend simultaneously on σ and σ'. Therefore $\mathrm{Tr}\left\{\hat{S}_i^z \hat{S}_j^z\right\} = 0$ and $\mathrm{Tr}\left\{\hat{S}_i^z \hat{S}_j^z \hat{H}\right\} = 0$ (using Eqs. D.12, D.13). Thus, for the quadratic high-T behavior we need to evaluate only the term $\mathrm{Tr}\left\{\hat{n}_{i\sigma}\hat{n}_{j\sigma'}\hat{H}^2\right\}$, out of which only the part involving virtual hopping there and back survives the test on simultaneous dependence on σ and σ'.

The $\mathrm{Tr}\left\{\hat{n}_{i\sigma}\hat{n}_{j\sigma'}\hat{H}_U^2\right\}$ generates terms of form

$$\begin{aligned} \mathrm{Tr}\left\{\hat{n}_{a\sigma}\hat{n}_{b\sigma'}\hat{n}_{i\uparrow}\hat{n}_{i\downarrow}\hat{n}_{j\uparrow}\hat{n}_{j\downarrow}\right\} &= \frac{\Theta}{64}\left[1 + \delta_{ai} + \delta_{bi} + \delta_{aj} + \delta_{bj} + 3\delta_{ij} + 2\delta_{ij}\left(\delta_{ia} + \delta_{ib}\right)\right] \\ &\qquad \text{for } a \neq b , \end{aligned} \tag{D.28}$$

$\mathrm{Tr}\left\{\hat{n}_{i\sigma}\hat{n}_{j\sigma'}\hat{H}_U\hat{H}_0\right\}$ generates

$$\begin{aligned} \mathrm{Tr}\left\{\hat{n}_{a\sigma}\hat{n}_{b\sigma'}\hat{n}_{k\uparrow}\hat{n}_{k\downarrow}\hat{n}_{i\sigma''}\right\} &= \frac{\Theta}{32}\left[1 + \delta_{ai}\delta_{\sigma\sigma''} + \delta_{bi}\delta_{\sigma'\sigma''} + \delta_{ik} + \delta_{ak} + \delta_{bk}\right. \\ &\quad \left. + \delta_{ik}\delta_{ka}\left(1 - \delta_{\sigma\sigma''}\right) + \delta_{ik}\delta_{kb}\left(1 - \delta_{\sigma'\sigma''}\right)\right] \\ &\qquad \text{for } a \neq b , \end{aligned} \tag{D.29}$$

$\mathrm{Tr}\left\{\hat{n}_{i\sigma}\hat{n}_{j\sigma'}\hat{H}_{0,\mathrm{local}}^2\right\}$ generates

$$\mathrm{Tr}\left\{\hat{n}_a\hat{n}_b\hat{n}_c\hat{n}_d\right\} = \frac{\Theta}{16}\left(1 + \delta_{ab} + \delta_{ac} + \delta_{ad} + \delta_{bc} + \delta_{bd} + \delta_{cd} + \delta_{ab}\delta_{bc}\delta_{cd}\right) , \tag{D.30}$$

[2] In a system with μ much lower than the bandwidth W, *i.e.* with $-\mu \gg W$, the density, energy per site, and entropy, all decreases rapidly with increasing β to zero.

and $\mathrm{Tr}\left\{\hat{n}_{i\sigma}\hat{n}_{j\sigma'}\hat{H}^2_{0,\mathrm{non-local}}\right\}$ generates

$$\begin{aligned}\mathrm{Tr}\left\{\hat{n}_{a\sigma}\hat{n}_{b\sigma'}\hat{c}^\dagger_{i\sigma''}\hat{c}_{j\sigma''}\hat{c}^\dagger_{j\sigma''}\hat{c}_{i\sigma''}\right\} &= \frac{\Theta}{16}\left[1+\delta_{\sigma\sigma''}\left(\delta_{ai}-\delta_{aj}\right)+\delta_{\sigma'\sigma''}\left(\delta_{bi}-\delta_{bj}\right)\right.\\ &\quad\left.-\delta_{\sigma\sigma''}\delta_{\sigma'\sigma''}\left(\delta_{aj}\delta_{bi}+\delta_{ai}\delta_{bj}\right)\right]\\ &\quad\text{for } a\neq b\,. \end{aligned} \tag{D.31}$$

Thus, up to second order in β, the spin-spin correlation is given by

$$\left\langle \hat{S}^z_i\hat{S}^z_j\right\rangle = -\frac{\beta^2}{32}\left|t_{ij}\right|^2+\mathcal{O}\left(\beta^3\right)\,. \tag{D.32}$$

List of publications

[1] Jakub Imriška, Mauro Iazzi, Lei Wang, Emanuel Gull, Daniel Greif, Thomas Uehlinger, Gregor Jotzu, Leticia Tarruell, Tilman Esslinger, and Matthias Troyer, "Thermodynamics and magnetic properties of the anisotropic 3D Hubbard model," Phys. Rev. Lett. **112**, 115301 (Mar 2014), http://link.aps.org/doi/10.1103/PhysRevLett.112.115301.

[2] Jakub Imriška, Emanuel Gull, and Matthias Troyer, "Thermodynamics of the Hubbard model on stacked honeycomb and square lattices," arxiv, 1509.08919(Sept 2015), http://arxiv.org/abs/1509.08919.

[3] Jakub Imriška, Lei Wang, and Matthias Troyer, "First order topological phase transition of the Haldane–Hubbard model," arxiv, 1604.03553(Apr 2016), http://arxiv.org/abs/1604.03553.

[4] Lei Wang, Ye-Hua Liu, Jakub Imriška, Ping Nang Ma, and Matthias Troyer, "Fidelity susceptibility made simple: A unified quantum Monte Carlo approach," Phys. Rev. X **5**, 031007 (Jul 2015), http://link.aps.org/doi/10.1103/PhysRevX.5.031007.

[5] Jakub Imriška, Mauro Iazzi, Lei Wang, Emanuel Gull, Daniel Greif, Thomas Uehlinger, Gregor Jotzu, Leticia Tarruell, Tilman Esslinger, and Matthias Troyer, "Erratum: Thermodynamics and magnetic properties of the anisotropic 3D Hubbard model [Phys. Rev. Lett. 112, 115301 (2014)]," Phys. Rev. Lett. **112**, 159903 (Apr 2014), http://link.aps.org/doi/10.1103/PhysRevLett.112.159903.

[6] M. Dolfi, J. Gukelberger, A. Hehn, J. Imriška, K. Pakrouski, T. F. Rønnow, M. Troyer, I. Zintchenko, F. Chirigati, J. Freire, and D. Shasha, "A model project for reproducible papers: critical temperature for the Ising model on a square lattice," arXiv(Jan. 2014), arXiv:1401.2000 [cs.CE], http://arxiv.org/abs/1401.2000

Bibliography

[7] G. Roati, E. de Mirandes, F. Ferlaino, H. Ott, G. Modugno, and M. Inguscio, "Atom Interferometry with trapped Fermi gases," Phys. Rev. Lett. **92**, 230402 (Jun 2004), http://link.aps.org/doi/10.1103/PhysRevLett.92.230402.

[8] J M Leinaas and J Myrheim, "On the theory of identical particles," Nuovo Cim. B Ser. 11 **37**, 1–23 (1977), ISSN 0369-3554, http://dx.doi.org/10.1007/BF02727953.

[9] Frank Wilczek, "Quantum mechanics of fractional-spin particles," Phys. Rev. Lett. **49**, 957–959 (Oct 1982), http://link.aps.org/doi/10.1103/PhysRevLett.49.957.

[10] Gregory Moore and Nicholas Read, "Nonabelions in the fractional quantum hall effect," Nucl. Phys. B **360**, 362–396 (Aug 1991), ISSN 0550-3213, http://www.sciencedirect.com/science/article/pii/055032139190407O.

[11] P. W. Anderson, "More is different," Science **177**, 393–396 (Aug 1972), http://www.worldscientific.com/doi/pdf/10.1142/9789812385123_others01.

[12] Gordon W. Semenoff, "Condensed-matter simulation of a three-dimensional anomaly," Phys. Rev. Lett. **53**, 2449–2452 (Dec 1984), http://link.aps.org/doi/10.1103/PhysRevLett.53.2449.

[13] K. S. Novoselov, A. K. Geim, S. V. Morozov, D. Jiang, M. I. Katsnelson, I. V. Grigorieva, S. V. Dubonos, and A. A. Firsov, "Two-dimensional gas of massless Dirac fermions in graphene," Nature **438**, 197–200 (Nov 2005), http://dx.doi.org/10.1038/nature04233.

[14] J. Bardeen, L. N. Cooper, and J. R. Schrieffer, "Microscopic theory of superconductivity," Phys. Rev. **106**, 162–164 (Apr 1957), http://link.aps.org/doi/10.1103/PhysRev.106.162.

[15] R. B. Laughlin, "Anomalous quantum Hall effect: An incompressible quantum fluid with fractionally charged excitations," Phys. Rev. Lett. **50**, 1395–1398 (May 1983), http://link.aps.org/doi/10.1103/PhysRevLett.50.1395.

[16] M. J. Rice and Y. R. Wang, "Excitations of a diamagnetic hole state in the copper oxide superconductors," Phys. Rev. B **36**, 8794–8797 (Dec 1987), http://link.aps.org/doi/10.1103/PhysRevB.36.8794.

[17] F. C. Zhang and T. M. Rice, "Effective Hamiltonian for the superconducting Cu oxides," Phys. Rev. B **37**, 3759–3761 (Mar 1988), http://link.aps.org/doi/10.1103/PhysRevB.37.3759.

[18] J. Hubbard, "Electron correlations in narrow energy bands," Proceedings of the Royal Society of London. Series A. Mathematical and Physical Sciences **276**, 238–257 (1963).

[19] M. Jarrell, Th. Maier, M. H. Hettler, and A. N. Tahvildarzadeh, "Phase diagram of the Hubbard model: Beyond the dynamical mean field," EPL **56**, 563 (2001), http://stacks.iop.org/0295-5075/56/i=4/a=563.

[20] T. A. Maier, M. S. Jarrell, and D. J. Scalapino, "Understanding high-temperature superconductors with quantum cluster theories," Physica C: Superconductivity and its Applications **460–462, Part 1**, 13–19 (2007), ISSN 0921-4534, proceedings of the 8th International Conference on Materials and Mechanisms of Superconductivity and High Temperature SuperconductorsM2S-HTSC {VIII}, http://www.sciencedirect.com/science/article/pii/S0921453407000871.

[21] Peter Staar, Thomas Maier, and Thomas C. Schulthess, "Two-particle correlations in a dynamic cluster approximation with continuous momentum dependence: Superconductivity in the two-dimensional Hubbard model," Phys. Rev. B **89**, 195133 (May 2014), http://link.aps.org/doi/10.1103/PhysRevB.89.195133.

[22] Emanuel Gull, Olivier Parcollet, and Andrew J. Millis, "Superconductivity and the pseudogap in the two-dimensional Hubbard model," Phys. Rev. Lett. **110**, 216405 (May 2013), http://link.aps.org/doi/10.1103/PhysRevLett.110.216405.

[23] M. Born and R. Oppenheimer, "Zur Quantentheorie der Molekeln," Annalen der Physik **389**, 457–484 (1927), ISSN 1521-3889, http://dx.doi.org/10.1002/andp.19273892002.

[24] P Hohenberg and W Kohn, "Inhomogeneous electron gas," Phys. Rev. **136**, B864–B871 (Nov 1964), http://link.aps.org/doi/10.1103/PhysRev.136.B864.

[25] W Kohn and L Sham, "Self-consistent equations including exchange and correlation effects," Phys. Rev. **140**, A1133–A1138 (Nov 1965), http://link.aps.org/doi/10.1103/PhysRev.140.A1133.

[26] Stefan Goedecker, "Linear scaling electronic structure methods," Rev. Mod. Phys. **71**, 1085–1123 (Jul 1999), http://link.aps.org/doi/10.1103/RevModPhys.71.1085.

[27] Kris Van Houcke, Evgeny Kozik, N. Prokof'ev, and B. Svistunov, "Diagrammatic Monte Carlo," Phys. Procedia **6**, 95–105 (Feb 2010), ISSN 1875-3892, http://www.sciencedirect.com/science/article/pii/S1875389210006498.

[28] E Kozik, K Van Houcke, E Gull, L Pollet, N Prokof'ev, B Svistunov, and M Troyer, "Diagrammatic Monte Carlo for correlated fermions," Europhys. Lett. **90**, 10004 (Jul 2010), http://stacks.iop.org/0295-5075/90/i=1/a=10004.

[29] Jan Gukelberger, *From non-unitary anyons to unconventional superfluidity*, Ph.D. thesis, ETH Zurich (2015), http://e-collection.library.ethz.ch/eserv/eth:47786/eth-47786-02.pdf.

[30] J. Hubbard, "Calculation of partition functions," Phys. Rev. Lett. **3**, 77–78 (Jul 1959), http://link.aps.org/doi/10.1103/PhysRevLett.3.77.

[31] J. E. Hirsch, "Discrete Hubbard-Stratonovich transformation for fermion lattice models," Phys. Rev. B **28**, 4059–4061 (Oct 1983), http://link.aps.org/doi/10.1103/PhysRevB.28.4059.

[32] G. C. Wick, "The evaluation of the collision matrix," Phys. Rev. **80**, 268–272 (Oct 1950), http://link.aps.org/doi/10.1103/PhysRev.80.268.

[33] H. F. Trotter, "On the product of semi-groups of operators," Proceedings of the American Mathematical Society **10**, 545–551 (1959), ISSN 00029939, 10886826, http://www.jstor.org/stable/2033649.

[34] Masuo Suzuki, "Relationship between d-dimensional quantal spin systems and $(d + 1)$-dimensional Ising systems: Equivalence, critical exponents and systematic approximants of the partition function and spin correlations," Progress of Theoretical Physics **56**, 1454–1469 (1976), http://ptp.oxfordjournals.org/content/56/5/1454.full.pdf+html, `http://ptp.oxfordjournals.org/content/56/5/1454.abstract`.

[35] Nicholas Metropolis, Arianna W. Rosenbluth, Marshall N. Rosenbluth, Augusta H. Teller, and Edward Teller, "Equation of state calculations by fast computing machines," The Journal of Chemical Physics **21**, 1087–1092 (1953), `http://scitation.aip.org/content/aip/journal/jcp/21/6/10.1063/1.1699114`.

[36] R. Blankenbecler, D. J. Scalapino, and R. L. Sugar, "Monte Carlo calculations of coupled boson-fermion systems. I," Phys. Rev. D **24**, 2278–2286 (Oct 1981), `http://link.aps.org/doi/10.1103/PhysRevD.24.2278`.

[37] J. E. Hirsch and R. M. Fye, "Monte Carlo method for magnetic impurities in metals," Phys. Rev. Lett. **56**, 2521–2524 (Jun 1986), `http://link.aps.org/doi/10.1103/PhysRevLett.56.2521`.

[38] S. M. A. Rombouts, K. Heyde, and N. Jachowicz, "Quantum Monte Carlo method for fermions, free of discretization errors," Phys. Rev. Lett. **82**, 4155–4159 (May 1999), `http://link.aps.org/doi/10.1103/PhysRevLett.82.4155`.

[39] E. Gull, P. Werner, O. Parcollet, and M. Troyer, "Continuous-time auxiliary-field Monte Carlo for quantum impurity models," EPL **82**, 57003 (May 2008), `http://stacks.iop.org/0295-5075/82/i=5/a=57003?key=crossref.a04bd39c153e80d2afe29b4a20da2527`.

[40] Mauro Iazzi and Matthias Troyer, "Efficient continuous-time quantum Monte Carlo algorithm for fermionic lattice models," Phys. Rev. B **91**, 241118 (Jun 2015), `http://link.aps.org/doi/10.1103/PhysRevB.91.241118`.

[41] E. Y. Loh, J. E. Gubernatis, R. T. Scalettar, S. R. White, D. J. Scalapino, and R. L. Sugar, "Sign problem in the numerical simulation of many-electron systems," Phys. Rev. B **41**, 9301–9307 (May 1990), `http://link.aps.org/doi/10.1103/PhysRevB.41.9301`.

[42] Matthias Troyer and Uwe-Jens Wiese, "Computational complexity and fundamental limitations to fermionic quantum Monte Carlo simulations," Phys. Rev. Lett. **94**, 170201 (May 2005), `http://link.aps.org/doi/10.1103/PhysRevLett.94.170201`.

[43] Lei Wang, Ye-Hua Liu, Mauro Iazzi, Matthias Troyer, and Gergely Harcos, "Split orthogonal group: A guiding principle for sign-problem-free fermionic simulations," Phys. Rev. Lett. **115**, 250601 (Dec 2015), http://link.aps.org/doi/10.1103/PhysRevLett.115.250601.

[44] Mauro Iazzi, Alexey A. Soluyanov, and Matthias Troyer, "Topological origin of the fermion sign problem," Phys. Rev. B **93**, 115102 (Mar 2016), http://link.aps.org/doi/10.1103/PhysRevB.93.115102.

[45] Steven R. White, "Density matrix formulation for quantum renormalization groups," Phys. Rev. Lett. **69**, 2863–2866 (Nov 1992), http://link.aps.org/doi/10.1103/PhysRevLett.69.2863.

[46] Steven R. White and Adrian E. Feiguin, "Real-time evolution using the density matrix renormalization group," Phys. Rev. Lett. **93**, 076401 (Aug 2004), http://link.aps.org/doi/10.1103/PhysRevLett.93.076401.

[47] A J Daley, C Kollath, U Schollwöck, and G Vidal, "Time-dependent density-matrix renormalization-group using adaptive effective Hilbert spaces," Journal of Statistical Mechanics: Theory and Experiment **2004**, P04005 (2004), http://stacks.iop.org/1742-5468/2004/i=04/a=P04005.

[48] Ulrich Schollwöck, "The density-matrix renormalization group in the age of matrix product states," Annals of Physics **326**, 96–192 (2011), ISSN 0003-4916, january 2011 Special Issue, http://www.sciencedirect.com/science/article/pii/S0003491610001752.

[49] J. Eisert, M. Cramer, and M. B. Plenio, "*Colloquium* : Area laws for the entanglement entropy," Rev. Mod. Phys. **82**, 277–306 (Feb 2010), http://link.aps.org/doi/10.1103/RevModPhys.82.277.

[50] Simeng Yan, David A. Huse, and Steven R. White, "Spin-liquid ground state of the S = 1/2 kagome Heisenberg antiferromagnet," Science **332**, 1173–1176 (2011), ISSN 0036-8075, http://science.sciencemag.org/content/332/6034/1173.full.pdf, http://science.sciencemag.org/content/332/6034/1173.

[51] Philippe Corboz, Román Orús, Bela Bauer, and Guifré Vidal, "Simulation of strongly correlated fermions in two spatial dimensions with fermionic projected entangled-pair states," Phys. Rev. B **81**, 165104 (Apr 2010), http://link.aps.org/doi/10.1103/PhysRevB.81.165104.

[52] Philippe Corboz, Steven R. White, Guifré Vidal, and Matthias Troyer, "Stripes in the two-dimensional t-j model with infinite projected entangled-pair states," Phys. Rev. B **84**, 041108 (Jul 2011), http://link.aps.org/doi/10.1103/PhysRevB.84.041108.

[53] Walter Metzner and Dieter Vollhardt, "Correlated lattice fermions in $d = \infty$ dimensions," Phys. Rev. Lett. **62**, 324–327 (Jan 1989), http://link.aps.org/doi/10.1103/PhysRevLett.62.324.

[54] Antoine Georges and Gabriel Kotliar, "Hubbard model in infinite dimensions," Phys. Rev. B **45**, 6479–6483 (Mar 1992), http://link.aps.org/doi/10.1103/PhysRevB.45.6479.

[55] Antoine Georges, Gabriel Kotliar, Werner Krauth, and Marcelo J. Rozenberg, "Dynamical mean-field theory of strongly correlated fermion systems and the limit of infinite dimensions," Rev. Mod. Phys. **68**, 13–125 (Jan 1996), http://link.aps.org/doi/10.1103/RevModPhys.68.13.

[56] A. I. Lichtenstein and M. I. Katsnelson, "***Ab initio*** calculations of quasiparticle band structure in correlated systems: LDA++ approach," Phys. Rev. B **57**, 6884–6895 (Mar 1998), http://link.aps.org/doi/10.1103/PhysRevB.57.6884.

[57] G. Kotliar and D. Vollhardt, "Strongly correlated materials: Insights from dynamical mean-field theory," Physics Today **57**, 53 (Mar 2004), http://scitation.aip.org/content/aip/magazine/physicstoday/article/57/3/10.1063/1.1712502.

[58] M. Karolak, G. Ulm, T. Wehling, V. Mazurenko, A. Poteryaev, and A. Lichtenstein, "Double counting in lda + dmft — the example of *nio*," Journal of Electron Spectroscopy and Related Phenomena **181**, 11–15 (2010), ISSN 0368-2048, proceedings of International Workshop on Strong Correlations and Angle-Resolved Photoemission Spectroscopy 2009, http://www.sciencedirect.com/science/article/pii/S0368204810001222.

[59] Thomas Maier, Mark Jarrell, Thomas Pruschke, and Matthias H Hettler, "Quantum cluster theories," Rev. Mod. Phys. **77**, 1027 (2005), http://rmp.aps.org/abstract/RMP/v77/i3/p1027_1.

[60] M. H. Hettler, A. N. Tahvildar-Zadeh, M. Jarrell, T. Pruschke, and H. R. Krishnamurthy, "Nonlocal dynamical correlations of strongly interacting electron systems," Phys. Rev. B **58**, R7475–R7479 (Sep 1998), http://link.aps.org/doi/10.1103/PhysRevB.58.R7475.

[61] Gabriel Kotliar, Sergej Y. Savrasov, Gunnar Pálsson, and Giulio Biroli, "Cellular dynamical mean field approach to strongly correlated systems," Phys. Rev. Lett. **87**, 186401 (Oct 2001), http://link.aps.org/doi/10.1103/PhysRevLett.87.186401.

[62] Gerald Knizia and Garnet Kin-Lic Chan, "Density matrix embedding: A simple alternative to dynamical mean-field theory," Phys. Rev. Lett. **109**, 186404 (Nov 2012), http://link.aps.org/doi/10.1103/PhysRevLett.109.186404.

[63] George H. Booth and Garnet Kin-Lic Chan, "Spectral functions of strongly correlated extended systems via an exact quantum embedding," Phys. Rev. B **91**, 155107 (Apr 2015), http://link.aps.org/doi/10.1103/PhysRevB.91.155107.

[64] J. P. F. LeBlanc, Andrey E. Antipov, Federico Becca, Ireneusz W. Bulik, Garnet Kin-Lic Chan, Chia-Min Chung, Youjin Deng, Michel Ferrero, Thomas M. Henderson, Carlos A. Jiménez-Hoyos, E. Kozik, Xuan-Wen Liu, Andrew J. Millis, N. V. Prokof'ev, Mingpu Qin, Gustavo E. Scuseria, Hao Shi, B. V. Svistunov, Luca F. Tocchio, I. S. Tupitsyn, Steven R. White, Shiwei Zhang, Bo-Xiao Zheng, Zhenyue Zhu, and Emanuel Gull (Simons Collaboration on the Many-Electron Problem), "Solutions of the two-dimensional hubbard model: Benchmarks and results from a wide range of numerical algorithms," Phys. Rev. X **5**, 041041 (Dec 2015), http://link.aps.org/doi/10.1103/PhysRevX.5.041041.

[65] S. M. Griffin, P. Staar, T. C. Schulthess, M. Troyer, and N. A. Spaldin, "A bespoke single-band Hubbard model material," Phys. Rev. B **93**, 075115 (Feb 2016), http://link.aps.org/doi/10.1103/PhysRevB.93.075115.

[66] Jannik C. Meyer, A. K. Geim, M. I. Katsnelson, K. S. Novoselov, T. J. Booth, and S. Roth, "The structure of suspended graphene sheets," Nature **446**, 60–63 (Mar 2007), http://dx.doi.org/10.1038/nature05545.

[67] Immanuel Bloch, Jean Dalibard, and Wilhelm Zwerger, "Many-body physics with ultracold gases," Rev. Mod. Phys. **80**, 885–964 (Jul 2008), http://link.aps.org/doi/10.1103/RevModPhys.80.885.

[68] Stefano Giorgini, Lev P. Pitaevskii, and Sandro Stringari, "Theory of ultracold atomic fermi gases," Rev. Mod. Phys. **80**, 1215–1274 (Oct 2008), http://link.aps.org/doi/10.1103/RevModPhys.80.1215.

[69] Tilman Esslinger, "Fermi-Hubbard physics with atoms in an optical lattice," Annual Review of Condensed Matter Physics **1**, 129–152 (Aug 2010), http://www.annualreviews.org/doi/abs/10.1146/annurev-conmatphys-070909-104059.

[70] Immanuel Bloch, Jean Dalibard, and Sylvain Nascimbene, "Quantum simulations with ultracold quantum gases," Nat Phys **8**, 267–276 (Apr 2012), http://dx.doi.org/10.1038/nphys2259.

[71] Alexander L. Gaunt, Tobias F. Schmidutz, Igor Gotlibovych, Robert P. Smith, and Zoran Hadzibabic, "Bose-Einstein condensation of atoms in a uniform potential," Phys. Rev. Lett. **110**, 200406 (May 2013), http://link.aps.org/doi/10.1103/PhysRevLett.110.200406.

[72] Daniel Greif, Gregor Jotzu, Michael Messer, Rémi Desbuquois, and Tilman Esslinger, "Formation and dynamics of anti-ferromagnetic correlations in tunable optical lattices," arXiv, 1509.00854(Sep 2015), http://arxiv.org/abs/1509.00854.

[73] G. Jotzu, M. Messer, R. Desbuquois, M. Lebrat, T. Uehlinger, D. Greif, and T. Esslinger, "Experimental realization of the topological Haldane model with ultracold fermions," Nature **515**, 237–240 (Nov 2014), http://dx.doi.org/10.1038/nature13915.

[74] S Trotzky, L Pollet, F Gerbier, U Schnorrberger, I Bloch, N V Prokof'ev, B Svistunov, and M Troyer, "Suppression of the critical temperature for superfluidity near the Mott transition," Nat Phys **6**, 998–1004 (Dec 2010), ISSN 1745-2473, http://www.nature.com/nphys/journal/v6/n12/abs/nphys1799.html.

[75] R. Jördens, L. Tarruell, D. Greif, T. Uehlinger, N. Strohmaier, H. Moritz, T. Esslinger, L. De Leo, C. Kollath, A. Georges, V. Scarola, L. Pollet, E. Burovski, E. Kozik, and M. Troyer, "Quantitative determination of temperature in the approach to magnetic order of ultracold fermions in an optical lattice," Phys. Rev. Lett. **104**, 180401 (May 2010), http://link.aps.org/doi/10.1103/PhysRevLett.104.180401.

[76] G. Rickayzen, *Green's functions and condensed matter* (Academic Press, London, 1980).

[77] Gerald D. Mahan, *Many-Particle Physics* (Kluwer Academic/Plenum Publishers, New York, 2000).

[78] M. H. Hettler, M. Mukherjee, M. Jarrell, and H. R. Krishnamurthy, "Dynamical cluster approximation: Nonlocal dynamics of correlated electron systems," Phys. Rev. B **61**, 12739–12756 (May 2000), http://link.aps.org/doi/10.1103/PhysRevB.61.12739.

[79] M. Jarrell, Th. Maier, C. Huscroft, and S. Moukouri, "Quantum Monte Carlo algorithm for nonlocal corrections to the dynamical mean-field approximation," Phys. Rev. B **64**, 195130 (Oct 2001), http://link.aps.org/doi/10.1103/PhysRevB.64.195130.

[80] A. I. Lichtenstein and M. I. Katsnelson, "Antiferromagnetism and d-wave superconductivity in cuprates: A cluster dynamical mean-field theory," Phys. Rev. B **62**, R9283–R9286 (Oct 2000), http://link.aps.org/doi/10.1103/PhysRevB.62.R9283.

[81] S. Okamoto, A. J. Millis, H. Monien, and A. Fuhrmann, "Fictive impurity models: An alternative formulation of the cluster dynamical mean-field method," Phys. Rev. B **68**, 195121 (Nov 2003), http://link.aps.org/doi/10.1103/PhysRevB.68.195121.

[82] Peter Staar, Thomas Maier, and Thomas C. Schulthess, "Dynamical cluster approximation with continuous lattice self-energy," Phys. Rev. B **88**, 115101 (Sep 2013), http://link.aps.org/doi/10.1103/PhysRevB.88.115101.

[83] K. Aryanpour, M. H. Hettler, and M. Jarrell, "Dynamical cluster approximation employing the fluctuation exchange approximation as a cluster solver," Phys. Rev. B **67**, 085101 (Feb 2003), http://link.aps.org/doi/10.1103/PhysRevB.67.085101.

[84] Emanuel Gull, Andrew J. Millis, Alexander I. Lichtenstein, Alexey N. Rubtsov, Matthias Troyer, and Philipp Werner, "Continuous-time Monte Carlo methods for quantum impurity models," Rev. Mod. Phys. **83**, 349–404 (May 2011), http://link.aps.org/doi/10.1103/RevModPhys.83.349.

[85] E. Khatami, C. R. Lee, Z. J. Bai, R. T. Scalettar, and M. Jarrell, "Cluster solver for dynamical mean-field theory with linear scaling in inverse temperature," Phys. Rev. E **81**, 056703 (May 2010), http://link.aps.org/doi/10.1103/PhysRevE.81.056703.

[86] Ansgar Liebsch and Wei Wu, "Coulomb correlations in the honeycomb lattice: Role of translation symmetry," Phys. Rev. B **87**, 205127 (May 2013), http://link.aps.org/doi/10.1103/PhysRevB.87.205127.

[87] Gregory E. Stewart, Donald D. Betts, and James S. Flynn, "Extension of the method of exact diagonalization of quantum spin models to finite face centred cubic lattices and estimation of the $t = 0$ properties of the $s = 1/2$ xy ferromagnet on the infinite fcc lattice," Journal of the Physical Society of Japan **66**, 3231 (1997), http://dx.doi.org/10.1143/JPSJ.66.3231.

[88] J. N. Lyness, T. Sørevik, and P. Keast, "Notes on integration and integer sublattices," Mathematics of computation **56**, 243 (Jan 1991), http://www.ams.org/journals/mcom/1991-56-193/S0025-5718-1991-1052101-8/.

[89] D. D. Betts and G. E. Stewart, "Estimation of zero-temperature properties of quantum spin systems on the simple cubic lattice via exact diagonalization on finite lattices," Canadian Journal of Physics **75**, 47 (1997), http://www.nrcresearchpress.com/doi/pdf/10.1139/p96-129, http://www.nrcresearchpress.com/doi/abs/10.1139/p96-129.

[90] D D Betts, H Q Lin, and J S Flynn, "Improved finite-lattice estimates of the properties of two quantum spin models on the infinite square lattice," Canadian Journal of Physics **77**, 353 (1999), http://www.nrcresearchpress.com/doi/pdf/10.1139/p99-041, http://www.nrcresearchpress.com/doi/abs/10.1139/p99-041.

[91] "Fastest Fourier transform in the west," Software library, http://fftw.org/.

[92] C.B. Barber, D.P. Dobkin, and H.T. Huhdanpaa, "The Quickhull algorithm for convex hulls," ACM Transactions on Mathematical Software **22**, 469 (Dec 1996), http://www.qhull.org.

[93] Lee C. Martin, *The Kondo lattice model: A dynamical cluster approximation approach*, Ph.D. thesis, Julius-Maximilians-Universität Würzburg (2010), http://opus.bibliothek.uni-wuerzburg.de/frontdoor.php?source_opus=4944&la=en.

[94] Maciej Lewenstein, Anna Sanpera, Veronica Ahufinger, Bogdan Damski, Aditi Sen, and Ujjwal Sen, "Ultracold atomic gases in optical lattices: mimicking condensed matter physics and beyond," Adv Phys **56**, 243–379 (Mar 2007).

[95] Robert Jördens, Niels Strohmaier, Kenneth Günter, Henning Moritz, and Tilman Esslinger, "A Mott insulator of fermionic atoms in an optical lattice," Nature **455**, 204–207 (Sep. 2008), http://www.nature.com/doifinder/10.1038/nature07244.

[96] U Schneider, L Hackermuller, S Will, Th Best, I Bloch, T A Costi, R W Helmes, D Rasch, and A Rosch, "Metallic and insulating phases of repulsively interacting fermions in a 3D optical lattice," Science **322**, 1520–1525 (Dec 2008), http://www.sciencemag.org/cgi/doi/10.1126/science.1165449.

[97] D Greif, T Uehlinger, G Jotzu, L Tarruell, and T Esslinger, "Short-range quantum magnetism of ultracold fermions in an optical lattice," Science **340**, 1307–1310 (Jun 2013), http://www.sciencemag.org/cgi/doi/10.1126/science.1236362.

[98] Daniel Greif, Leticia Tarruell, Thomas Uehlinger, Robert Jördens, and Tilman Esslinger, "Probing nearest-neighbor correlations of ultracold fermions in an optical lattice," Phys. Rev. Lett. **106**, 145302 (Apr 2011), http://link.aps.org/doi/10.1103/PhysRevLett.106.145302.

[99] Thomas Uehlinger, Gregor Jotzu, Michael Messer, Daniel Greif, Walter Hofstetter, Ulf Bissbort, and Tilman Esslinger, "Artificial graphene with tunable interactions," Phys. Rev. Lett. **111**, 185307 (Oct 2013), http://link.aps.org/doi/10.1103/PhysRevLett.111.185307.

[100] R. Staudt, M. Dzierzawa, and A. Muramatsu, "Phase diagram of the three-dimensional Hubbard model at half filling," The European Physical Journal B **17**, 411 (Oct 2000), http://link.springer.com/article/10.1007%2Fs100510070120.

[101] P. R. C. Kent, M. Jarrell, T. A. Maier, and Th. Pruschke, "Efficient calculation of the antiferromagnetic phase diagram of the three-dimensional Hubbard model," Phys. Rev. B **72**, 060411 (Aug 2005), http://link.aps.org/doi/10.1103/PhysRevB.72.060411.

[102] Sebastian Fuchs, Emanuel Gull, Lode Pollet, Evgeni Burovski, Evgeny Kozik, Thomas Pruschke, and Matthias Troyer, "Thermodynamics of the 3D Hubbard model on approaching the Néel transition," Phys. Rev. Lett. **106**, 030401 (Jan 2011), http://link.aps.org/doi/10.1103/PhysRevLett.106.030401.

[103] Thereza Paiva, Yen Lee Loh, Mohit Randeria, Richard T. Scalettar, and Nandini Trivedi, "Fermions in 3D optical lattices: Cooling protocol to obtain antiferromagnetism," Phys. Rev. Lett. **107**, 086401 (Aug 2011), http://link.aps.org/doi/10.1103/PhysRevLett.107.086401.

[104] E. Kozik, E. Burovski, V. W. Scarola, and M. Troyer, "Néel temperature and thermodynamics of the half-filled three-dimensional Hubbard model by

diagrammatic determinant Monte Carlo," Phys. Rev. B **87**, 205102 (May 2013), http://link.aps.org/doi/10.1103/PhysRevB.87.205102.

[105] C. Yasuda, S. Todo, K. Hukushima, F. Alet, M. Keller, M. Troyer, and H. Takayama, "Néel temperature of quasi-low-dimensional Heisenberg antiferromagnets," Phys. Rev. Lett. **94**, 217201 (Jun 2005), http://link.aps.org/doi/10.1103/PhysRevLett.94.217201.

[106] V. W. Scarola, L. Pollet, J. Oitmaa, and M. Troyer, "Discerning incompressible and compressible phases of cold atoms in optical lattices," Phys. Rev. Lett. **102**, 135302 (Mar 2009), http://link.aps.org/doi/10.1103/PhysRevLett.102.135302.

[107] Qi Zhou and Tin-Lun Ho, "Universal thermometry for quantum simulation," Phys. Rev. Lett. **106**, 225301 (2011), http://link.aps.org/doi/10.1103/PhysRevLett.106.225301.

[108] Simone Chiesa, Christopher N. Varney, Marcos Rigol, and Richard T. Scalettar, "Magnetism and pairing of two-dimensional trapped fermions," Phys. Rev. Lett. **106**, 035301 (Jan 2011), http://link.aps.org/doi/10.1103/PhysRevLett.106.035301.

[109] Emanuel Gull, Peter Staar, Sebastian Fuchs, Phani Nukala, Michael S Summers, Thomas Pruschke, Thomas C Schulthess, and Thomas Maier, "Submatrix updates for the continuous-time auxiliary-field algorithm," Phys. Rev. B **83**, 075122 (Feb 2011), http://link.aps.org/doi/10.1103/PhysRevB.83.075122.

[110] Th. A. Maier and M. Jarrell, "Comparison of two-quantum-cluster approximations," Phys. Rev. B **65**, 041104 (Jan 2002), http://link.aps.org/doi/10.1103/PhysRevB.65.041104.

[111] Shinya Yasuda and Synge Todo, "Monte Carlo simulation with aspect-ratio optimization: Anomalous anisotropic scaling in dimerized antiferromagnets," Phys. Rev. E **88**, 061301 (Dec 2013), http://link.aps.org/doi/10.1103/PhysRevE.88.061301.

[112] J. E. Hirsch, "Simulations of the three-dimensional Hubbard model: Half-filled band sector," Phys. Rev. B **35**, 1851–1859 (Feb 1987), http://link.aps.org/doi/10.1103/PhysRevB.35.1851.

[113] A. N. Rubtsov and A. I. Lichtenstein, "Continuous-time quantum Monte Carlo method for fermions: Beyond auxiliary field framework," JETP Letters **80**, 61 (2004), http://link.springer.com/article/10.1134%2F1.1800216.

[114] A. N. Rubtsov, V. V. Savkin, and A. I. Lichtenstein, "Continuous-time quantum Monte Carlo method for fermions," Phys. Rev. B **72**, 035122 (Jul 2005), http://link.aps.org/doi/10.1103/PhysRevB.72.035122.

[115] G. Rohringer, A. Valli, and A. Toschi, "Local electronic correlation at the two-particle level," Phys. Rev. B **86**, 125114 (Sep 2012), http://link.aps.org/doi/10.1103/PhysRevB.86.125114.

[116] Jens Keiner, Stefan Kunis, and Daniel Potts, "Nonequispaced fast Fourier transform," Software library, https://www-user.tu-chemnitz.de/~potts/nfft/.

[117] Thereza Paiva, Richard Scalettar, Mohit Randeria, and Nandini Trivedi, "Fermions in 2d optical lattices: Temperature and entropy scales for observing antiferromagnetism and superfluidity," Phys. Rev. Lett. **104**, 066406 (Feb 2010), http://link.aps.org/doi/10.1103/PhysRevLett.104.066406.

[118] Anders W. Sandvik, "Critical temperature and the transition from quantum to classical order parameter fluctuations in the three-dimensional Heisenberg antiferromagnet," Phys. Rev. Lett. **80**, 5196–5199 (Jun 1998), http://link.aps.org/doi/10.1103/PhysRevLett.80.5196.

[119] Nan Lin, *Cluster dynamical mean-field theory: Applications to high-T_c cuprates and to quantum chemistry*, Ph.D. thesis, Columbia University (2012), http://academiccommons.columbia.edu/catalog/ac:147701.

[120] E. V. Gorelik, D. Rost, T. Paiva, R. Scalettar, A. Klümper, and N. Blümer, "Universal probes for antiferromagnetic correlations and entropy in cold fermions on optical lattices," Phys. Rev. A **85**, 061602 (Jun 2012), http://link.aps.org/doi/10.1103/PhysRevA.85.061602.

[121] Antoine Georges, "Condensed matter physics with light and atoms: Strongly correlated cold fermions in optical lattices," arXiv:cond-mat/0702122(2007), http://arxiv.org/abs/cond-mat/0702122.

[122] Thierry Giamarchi, *Quantum Physics in One Dimension* (Clarendon Press, 2003) ISBN 9780198525004.

[123] D. J. Scalapino, "Perspectives in many-particle physics," (North-Holland, 1994) Chap. Does the Hubbard model have the right stuff?, pp. 95–125.

[124] D. Scalapino, "Numerical studies of the 2D Hubbard model," in *Handbook of High-Temperature Superconductivity*, edited by J. Schrieffer and James Brooks (Springer New York, 2007) pp. 495–526, ISBN 978-0-387-68734-6.

[125] D. Zanchi and H. J. Schulz, "Superconducting instabilities of the non-half-filled Hubbard model in two dimensions," Phys. Rev. B **54**, 9509–9519 (Oct 1996).

[126] S. Sorella, G. B. Martins, F. Becca, C. Gazza, L. Capriotti, A. Parola, and E. Dagotto, "Superconductivity in the two-dimensional $t - J$ model," Phys. Rev. Lett. **88**, 117002 (Feb 2002), http://link.aps.org/doi/10.1103/PhysRevLett.88.117002.

[127] S. Raghu, S. A. Kivelson, and D. J. Scalapino, "Superconductivity in the repulsive Hubbard model: An asymptotically exact weak-coupling solution," Phys. Rev. B **81**, 224505 (Jun 2010).

[128] T. A. Maier, M. Jarrell, T. C. Schulthess, P. R. C. Kent, and J. B. White, "Systematic study of d-wave superconductivity in the 2D repulsive Hubbard model," Phys. Rev. Lett. **95**, 237001 (Nov 2005), http://link.aps.org/doi/10.1103/PhysRevLett.95.237001.

[129] C. Huscroft, M. Jarrell, Th. Maier, S. Moukouri, and A. N. Tahvildarzadeh, "Pseudogaps in the 2D Hubbard model," Phys. Rev. Lett. **86**, 139–142 (Jan 2001), http://link.aps.org/doi/10.1103/PhysRevLett.86.139.

[130] B. Kyung, S. S. Kancharla, D. Sénéchal, A.-M. S. Tremblay, M. Civelli, and G. Kotliar, "Pseudogap induced by short-range spin correlations in a doped Mott insulator," Physical Review B (Condensed Matter and Materials Physics) **73**, 165114 (2006), http://link.aps.org/abstract/PRB/v73/e165114.

[131] Nan Lin, Emanuel Gull, and Andrew J. Millis, "Physics of the pseudogap in eight-site cluster dynamical mean-field theory: Photoemission, Raman scattering, and in-plane and c-axis conductivity," Phys. Rev. B **82**, 045104 (Jul 2010), http://link.aps.org/doi/10.1103/PhysRevB.82.045104.

[132] Federico Becca and Sandro Sorella, "Nagaoka ferromagnetism in the two-dimensional infinite-U Hubbard model," Phys. Rev. Lett. **86**, 3396–3399 (Apr 2001), http://link.aps.org/doi/10.1103/PhysRevLett.86.3396.

[133] Yosuke Nagaoka, "Ferromagnetism in a narrow, almost half-filled s band," Phys. Rev. **147**, 392–405 (Jul 1966), http://link.aps.org/doi/10.1103/PhysRev.147.392.

[134] Chia-Chen Chang, Shiwei Zhang, and David M. Ceperley, "Itinerant ferromagnetism in a Fermi gas with contact interaction: Magnetic properties in a dilute Hubbard model," Phys. Rev. A **82**, 061603 (Dec 2010), http://link.aps.org/doi/10.1103/PhysRevA.82.061603.

[135] J. Bonča, J. E. Gubernatis, M. Guerrero, Eric Jeckelmann, and Steven R. White, "Stripes in a three-chain Hubbard ladder: A comparison of density-matrix renormalization group and constrained-path Monte Carlo results," Phys. Rev. B **61**, 3251–3254 (Feb 2000), http://link.aps.org/doi/10.1103/PhysRevB.61.3251.

[136] R. Rodríguez-Guzmán, Carlos A. Jiménez-Hoyos, and Gustavo E. Scuseria, "Variational description of the ground state of the repulsive two-dimensional Hubbard model in terms of nonorthogonal symmetry-projected Slater determinants," Phys. Rev. B **90**, 195110 (Nov 2014), http://link.aps.org/doi/10.1103/PhysRevB.90.195110.

[137] R. A. Hart, P. M. Duarte, T.-L. Yang, X. Liu, T. Paiva, E. Khatami, R. T. Scalettar, N. Trivedi, D. A. Huse, and R. G. Hulet, "Observation of antiferromagnetic correlations in the Hubbard model with ultracold atoms," Nature **519**, 211–214 (Mar 2015), http://dx.doi.org/10.1038/nature14223.

[138] Z. Y. Meng, T. C. Lang, S. Wessel, F. F. Assaad, and A. Muramatsu, "Quantum spin liquid emerging in two-dimensional correlated Dirac fermions," Nature **464**, 847–851 (Apr 2010), http://dx.doi.org/10.1038/nature08942.

[139] Sandro Sorella, Yuichi Otsuka, and Seiji Yunoki, "Absence of a spin liquid phase in the Hubbard model on the honeycomb lattice," Sci. Rep. **2**, 992 (Dec 2012), http://dx.doi.org/10.1038/srep00992.

[140] Fakher F. Assaad and Igor F. Herbut, "Pinning the order: The nature of quantum criticality in the Hubbard model on honeycomb lattice," Phys. Rev. X **3**, 031010 (Aug 2013), http://link.aps.org/doi/10.1103/PhysRevX.3.031010.

[141] Baoming Tang, Thereza Paiva, Ehsan Khatami, and Marcos Rigol, "Short-range correlations and cooling of ultracold fermions in the honeycomb lattice," Phys. Rev. Lett. **109**, 205301 (Nov 2012), http://link.aps.org/doi/10.1103/PhysRevLett.109.205301.

[142] Baoming Tang, Thereza Paiva, Ehsan Khatami, and Marcos Rigol, "Finite-temperature properties of strongly correlated fermions in the honeycomb lattice," Phys. Rev. B **88**, 125127 (Sep 2013), http://link.aps.org/doi/10.1103/PhysRevB.88.125127.

[143] N. D. Mermin and H. Wagner, "Absence of ferromagnetism or antiferromagnetism in one- or two-dimensional isotropic Heisenberg models," Phys. Rev. Lett. **17**, 1133–1136 (Nov 1966), http://link.aps.org/doi/10.1103/PhysRevLett.17.1133.

[144] P. C. Hohenberg, "Existence of long-range order in one and two dimensions," Phys. Rev. **158**, 383–386 (Jun 1967), http://link.aps.org/doi/10.1103/PhysRev.158.383.

[145] Jan Kuneš, "Efficient treatment of two-particle vertices in dynamical mean-field theory," Phys. Rev. B **83**, 085102 (Feb 2011), http://link.aps.org/doi/10.1103/PhysRevB.83.085102.

[146] Michele Dolfi, Adrian Kantian, Bela Bauer, and Matthias Troyer, "Minimizing nonadiabaticities in optical-lattice loading," Phys. Rev. A **91**, 033407 (Mar 2015), http://link.aps.org/doi/10.1103/PhysRevA.91.033407.

[147] F. Werner, O. Parcollet, A. Georges, and S. R. Hassan, "Interaction-induced adiabatic cooling and antiferromagnetism of cold fermions in optical lattices," Phys. Rev. Lett. **95**, 056401 (Jul 2005), http://link.aps.org/doi/10.1103/PhysRevLett.95.056401.

[148] Shintaro Taie, Rekishu Yamazaki, Seiji Sugawa, and Yoshiro Takahashi, "An SU(6) Mott insulator of an atomic Fermi gas realized by large-spin Pomeranchuk cooling," Nat Phys **8**, 825–830 (Nov 2012), http://dx.doi.org/10.1038/nphys2430.

[149] Ehsan Khatami and Marcos Rigol, "Thermodynamics of strongly interacting fermions in two-dimensional optical lattices," Phys. Rev. A **84**, 053611 (Nov 2011), http://link.aps.org/doi/10.1103/PhysRevA.84.053611.

[150] Jean-Sébastien Bernier, Corinna Kollath, Antoine Georges, Lorenzo De Leo, Fabrice Gerbier, Christophe Salomon, and Michael Köhl, "Cooling fermionic atoms in optical lattices by shaping the confinement," Phys. Rev. A **79**, 061601 (Jun 2009), http://link.aps.org/doi/10.1103/PhysRevA.79.061601.

[151] Lorenzo De Leo, Jean-Sébastien Bernier, Corinna Kollath, Antoine Georges, and Vito W. Scarola, "Thermodynamics of the three-dimensional Hubbard model: Implications for cooling cold atomic gases in optical lattices," Phys. Rev. A **83**, 023606 (Feb 2011), http://link.aps.org/doi/10.1103/PhysRevA.83.023606.

[152] Michael Messer, Rémi Desbuquois, Thomas Uehlinger, Gregor Jotzu, Sebastian Huber, Daniel Greif, and Tilman Esslinger, "Exploring competing density order in the ionic Hubbard model with ultracold fermions," Phys. Rev. Lett. **115**, 115303 (Sep 2015), http://link.aps.org/doi/10.1103/PhysRevLett.115.115303.

[153] F. D. M. Haldane, "Model for a quantum Hall effect without Landau levels: Condensed-matter realization of the "parity anomaly"," Phys. Rev. Lett. **61**, 2015–2018 (Oct 1988), http://link.aps.org/doi/10.1103/PhysRevLett.61.2015.

[154] M Z Hasan and C L Kane, "Colloquium: Topological insulators," Rev. Mod. Phys. **82**, 3045–3067 (Nov. 2010), http://link.aps.org/doi/10.1103/RevModPhys.82.3045.

[155] Xiao-Liang Qi and Shou-Cheng Zhang, "Topological insulators and superconductors," Rev. Mod. Phys. **83**, 1057–1110 (Oct. 2011), http://link.aps.org/doi/10.1103/RevModPhys.83.1057.

[156] M Hohenadler and F F Assaad, "Correlation effects in two-dimensional topological insulators," J. Phys.: Condens. Matter **25**, 143201 (Mar. 2013), http://stacks.iop.org/0953-8984/25/i=14/a=143201?key=crossref.153440670502dcce4d049f7a3a249d47.

[157] M. Hohenadler, T. C. Lang, and F. F. Assaad, "Correlation effects in quantum spin-Hall insulators: A quantum Monte Carlo study," Phys. Rev. Lett. **106**, 100403 (Mar 2011), http://link.aps.org/doi/10.1103/PhysRevLett.106.100403.

[158] Hsiang-Hsuan Hung, Lei Wang, Zheng-Cheng Gu, and Gregory A. Fiete, "Topological phase transition in a generalized Kane-Mele-Hubbard model: A combined quantum Monte Carlo and Green's function study," Phys. Rev. B **87**, 121113 (Mar 2013), http://link.aps.org/doi/10.1103/PhysRevB.87.121113.

[159] Martin Bercx, Martin Hohenadler, and Fakher F. Assaad, "Kane-Mele-Hubbard model on the π-flux honeycomb lattice," Phys. Rev. B **90**, 075140 (Aug 2014), http://link.aps.org/doi/10.1103/PhysRevB.90.075140.

[160] C. Hickey, P. Rath, and A. Paramekanti, "Competing chiral orders in the topological Haldane-Hubbard model of spin-$\frac{1}{2}$ fermions and bosons," Phys. Rev. B **91**, 134414 (Apr 2015), http://link.aps.org/doi/10.1103/PhysRevB.91.134414.

[161] Ciarán Hickey, Lukasz Cincio, Zlatko Papić, and Arun Paramekanti, "Haldane-Hubbard Mott insulator: From tetrahedral spin crystal to chiral spin liquid," arxiv, 1509.08461(2015), http://arxiv.org/abs/1509.08461.

[162] D. Prychynenko and S. D. Huber, "Z2 slave-spin theory of a strongly correlated Chern insulator," arXiv, 1410.2001v1(2014), http://arxiv.org/abs/1410.2001v1.

[163] Jing He, Yan-Hua Zong, Su-Peng Kou, Ying Liang, and Shiping Feng, "Topological spin density waves in the Hubbard model on a honeycomb lattice," Phys. Rev. B **84**, 035127 (Jul 2011), http://link.aps.org/doi/10.1103/PhysRevB.84.035127.

[164] Wei Zheng, Huitao Shen, Zhong Wang, and Hui Zhai, "Magnetic-order-driven topological transition in the Haldane-Hubbard model," Phys. Rev. B **91**, 161107 (Apr 2015), http://link.aps.org/doi/10.1103/PhysRevB.91.161107.

[165] Jing He, Su-Peng Kou, Ying Liang, and Shiping Feng, "Chiral spin liquid in a correlated topological insulator," Phys. Rev. B **83**, 205116 (May 2011), http://link.aps.org/doi/10.1103/PhysRevB.83.205116.

[166] V. S. Arun, R. Sohal, C. Hickey, and A. Paramekanti, "Mean field study of the topological Haldane-Hubbard model of spin-1/2 fermions," arxiv, 1510.08856(2015), http://arxiv.org/abs/1510.08856.

[167] Renate Landig, Lorenz Hruby, Nishant Dogra, Manuele Landini, Rafael Mottl, Tobias Donner, and Tilman Esslinger, "Quantum phases emerging from competing short- and long-range interactions in an optical lattice," arxiv, 1511.00007(2015), http://arxiv.org/abs/1511.00007.

[168] J. E. Gubernatis, Mark Jarrell, R. N. Silver, and D. S. Sivia, "Quantum Monte Carlo simulations and maximum entropy: Dynamics from imaginary-time data," Phys. Rev. B **44**, 6011–6029 (Sep 1991), http://link.aps.org/doi/10.1103/PhysRevB.44.6011.

[169] B Bauer, L D Carr, H G Evertz, A Feiguin, J Freire, S Fuchs, L Gamper, J Gukelberger, E Gull, S Guertler, A Hehn, R Igarashi, S V Isakov, D Koop, P N Ma, P Mates, H Matsuo, O Parcollet, G Pawlowski, J D Picon, L Pollet, E Santos, V W Scarola, U Schollwock, C Silva, B Surer, S Todo, S Trebst, M Troyer, M L Wall, P Werner, and S Wessel, "The ALPS project release 2.0: open source software for strongly correlated systems," Journal of Statistical Mechanics: Theory and Experiment **2011**, P05001 (2011), http://stacks.iop.org/1742-5468/2011/i=05/a=P05001.

[170] Zhong Wang and Binghai Yan, "Topological Hamiltonian as an exact tool for topological invariants," Journal of Physics: Condensed Matter **25**, 155601 (2013), http://stacks.iop.org/0953-8984/25/i=15/a=155601.

[171] Takahiro Fukui, Yasuhiro Hatsugai, and Hiroshi Suzuki, "Chern numbers in discretized Brillouin zone: Efficient method of computing (spin) Hall conductances," Journal of the Physical Society of Japan **74**, 1674–1677 (2005), http://dx.doi.org/10.1143/JPSJ.74.1674, http://dx.doi.org/10.1143/JPSJ.74.1674.

[172] Jingxiang Wu, Jean Paul Latyr Faye, David Sénéchal, and Joseph Maciejko, "A quantum cluster approach to the spinful Haldane-Hubbard model," arxiv, 1512.04498(2015), http://arxiv.org/abs/1512.04498.

[173] Zhao-Long Gu, Kai Li, and Jian-Xin Li, "Topological phase transitions and topological Mott insulator in Haldane-Hubbard model," arxiv, 1512.05118(2015), http://arxiv.org/abs/1512.05118.

[174] Wei Wu and A.-M. S. Tremblay, "Phase diagram and Fermi liquid properties of the extended Hubbard model on the honeycomb lattice," Phys. Rev. B **89**, 205128 (May 2014), http://link.aps.org/doi/10.1103/PhysRevB.89.205128.

[175] N. Paris, K. Bouadim, F. Hebert, G. G. Batrouni, and R. T. Scalettar, "Quantum Monte Carlo study of an interaction-driven band-insulator–to–metal transition," Phys. Rev. Lett. **98**, 046403 (Jan 2007), http://link.aps.org/doi/10.1103/PhysRevLett.98.046403.

[176] S. S. Kancharla and E. Dagotto, "Correlated insulated phase suggests bond order between band and Mott insulators in two dimensions," Phys. Rev. Lett. **98**, 016402 (Jan 2007), http://link.aps.org/doi/10.1103/PhysRevLett.98.016402.

[177] K. Bouadim, N. Paris, F. Hébert, G. G. Batrouni, and R. T. Scalettar, "Metallic phase in the two-dimensional ionic Hubbard model," Phys. Rev. B **76**, 085112 (Aug 2007), http://link.aps.org/doi/10.1103/PhysRevB.76.085112.

[178] H.-F. Lin, H.-D. Liu, H.-S. Tao, and W.-M. Liu, "Phase transitions of the ionic Hubbard model on the honeycomb lattice," Sci. Rep. **5** (2015), doi: \bibinfo{doi}{10.1038/srep09810}, http://theory.iphy.ac.cn/English/paper/srep.5.9810.pdf.

[179] Tuomas I. Vanhala, Topi Siro, Long Liang, Matthias Troyer, Ari Harju, and Päivi Törmä, "Topological phase transitions in the repulsively interacting haldane-hubbard model," Phys. Rev. Lett. **116**, 225305 (Jun 2016), http://link.aps.org/doi/10.1103/PhysRevLett.116.225305.

[180] Ansgar Liebsch, "Comment on "Absence of spin liquid in nonfrustrated correlated systems"," Phys. Rev. Lett. **111**, 029701 (Jul 2013), http://link.aps.org/doi/10.1103/PhysRevLett.111.029701.

[181] S. R. Hassan and David Sénéchal, "Hassan and Sénéchal reply:," Phys. Rev. Lett. **111**, 029702 (Jul 2013), http://link.aps.org/doi/10.1103/PhysRevLett.111.029702.

[182] Christopher N. Varney, Kai Sun, Marcos Rigol, and Victor Galitski, "Interaction effects and quantum phase transitions in topological insulators," Phys. Rev. B **82**, 115125 (Sep 2010), http://link.aps.org/doi/10.1103/PhysRevB.82.115125.

[183] Lei Wang, Hao Shi, Shiwei Zhang, Xiaoqun Wang, Xi Dai, and X. C. Xie, "Charge-density-wave and topological transitions in interacting Haldane model," arxiv, 1012.5163(2010), http://arxiv.org/abs/1012.5163.

[184] Christopher N. Varney, Kai Sun, Marcos Rigol, and Victor Galitski, "Topological phase transitions for interacting finite systems," Phys. Rev. B **84**, 241105 (Dec 2011), http://link.aps.org/doi/10.1103/PhysRevB.84.241105.

[185] Peter W. J. Staar, *Dynamical cluster approximation with continuous lattice self-energy*, Ph.D. thesis, ETH Zurich (2013), http://e-collection.library.ethz.ch/view/eth:8018.

[186] R. T. Scalettar, D. J. Scalapino, R. L. Sugar, and D. Toussaint, "Hybrid molecular-dynamics algorithm for the numerical simulation of many-electron systems," Phys. Rev. B **36**, 8632–8641 (Dec 1987), http://link.aps.org/doi/10.1103/PhysRevB.36.8632.

[187] Hiroaki Kusunose, "Influence of spatial correlations in strongly correlated electron systems: Extension to dynamical mean field approximation," Journal of the Physical Society of Japan **75**, 054713 (2006), http://dx.doi.org/10.1143/JPSJ.75.054713, http://dx.doi.org/10.1143/JPSJ.75.054713.

[188] A. Toschi, A. A. Katanin, and K. Held, "Dynamical vertex approximation: A step beyond dynamical mean-field theory," Phys. Rev. B **75**, 045118 (Jan 2007), http://link.aps.org/doi/10.1103/PhysRevB.75.045118.

[189] Gang Li, Nils Wentzell, Petra Pudleiner, Patrik Thunström, and Karsten Held, "Efficient implementation of the Parquet equations – role of

the reducible vertex function and its kernel approximation," arxiv, 1510.03330(2015), http://arxiv.org/abs/1510.03330.

[190] A. N. Rubtsov, M. I. Katsnelson, and A. I. Lichtenstein, "Dual fermion approach to nonlocal correlations in the Hubbard model," Phys. Rev. B **77**, 033101 (Jan 2008), http://link.aps.org/doi/10.1103/PhysRevB.77.033101.

[191] C Slezak, M Jarrell, Th Maier, and J Deisz, "Multi-scale extensions to quantum cluster methods for strongly correlated electron systems," Journal of Physics: Condensed Matter **21**, 435604 (2009), http://stacks.iop.org/0953-8984/21/i=43/a=435604.

[192] C. Knecht, Master's thesis, Johannes Gutenberg - Universität Mainz (2002).

[193] A. Comanac, *Dynamical mean field theory of correlated electron systems: New algorithms and applications to local observables*, Ph.D. thesis, Columbia University (2007).

[194] Carsten Lothar Knecht, *Numerical and analytical approaches to strongly correlated electron systems*, Ph.D. thesis, Johannes Gutenberg - Universität Mainz (2006).

[195] Emanuel Gull, *Continuous-time quantum Monte Carlo algorithms for fermions*, Ph.D. thesis, ETH Zürich (2008), http://e-collection.library.ethz.ch/eserv/eth:31103/eth-31103-02.pdf.

[196] Nan Lin, Emanuel Gull, and Andrew J. Millis, "Two-particle response in cluster dynamical mean-field theory: Formalism and application to the raman response of high-temperature superconductors," Phys. Rev. Lett. **109**, 106401 (Sep 2012), http://link.aps.org/doi/10.1103/PhysRevLett.109.106401.

[197] Gareth O. Roberts and Jeffrey S. Rosenthal, "Optimal scaling of discrete approximations to Langevin diffusions," Journal of the Royal Statistical Society: Series B (Statistical Methodology) **60**, 255–268 (1998), ISSN 1467-9868, http://dx.doi.org/10.1111/1467-9868.00123.

[198] Joaquín E. Drut and Amy N. Nicholson, "Lattice methods for strongly interacting many-body systems," Journal of Physics G: Nuclear and Particle Physics **40**, 043101 (2013), http://stacks.iop.org/0954-3899/40/i=4/a=043101

Acknowledgement

Thanks to my supervisor, Matthias Troyer, I was given the opportunity to spend four and half years at the top of world's research in physics, at ETH Zurich. I am very grateful to him for this unique chance. His courses on computational quantum physics, programming techniques, and high performance computation were an essential prerequisite to my projects during the PhD study, and valueable to my future career. His management skills and great visions are building blocks for a vital group of capable people provided with all resources needed to conduct a first quality research. In the process of paper writing, he always managed to significantly improve the manuscripts with respect to its logic, readability, self-contained presentation, and other aspects.

With Emanuel Gull I started my initial project and he was my first address for questions considering DCA and CT-AUX. Although we met in person only few times, his remote support was important for me to get started and to develop an understanding for the methods. His implementation of CT-AUX allowed me to start my first project without writing the impurity solver from scratch. In the role of the co-examiner his guidance continued over my entire PhD.

Philipp Werner taught an advanced course on *Extensions of Dynamical Mean Field Theory* for a handful of students during my first semester at ETH. By that he provided my first intensive contact with DMFT, which turned out to be another useful ingredient for my future projects.

Lei Wang was undoubtedly the most influential adviser in the second half of my study. He introduced me to the interacting topologically non-trivial models, which was the topic of my last project. With him I was fortunate to participate at the development of his genuine fidelity susceptibility Monte Carlo estimator.

With Jan Gukelberger I spent, apart from physical discussions on Feynman diagram related topics, as well several tours in the Swiss Alps, among them as well my first glacier skitour. In addition, the LaTeX template of this thesis is based on his template. Special thanks goes to Michele Dolfi, who patiently solved my issues with building ALPS anytime I was stuck. The former postdoc Mauro Iazzi was

a great help to fill my missing pieces of knowledge and address them appropriately. All present and former group members deserve my gratitude for creating a pleasant workplace with immense amount of skills and experience, and for willingness to share them – *merci vielmol* to Alexey Soluyanov, Hiroshi Shinaoka, Kiryl Pakrouski, Iztok Pizorn, Georg Winkler, Juan Osorio, Ilia Zintchenko, Andreas Hehn, and to all others.

An intensive collaboration with experimentalists in the optical lattice team of Prof. Esslinger's group enabled me an exciting connection of the numerical outcomes with extremely clean experiments performed *in vitro*. Our relations went beyond the common publication and included feedback on my manuscript dealing with stacked lattices. Thanks to Daniel Greif, Thomas Uehlinger, Gregor Jotzu, and Michael Messer.

Members of the Thomas Schulthess' computational group shall not be avoided in this acknowledgement, especially Peter Staar, with whom I discussed various DCA specific topics.

As a devoted teaching assistant of the Institute of theoretical physics (ITP) I wish to appreciate great collaboration with professors M. Gaberdiel, V. Geshkenbein, M. Sigrist, R. Teyssier, and M. Troyer. A fact which makes me happy is that several of my former students are now members of ITP.

To my former supervisor of the master and bachelor thesis, Richard Hlubina, I want to express thanks for many hours of individual consultations, from which I profited during my studies at ETH. I kept his lecture notes always at hand as a reliable source of information for topics on condensed matter.

For reading parts of the manuscript I wish to thank to Tomáš Bzdušek, Samuel and Jana I., Georg Winkler, Andreas Hehn, Michael Messer, Guglielmo Mazzola, and Juan Osorio.

From the non-academic community I want to thank at most to my wife Eva for support during my PhD studies.